Solution-Processed Lead Zirconate Titanate as an Interfacial Modifier in Hybrid Oxide/Polymer Solar Cells

Robert Merrill Hewlett

Imperial College London

Department of Materials

A thesis submitted in fulfilment of the requirements for the degree of

Doctor of Philosophy

January 2015

Foreword

This thesis was written on the basis of research undertaken at the Department of Materials, Imperial College London in the between October 2010 and April 2014, excluding the period June to August 2013. The work reported here is my own with the exception of the following:

1. Transmission electron microscopy images presented in this work were carried out as follows: in Figure 3.5, sample *iv)* was prepared and imaged by Dr James B. Gilchrist. In the same figure, the cross-section of the ZnO–P3HT film in *ii)* was prepared by Claire Burgess and imaged by Dr Catriona McGilvery, who also obtained the micrographs displayed in Figures 3.4, 3.13, and 3.14. The ZnO–PZT images presented in Figures 3.13, 3.14, and 3.15 were carried out by Dr James B. Gilchrist (preparation) and Dr Catriona McGilvery (imaging).

2. The secondary ion mass spectrometry data presented in Figures 3.12 and 4.5 was acquired by Dr Sarah Fearn.

3. The X-ray photoelectron spectroscopy measurements presented in Figures 4.3 & 4.4 were carried out and processed at the Department of Chemistry, University of Arizona by Dr Erin Ratcliff.

4. The transient absorption spectroscopy data shown in Figure 5.4 were recorded by Karunanantharajah Prashanthan in the Department of Chemistry, Imperial College London whilst working towards his Master's thesis under the supervision of Dr Saif Haque; the results were originally presented in his work "Transient Absorption Studies on Metal Oxide/Polymer Solar Cells", whilst additional analysis and interpretation of the data are added here.

The experimental results from this study have been the subject of an oral presentation at the following conference:

Hewlett, R. M.; Zhang, Q.; Stingelin, N.; McLachlan, M. A.; *The role of ferroelectric interlayers on hybrid photovoltaic device performance*, Symposium O: Next-Generation Polymer-based Organic Photovoltaics, Materials Research Society Fall Meeting, Boston November 2012.

Abstract

Due to its excellent optoelectronic properties and ease of processing. ZnO has been considered a promising acceptor material in oxide:polymer hybrid photovoltaics (hPVs); however, devices have consistently underperformed for a number of reasons including poor charge generation and high recombination rates. The characteristics of the oxide:polymer interface have been cited as crucial in determining device performance: to this end, modification of the interface with both molecular and inorganic species has been shown to yield significant improvement. In this study, growth of the perovskite ferroelectric material lead zirconate titanate (PZT) is carried out on ZnO using sol-gel deposition. Subsequently, the PZT layers are used to modify the donor–acceptor interface in ZnO:poly(3-hexylthiophene) (P3HT) hPV devices: this study is carried out in order to lay the foundations for future investigations into the effect of ferroelectric properties on organic-based photovoltaics using inorganic ferroelectric materials.

PZT was confirmed to crystallise on ZnO in the tetragonal phase and microstructural characterisation by atomic force microscopy revealed that the ZnO–PZT films consist of small, tightly packed PZT grains, indicating that the ZnO substrates provide a high seeding density for PZT. The ZnO–PZT interface was studied to determine the way by which growth proceeds in these films: whilst it was found that intermixing between the constituent elements of the two materials does not occur, transmission electron microscopy of the interface revealed the presence of a secondary phase thought to be orthorhombic PbO — it is hypothesised that this phase plays a role in the crystallisation of PZT. Growth and characterisation of low thickness PZT (< 15 nm) was conducted, confirming the crystallisation of tetragonal PZT for a film thickness of ~ 11 nm.

Finally, the modification of the ZnO:P3HT with PZT was shown to have a positive effect on hPV performance: using transient absorption spectroscopy, the presence of the PZT layer was seen to increase the hole polaron lifetime from 15 μs to 2 ms, indicating a suppression of charge recombination. The open-circuit voltage (V_{oc}) of the hPV devices was observed to increase from 0.162 to 0.734 V; moreover, prolonged illumination of up to 30 minutes led to further increases in V_{oc}, reaching a maximum of 0.947 V — this was attributed to the progressive filling of electron traps with photoexcited charges, leading to a reduction in trap-assisted charge recombination.

Acknowledgements

I have been extremely fortunate to have had so much support throughout the last four years, both in my research and personally. No thesis is completed alone and this no exception — future reflection on this work will forever remind me not only of my own efforts, but also the efforts of others and their support which has gone above and beyond what I ever could have expected.

Firstly, I am eternally grateful to my supervisor Dr Martyn McLachlan who not only gave me the freedom to follow my interests, but also who has worked hard to set up collaborations for me and to give me every chance to succeed. I have been extremely well looked after over the last few years, especially in the last two which have proved to be particularly difficult — I feel extremely fortunate to have had such patient support when it would have been easy for me to fall by the wayside.

I've received plenty of help over the course of my research: Dr Qi Zhang at Cranfield University who made this project possible by supplying both the PZT sol-gel and excellent advice in processing the material; Dr Cephas Small who taught me so much about photovoltaics in an extremely short amount of time and helped me to design the experiments in Chapter 5; Dr Erin Ratcliff at the University of Arizona for the XPS data and guidance in interpretation; Dr James B. Gilchrist and Dr Catriona McGilvery for carrying out the TEM imaging; Dr Ali Nedoma for some excellent (and fun!) discussions on AFM; Dr Sarah Fearn for the ToF-SIMS data and her help with the analysis.

I would also like to thank the McLachlan group: Dr Jon Downing for showing me the ropes during my first couple of years; Portuguese Jorge Costa for enduring my abuse, ramblings, and incessant music recommendations (as well as providing excellent discussion in device physics *et al.*); Kirsty Roy for making the office that bit more fun and for letting me burn down her equipment; and to Claire Burgess, Yoann Porte, Rob Maller, and Jiaqi Zhang for anime, crude drawings, chocolate, gifts from the East and helping me out with bits and pieces (such as TEM sample preparation!).

Lastly, I owe so much to my friends especially Clemy, Toby, Jimmy, and especially the long-suffering Katie Bank without whom I likely wouldn't be writing this — she has been there for me in spite of everything that I've thrown at her and has been a true companion.

Contents

List of Acronyms

3DOM . . . . . .3-dimensional ordered macroporous [structure]

AES . . . . . .Auger electron spectroscopy

AFM . . . . . .Atomic force microscopy

ALD . . . . . .Atomic layer deposition

BHJ . . . . . .Bulk-heterojunction

CB . . . . . .Conduction band

CT . . . . . .Charge-transfer [state]

CVD . . . . . .Chemical vapour deposition

D_f . . . . . .Fractal dimension

D–A . . . . . .Donor–acceptor

DSSC . . . . . .Dye-sensitised solar cell

E_g . . . . . .Band-gap energy

EBL . . . . . .Electron blocking layer

FE . . . . . .Ferroelectric

FF . . . . . .Fill-factor

FWHM . . . . . .Full-width at half-maximum

GI-XRD . . . . . .Grazing-incidence X-ray diffraction

HBL . . . . . .Hole-blocking layer

HHCF . . . . . .Height-height correlation function

HOMO . . . . . .Highest occupied molecular orbital

hPV . . . . . .Hybrid photovoltaic

IM . . . . . .Interface modifier

IPA . . . . . .Isopropyl alcohol

ITO . . . . . .Indium tin oxide

J–V . . . . . .Current density–Voltage

J_{sc} . . . . . .Short-circuit current density

L_{ex} . . . . . .Exciton diffusion length

LED . . . . . .Light-emitting diode

LUMO . . . . . .Lowest unoccupied molecular orbital

M_n . . . . . .Number-average molecular weight

M_w . . . . . .Weight-average molecular weight

MeOH . . . . . .Methanol

NP . . . . . .Nanoparticle

NR . . . . . .Nanorod

OPV . . . . . .Organic photovoltaic

P(VDF–TrFE) . . . .poly(vinylidene difluoride–tetrafluoroethylene)

P3HT . . . . . .poly(3-hexyl)thiophene

PCBA . . . . . .phenyl-C_{61}-butyric acid

PCBM . . . . . .phenyl-C_{61}-butyric acid methyl ester

PCE (or η) . . . . . .Power conversion efficiency %

PEDOT:PSS . . . . .poly(3,4-ethylenedioxythiophene):polystyrene sulphonate

PES . . . . . .Photoelectron spectroscopy

PFM . . . . . .Piezoresponse force microscopy

PL . . . . . .Photoluminescence [spectroscopy]

PLD . . . . . .Pulsed laser deposition

PrH . . . . . .Preheated furnace

PSD . . . . . .Power spectral density [function]

PV . . . . . .Photovoltaic

PZT . . . . . .Lead zirconate titanate

R_{RMS} . . . . . .Roughness (root mean squared)

R_s . . . . . .Series resistance

R_{sh} . . . . . .Shunt resistance

R-PSD . . . . . .Radial power spectral density [function]

R_a . . . . . .Roughness (arithmetic)

RPI . . . . . .Relative peak intensity

SAM . . . . . .Self-assembled monolayer

SEM . . . . . .Scanning electron microscopy

SG . . . . . .Sol-gel

Sol-Z . . . . . .Sol-gel-derived ZnO

SP . . . . . .Spray pyrolysis

SP-Z . . . . . .Spray-pyrolysed ZnO

TAS . . . . . .Transient absorption spectroscopy

TCO . . . . . .Transparent conducting oxide

TEM . . . . . .Transmission electron microscopy

TFT . . . . . .Thin-film transistor

ToF-SIMS . . . . . .Time-of-flight secondary ion mass spectrometry

UHV . . . . . .Ultra-high vacuum

UPS . . . . . .Ultraviolet photoelectron spectroscopy

UV-vis . . . . . .Ultraviolet-visible spectroscopy

UV–O_3 . . . . . .UV–ozone [treatment]

V_{oc} . . . . . .Open-circuit voltage

VB . . . . . .Valence band

XPS . . . . . .X-ray photoelectron spectroscopy

XRD . . . . . .X-ray diffraction

Chapter 1

Introduction to Hybrid Inorganic–Organic Photovoltaics

1.1 History of Photovoltaics

Although the Becquerels first discovered the photovoltaic effect over 170 years ago, the advent of solar energy as a relevant power source has taken a long time, predominantly due to the plentiful supply of non-renewable fuel sources and the only relatively recent understanding of the environmental concerns associated with fossil fuel consumption. After the development of the first photovoltaic (PV) cell by Fritts in 1883 — a layer of selenium sandwiched between two gold electrodes — these devices received little attention until the latter half of the 1940s, when Ohl's ground-breaking work on the semiconductor p–n junction at Bell Labs paved the way for the development of modern electronic devices, such as the transistor, diode, and solar cell [1]. In 1946, Ohl was granted the first patent for a p–n junction based, 'Light-sensitive electric device' [2], and within a decade, Bell Labs unveiled the first modern solar cell, operating with a power conversion efficiency (PCE) of 6 % [3]. However, processing costs proved to be prohibitive in commercialising the product as producing silicon of requisite purity was expensive at the time; as a result, the technology was mostly restricted to niche applications, most notably as a key component for spacecraft and satellites.

PV research experienced a surge in the 1970s due to changes in manufacturing and politics, leading to developments that would see solar power grow into an important technology: firstly, the booming electronics industry created an ever-increasing demand for large volumes of cheaper Si, leading to advances in semiconductor processing which, in turn, decreased the manufacturing costs for PV technology owing to economies of scale — moreover, the development of efficient devices using lower grade material led to another significant drop in costs; secondly, the 1973 Oil Crisis caused major supply and economy disruptions to NATO countries and, consequently, pressured both oil and

technology companies into making significant investments into fledgling renewable energy solutions, including solar power. These two factors brought around ideal conditions for massive growth in solar research, and led to numerous key breakthroughs including: in crystalline solar cells, the implementation of 'impure' forms of Si such as polycrystalline (pc-Si) and amorphous (a-Si) [4] into devices, as opposed to the much more costly wafer-produced monocrystalline Si (mono-Si); the development of alternative semiconducting materials such as GaAs [5] and CdTe [6]; and the growth of thin-film device technology, which opened the door towards lower cost and lower profile solar cells.

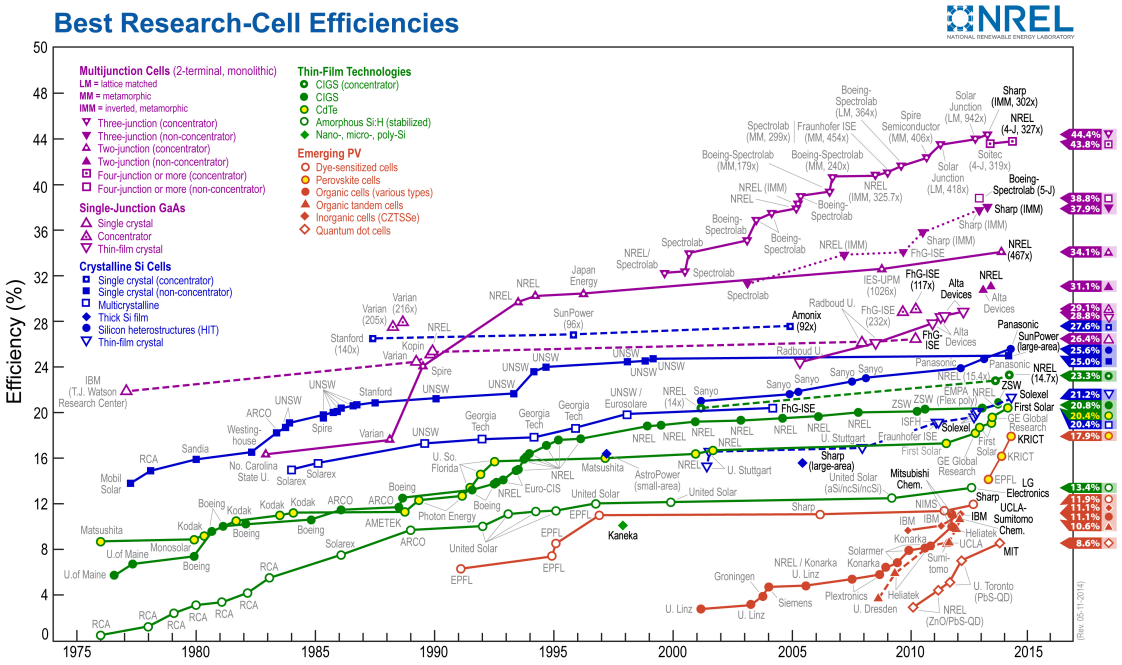

Figure 1.1 – Chart of certified efficiencies for research solar cells as of May 2014. This plot is courtesy of the National Renewable Energy Laboratory, Golden, CO [7].

'Emerging photovoltaics' is a term applied to the third generation of photovoltaic technology, encompassing organic photovoltaics (OPVs), hybrid photovoltaics (hPVs), dye-sensitised solar cells (DSSCs), and ink-based inorganic cells which use materials such as CIGS (copper–indium–gallium–selenium) [8]. Although the concepts underpinning these types of devices have been known for a comparatively long time — the electrochemical principles of DSSCs were first demonstrated using chlorophyll in 1972 [9], and the photovoltaic effect was demonstrated in organic materials by Kearns and Calvin in 1958 [10] — the development of appropriate materials was required before these could be implemented in PV: for DSSCs, the advent of nanostructured TiO_2 and an effective electrolyte culminated in the development of the Grätzel–O'Regan cell [11] in 1988; for OPVs, the development of both the donor–acceptor (D–A) heterojunction cell [12] and new semi-

conducting organic materials (especially polymers such as the poly(alkylthiophenes) [13]) in the mid-1980s led to widespread research and interest in the field.

1.2 Organic-based Emerging Photovoltaic Technologies

Organic-based emerging PV, encompassing OPVs[1] and DSSCs, are different materials systems to inorganic PV in that they use molecular components (such as dyes, polymers, and small molecules) as light-absorbers. Both OPVs and DSSCs are based on the concept of a heterojunction between a light-absorbing donor species and an electron-accepting acceptor species, rather than the asymmetrically doped p–n junction used in inorganic PV technologies. Typical device architectures for these two groups are shown in Figure 1.2.

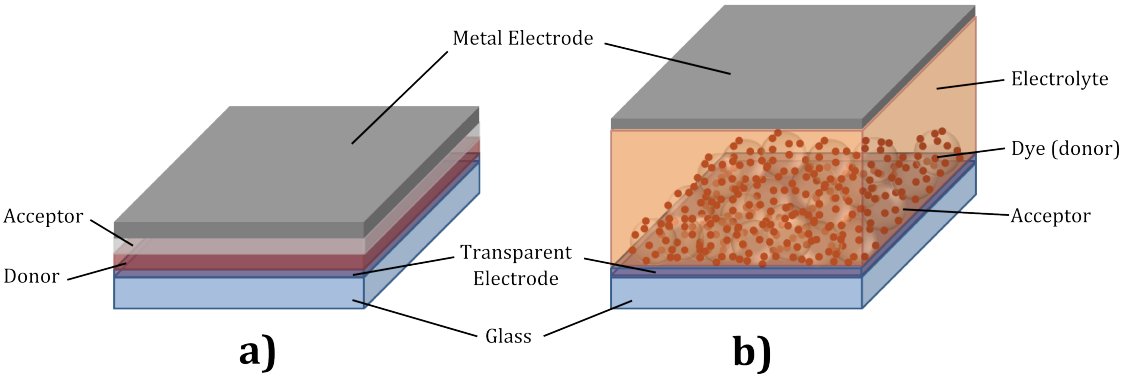

Figure 1.2 – Simple representations of a) a bilayer organic solar cell, and b) a dye-sensitised solar cell.

Both OPVs and DSSCs are multilayered structures, consisting of a transparent electrode on a transparent substrate, onto which the active layer (consisting of donor and acceptor components) is deposited and capped with a top electrode, typically a metal. Although OPVs and DSSCs share some underlying principles, the two classes of cells operate differently: OPVs are based on organic semiconductors, whereas DSSC technology is rooted in electrochemical foundations.

A basic OPV device consists of two electrodes sandwiching a two-component active layer consisting of *i)* a photoactive, low band-gap organic species, such as a polymer or a small molecule, and *ii)* a suitable acceptor species. The basic mode of operation for

[1] As the operating principles of OPVs and hPVs are very similar, in Sections 1.2 and 1.3 the use of the abbreviation 'OPV' implicitly includes 'hPV'; the abbreviation OPV is used as this is the dominant technology.

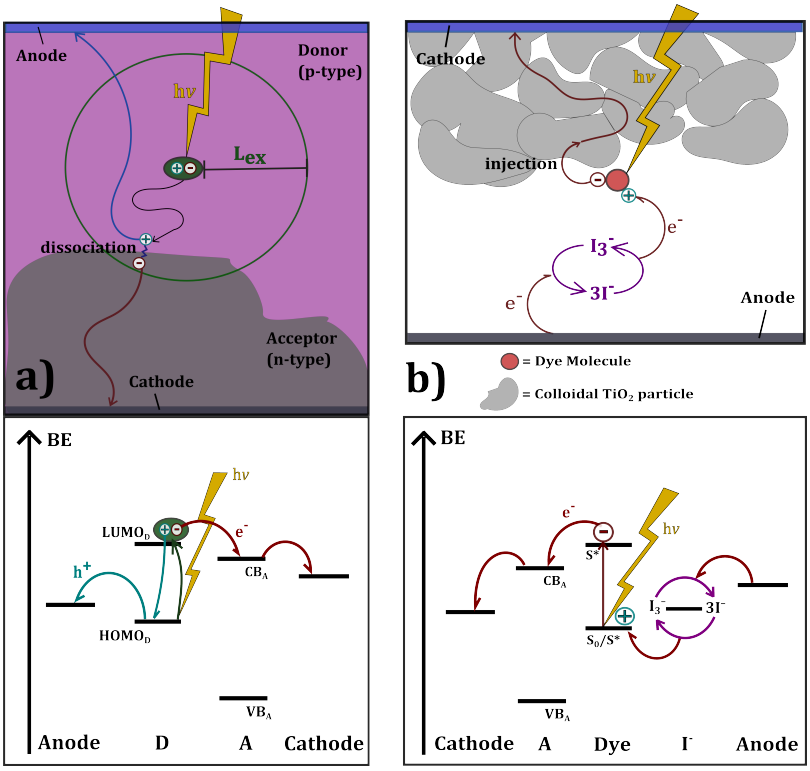

Figure 1.3 – Simple representation of operation and corresponding energy level diagrams for a typical a) OPV and b) electrochemical solar cell (DSSC). BE is the binding energy for the different energy levels; hν represents incident photons; L_{ex} is the exciton diffusion length, the maximum distance that an exciton may diffuse before it decays back to its ground state – this is also represented by the green circle, as an exciton may travel in any direction; the LUMO (lowest unoccupied molecular orbital) and HOMO (highest occupied molecular orbital) are the valence energy levels of an organic species, whilst CB (conduction band) and VB (valence band) are the energy levels for an inorganic solid. In b), the dye molecule is excited from the ground state, S_0 to a photoexcited state, S^*, from which the electronically excited electron may be transferred from the dye to the CB of the acceptor.

an OPV is as follows: when irradiated with light, the donor species is photoexcited and forms electronically excited, bound electron–hole polaron pairs called Frenkel excitons. When the excitons reach the D–A interface, the exciton may dissociate into free charges — the hole remaining in the highest occupied molecular orbital (HOMO) of the donor, and the electron moving from the higher energy lowest unoccupied molecular orbital (LUMO, in the case of a molecular species) to the LUMO or conduction band (CB, for the case of an inorganic species) of an acceptor — which subsequently are able to diffuse towards their respective electrodes to drive the current.

In contrast, the DSSC active layer typically consists of three components — a dye, an acceptor, and an electrolyte, where the dye is adsorbed to the surface of the acceptor layer (typically a metal oxide network). In this system, the dye absorbs incident light,

leading to the photoexcitation of an electron — this can be injected into the CB of the acceptor species and then diffuse towards the bottom electrode. The dye is subsequently regenerated through transfer of an electron from the electrolyte. A comparison of these two systems is illustrated in Figure 1.3.

1.2.1 Motivation for Organic Photovoltaic Technology

Although the PCEs of organic-based emerging PV cells currently lag behind crystalline inorganic technology[2], they do possess a number of distinct advantages and make them well suited to small scale applications:

i) low-cost devices due to inexpensive starting materials and low energy materials processing from solution.

ii) low profile — a typical DSSC is ~ 5 μm thick and a typical OPV is on the order of 0.5 μm thick. As such, these cells are suitable for portable applications and allows for the possibility of flexible devices.

iii) good performance under reduced illumination — in crystalline solar cells, recombination kinetics dominate increasingly as incident light intensity decreases leading to sharp drops in performance under low light conditions. Due to the D–A nature of both OPVs and DSSCs involving single carrier injection, these particular recombination processes are much slower, and performance drops much less severely under such conditions.

iv) well suited to coating applications due to high transparency.

v) organic semiconductors may be designed and tuned to possess specific band gaps and energy levels, allowing tailoring of materials design to application.

The low cost and low profile of these types of devices likewise make them suitable for applications in the developing world, especially for rural electrification — for example, the introduction of photovoltaic–light-emitting diode (PV–LED) lamps in Cambodia as an alternative to kerosene lamps [14].

Whilst crystalline inorganic solar cells have been the primary driving force for the expansion of the solar energy market, mainly due to falling processing costs (the price

[2]Although organic-based PV is not seen as a technology to compete with inorganic PV at present, there are no theoretical limits to suggest that they cannot do so in the future, given sufficient development in materials and processing.

of crystalline Si cells has fallen by around 100 times between 1977 and 2013, from US$ 76.67 to US$ 0.74 per watt owing to economy of scale [15]), the current rate of solar energy uptake is still not sufficient to meet or exceed international targets for the next 20 – 30 years [16]. Although many of the current issues with solar power are engineering problems (*e.g.* energy storage), there is a need to expand its presence in the consumer sector (which also has the advantage of not being directly subjected to energy politics) encompassing both static, house-mounted solar panels and smaller scale applications, such as chargers for portable electronics. The latter is an apt niche for emerging photovoltaics, especially for OPVs and DSSCs — in 2010, G24i launched a laptop bag with a DSSC mounted on it for charging, the first example of its kind [17].

Type	GER (MJ m^{-2})	Solar Radiation (kWh m^{-2})	PCE	EPBT (years)	Ref
mono-Si	2900	1700	14 %	1.8	[18]
pc-Si	2300	1700	13 % 17 % 18 %	3.8 2.2 1.5	[19]
CdTe (TF)	966	1700	10.9 %	0.8	[20]
DSSC (TF)	1455	1700	8 %	0.8	[21]
OPV (TF)	2801	1700	5 % 10 %	4 2	[22]

Table 1.1 – Energy payback time (EPBT) for different photovoltaic devices. TF denotes thin-film cells.

Although solar cells are most often compared in terms of PCE, this alone speaks little as to a device's performance under real-world conditions, or to its viability in commercial terms. Energy sources may be more appropriately evaluated by using the concept of 'energy payback', the energy payback time (EPBT) being the period of time required for an energy source to generate enough power to compensate the energy consumed during its fabrication. This takes into account three major factors: gross energy requirement (GER), the total amount of 'embodied' energy, *i.e.* the amount of energy consumed in fabrication; the PCE of the device; device illumination which is heavily dependent on location — this can be difficult to model given the unpredictable nature of weather systems and the non-linear relationship between illumination and photocurrent generation. Table 1.1 gives a comparison of the EPBT values for different PV technologies.

Crystalline Si solar cells typically have a very high gross energy input, as fabrication often requires energy-intensive deposition techniques – mono-Si wafers are produced

by the Czochralski method which requires sufficient temperatures ($\sim$ 1500 °C) to melt Si, whilst the predominant technique for depositing pc-Si is chemical vapour deposition (CVD), which requires an inert atmosphere and moderately high temperatures (600 °C) to grow silicon crystallites from SiH_4 gas. As OPVs have not yet entered mass production, the GER is currently quite high: in García-Valverde's 2010 paper detailing the life-cycle analysis (LCA) of a typical bulk-heterojunction (BHJ — this term is defined below in Section 1.3.3) OPV device (using indium tin oxide (ITO) as the anode, a blend of poly(3-hexylthiophene) (P3HT, a donor polymer) and phenyl-C_{61}-butyric acid methyl ester (PCBM, a fullerene acceptor molecule) as the active D–A layer, poly(3,4-ethylenedioxythiophene) poly(styrenesulfonate) (PEDOT:PSS) as a hole-blocking layer, and Ca/Al as a top contact) [22], this was calculated to be 2800.79 MJ m^{-2}, compared to 2900 – 5240.00 MJ m^{-2} for a mono-Si cell [23, 18] and 1110.0 MJ m^{-2} for a thin film a-Si cell [24], a technology which is hoped to be superseded by OPVs when they are commercialised. However, it was found that, in terms of the embodied energy of the input materials, the production of ITO electrodes was the most energy-intensive process (50.39 % of the total embodied energy), whilst the second was the maintenance of an N_2 atmosphere (48.19 %). The other materials accounted for a mere 1.33 % of the total embodied energy. New, more easily processable materials are being developed as a replacement for ITO, whilst there are a number of ambient deposition techniques which may be used in OPV fabrication, and it is expected that these developments will drastically reduce the GER of OPVs and, ergo, the EPBT.

1.2.2 Comparison of OPVs and DSSCs

Although OPVs have historically been less efficient than DSSCs, as of 2014 the gap has been closed with the highest recorded efficiencies of single-junction OPV and DSSC cells exhibiting PCEs of 10.7 ± 0.3 % and 11.9 ± 0.4 % respectively [25]. At this point, DSSCs are a better-established technology and have already been commercialised. However, although there is some overlap between applications for these two technologies, each has its own strengths and weaknesses which make them suited to different niches. The main advantages of OPVs over DSSCs are as follows: firstly, OPVs are generally about 10 times thinner than DSSCs and are much more applicable to flexible devices; secondly, the most effective dyes used in DSSCs are Ru complexes which cost much more than a mass-produced polymer light absorber[3]; thirdly, typical DSSC cells contain a liquid electrolyte to replenish electrons which are injected from the dye to the electron transport layer — this poses stability and encapsulation issues and, whilst solid-state DSSCs using

[3]Whilst metal-free dyes do exist, light absorption is currently inferior to that seen in the metal-based dyes.

hole-transporting polymers have been developed, these still do not produce the same efficiency as liquid electrolyte DSSCs.

1.3 Principles of Organic Solar Cells

1.3.1 Operation and Device Characteristics

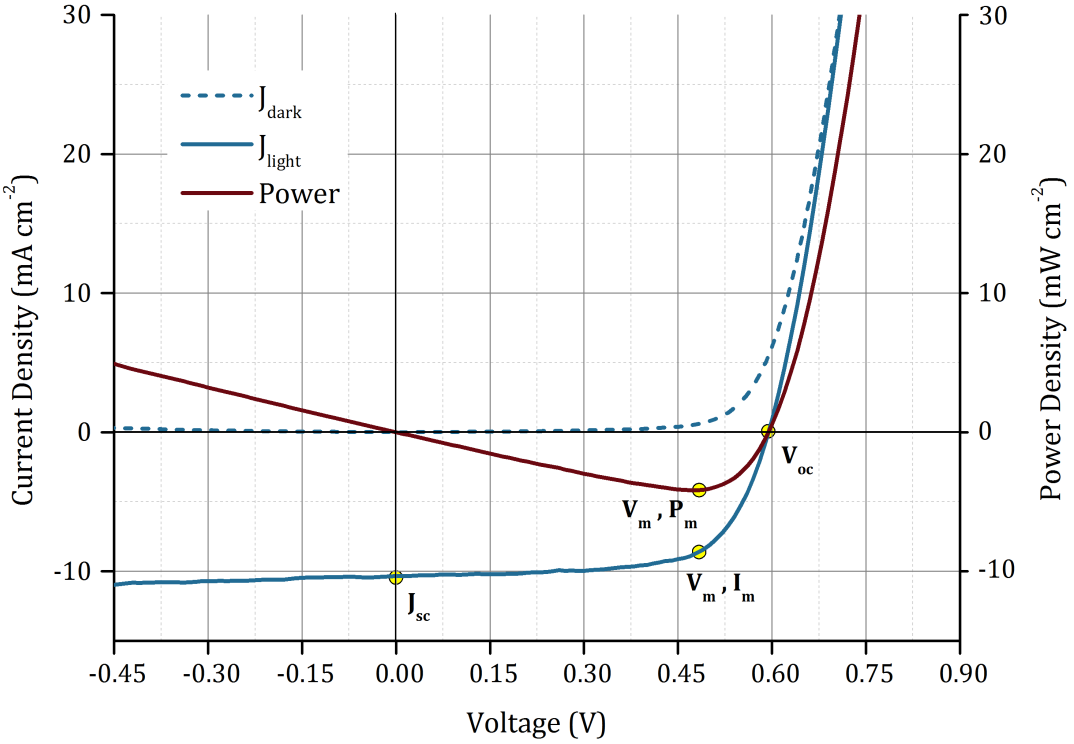

Figure 1.4 – Example of current density–voltage (J–V) curves, obtained for an OPV BHJ device with a normal architecture and layer structure ITO/PEDOT:PSS/P3HT:PCBM (1:0.7)/Ca/Al — PEDOT:PSS, poly(3,4-ethylenedioxythiophene) is a functional interlayer, whilst P3HT (poly(3-hexylthiophene)) and PCBM (phenyl-C_{61}-butyric acid methyl ester) are the respective donor and acceptor materials. Dark current, light current, and power density curves are shown. Data provided by Dr N. Treat.

As stated above, OPVs require a D–A heterojunction to operate effectively: when illuminated with photons of sufficient energy, an organic semiconductor will generate a bound electron–hole polaron state, called an exciton. To generate free charges, dissociation of the exciton must occur, requiring that the exciton binding energy (on the order of meV) must be overcome. The first OPV devices consisted of a single layer of an organic semiconductor sandwiched between two electrodes with differing work functions to create an electric field across the film; however, this electric field is insufficient to initiate dissociation in a large proportion of these excitons, hence few free charges are generated

and little photocurrent observed. This behaviour lies in contrast with inorganic solar cells: due to the generally higher dielectric constant (ϵ) of inorganic semiconductors, the exciton binding energy is overcome much more easily as the separated charges are screened much more effectively from each other, and thus a greater proportion of these species will be thermalised under standard conditions.

A D–A heterojunction requires that the acceptor level (usually the LUMO for a molecule or the conduction band for a crystal) is lower in energy than the donor level (HOMO) with the resulting energy level offset provides the driving force for exciton dissociation into free charge — this offset is generally referred to as ΔE[4]. A simple representation of this is shown in Figure 1.3 and more detailed description of charge generation is described in Section 1.3.2. These free charges subsequently diffuse to their relevant electrode, generating a photocurrent. Solar cell characteristics are derived by measuring the current density–voltage (J–V) characteristics for both forward and reverse bias regimes under both dark and illuminated conditions. From this, its quantitative characteristics are then derived by using the superposition principle: this assumes that the J–V characteristics of an illuminated solar cell is equal to the linear sum of its behaviour under dark conditions (where it behaves like a diode) and the generated photocurrent when the cell is illuminated; this assumption is only approximate for a solar cell, but is adequate for device characterisation [28]. There are four main quantities which are used to evaluate a PV device: short-circuit current (J_{sc}), open circuit voltage (V_{oc}), fill-factor (FF) and power conversion efficiency (PCE or η):

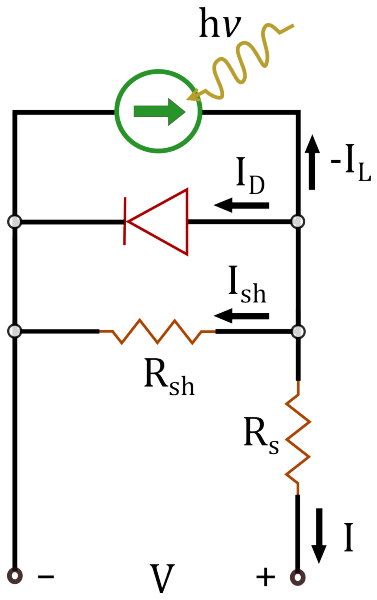

Figure 1.5 – The equivalent circuit of a typical solar cell. I_D is dark current, I_L illuminated current, R_{sh} the shunt resistance, and R_s the series resistance.

J_{sc} is the maximum attainable current density for a photovoltaic device and is derived from the J–V curve at short circuit conditions, *i.e.* when $V = 0$. J_{sc} essentially measures the efficiency of charge collection in a device, encompassing both generation

[4]It is often quoted that ΔE must be at least 0.3 eV in magnitude to drive efficient charge generation [26]; however, more recently, this point has been disputed and has only been shown experimentally to apply to PPV blend systems [27].

and extraction, and thus it is governed by a multitude of factors ranging from the absorption characteristics of the donor material, to the efficiency of charge collection at the electrodes. As J_{sc} is heavily affected by the incident radiation, different devices can only be meaningfully compared if they are tested under the same illumination conditions.

V_{oc} is the maximum voltage output that a device may generate, which occurs at open-circuit conditions (where $J = 0$). V_{oc} is measured under illumination and occurs at the breakdown of the reverse bias regime where the J–V curve intersects the x-axis. Several factors affect V_{oc} — in OPVs, the theoretical maximum V_{oc} that a system may attain is given by the offset between the $LUMO_A$ (or CB_A) and the $HOMO_D$. V_{oc} and J_{sc} are closely related, as shown by the following relationship[5]

$$V_{oc} = \frac{nkT}{q} \ln\left(\frac{J_{sc}}{J_0} + 1\right) \tag{1.1}$$

where q is the charge of an electron, n the diode ideality factor (dependent on recombination and current leakage), and J_0 is the dark saturation current; due to the strong dependence of V_{oc} on J_0, it is strongly affected by charge recombination.

FF is the ratio between the maximum power output of a solar cell and the product of J_{sc} and V_{oc} (where $P = 0$ for both these parameters) and, qualitatively, is the 'squareness' of a cell's J–V curve.

$$FF = \frac{V_m\, J_m}{V_{oc}\, J_{sc}} \tag{1.2}$$

FF is heavily affected by device recombination (due to its dependence on V_{oc}) and parasitic resistances which are explained below.

PCE or η is the most widely used benchmark for comparing solar cells — it is the ratio of the peak power density output (P_{max}) to the incident light intensity (P_{in}), and thus it normalises all cells with respect to illumination.

$$\eta = \frac{P_{max}}{P_{in}} = \frac{V_{oc}\, J_{sc}\, FF}{P_{in}} \tag{1.3}$$

The standard conditions for measuring solar cell characteristics are 1 sun intensity ($100\ mW\ cm^{-2}$) at AM 1.5G (the optical spectrum of photons incident on the Earth,

[5]The equation for V_{oc} should use the term J_L, the illumination current, instead of J_{sc}. In most cases, however, it can be assumed that they are equal and hence J_{sc} is used for simplicity. It should be noted that this does not hold for cells with high series resistances.

adjusted for atmospheric absorption and reflection) at 298 K — cell performance can only be compared meaningfully to other cells tested under the same conditions due to the dependence of photocurrent generation on irradiation intensity.

Other important solar cell characteristics include parasitic resistances and quantum efficiencies. The most relevant parasitic resistances are characteristic resistance (R_{ch}), series resistance (R_s), and shunt resistance (R_{sh}). R_{ch} is the ratio of maximum voltage to maximum current ($R_{ch} = {}^{V_m}/_{J_m}$) — if this is equal to the resistance of the load on the cell, the cell may operate at its maximum power point. R_s primarily affects the fill factor, and very high values will decrease the J_{sc} of a device; this arises from contact resistance between the electrodes and the active layer components, and from the resistance of the electrodes themselves. For organic solar cells, the relatively low mobilities of organic semiconductors will lead to further resistance due to the slow movement of generated charges. R_{sh} is the resistance of the pathway between the anode and the cathode; consequently, cells with low shunt resistances suffer from current leakage which reduces overall cell performance. Shunt resistance can be improved by eliminating the presence of pinholes in device layers and by including charge-selective layers (electron-blocking and hole-blocking layers, or EBLs and HBLs respectively) between the electrodes and the active layer.

The quantum efficiency of a cell is a measure of how many charge carriers are collected by a cell compared to the number of incident photons and may be broken down into two quantities: internal quantum efficiency (IQE) and external quantum efficiency (EQE): **EQE** is the number of charge carriers generated divided by the number photons incident onto the cell, whereas **IQE** is the number of charge carriers generated by photons which are absorbed by the cell. EQE is usually determined by measuring the optical losses from a solar cell (from transmission and reflection) and adding these to the IQE. The IQE is a measure of efficient charge generation, separation, and extraction, and should approach 100 % for an efficient solar cell, and a comparison with the EQE reveals its ability to absorb light.

1.3.2 Charge Generation in Excitonic Solar Cells

Although generation of free charges from an exciton at a D–A interface is often depicted as a simple one-step process, research from the last decade suggests that the actual process is much more complex and may be broken down into three fundamental steps [29]:

i) transfer of the electron from the donor exciton to the HOMO_A or CB_A.

ii) formation of a charge-transfer (CT) state where the newly separated electron and hole are bound by Coulombic attraction.

iii) thermalisation of the electron, leading to the formation of a charge-separated (CS) state.

Models for electron transfer have been developed using Marcus Theory [30] as a basis, whilst those for CT states have been derived from Onsager's theory of geminate recombination.

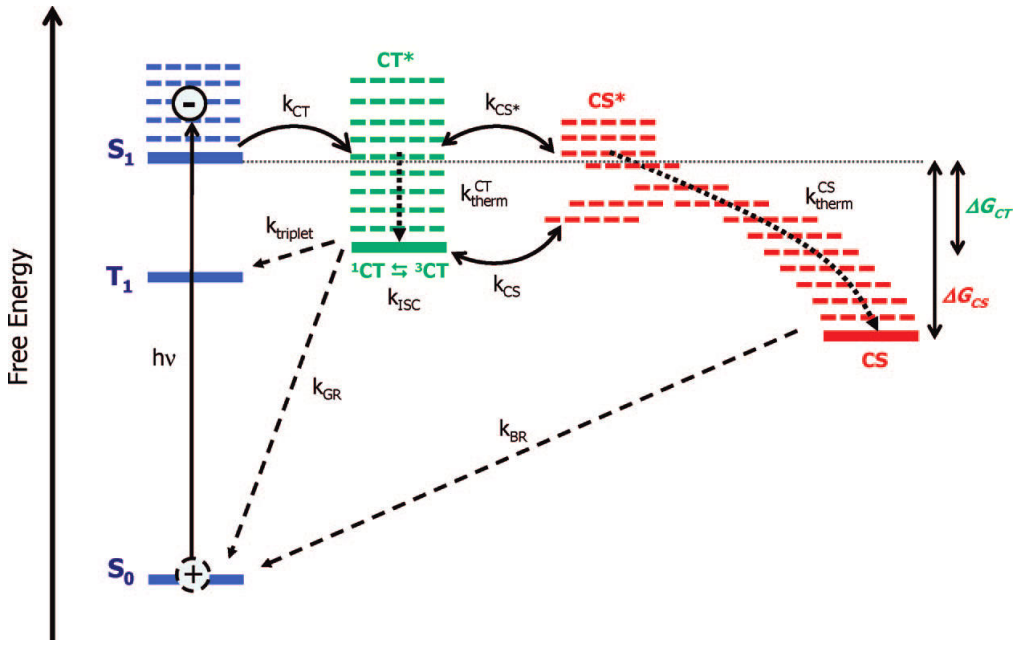

Figure 1.6 – Jablonski diagram representing charge photogeneration in excitonic solar cells, starting with a $S_0 \rightarrow S_1$ photoexcitation to form a singlet exciton. k_{CT} represents exciton dissociation to a thermally excited (hot) CT state; k_{therm}^{CT} is the relaxation of the hot CT state; k_{ISC} is intersystem crossing of the CT state; $k_{triplet}$ is geminate recombination of ^{3}CT to T_1; k_{GR} is geminate recombination of the singlet CT state to re-form S_0; k_{CS^*} is dissociation of a hot CT state into a CS state, followed by thermal relaxation and migration from the D–A interface, k_{therm}^{CS}; k_{CS} is dissociation of a relaxed CT state to a CS state; k_{BR} is bimolecular recombination of separated charges (non-geminate recombination, also referred to as back recombination) which is a diffusion limited process. CS states may also re-form CT states, leading to geminate recombination. ΔG_{CT} and ΔG_{CS} are the free energy changes for formation of CT and CS states respectively from S_1. Reprinted with permission from [29], originally adapted from [31] — © American Chemical Society, 2009.

1.3.2.1 Electron Transfer

Marcus theory is a model for electron transfer between two species, and uses two overlapping harmonic oscillators to represent the potential energy surfaces of the reactant (in

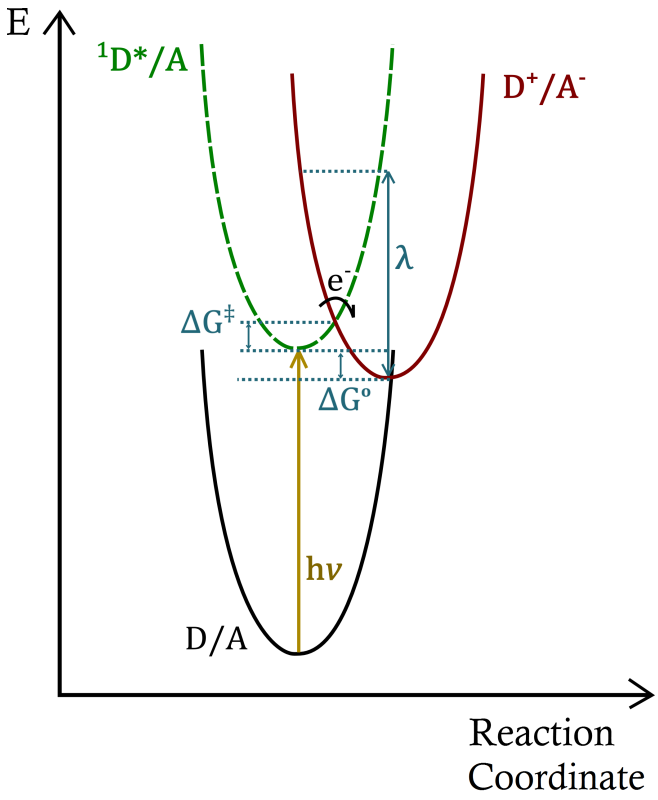

Figure 1.7 – Representation of Marcus electron transfer between two harmonic oscillator potential energy surfaces, ^{1}D*/A (reactant — photoexcited excitonic state) and D$^+$/A$^-$ (product — separated charge state). D/A represents the ground state of the system. $\Delta G^\ddagger$ is the activation barrier for electron transfer at the point of intersection between reactant and product curves; ΔG° is the energy minimum offset between reactant and product; λ is the reorganisation energy. Adapted from [29].

this case, the photoexcited singlet exciton ^{1}D*/A state) and product (a charge separated state, D$^+$/A$^-$). The Franck–Condon principle is applied to the system which assumes that electron transfer occurs on a much shorter timescale than that for nuclear motion — as such, electron transfer is considered to occur at the point of intersection between the reactant and product curves, which carries an associated activation energy barrier, given by:

$$\Delta G^\ddagger = \frac{(\lambda + \Delta G^\circ)^2}{4\lambda} \tag{1.4}$$

$\Delta G^\ddagger$ is the activation energy for the reaction, depending on both the free energy offset of the excited and charge separated states (ΔG°), and the reorganisation energy, λ which arises from changes in conformation of the system (internal) and changes in the polarisation of the surroundings resulting from the electron transfer from donor to

acceptor. The rate constant (k_{et}) may be determined by applying Fermi's Golden Rule, such that:

$$k_{et} = \frac{2\pi}{\hbar\sqrt{4\pi\,\lambda\,k_B T}} \cdot V^2 \cdot exp\left(-\frac{(\lambda + \Delta G^\circ)^2}{4\lambda\,k_B T}\right) \tag{1.5}$$

V is a function relating to the degree of coupling between the electronic wavefunctions of the donor and acceptor — in the case of organic D–A systems, the coupling is considered to be weak, *i.e.* smaller than $k_B T$, leading to non-adiabatic electron transfer. It can be inferred that, due to the exponential dependence in Equation 1.5 on ${}^{(\lambda + \Delta G^\circ)^2}/_{\lambda}$, k_{et} increases until a maximum at $-\Delta G^\circ = \lambda$ where electron transfer carries no activation barrier. If ΔG° increases further, the rate starts to decrease due to increasing activation energy requirements — this effect is referred to as the Marcus inverted region. Equation 1.5 may be modified to account for donor/acceptor electronic band structures by integrating k_{et} over the density of states.

1.3.2.2 Charge Transfer States

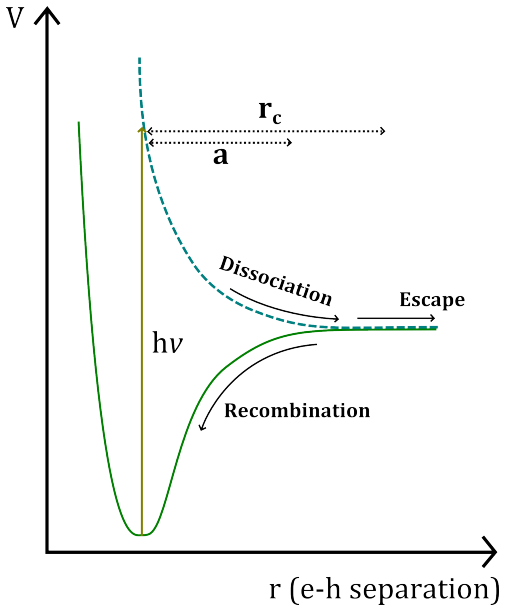

Figure 1.8 – Simple potential energy diagram for geminate recombination/autoionisation in a photoexcited system. The green potential curve represents the Coulomb attraction between an electron and hole, and the blue curve the potential energy for an excited, mobile electron generated by $h\nu$. r_c is the Coulomb capture radius and a is the thermalisation length of the excited electron.

After the initial charge transfer of an electron from donor to acceptor (as detailed above), a bound electron–hole pair (CT state) may be formed if the free charges are not effectively screened by the donor and acceptor materials, as is the case for low ϵ organic systems. A failure to break up the CT states will result in geminate recombination of the electron and hole. Onsager's model for geminate recombination — illustrated in Figure 1.8 — can be applied to these systems: photoexcitation of the donor species generates an exciton comprised of a localised hole and a mobile, electronically excited electron which thermalises at a distance, a, from the hole; at this point the electron may either escape or recombine with the hole. The Coulomb capture radius, r_c, is the distance at which the Coulombic attraction between electron and hole is equal to $k_B T$, thus the point at which a CT

state may be dissociated by thermal energy; if a is greater than r_c, it can be considered that all excited electrons escape; if the converse is true (as is the case for most organic–organic systems), the electron–hole CT states can either recombine or undergo dissociation. r_c is defined as:

$$r_c = \frac{e^2}{4\pi\,\epsilon_r\epsilon_0\,k_B T} \tag{1.6}$$

e is the charge of an electron, ϵ_r the dielectric constant of the material, and ϵ_0 the dielectric permittivity of free space. As Equation 1.6 shows, recombination is strongly dependent on the electronic screening of charge, and high ϵ_r materials favour effective charge separation, as stated in Section 1.3.1. In the case of an excitonic solar cell, CT dissociation can be modelled in terms of electric-field dependent escape probability, $P(E)$ — the strength of the electric field, E, is assumed to be low, a valid assumption for organic D–A systems. The original Onsager model in Equation 1.7 has been modified by Braun to take into account the fact that CT states have a finite lifetime and that the CT dissociation process is reversible[6]. As a result, $P(E)$ depends on the rate of geminate combination, $k_d(E)$. The Braun-modified model is given below in Equation 1.8:

$$P(E) = exp\left(\frac{-r_c}{a}\right)\left(1 + \frac{e\,r_c}{2\,k_B T}\,E\right) \tag{1.7}$$

$$P(E) = k_d(E)\,\tau(E) = \tau(E)\cdot\frac{3\langle\mu\rangle e}{4\pi\langle\epsilon_r\rangle\epsilon_0\,a^3}\,exp\left(\frac{-\Delta E}{k_B T}\right)\left[1 + b + \frac{b^2}{3} + \frac{b^3}{18} + ...\right] \tag{1.8}$$

$$\Delta E = \frac{e^2}{4\pi\langle\epsilon_r\rangle\epsilon_0\,a}$$

$$b = \frac{e^3 E}{8\pi\langle\epsilon\rangle\epsilon_0\,k_B^2 T^2}$$

where $\tau(E)$, the lifetime of the CT state; $\langle\mu\rangle$, a spatial average of electron and hole mobilities in their respective materials; $\langle\epsilon_r\rangle$, a spatial average of the materials' dielectric constants; $\Delta(E)$, the Coulombic force between electron and hole after thermalisation.

[6]Onsager's model was originally developed for geminate recombination in the solution phase in which the rate of electron–hole pair re-formation is negligible. However, in a solid-state OPV system where materials have relatively low carrier mobilities, CT state separation must be considered a reversible process.

Although the Onsager and Braun models have proved useful for predicting charge generation behaviour in OPVs, these models do neglect several factors and fail under a number of conditions, *e.g.* in systems with highly asymmetric carrier mobilities (generally where $\mu_{electron} \gg \mu_{hole}$ — this is particularly relevant in the case of hPVs where the carrier mobility of the acceptor is some orders of magnitude greater than for the donor. In addition, the model also neglects reorganisation energy, a key concept used in the Marcus model for the initial electron transfer process, and the presence of interfacial dipoles which may change the electron–hole Coulombic energy profile. However, the standard Braun model has proven to be a good tool for initial analysis.

1.3.3 Architecture

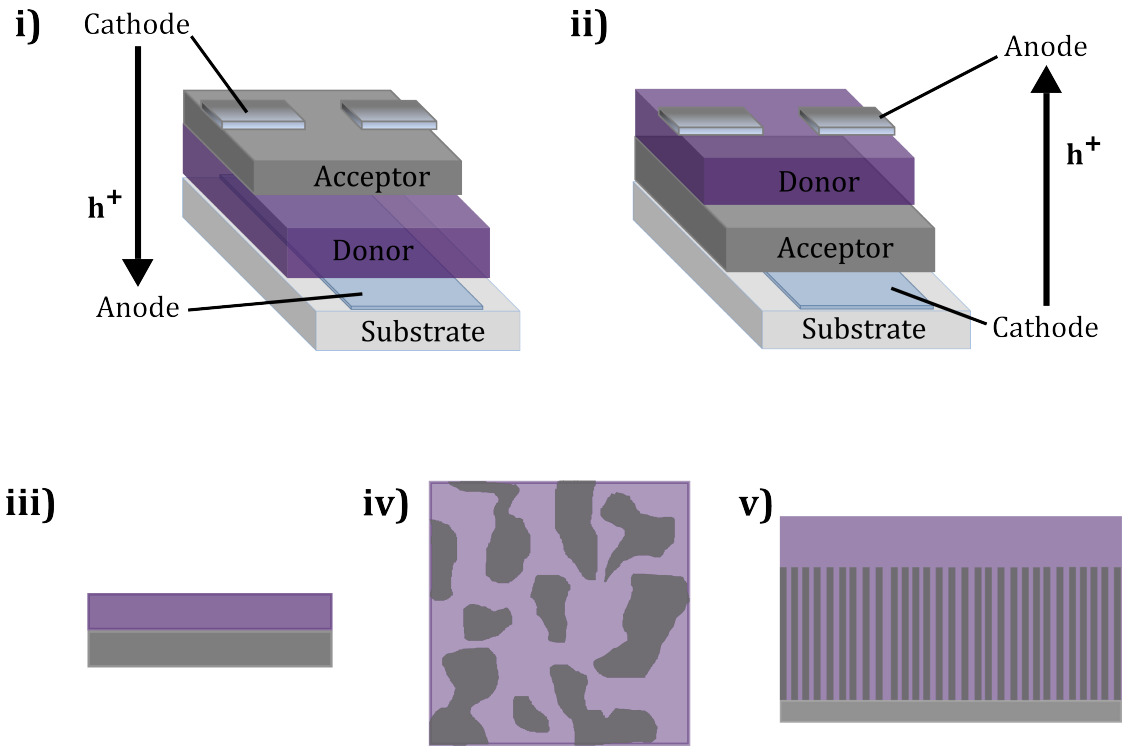

Figure 1.9 – Representations of different OPV architectures. *i)* and *ii)* display normal and inverted architecture, respectively. *iii)* – *v)* show variations in the structure of donor–acceptor layers: *iii)* is a bilayer system; *iv)* a BHJ with a blended active layer; *v)* an ordered, interdigitated interface. These representations, in particular *iv)* are heavily simplified: in reality, the microstructure tends to be much more complex with regions of varying degrees of crystallinity and donor–acceptor material mixing [32].

OPV and hPV devices are multilayered structures: a basic heterojunction device consists of 4 functional components: a transparent substrate (glass or plastic), a transparent bottom electrode, the active layer (containing the donor and acceptor materials), and a

top electrode (usually a metal). Additional functional layers may also be employed, such as charge-selective extraction layers at the organic–electrode interface (either EBLs or HBLs, depending on which electrode interface they are situated). There are two different types of basic architecture — *i.e.* the order in which these functional layers are present in the device — employed in OPVs, illustrated in Figure 1.9 below.

In normal cell architecture, the bottom electrode acts as the hole-extracting layer (cathode), with the top electrode extracting electrons (anode), whilst in the inverted architecture, the roles of these electrodes is reversed. Early work on OPV devices focussed almost exclusively on devices with the normal architecture — the ubiquitous transparent conducting oxide (TCO) ITO is the electrode material of choice for OPVs which, due to its high work-function (typically 4.5 eV [33]), is an efficient hole collecting layer. For efficient electron collection, low work-function metals such as Ca or Ca/Al are used as a top contact. In the inverted architecture, ITO becomes the electron collecting layer which, due to the large energetic offset between the ITO and the typical CB/LUMO of an acceptor species, can present a larger barrier to charge collection than for the normal case. A higher work-function metal is used as the top contact in an inverted cell, usually Ag (4.73 eV) or Au (5.1 eV) [34]. Despite the less favourable electrode energy alignment in inverted cells, these have usurped the place of normal cells as the favoured architecture for OPV research due to their improved stability: the necessity of using low work-function metals in normal architecture is problematic due to the proclivity of these metals to oxidise when exposed to air and, as a result, these devices tend to degrade very quickly unless they are appropriately encapsulated. hPV devices are almost exclusively fabricated with inverted architecture, especially for devices with a discrete acceptor layer as these are grown directly onto the ITO; however, the fabrication of such devices has been demonstrated by depositing ZnO onto the donor polymer by pulsed laser deposition (PLD) [35].

The structure of the D–A heterojunction may also take on different forms, as shown in Figure 1.9. The simplest case is a D–A bilayer (also referred to as planar) architecture in which the two materials are deposited as dense, 'flat' layers in contact with each other. In this case, the interfacial area is very small and, due to the short exciton diffusion length (L_{ex}) of organic donor species — typically less than 10 nm — only a small fraction of excitons generated in this system will be close enough to the interface to be able to generate charge; however, due to the simplicity of this architecture, these cells are often used as a testbed for new device concepts. Most OPV devices contain a BHJ active layer in which the donor and acceptor materials are blended together and subsequently cast as a film. This approach generates an intimately mixed active layer in which the size of the donor and acceptor domains are on comparable length scales

to L_{ex}, allowing harvesting of a much greater proportion of excitons than in the bilayer case. However, the inherent randomness of this approach can be problematic: charge extraction pathways can be relatively long and inefficient, leading to recombination of separated charges; large regions of donor or acceptor material may be formed during casting rather than mixing more thoroughly; over time, phase separation of donor and acceptor may occur. Therefore, it is seen as advantageous to have a nanostructured, ordered active layer with features separated by distances comparable to L_{ex}, leading to a large interfacial surface area with continuous charge extraction pathways — this form of heterojunction is one of the driving forces for research into hPVs due to the relative ease of creating nanostructures of inorganic materials compared to organic materials. Nanorods (NRs) and 3-dimensional ordered macroporous (3DOM) structures are the mostly widely researched nanostructures for use in photovoltaic applications.

Also of interest are tandem cells which combine two different solar cells into one device [36] — for such a system, the V_{oc} is equal to the sum of the V_{oc} for the individual cells, and it is possible to design a cell with complementary absorbing materials in each separate layer, allowing absorption of light over a wider range of the solar spectrum; however, there are a number of engineering challenges relating to cell fabrication and connecting the two cells. As of 2014, the highest efficiency tandem cell was recorded at 11.5 % [37]. Another promising, novel approach involves tandem hybrid cells which combines an inorganic cell with an OPV component — in this type of system, the inorganic material (such as CIGS) will typically have a lower band-gap than the organic material which allows a better range of absorption than an all-organic tandem device as stable, low band-gap organic absorbers have, to this point, been difficult to design and synthesise [38].

1.4 Hybrid Photovoltaics

hPVs are closely related to OPVs in that the organic acceptor species is replaced with an inorganic material such as CdS, CdSe, PbS, TiO_2, or ZnO which exploits the higher electron mobility and chemical stability that these compounds offer compared to their organic counterparts; additionally, enhancement in photocurrent is expected for devices with narrow band-gap semiconductor materials which also contribute to visible light absorption. Both bilayer and bulk-heterojunction blend (using inorganic nanoparticles (NPs)) architectures are common, as for OPVs; however, one of the main attractions of hPVs is the ability to incorporate ordered, nanostructured arrays of the inorganic acceptor ideally with structural spacing comparable to the L_{ex} of a donor polymer. ZnO

is particularly favoured in this regard as a huge variety of nanostructures may be grown using a number of different of solution and vacuum-based deposition techniques — this will be covered in more detail in Section 1.4.1. It should be noted that it has become common practice to incorporate wide band-gap metal oxides — particularly ZnO and its doped derivatives — as functional layers in OPVs. These devices are not considered to be 'true' hPV cells as the primary role of the inorganic layer is not as an acceptor material.

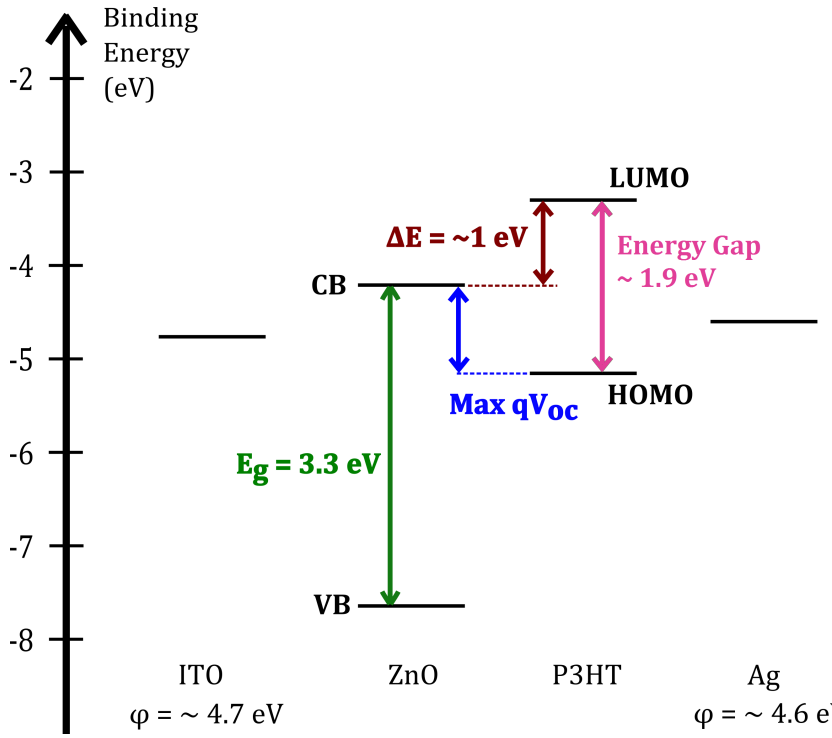

Figure 1.10 – Simple flat-band energy level diagram for a typical inverted ITO/ZnO/P3HT/Ag device. E_g is the band gap, ϕ the work function; qV_{oc} the maximum open-circuit voltage that the device may attain; ΔE the energetic offset between the $LUMO_D$ and CB_A.

The work in this report focusses on hPV devices incorporating ZnO as a functional layer; this section contains reviews of the material properties of ZnO (Section 1.4.1), and reviews of the use of ZnO in both OPVs (Section 1.4.2) and hPVs (Section 1.4.3).

1.4.1 Zinc Oxide

As stated in Section 1.4, a number of different materials may be used as an inorganic acceptor in hPV devices: narrow band-gap semiconductors[7] CdS [40], CdSe [41], CdTe [42]

[7]Nanoparticles of these materials, particularly PbS, are also used as sensitisers for quantum dot-sensitised solar cells (QDSSCs) [39] — the band gap of QDs may be modulated through the particle size

(II–VI semiconductors), PbS [43] (IV–VI), $CuInS_2$ [44] NPs have been used to create BHJ-type hPV devices — branched NPs of these materials may also be grown to increase the interfacial area in these devices [45]; Si has also been investigated as an acceptor material [46]. Although these materials may contribute significantly to photocurrent generation due to their narrow band-gap (absorption in the visible range), growth of solid arrays of these materials has proved to be challenging, and the the toxicity of elements such as Pb, Cd, and Se are a cause for concern. In contrast, the wide band-gap semiconductors ZnO [47], TiO_2 [48], do not contribute significantly to light absorption, but solid thin-films and nanostructured arrays are much easier to synthesise using these materials — especially ZnO — and the raw materials are both cheaper and generally much less toxic.

ZnO is a versatile material with a unique set of properties which make it suitable for variety of different applications, from a UV-absorber in sunscreen to an n-type semiconductor in electronics. Such properties include: wide, direct band-gap ~ 3.3 eV; high exciton binding energy ~ 60 meV; piezoelectric properties (suitable for use in sensors, actuators, and transducers); strong luminescence; sensitivity of surface conductivity to adsorbate (appropriate for sensing applications); relatively high electron mobility; high thermal conductivity; hardness to radiation. This section covers the main properties of ZnO and their origins, and includes a comparison to TiO_2, which is often used in photovoltaic applications and has become the acceptor material of choice for DSSCs.

1.4.1.1 Structural Properties

There are three polymorphs of ZnO: wurtzite (hexagonal), sphalerite (also known as zinc blende), and rock salt (both cubic). The latter two forms of ZnO are metastable — the sphalerite form may be grown epitaxially on cubic substrates, whereas the rock salt form requires high pressure (~ 10 GPA) [49]; in this work, ZnO was grown exclusively in the wurtzite structure. Hexagonal ZnO belongs to the space group $P6_3mc$ and has a coordination number of 4:4 with Zn^{2+} ions filling half of the tetrahedral holes in the structure. The crystal structure of ZnO is depicted in Figure 1.11 below, reproduced from structural coordinates determined by Rietveld refinement of diffraction data collected from ZnO powder [50].

The wurtzite structure consists of two interpenetrating hcp sublattices, with each sublattice containing a displaced atom along the C_3 axis by $3/8$ with respect to the other [49]. Bonding in ZnO is tetrahedral through sp^3 hybridisation of the anion and

as opposed to doping, allowing tuning of light absorption.

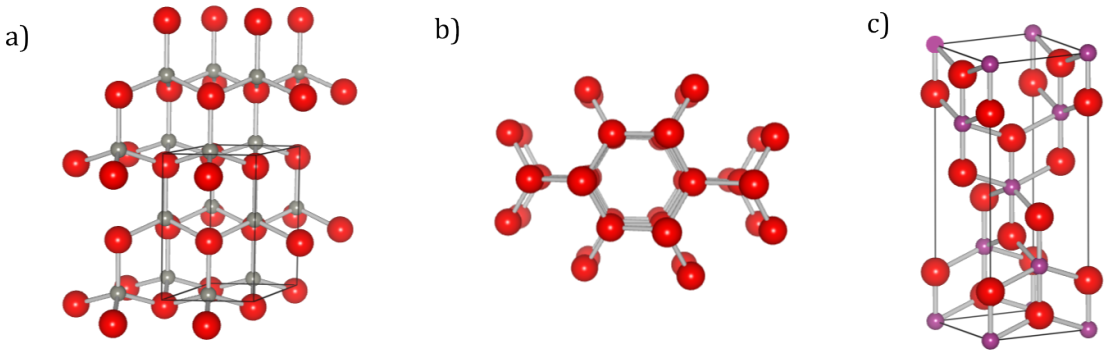

Figure 1.11 – Stick-and-ball crystal structures for a) ZnO; b) ZnO, as viewed down the c-axis (*002*) plane; c) anatase TiO_2. The red spheres represent O^{2-} ions, the grey spheres Zn^{2+} ions, and purple spheres Ti^{4+} ions. ZnO structure is reproduced using structural coordinates determined by Yamashita *et al.* [50], and TiO_2 from structural data determined from powder diffraction carried out by Burdett *et al.* [51]. Structural was data obtained from the Inorganic Crystal Structure Database (ICSD), and the crystal structure was generated using the VESTA programme [52].

cation atomic orbitals, although due to the reasonably large disparity between the Pauling electronegativities of Zn and O (1.65 and 3.44 respectively [53]) there is a large ionic contribution to the bonding which has a significant effect on the electronic properties of the material. Typically, the Zn–O bond length in the structure will be around 1.98 Å.

One of the main attractions for using ZnO in polymer solar cells and other applications requiring large surface areas (such as sensing) is the relative ease of growing a wide range of nanostructures, usually by solution-based methods. These include, but are not limited to: NPs, NRs [54], 3DOM inverse opals [55], nanowires (NW) [56], platelets [57], honeycomb [58], nanohelices [59], nanotubes [60], and tetrapods [61]. Due to the crystal anisotropy of ZnO, nanostructures generally arise from highly preferential growth — for example, ZnO NRs grown by hydrothermal growth grow up the c-axis, thus exhibiting almost complete preference for (*002*) orientation — through careful control of the composition growth solution, lateral growth is inhibited leading to the vertical growth of NR arrays relative to the substrate. Control of the conditions also allows tuning of the physical properties of the NRs, such as length and aspect ratio.

1.4.1.2 Electronic Properties

The n-type conductivity of ZnO is intrinsically linked to its rich defect chemistry which is described below in Section 1.4.1.3; the conductivity of ZnO is highly variable, with a maximum carrier concentration of around 2 x 10^{21} cm^{-3} in heavily doped material [62], compared to a 'typical' bulk value of 1 x 10^{17} cm^{-3} [63], thus making ZnO a suitable material for a wide range of optoelectronic applications. The bulk electron mobility

for ZnO is relatively high with a typical value of 205 cm V^{-1} s^{-1}. Although this figure is usually lower for thin-films, electron mobilities still remain at a viable level for a variety of applications, especially compared to competing materials such as a-Si: for example, ZnO-based thin-film transistors (TFTs) have been fabricated in ambient conditions using atomic layer deposition (ALD), yielding high field-effect mobilities of over 12 cm V^{-1} s^{-1} [64], whereas devices fabricated by vacuum-based magnetron sputtering have possessed higher mobilities of around 70 cm V^{-1} s^{-1} [65]. It has been suggested that the surface conductivity of ZnO can differ significantly to that of the bulk due to higher densities of defects [66, 67, 68]: this can play a significant role in the transport properties of the material and may affect transport measurements as well as the performance of ZnO-based electronic devices.

Due to the non-centrosymmetric nature of the ZnO crystal structure, ZnO is a piezoelectric material (*i.e.* application of mechanical stress will induce electrical polarisation in the material), with polarisation occurring along the *c*-axis; the piezoelectric tensor for ZnO is extremely high for a tetrahedrally bonded material and is comparable to materials such as GaN and AlN [62]. As a result, ZnO has attracted interest in applications such as sensing and as piezoelectric nanogenerators due to the low cost of the material and due the facile growth of nanostructured arrays.

1.4.1.3 Defects

ZnO has a rich defect chemistry which governs its electronic properties — both native (lattice defects involving only constituent atoms, otherwise known as intrinsic defects) and extrinsic defects play a significant role in the properties of ZnO. A shallow defect centre relates to a species which lies within the band gap close to the CB or VB maxima band edges (for a donor and acceptor, or n- and p-dopants respectively) and are expected to be thermally ionised at room temperature. Conversely, deep levels lie further within the band gap and are generally not ionised at room temperature, but may be activated by other means.

1.4.1.3.1 Intrinsic Defects

Native point defects observed in ZnO in order of increasing formation energy are: oxygen vacancies (V_O), zinc vacancies (V_{Zn}), zinc interstitials (Zn_i), zinc anti-sites (Zn_O), oxygen interstitials (O_i), and oxygen anti-sites (O_{Zn}); V_O, Zn_i, and Zn_O act as donor defects, whereas Zn_i, O_i, and O_{Zn} are acceptor defects [69]. For a long time, V_O were cited as the origin of the unexpected n-type conductivity of ZnO [70] due to the observable effects of oxygen partial pressure on conductivity and their low enthalpy of formation;

however, more recent research has cast doubt on this conclusion with most calculations showing that V_O is, in fact, a deep centre which therefore cannot contribute to the room temperature conductivity of ZnO [71, 72]. Recent research has proposed that the inherent n-type conductivity observed in ZnO arises from unintentional extrinsic doping of hydrogen: due to its small size, H is expected to be incorporated into most systems and in most cases is expected to act as an amphoteric impurity, forming H_i^+ in n-type materials and H_i^- in p-type materials, *i.e.* acting contrary to the n- or p- character of the semiconductor; however, in ZnO, it has been proposed that H always exists in its donor form, H_i^+, and acts as a major source of conductivity [69]. Hydrogen can form an –OH species within the lattice, allowing it to act in an analogous fashion to Group VII (halide) dopants such as F and Cl. Controlling the presence of H in systems is not a trivial matter due to the element's ubiquitousness, and therefore it has been difficult to demonstrate this effect in experiments, although work by Baik *et al.* has shown some some evidence for the correlation of H incorporation with conductivity [73]; overall, this hypothesis is a compelling one, considering that most ZnO synthesis provides plenty of opportunity for unintentional H incorporation, especially for cases where ZnO is grown from an aqueous environment.

1.4.1.3.2 Extrinsic Doping

As discussed above, the unintentional incorporation of hydrogen as an extrinsic n-type dopant in ZnO is thought to give rise to its semiconductivity. As a result, controlling the semiconducting properties of ZnO is a serious challenge, especially for solution-based processes which are generally less easy to control than vacuum techniques such as PLD and ALD. However, extrinsic n-type doping is often used to stabilise the electronic properties and increase its conductivity. Doping in ZnO may be substitutional (directly replacing the Zn^{2+} cation) or interstitial; in the case of some dopants such as Li, they may be both substitutional and interstitial.

The band gap of ZnO may be modulated by incorporation of +2 ions as Zn substituents: alloys of ZnO with small atoms such as Mg [74] and Be have been shown to augment the band gap [75]: Ohtomo *et al.* reported a band gap of 3.99 eV for a Mg concentration of $\sim$ 33 %at [76] before the material underwent a transition to a cubic phase at higher concentrations; film resistivity tends to increase with increasing Mg concentration. Addition of Cd has been shown to reduce the band gap, as well as increasing the a and c lattice parameters due to the larger size of the Cd^{2+} ion; in the CdZnO alloy system, the band gap contraction is expected to occur mostly through a lowering of the CB band-edge, rather than through a raising of the VB [77]. Experimentally, Makino *et*

al. have shown that doping 7 % of Cd into ZnO by PLD yielded a band gap contraction to 3.0 eV [78].

The Group III elements B [79], Al, Ga, and In [80] are widely used shallow donors for ZnO due to their tendency to exist as 3+ ions — as these elements substitute directly for Zn^{2+} in the lattice, the extra electron is localised on the atom and may be ionised to the CB at room temperature, thereby increasing the carrier concentration of the material. For Al and Ga, carrier concentrations on the order of 10^{20} cm^{-3} can be attained [81, 82] whilst maintaining transparency of > 80 % and, as discussed later in Section 1.6.1, these compounds are being considered for use as cheap alternative transparent conducting oxides (TCOs) to ITO.

P-type doping of ZnO has been highly sought after to enable the fabrication of ZnO p–n junctions for used in LEDs and other electronic applications using less expensive materials than the current industry standard (GaN); however, although p-type conductivity has been reported by some groups, irrefutable and repeatable evidence of true p-type ZnO has been hard to come by. The main candidates for p-type doping in ZnO are the Group IA and IB elements (Li, Na, K, Cu, Ag), and Group V (N, P, As, Sb); additionally III–V co-doping has been attempted (N:Ga and N:Al) [83, 84, 85] which leads to the formation of N–Ga–N or N–Al–N acceptor species. Problems with Li and Na arise from their high mobility within the lattice; additionally, it has been found that Li may act both as the desired substituent for Zn (thereby acting as an acceptor) and as a donating interstitial species and is effectively self-compensating [86]. Generally, the intrinsic donor levels in ZnO may act as 'killer' levels, in particular the ubiquitous V_O and Zn_i, and careful control of these defects, as well as the introduction of dopant species is required before true p-type ZnO can be realised.

1.4.1.3.3 Surface Defects

As with the bulk, the surface chemistry of ZnO is extensive and, although not well studied, is of key importance in terms of interfaces: recent research has shown that the surface defect chemistry of ZnO may have a significant impact on both the surface transport of ZnO (Allen *et al.* propose that the mobility of electrons at the ZnO surface can be some order of magnitude smaller than in the bulk [88]), as well as interspecies charge transfer [87], both of which have implications for the use of ZnO in PV applications. The extensive surface chemistry of ZnO arises both from native and extrinsic defects, particularly from the adsorption of hydrogen-containing species and carbon. Additionally, the behaviour of polycrystalline ZnO — which is used more extensively in such applications than single crystal ZnO — is hard to predict due to the presence of neutral, Zn-terminated, and O-terminated faces, all of which have different surface properties.

Work by Li *et al.* considers the Zn-terminated (*0002*) face of ZnO, and compares both theoretical data derived from a number of different models containing different defect types (by density functional theory, DFT) and experimental data (from photoelectron spectroscopy, PES): this work proposes that presence of V_{Zn} (acceptor) and V_O (donor) defects and subsequent hydroxylation (particularly relevant for solution-processed ZnO) are key to determining the surface properties, especially the work function. Hydroxylation may produce two distinct species: an –OH group that fills a V_O donor site, and a bridging –OH between two surface Zn atoms. Filling of the donor V_O site leads to an increase in work function as it negates the donor characteristic of the site; furthermore, the presence of V_{Zn} acceptor levels also increase the work function; this study therefore proposes that such defects may be detrimental to device performance. Rinke has proposed that the presence of hydroxylate on the ZnO surface can result in H-bonding between the ZnO and organic species deposited on the surface, as opposed to more covalent-like chemisorption; as a result, this hinders electron transfer reactions between the two species [89, 90]. In any case, it is clear that further modelling of ZnO-based OPV systems must consider both intrinsic and extrinsic surface doping as it is clear that these play a critical role in the hitherto unpredictable behaviour of ZnO-based devices.

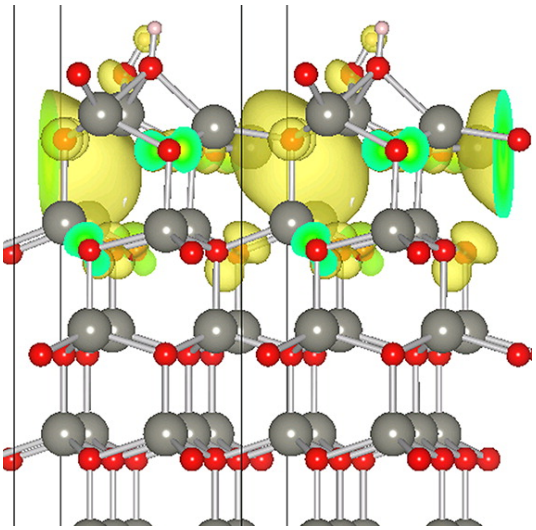

Figure 1.12 – Model of the ZnO surface calculated by DFT. Oxygen and zinc vacancy native defects are shown, as well as two variants of hydroxylate defects, dangling and bridging. Reprinted with permission from [87]. © 2012 American Chemical Society.

1.4.1.4 Comparison to TiO_2

TiO_2 is an n-type, wide band-gap semiconductor also used extensively in photovoltaic applications and is particularly prevalent as the acceptor in DSSCs and oxide hPVs. TiO_2 occurs in three forms: brookite (orthorhombic, $Pcab$), rutile (tetragonal, $P4/mnm$), and anatase (tetragonal, $I4_1/amd$) [53], as well as other metastable and high pressure forms. Anatase, the crystal structure of which is represented in Figure 1.11, is the polymorph used most extensively in optoelectronic applications. There are many similarities in the properties between anatase TiO_2 and ZnO: TiO_2 has a band gap of 3.2 eV [91] and is transparent in the visible region; additionally, the CB energy level is similar for both

materials. In terms of electron transport, ZnO is considered to be superior to TiO_2 and generally exhibits high electron mobilities (205 cm V^{-1} s^{-1} for bulk ZnO, 20 cm V^{-1} s^{-1} for TiO_2 [92]). This high electron mobility is a key reason for choosing ZnO for electronic devices over TiO_2; on top of this, ZnO has a more extensive range of nanostructures available and synthesising nanostructures with TiO_2 generally requires more complex methods. hPV devices containing TiO_2 and ZnO are compared below in Section 1.4.3.

1.4.2 ZnO in OPVs

Although OPVs do not employ metal oxides as an 'active' (*i.e.* donor or acceptor) component, ZnO species have been used extensively in BHJ-type solar cells as transparent electrodes, HBLs, or as optical spacers owing to the favourable band energies, transparency, good charge transport characteristics, chemical stability, and solution processing. As such, it is seen as a viable electrode replacement for ITO or as an HBL for OPVs with the inverted architecture. Additionally, ZnO has been used as an optical spacer and is thought to increase light absorption in the device through modulation of optical in-coupling within the device [93]; however, the efficacy of such layers is debated, and it has been proposed that optical spacers can only be effective for devices in which the active layer has not been optimised for absorption [94].

1.4.2.1 Electrodes

Although ITO is the TCO of choice in the electronics industry, a less expensive and more easily processed replacement is sought after: as discussed in Section 1.2.1, ITO synthesis is associated with a high GER due to vacuum processing; additionally, ITO is a solid solution comprising of around 90 % In_2O_3 — although ITO is an industry standard material and used extensively as an electrode in commercial applications (such as for electronic displays), indium is becoming an increasingly scarce (and thereby expensive) resource. Additionally, ITO is unsuitable for flexible device applications due to its inherent rigidity.

ZnO has been considered as a potential alternative to ITO due to its relatively low cost, transparency to visible light, and high conductivity, even in the absence of intentional dopants. For transparent electrodes, ZnO is doped with elements such as Ga or Al which increase — and, more importantly, stabilise — the conductivity of the material. Despite the increase in carrier concentration which leads to an increase in light scattering, these films retain an adequate degree of optical transparency for PV applications. However, ZnO has its drawbacks as a TCO: whilst ITO is quite resilient and its properties largely unaffected by harsh processing conditions, the electronic properties of ZnO

are much more sensitive to changes in both processing and ambient conditions: in particular, ITO is much more resistant to moisture than ZnO and degrades at a much slower rate under such conditions. In spite of this, some initial work has been carried out using alternative TCOs in OPVs: sputtered Ga-doped ZnO (GZO, Ga content $\sim$ 3 %wt) was tested by Owen *et al.* for both normal and inverted architecture P3HT:PCBM devices [95]. The results showed that, for normal device architecture, GZO cells produced 14 % of the device efficiency of the equivalent ITO cells which may be partly attributed to the lower work-function of GZO compared to ITO; however, for inverted architecture, GZO fared much better with overall PCE of 1.4 % (*cf.* 2.54 % for a normal architecture ITO device). Copper phtalocyanine (CuPc)/C_{60} devices employing a PLD GZO layer have also been reported, achieving a PCE of 1.25 % [96].

Al-doped ZnO (AZO) has shown to produce device performances on par with ITO reference devices for the CuPc/C_{60} active layer D–A blend (1.3 % for AZO with UV–ozone treatment (UV–O_3), 1.1 % for ITO) [97], showing the potential that these films have as an alternative to ITO. Another approach to this problem has been to use multilayer 'sandwich' electrodes of construction AZO/Ag/AZO or GZO/Ag/GZO in which the sheet resistances rely on the thickness of the Ag layer. This metallic layer also affects the optical transparency — the layer with the highest transmission (84 %) was an AZO/Ag (14 nm)/AZO layer. Compared to the single AZO/GZO layers, these multilayers electrodes yielded 57 % and 80 % increases in PCE respectively; additionally, their growth at room temperature may help to minimise the energy required to produce the films [98].

1.4.2.2 Hole-blocking Layers

Blocking layers are used in OPVs primarily to increase R_{sh} in devices by eliminating short circuit pathways and to increase the charge selectivity of the electrode, leading to gains in J_{sc}. Although the bulk of OPV research focusses on normal architecture cells, in recent years there has been a greater preference for inverted cells: although the main motivation for this is the removal of the requirement for a low work-function metal top contact, it also removes the need for a layer of PEDOT:PSS on the ITO contact. In a normal cell, PEDOT:PSS acts as both an EBL and as a work function modifier for ITO; however, due to the acidity of the PSS component, degradation of ITO has been observed. By using an inverted architecture, ZnO can be used as the electrode modifier instead, leading to a more chemically stable device. ZnO also offers other advantages such as fast electron transport, and the potential for nanostructured oxide layers which may increase charge transport in the device. Many groups fabricate inverted OPVs with an EBL of

PEDOT:PSS on top of the active layer to increase the R_{sh} of the devices, although more chemically inert alternatives such as MoO_x and WO_x are also being researched.

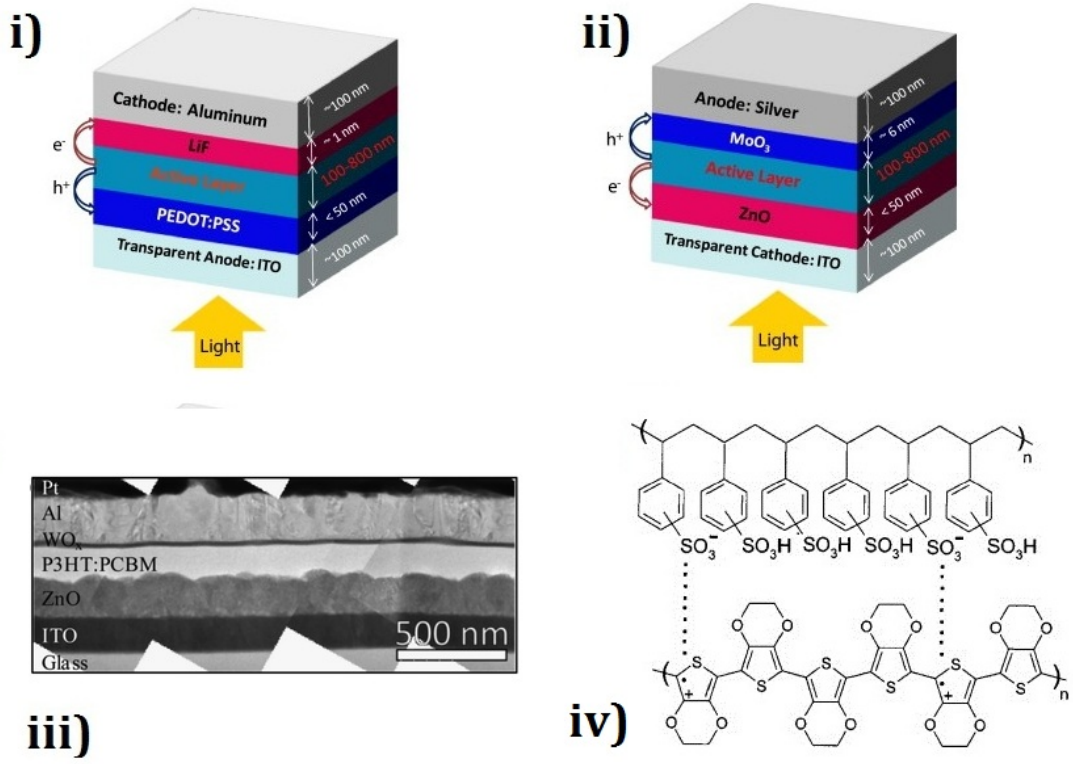

Figure 1.13 – *i)* and *ii)* typical OPV devices for normal and inverted architectures respectively, reprinted from [99], © 2013, with permission from Elsevier; *iii)* transmission electron micrograph of an inverted P3HT:PCBM OPV with an electrodeposited ZnO HBL between the bottom ITO electrode and the active layer, reproduced with permission from [100] with permission of The Royal Society of Chemistry; *iv)* structure of the polymer mixture PEDOT:PSS, reproduced from [101] © 2008, with permission from Elsevier.

Planar ZnO interlayers for OPVs have been produced using a number of different processing methods such as magnetron sputtering [102], sol-gel deposition [103], NP spin-coating [104], spray pyrolysis (SP), electrodeposition (ED) [100], ALD [98], and ink spin-coating [105]. Ink-based deposition techniques are of particular interest as they are compatible with roll-to-roll processing, a production technique which may be viable in the future and yield a very high throughput [106]; additionally, due to the low processing temperatures required by the ink-based ZnO deposition methods (< 150 °C), it is possible to use this technique to deposit ZnO on top of the polymer layer in a normal architecture device without causing major changes in the polymer blend crystal structure [107].

Gains in device performance from the presence of HBLs are attributed to a number of effects: HBLs increase the R_{sh} by removing short-circuit pathways which makes charge extraction more selective; fast electron transport in the oxide layer can lead to a more efficient extraction of electrons from the device; the creation of a cascading electronic structure from the $LUMO_D$ to the electrode which can lead to enhanced separated charge lifetimes and increase the probability of their extraction. Both the deposition method and processing of the ZnO films affect both the structural (preferred crystallite orientation and film texture) and electronic (work function) properties, and these will in turn affect the efficacy of the HBLs: for example, Schumann *et al.* noted that the J_{sc} seemed to exhibit an inversely proportional relationship to the texture coefficient of the polar (*002*) ZnO crystallite orientation. As the different planes exhibit different work functions and electron affinities, it may be the case that the neutral ($10\bar{1}0$) faces may provide a better energy level match for the $LUMO_{PCBM}$, thus leading to more efficient charge extraction for films with greater proportions of this crystallite orientation. The rich defect chemistry of ZnO often poses problems in electronic devices as the presence of electron traps can have an adverse effect on device performance: Manor *et al.* propose that the O_2^- defect is generated when ZnO is kept in the dark, leading to negative space-charge regions in the layer which lowers both the conductance and R_{sh} and consequently has a negative impact on diode behaviour of the device. They propose a course of UV treatment and reverse bias pulsing to remove these defects, although the authors do not comment on the long-term efficacy of such treatment [108].

Further improvements to device performance have been achieved by surface modification: modification of a NP–ZnO surface at the polymer–oxide interface with C_{60} has been shown to improve PCE through improved electron selectivity and inorganic–organic electron coupling [109]. Yip *et al.* modified ZnO layers in normal cells with functionalised benzoic acid at the ZnO–metal interface: this effectively lowers the Schottky barrier to electron transfer and leads to improvement in device performance. The greatest gains were obtained when using para-methoxybenzoic acid [110].

In addition to using planar electron extraction layers, groups have experimented with using nanostructured ZnO in the same role. Essentially, this increases the surface area of the electrode as well as reducing the average distance from the electron acceptor molecule to the electrode — the electron transport path length is a limiting factor for OPVs due to relatively slow electron mobility of organic materials and can lead to losses in photocurrent. Therefore, electrodes extending into the active layer may allow for the fabrication of devices with thicker active layers which would exhibit improved light ab-

sorption. Different morphologies such as NRs and dye-modified NRs [111, 112], NW [47], and nanoridge [113] films have been used in this role.

1.4.3 ZnO in hPVs

Using ZnO as an acceptor in lieu of a molecule brings a number of advantages such as high electron mobility, chemical stability [114], and relatively low-cost of the material of both materials and processing: to demonstrate the potential of such devices Krebs *et al.* have shown that it is possible to produce a working hybrid cell — produced entirely by non-vacuum solution processing — using industry-compatible methods [115]. Additionally, there is a large number of nanostructures available to ZnO and thus it is fairly simple to realise an ordered heterojunction device with arrays that not only offer large, stable interfacial areas, but also may be designed to act as light traps.

Acceptor Type	$\mathbf{V}_{oc}$ (V)	$\mathbf{J}_{sc}$ (mA cm^{-2})	**FF**	η (%)	**Ref.**
Bilayer ZnO	0.40	0.31	0.44	0.06	[116]
Bilayer TiO_2	0.60	0.85	0.67	0.34	[117]
Nanofibre ZnO	0.49	2.15	0.39	0.51	[118]
Nanofibre TiO_2	0.62	1.89	0.50	0.59	[119]
DEZ ZnO-NPs (Blend)	0.75	5.20	0.52	2.00	[120]
Bilayer ZnO (PCBA modification)	0.32	1.10	0.50	0.18	[121]
300 nm NR-ZnO	0.38	2.91	0.50	0.55	[122]
600 nm NR-ZnO	0.54	2.67	0.53	0.76	[123]
Porous ZnO	0.36	2.18	0.44	0.35	[124]
SWNT/ZnO NW	0.46	2.30	0.63	~ 0.60	[125]

Table 1.2 – Device characteristics for different oxide:P3HT hPV devices, including ZnO and TiO_2 device comparison, nanostructured, and modified devices. DEZ stands for diethylzinc, an organometallic ZnO precursor; SWNT refers to single-walled carbon nanotubes.

Despite their promise, hPV devices do not perform as well as OPV devices. Although NP:polymer composite blend devices have been made which exhibit PCEs comparable

to P3HT:PCBM — 2.0 % for ZnO:P3HT [120] and 3.09 % for CdSe:P3HT [126] — structured array devices fare much less well. ZnO NR array devices have reached a PCE of 0.82 % [123], a figure not commensurate with the large increase in D–A area over a simple bilayer device.

1.4.3.1 Nanoparticle Bulk Heterojunctions

BHJ-type ZnO devices which use blends of oxide NPs and polymer have achieved better PCEs than any of the bulk film devices: although the material network may be considered to be formed in a somewhat fortuitous manner compared to a structured array, their performances are quite promising despite of lagging behind their OPV counterparts. Beek *et al.* have carried out extensive work in this area, firstly using different polymers and optimising the blend composition: the group found that the optimal blend for P3HT contained 26 %vol ZnO (PCE 0.92 %) [127], compared with 30 %vol ZnO (PCE 1.6 %) for the semiconductor poly[2-methoxy-5-(3,7-dimethyloctyloxy)-1,4-phenylenevinylene] (MDMO-PPV) [128]; the performance of these devices is highly dependent on the ZnO content [129] and, interestingly, these optimised volume fractions of ZnO are low vis-à-vis polymer:PCBM blends (for example, optimal P3HT:PCBM blends typically employ 40 – 50 %vol PCBM)[8] [130]. Further work on the MDMO-PPV:ZnO system determined that the hole mobility hamstrings the performance of these devices — this is in contrast to MDMO-PPV:PCBM systems in which the hole mobility of the polymer increases due to intercalation of PCBM; as ZnO cannot intercalate in the same manner, it cannot affect the electronic properties of the polymer in this way [131].

Conventional ZnO NP synthesis is a rather time-consuming process [132], although the efficiency of the process may be accelerated by using the precursor diethylzinc (DEZ) which hydrolyses to form ZnO in the presence of water [133] — DEZ is blended with the polymer and deposited on the substrate, followed by a short aging process which allows devices to be fabricated on a very short timescale. Work on this method by Moet *et al.* has been encouraging with the best device yielding 1.4 % PCE under standard illumination conditions. Oosterhout *et al.* used electron tomography techniques to map the 3-dimensional distribution of P3HT and ZnO in DEZ-derived NP blends which showed that finer phase domains existed for thicker blend layers, reflected in improved device performances with increased active layer thickness [120] (this behaviour is contrary to

[8]Recent studies into polymer:PCBM systems suggest that the blend microstructure in these films is much more complex than originally thought [32]; as such, this model is not analogous to the ZnO:polymer mixture given the inherently crystalline nature of the oxide NPs.

that observed in P3HT:PCBM blend devices: thicker layers tend to diminish device performance as extended free charge path lengths in low carrier mobility systems increase the probability of non-geminate recombination). The best device in this work yielded a PCE of ~ 2.0 % and a reasonable V_{oc} of 0.75 V (*cf.* 0.5 – 0.6 V for a 'good' ZnO NR hPV device). However, in general, ZnO NP devices have so far lagged behind those using NPs of semiconductors such as CdS and CdSe: these are narrow band-gap semiconductors which absorb in the visible spectrum, whereas ZnO absorbs in the UV range, and as a result the narrow band-gap semiconductors contribute to visible light absorption and exciton generation, rather than acting purely as an acceptor.

Surface modification of the ZnO NPs is an effective route for enhancement of device performance: such work has been carried out using dyes such as porphyrins and safranin-O. Said *et al.* created ZnO:P3HT blends using NR particles and grafted the porphyrins onto the oxide surface, primarily aiming to increase the spectral response of the devices. Despite the complementary absorption afforded by the dye, device performance fell with increasing dye concentration as it was found that the presence of the porphyrin encouraged aggregation of the ZnO NRs as well as introducing trap states between the dye and the oxide, thus leading to a greater rate of recombination [134]. Suresh *et al.* incorporated the organic dye safranin-O into ZnO:poly(3-phenylhydrazonethiophene) (PPHT) devices leading to a large increase in device performance by over 4.5 times, attributed to the presence of a wider absorption spectrum and through increasing the degree of exciton dissociation [135].

Lastly, with the recent surge in research funding for graphene, composite NPs of graphene:ZnO have been tested as an acceptor species: for a device with 15 %wt graphene:ZnO in P3HT, the device characteristics seem promising with a high V_{oc} of 0.81 V and a PCE of 0.98 %, albeit with poor diode behaviour (FF of 0.25) [136].

1.4.3.2 Nanostructure Array Heterojunctions

As previously stated, ZnO may form a wide range of nanostructures and, consequently, devices employing NRs [137], nanoporous arrays [138], nanofibres, NWs, nanodisks [139], and NPs have been made in an attempt to increase the interfacial area. There is also interest in single nanowire cells, where the donor is grafted onto the oxide surface [140] — ZnO NWs may potentially yield loss-free electron transport and thus are a material of great interest for electronic applications in the future. ZnO NRs have been well studied for a number of applications, especially for photovoltaics: control of growth and rod characteristics (length, aspect ratio, *etc.*) may be attained by varying growth conditions and seed layer grain size. Rod growth has also been demonstrated on different substrates

Yin *et al.* fabricated some electrodeposited NR array devices on reduced graphene oxide (rGO) a potential TCO alternative to ITO with an optimised PCE of 0.31 % [141].

TiO_2 NRs, whilst also desirable, have been harder to obtain by simple solution processing methods: titania-based arrays often require more convoluted methods, such as the use of anodised templates [142] and, although hydrothermal growth (similar to the methods used for ZnO) of titania NRs has been reported, the methods do not possess the same degree of control as those for ZnO [143]. TiO_2 NRs may be grown in solution (as a suspension, rather than an ordered array) and incorporated into HPVs, as demonstrated by Lin *et al.* who created a TiO_2 rod:P3HT blend followed by infiltration into a ZnO NR array; in addition to this, devices containing this blend were also made from ZnO NR arrays which had been coated in a thin layer of these TiO_2 rods. Such treatment led to increases in J_{sc} of between 6 – 9 times and the highest PCE achieved was 0.59 % [144]. Efficiencies of ZnO NR devices have slowly increased as improvements to polymer infiltration and the quality of the arrays have been made with the highest reported efficiency being 0.82 %.

1.4.3.2.1 Polymer Filling of Nanostructures

Complete infiltration of nanostructured arrays with donor material is one of the main challenges with these devices — incomplete filling will result in poor device performance due to poor polymer–oxide contact or disruption of charge transport due to film discontinuity. Olson *et al.* have investigated polymer filling of NR devices, emphasising the importance of polymer processing conditions in achieving good structural infiltration, as well as additional post-process annealing steps to enhance the charge mobility. Device PCEs in this work ranged from 0.17 % to 0.28 %, the best performance achieved for spin-coating of P3HT dissolved in dichlorobenzene followed by annealing at 225 °C [145]: this step leads to polymer melting and allows the liquid to fill the nanostructure before crystallising during the cooling phase. The authors also note in this work that the differing polarity of the ZnO faces may directly affect polymer infiltration due to the use of apolar solvents during processing. This is confirmed by Conings *et al.* who probed mobility in ZnO NR/P3HT systems using impedance analysis: the authors note that polymer stacking on the non-polar $(10\bar{1}0)$ face of the ZnO NRs is not conducive to fast transport in the normal direction [146].

A number of papers have been published on the subject of polymer filling of TiO_2 nanostructures, an important consideration for solid-state DSSCs (SSDSC). The content of these papers also bears relevance to the filling of similar ZnO nanostructures as the confined space can affect polymer conformation and, therefore, charge mobility and L_{ex}.

The anode for the Grätzel–ORegan cell consists of a mesoporous TiO_2 layer, usually prepared either by sintering of a TiO_2 NP paste [147], or by block co-polymer assisted synthesis [148]. Such arrays usually have a very high surface area, owing to small pore sizes which are around 5 – 30 nm in diameter; however, whilst these films are excellent in DSSC applications which use a liquid electrolyte, the labyrinthine structure and lack of some form of order may be problematic when it comes to polymer infiltration for SSDSC or hPV fabrication: difficulties in this process may arise when the structural pores are smaller in diameter than the radius of gyration of the polymer — this forces a loss in the conformational entropy of the chain and can impede infiltration [149]. On top of this, the confined space also prevent the polymer from crystallising in the desired fashion (through chain stacking), forcing the chains to coil up which will both disrupt the intermolecular coupling and break conjugation between the residues, leading to large losses in charge mobility. As a result, the hole transport through the organic layer is slow, increasing the probability of charge combination which, in turn, will lower device performance; however, Coakley *et al.* have noted that there was a significant increase in performance for mesoporous TiO_2 hPVs over planar devices as the increased interfacial area [150] and the concomitant rise in the efficiency of exciton harvesting outweigh the losses in charge transport.

1.4.3.3 ZnO Processing

As covered in Section 1.4.1.3, ZnO has a rich defect chemistry which leads to highly variable electronic properties: the work function of ZnO can span over a range of 1 eV (with values ranging from $\sim$ 3.5 eV to $\sim$ 4.7 eV) and surface defects can lead to significant degrees of band-bending which, likewise, will profoundly affect device behaviour. Consequently, these properties are sensitive to deposition method, processing conditions, and post-processing treatment, although it is not easy to isolate the precise effect of a single property on hPV performance. For example, work by Olson *et al.* highlights variability of surface electronic properties in ZnO — sol-gel-derived ZnO films were treated either by annealing at 150 °C in air or by UV–O_3 treatment (which greatly increases the hydrophilicity of the substrate) with the annealed devices performing much better than those treated with UV–O_3 (PCEs of 0.09 % and 0.02 % respectively) [151], although results from untreated ZnO were not stated. This work was followed up by fundamental photoelectron studies on both ZnO single-crystal and NR arrays, showing that UV–O_3 treatment may introduce interfacial dipole moments on the NRs; in addition to this, it also highlights the differences in electronic structure of the different ZnO crystal faces [152]. This must be taken into consideration for devices which employ polycrystalline ZnO as the polymer–oxide interaction will be different for the non-polar and polar faces,

and thus the nature of this interface will vary depending on the crystallite orientation ratios of the different ZnO films. Plank *et al.* investigated the effects of both deposition method (SP, oxidation of sputtered Zn) and thickness of the ZnO backing layer on the performance of ZnO NW cells: the result was a significant variation in device performance, especially in V_{oc}. Whilst this may partially be attributed to the differences in film morphology and presence of pinholes, the differences in processing will affect the electronic properties of the films [153].

1.4.3.4 Oxide Engineering

Changes in electronic and structural properties of ZnO, such as band gap, carrier mobility, carrier concentration, and preferential crystallite orientation may be brought about through extrinsic doping within the crystal lattice (this is covered in Section 1.4.1.3.2). ZnO layers doped with Li, Mg, and Ca have been reported for hPV devices: those incorporating these films have generated significantly better performances than those with undoped ZnO. Lloyd *et al.* have reported relatively high device efficiencies (the highest PCE measured being 0.44 %) for planar sol-gel $Zn_{1-x}Li_xO$/P3HT cells, the optimum Li concentration lying around 15 – 20 %at [154]. Although Li acts as a shallow acceptor when substitutionally doping for Zn^{2+}, it may also occupy interstitial sites in the lattice, in which case it acts as an electron donor and increases the film carrier concentration; the site occupation preference depends on the doping concentration of Li^+, and therefore it is difficult to ascertain the true nature of the film. In this paper, Li incorporation is seen to decrease the work function and induce a slight increase in CB energy, although the optical band-gap does not change significantly from that of undoped ZnO. Additionally, grazing incident x-ray diffraction (GIXD) data show that P3HT on $Zn_{1-x}Li_xO$ exhibits a better degree of order than for the pure ZnO films, although the exact origin of the effect is unclear; nevertheless, this would also contribute to increases in device performance. Ruankham *et al.* have extended this approach, synthesising $Zn_{1-x}Li_xO$ NRs through hydrothermal growth. Increases in PCE were not as great as in the case of bilayer devices with the greatest increase in PCE being 0.26 % to 0.37 % for a doping concentration of 5 %at. Electron energy loss spectroscopy (EELS) data showed that incorporation of Li into the structure was not uniform and that undoped ZnO growth was preferred until the relative solution concentration of Zn^{2+} to Li^+ decreased sufficiently to drive incorporation of the latter into the structure. Again, in this case Li uptake occurred on both Zn and interstitial sites, depending on the Li^+ concentration in the chemical bath [155].

Mg and Ca may substitute for Zn within the ZnO lattice; as these species preferentially adopt the same oxidation state as Zn (2+), the conductivity is not expected

to change significantly; however, the introduction of both Mg^{2+} and Ca^{2+} into the lattice yields an increase in optical band-gap, which has been shown to occur due to a shift of the CB level closer to vacuum [156]. This effect may be exploited to tune the $HOMO_D$–CB_A offset which, in turn, affects the V_{oc} of the devices — for Mg doping, values ranged from 0.5 V for undoped ZnO to over 0.9 V for a 65:35 Zn:Mg ratio [157]; it should be noted, however, that increased Mg content increased the R_s of the devices, leading to a progressive decrease in FF. The optimal composition for these devices was found to be $Zn_{0.75}Mg_{0.25}O$: devices were made with both low molecular weight (M_w) P3HT (11,000 g mol^{-1}) and Rieke Metals P3HT (49,200 g mol^{-1}) and, for the former, doping increased the cell performance almost two-fold. The maximum PCE obtained for these devices — using 25 %mol Mg content and the heavier P3HT — was 0.49 %, an extremely high value for a bilayer device, eclipsing the performance of many reported nanostructured devices. Ca doping reported by Wang *et al.* [158] yielded similar results – increasing band-gap with Ca content to a doping limit x = 0.10 and a concomitant decrease in work function. PCE was observed to double from 0.06 % to 0.12 %, mainly due to a large increase in V_{oc} from 0.56 V to 0.80 V [158]; however, electrical measurements were not carried out to probe changes in film resistivity with doping concentration.

Whilst the works detailed above focussed on bulk doping of ZnO, Oh *et al.* took a different approach to doping, aiming to dope the the ZnO surface with N^{3-}, leading to passivation of surface O vacancies [159] — this compensates for these donating vacancies and prevents them from acting as interfacial electron traps. This was carried out on a NR array of ZnO by using a nitrogen plasma, allowing complete treatment of the ZnO surface. The filling of oxygen vacancies by N led to the formation of a resistive surface layer which acts as a recombination barrier, seen in the significant reduction of J_0. In terms of device performance, although the J_{sc} was reduced slightly, the V_{oc} increased from 0.30 V to 0.71 V, leading to an overall increase in PCE.

1.4.3.5 Suitability of Oxide Acceptors in OPV Systems

Although a significant amount of research has been carried out into ZnO-based hPVs, there is still not a consensus as to why inorganic materials seem to be less suitable acceptor species than molecular materials or, indeed, why ZnO-based devices perform less well than those using TiO_2 as an acceptor. Noori and Giustino's paper modelling the ZnO:P3HT interface concludes that charge transfer should occur readily from P3HT to ZnO, and the band alignment in this system is such that the maximum V_{oc} should be 2.07 V [160]. However, this work neglects to include defects in the model. An experimental interfacial band alignment study into this system by Nagata *et al.* found that the maximum V_{oc} for their system would be around 1.50 eV, although this is

diminished by high rates of recombination due to the short depletion layer in ZnO which prevents charges from being sufficiently spatially separated.

As covered in Section 1.4.1.3.3, the theoretical and experimental study by Li *et al.* into the role of surface defects in the electronic behaviour of ZnO suggest that –OH groups formed from V_O could be detrimental to device performance [87]; moreover, the presence of –OH groups is thought to affect the interaction between organic and inorganic species, potentially leading to less favourable conditions for charge transfer [90]. A study by Tiwana *et al.* investigating the rate of electron injection from the Z907 dye into TiO_2, SnO_2, and ZnO by optical pump terahertz probe spectroscopy showed that charge injection from the dye into ZnO is a slower process than for injection into TiO_2, despite the fact that VB and CB levels are at very similar energies for each material[9] [161]. Although the precise reason for this effect is not elucidated in this work, the authors posit that poor electronic coupling between ZnO and the dye (*cf.* TiO_2) could lead to the observed effects — this could potentially be related to different modes of bonding between the dye and the different oxide species.

Work by Piris which uses time-resolved microwave conductivity (TRMC) measurements to analyse charge dynamics in Mg:ZnO–P3HT devices (including results for undoped ZnO) has suggested that there is not a significant contribution to photocurrent arising from exciton quenching at the D–A interface for both doped and undoped ZnO [162]; the authors propose that photocurrent in these systems is generated predominantly through auto-dissociation of excitons in the P3HT bulk. Although this work does not give a hypothesis as to why exciton quenching in this system is poor, a number of factors may be considered: poor electronic overlap between the donor and acceptor materials; unfavourable polymer conformation at the interface; poor P(E) for charges in CT states. It may be the case that P3HT is simply an unsuitable species to pair with ZnO, although reports of hPV devices with polymers other that P3HT are few and far between.

1.4.3.6 Interface Modification

Interface modifiers (IMs) have been used extensively in hPVs to change the properties of the oxide surface leading to improvements in device performance. The application of IMs can have a number of effects on the oxide depending on the species used, and a single IM can produce one or more of the following effects:

i) Introduction of a surface dipole (δ) which can change both the work function of the oxide and shift in the conduction band-edge, affecting the D–A orbital offset and, therefore, V_{oc} and ΔE.

[9] Although this study relates specifically to the dye–metal oxide complexes used in DSSCs, some of the principles may hold for polymer–oxide charge transfer.

ii) Use of a species with high electron affinity can enhance the rate of electron transfer to the oxide — such a species will also create a surface dipole and can also increase the depletion length in the oxide.

iii) IMs with an acceptor level lying between the $LUMO_D$ and the CB_A can create a 'cascading' band structure at the interface and increase the lifetime of separated charges.

iv) Some IMs can provide a spatial barrier for separated charges, reducing the probability of recombination.

v) IMs can act to passivate traps in the oxide which may reduce recombination.

vi) High surface energies can affect polymer conformation at the D–A interface, leading to reduction in properties such as hole mobility and increasing recombination probabilities. Some IMs can lower the surface energy, leading to more favourable polymer conformations, and therefore better device performance.

IMs may be either organic or inorganic in nature: the former generally form self-assembled monolayers (SAMs) on the oxide surface, anchored to the oxide through a polar head group such as –COOH, –OH, or –SH, whereas the latter tend to be deposited on top of the oxide as a thin layer (typically < 20 nm) of either crystalline or amorphous material.

1.4.3.6.1 Organic Modification

Organic modification has been widely investigated for both ZnO and TiO_2 using a variety of different organic species, such as porphyrin dyes, benzoic acid derivatives, and fullerene derivatives. Goh *et al.* carried out one of the first studies into hPV IMs on the TiO_2/P3HT system: although this work does not feature ZnO-based devices, the results of this work do bear relevance to them. This work is split into two components: firstly, the modification of the oxide surface with SAMs of differently functionalised benzoic acid derivatives is reported; in the second half, work detailing oxide functionalisation by Ru-based dyes (N3, Z907, and N719) used in DSSCs[10] [117].

In the first part of the paper, different functional groups were chosen, ranging from electron-donating groups such as –NH2 (δ = +4.5, calculated by DFT) to electron-withdrawing groups such as $–SO_2F$ (δ = -4.5) to change the electron affinity of the

[10]Whilst these dyes will make contributions to the photocurrent, the dye-loading in these systems is far smaller than is the case for nanostructured DSSC devices and the device performance trends can be taken to reflect the interfacial properties of these cells.

molecule; in this way, trends in device performance could be correlated to the changes in dipole moment, given the similarities between the IM species. The effect of IMs on the hPV band structure is shown in Figure 1.14.

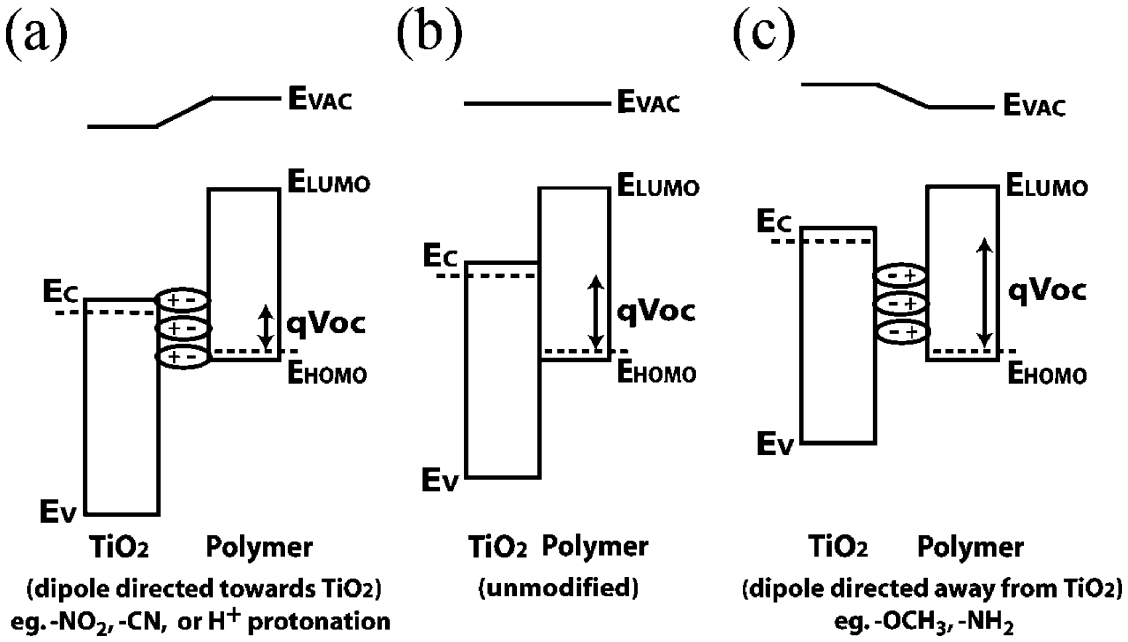

Figure 1.14 – Flat-band representation of a TiO_2:polymer hPV device showing the cases of: a) oxide modified with a δ^- IM; b) unmodified oxide; c) oxide modified with δ^+ IM. Reprinted with permission from [117]. © 2007, AIP Publishing LLC.

Although the δ^+ IMs displayed a small increase in V_{oc} — expected due to an increase in the $HOMO_D$–CB_A offset — it is thought that protonation of the oxide by the IMs act to counter the dipole moment, limiting the performance gains. For δ^- IMs, compared to the unmodified oxide the V_{oc} declined, but a $\sim$ 2x improvement in J_{sc} was observed — due to the electron withdrawing nature of these IMs, they are thought to mediate charge transfer from the polymer to the oxide.

Dyes, such as the Ru complexes mentioned above, will also create a dipole at the oxide surface. As well as this, they may provide further benefits: if the energy levels are well aligned with the metal oxide and may create a 'cascading' band structure — this is analogous to the electron transport chains used in photosynthesis which increase the longevity of the charge separated states [163]; additionally, the central Ru species and its corresponding redox properties make these dyes effective electron transfer complexes. It was shown that the N3 dye increased the J_{sc} from 0.85 mA cm^{-2} to 1.86 mA cm^{-2} and the overall PCE from 0.34 % to 0.60 %. Work by Ravirajan *et al.* on ZnO/P3HT systems employing the Ru-based dye Z907 increased device performance as well as showing that the dye greatly impedes charge recombination such that separated charges have a half

life of $\sim$ 6 ms — around 2 orders of magnitude greater than for a BHJ NP–ZnO/P3HT device [164, 129]. NR arrays have also been modified using metal-free mercurochrome dyes [165] work by Lin *et al.* presents increases in V_{oc}, J_{sc}, and a four-fold increase in PCE for ZnO NR/P3HT devices compared to the unmodified array [166].

C_{60} derivatives are now commonplace as acceptor molecules for OPVs and have also been used as IMs for polymer:metal electrode interfaces. Vaynzof *et al.* used a SAM of the fullerene derivative PCBA (carboxyl derivative of PCBM) to modify the ZnO/P3HT interface, achieving a 4.5-fold increase in PCE (0.04 % to 0.18 %) [121]. This significant increase in performance is attributed to multiple effects: firstly, the PCBA adsorption on the ZnO surface creates a δ^- pointing towards the oxide; secondly, the work function increases from 3.6 eV to 4.1 eV, attributed to a decrease of electron density at the oxide surface, thereby increasing the depletion length within ZnO; thirdly, the charges are separated rapidly due to the fast electron transport properties of the C_{61} component; lastly, the PCBA itself spatially separates the charges and acts as a barrier to recombination. Moreover, increases in the EQE and increased J_{sc} of the modified device suggest that the IM contributes to exciton quenching and provides an effective route for enhancing the photocurrent in these devices. A follow-up paper on this work proposes the existence of bound-charge pairs (BCPs) in organic–inorganic systems based on evidence from a novel optical pump-push photocurrent probe technique: BCPs are analogous to CT states — discussed in Section 1.3.2.2 — observed in OPVs[11]; it is suggested that the presence of the PCBA layer significantly reduces the fraction of bound charges present in the device [167].

Alkanes with polar head groups, such as alkanethiols and alkanephosphonates, have been used extensively in fields such as nanolithography and organic electronics (particularly as organic dielectrics) due to their tendency to form SAMs on oxide surfaces. Papers by Monson and Lloyd report the modification of hPV devices with such molecules: the SAMs assemble such that the head groups form strong Zn–S or Zn–O–S [168] interactions with the oxide, leaving the alkane chains pointing in the direction normal to the substrate. Despite the fact that such molecules are insulators, both decanethiol and octadecanethiol were shown to improve the PCE through increases in J_{sc} from 0.28 mA cm^{-2} in the unmodified devices to 0.35 and 0.42 mA cm^{-2} for decane and octadecane derivatives respectively [169]. This work has been followed up by Lloyd *et al.* who used GIXD to probe the structure of the polymer on this SAM layer and transient absorption

[11]BCPs do differ from CT states in that an organic–inorganic interface contains a delocalised acceptor band structure as opposed to the case for the LUMO of a small molecule, as is the case for species such as PCBM.

spectroscopy (TAS) to investigate the recombination dynamics [170]. The GIXD measurements confirm the increasing order of polymer deposited on the alkanethiol-modified ZnO compared to bare ZnO; TAS measurements showed that there is a greater rate of polaron recombination for P3HT/ZnO compared to P3HT/Glass and P3HT/SAM-ZnO, which also points to a reduction in order of the polymer on the bare, high energy ZnO surface, and a greater separated charge lifetime in layers with greater crystallinity of the polymer. In addition to this, it was determined that significant exciton dissociation occurs in the P3HT bulk regardless of the substrate used which concurs with Piris TRMC measurements on $Zn_{1-x}Mg_xO$ layers. Baker *et al.* have also used the same approach to IM, instead using the organosilicon compounds octadecyltriethoxysilane (OTES) and phenyltriethoxysilane (PTES). n-butylamine catalyses the formation of Si–O–Zn linkages between the IM and the oxide, whilst the alkyl chains are directed towards the polymer and interact in the same way as the alkanethiols. However, the OTES sample appeared to hinder the polymer infiltration through unfavourable wetting characteristics; with PTES, the reaction conditions resulted in condensation of the organosilicon units, resulting in the formation of multilayers and inhibiting charge transfer [171].

Most IM candidates studied to this point have been materials readily available and many have been used previously in other applications (such as the use of alkanethiols in the production of organic field-effect transistors (FETs)). Weickert *et al.* propose that purposefully designing IMs may lead to greater performance gains and have established some general design rules [172]:

i) Energy levels allow efficient charge injection from the polymer to the oxide.

ii) Complete coverage of the oxide and intimate contact between the IM and the donor.

iii) Physical spacers can prevent recombination but must not inhibit forward charge transfer and thus the photocurrent.

iv) Modifiers should neither generate interfacial traps, nor disturb the order and crystallinity of the organic donor.

v) Crystalline interfacial layers must possess suitable energy levels and not inhibit exciton dissociation.

This group have recently reported modification of TiO_2 with specifically designed IMs such that its HOMO lies between the $HOMO_D$ and CB_A, as well as possessing large, negative dipoles pointing towards the polymer [173]. The best IM used in this work produced an order of magnitude increase in both J_{sc} and PCE (0.60 mA cm^{-2} to 6.79 mA cm^{-2},

and 0.20 % to 2.87 %) as well as large increases in EQE, implying that these IMs promote exciton dissociation.

1.4.3.6.2 Inorganic Modification

Inorganic IMs usually consist of either amorphous or crystalline thin-films of semiconducting materials deposited on top of the ZnO. Narrow-band species used include CdS and Sb_2S_3: Spoerke *et al.* modified ZnO surfaces with a 20 nm-thick CdS layer, creating a P3HT/CdS/ZnO band level cascade [116]. CdS effectively raises the acceptor conduction band level, and this likely contributes to the near doubling of the V_{oc} from the unmodified device; the photocurrent remains unaffected however[12]. Sb_2S_3 has been used to modify mesoporous TiO_2/P3HT hPVs leading to increases in PCE from 0.092 % to a maximum of 5.06 % — it should be noted that in this case, Sb_2S_3 acts as a sensitiser and seems to contribute the bulk of the device's photocurrent [174]. However, these initial results are very promising with performances comparable to OPVs.

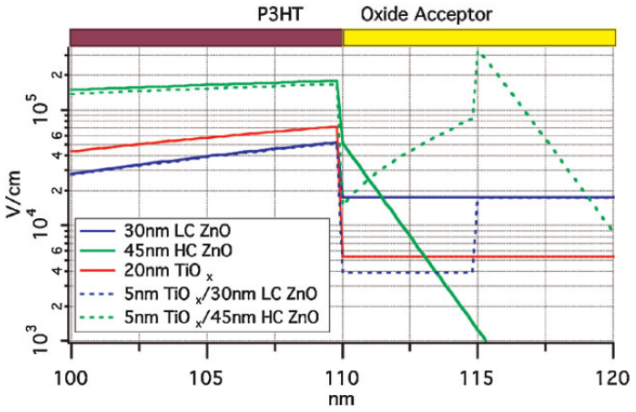

Figure 1.15 – Modelled electric field variation in the interfacial region for different ZnO/P3HT and ZnO/TiO_x/P3HT devices. Reproduced with permission from [175].

TiO_2 and TiO_x layers are generally effective at raising the V_{oc} of hPV devices. Atienzar *et al.* deposited a thin layer of TiO_2 onto a ZnO NR array using a $TiCl_4$ solution — the presence of TiO_2 appears to increase the J_{sc} which is attributed to a reduction in recombination and possibly increased exciton dissociation, leading to a near three-fold PCE increase from 0.025 to 0.070 % [176]. Using amorphous layers, Lee *et al.* have shown that deposition of 5 nm of TiO_x on ZnO may increase the V_{oc} from 0.4 V to

[12] As a narrow band-gap material, CdS will contribute to the photocurrent; however, due to its poorer transport properties, the net result is no gain in J_{sc}

0.8 V. TAS measurements suggest that the interlayer does not alter the charge separation/recombination dynamics as both modified and unmodified devices exhibit similar hole lifetimes [177] and cite passivation of ZnO surface traps as the source of device improvement. Follow-up work was carried out on this system — the authors present the hypothesis that TiO_x layers affect the ZnO depletion length in these devices, depending on the conductivity of the ZnO — a low internal electric field results in slow charge separation at the interfacial region and increases recombination probabilities. ZnO films of high carrier (HC) and low carrier concentration (LC) were deposited by PLD, modified with TiO_x, and the device performances measured. This was carried out concurrently with 1D Poisson modelling of the internal electric field in these devices, the results of which are shown in Figure 1.15 [175].

The application of the thin TiO_x layer is shown to increase the device performance performance for HC ZnO, whilst decreasing it for the LC films. For HC ZnO, the electric field modelling suggests that TiO_x prevents a total drop in electric field in the oxide interfacial region (*cf.* a drop to $< 10^{-3}$ V cm^{-1} within 5 nm of the interface for the unmodified HC ZnO film), whereas in the LC ZnO case, this field is reduced. As a result, for a 10 nm layer of TiO_x, HC ZnO devices show large increases in V_{oc} (0.217 V to 0.596 V) and PCE (0.027 % to 0.053 %), whilst LC ZnO devices show only slight increases in V_{oc} (0.421 V to 0.516 V) and overall reduction in PCE (0.050 % to 0.014 %). These experiments show that inorganic modification of the interface is an effective method for increasing V_{oc} in hPVs. However, save for the case of Sb_2S_3, these layers tend not to enhance the device photocurrent and, in some cases, can provide a barrier to charge transfer from the oxide to polymer.

1.4.4 Summary

From the literature review, it is clear that whilst oxide:polymer hPV devices have plenty of potential, significant progress in the field is required before these devices can become a viable technology. Given the complex defect chemistry of oxides such as ZnO, interface modification of these materials has been shown to be an effective and perhaps necessary route towards closing the gap between hybrid and organic photovoltaics. The work presented in this thesis proceeds with the inorganic modification route: the presence of these interlayers removes some of the negative effects of the ZnO surface chemistry; additionally, the materials chosen also possess additional functionality in the form of ferroelectric polarisation. The rest of this chapter covers two main areas: ferroelectricity, materials, and roles in photovoltaics (Section 1.5), and secondly the materials chosen for the fabrication of hPV devices in this work (Section 1.6). The last section covers the aims and structure of this work (Section 1.7).

1.5 Ferroelectrics

The unique functional properties of ferroelectric materials have led to their widespread use in a number of applications which exploit their excellent polarisation characteristics (due to high dielectric constants), piezo- and pyroelectric properties and/or ferroelectricity: ferroelectric materials are used extensively in capacitors, notably in switchable ferroelectric capacitors which may be integrated into standard silicon chips; additionally, there is ongoing research into areas including memory applications, radio-frequency identification technology, weak-magnetic field sensors, and ferroelectric liquid crystals [178]. Recently, there has been interest in exploiting ferroelectric properties in PV applications — this is described in more detail in Section 1.5.2.

1.5.1 Ferroelectricity

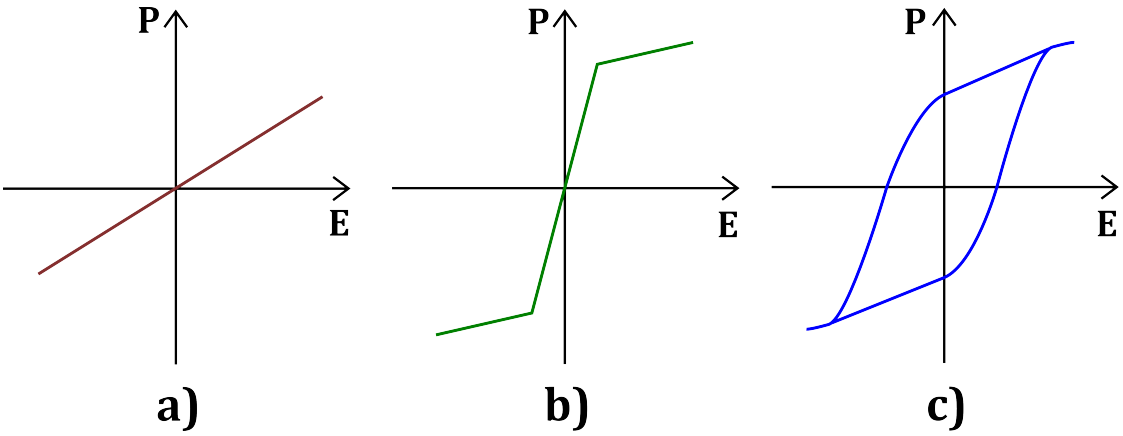

Figure 1.16 – Simple representation of polarisation (P) behaviour of a) dielectric, b) paraelectric, and c) ferroelectric materials under the influence of an external electric electric field (V).

Most materials exhibit dielectric behaviour in which the electrical polarisation (the total dipole moment per unit volume), P, is proportional to the magnitude of the external electric field [179].

$$P = \frac{\Sigma \mu}{V} \tag{1.9}$$

where μ is a dipole moment and V the volume. Ferroelectric (FE) materials exhibit non-linear polarisation behaviour, as illustrated in Figure 1.16, with the materials possessing a spontaneous non-zero residual polarisation, P_R, after the removal of the applied electric field. Additionally, the polarisation of the ferroelectric may be permanently and

reversibly switched in either the positive or negative electric direction by the application of a sufficiently strong electric field, making FE materials extremely well suited to memory applications. FE materials possess domains, regions of crystal with uniform and homogeneous dipoles along a specific crystallographic direction; domains are separated by boundary regions referred to as a domain walls which exhibit their own complex polarisation behaviour. For a newly grown FE material, the domain structure will be fairly complex, and many of the dipoles order in a head-to-tail (180°) manner to minimise stray field energy leading to a zero net polarisation or a small non-zero polarisation (which may arise due to other effects, such as thin-film strain).

The origin of the characteristic FE hysteresis loop shown in Figure 1.17 is as follows (taking the saturation polarisation point P_s, the maximum polarisation the material may hold, as a starting point): at P_s, the majority of domains are polarised in the direction of the electric field. As the electric field is swept in the opposite direction, new domains of opposite polarity begin to nucleate at the electrodes. As the electric field increases in this direction, the new domains grow rapidly in the direction of the electric field (*i.e.* normal to the substrate). At the coercive field, E_c, the net polarisation in the material is 0. At the point where the domains stretch across the material perpendicular to the substrate, the domains start to widen: as the domains grow more slowly in this direction, the rate of polarisation increase with electric field slows as the material approaches saturation. When the saturation field is reached, the material has been fully switched in polarity. Ferroelectricity is a low-temperature effect and above a certain temperature (dependent on materials system and quality of material), FE materials will exhibit paraelectric behaviour. As ferroelectricity is an effect arising from structural modulations such as ion displacement in perovskites (covered in Section 1.5.3) or conformation in polymers, increase in thermal motion can negate these effects and the material undergoes an order-disorder phase transition: this point is referred to as the Curie temperature (T_c). This transition is reversible, however, and FE properties are restored on cooling below T_c.

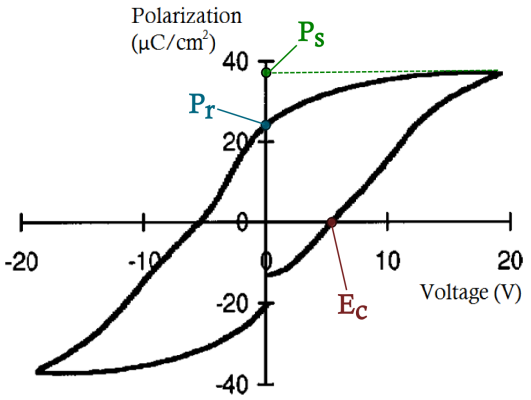

Figure 1.17 – A polarisation-voltage loop for a ferroelectric material showing polarisation hysteresis behaviour. P_R is the remnant polarisation; P_S the saturation polarisation; E_C the coercive field. Adapted with permission from [180]. © 1999, AIP Publishing LLC.

Ferroelectricity is effectively a co-operational effect between unit cells and therefore a critical thickness limit exists for thin-films of these materials. For ceramic perovskite oxides, the FE critical thickness was thought to be on the order 20 nm; however, experimental work has shown that $PbTiO_3$ can exhibit ferroelectricity at a thickness of 3 unit cells (1.2 nm) [181]. At short length scales, surface effects become much more important in governing the polarisation characteristics of the material: in this regime, defects and uncompensated bonds can create surface tension and the resulting surface charge density may generate a depolarisation field which acts in opposition to the ferroelectric polarisation. In early calculations, it was shown that depolarisation fields would dominate the material characteristics at short length scales leading to large critical thickness values. However, depolarisation fields appear to play a much lesser role than originally thought, and surface domains may effectively oppose these [182].

1.5.2 Ferroelectrics in Photovoltaics

Research incorporating FE materials in PV applications is a recent development and has generated interest in two different areas: firstly, the development of the ferroelectric photovoltaic (FE-PV) cell in which the FE material acts as the active layer; secondly, the deployment of FE materials into OPVs as functional layers to improve device performance without contributing as a light-absorber. Despite the marked difference between these two research topics, both exploit the unique properties of FE materials and possess intriguing potential.

1.5.2.1 Ferroelectric PV Cells

Although the photovoltaic effect in inorganic FE materials has been known about for a long time, it is only recently that interest in this area has picked up and more extensive studies carried out. The mechanism of photocurrent generation in FE materials is different to the case of a standard p–n junction: whereas the V_{oc} in the latter is limited to the band gap of the device, FE-PV devices are capable of generating large voltages in excess of the band gap. The photovoltaic effect in these materials originates at specific domain walls in which the polarisation changes from that within the domain — as a result, there is significant charge imbalance and band-bending occurs across the domain wall, leading to the creation of a very strong electric field and resulting in separation of charges generated in this region[13] [183, 184]. This effect has been probed most extensively in $BiFeO_3$ and $(Pb_{1-x}La_x)(Zr_{1-y}Ti_y)O_3$ [185]. The main obstacles in this field stem from the large band-gaps of these ferroelectric materials (2.57 eV for $BiFeO_3$) and

[13]Photocurrent from the bulk of the material is negligible as charges in this region are strongly localised.

the poor charge transport in the films: the latter is problematic as more conducting FE materials can hold a lesser degree of polarisation. However, the generation of very high voltages is a significant attraction as conventional solar cells typically generate < 1 V; moreover, the photoresponse can be tuned through control of the ferroelectric domains by application of external electric fields across the device.

1.5.2.2 Ferroelectrics in OPVs

The concept of the the ferroelectric OPV (FE-OPV) was first described in 2011 by Yuan *et al.* who proposed that the presence of two thin ferroelectric polymer layers (consisting of poly(vinylidene difluoride – tetrafluoroethylene), P(VDF–TrFE)) at the two interfaces between the active layer and the electrodes would generate an electric field across the active layer which would aid in splitting up CT states, thereby increasing the photocurrent [186]. Further work has been carried out by this group and others using both this architecture and variations thereof, shown in Figure 1.18.

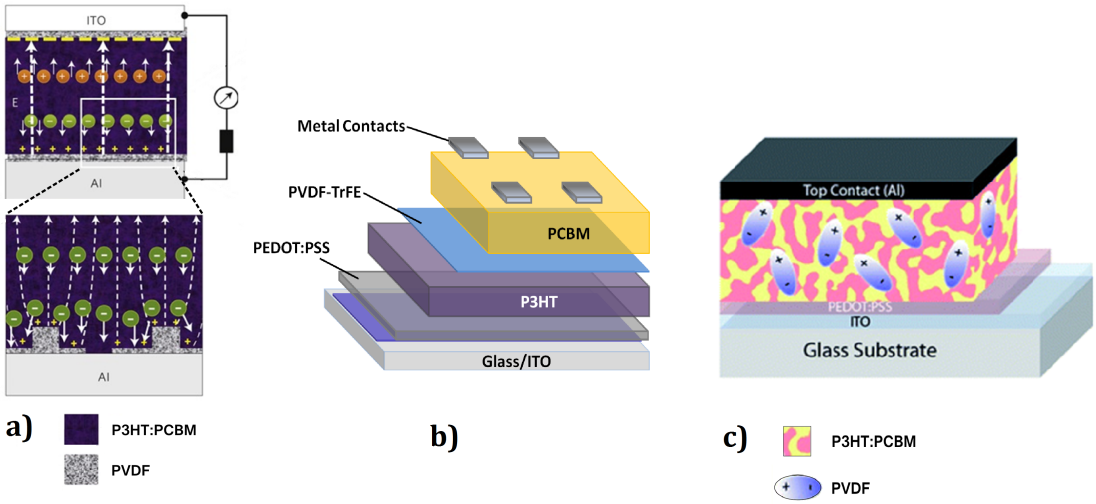

Figure 1.18 – Representation of OPV devices containing the FE polymer components: a) P3HT:PCBM blend BHJ modified with P(VDF–TrFE) at the metal:polymer interfaces, reprinted by permission from Macmillan Publishers Ltd: Nature [186], © 2011; b) a P3HT/PCBM bilayer device containing a P(VDF–TrFE) interlayer between the donor and acceptor materials; c) BHJ device using a P3HT:P(VDF–TrFE):PCBM blend as the active layer, reproduced from [187] with permission of The Royal Society of Chemistry.

In the first demonstration of the FE-OPV concept, the thickness of PVDF–TrFE was varied between 0–3 monolayers (to approximately 5 nm) and the layers were poled by pulsing high positive or negative voltages across the device. The authors assert that a three monolayer-thick film of P(VDF–TrFE) (with a remnant polarisation of 100 mC m^{-1}) will induce an electric field of 50 V μm^{-1} across a 150 nm-thick layer of

P3HT:$PC_{70}BM$, thereby suppressing CT state recombination. Whilst some intriguing results are reported in this study — for one device series, the presence of 2 monolayers of P(VDF–TrFE) increased the PCE of device from 1.7 % to 4.5 %, as well as improvements in device performance after poling the devices — it is not without flaws. The controls presented are not adequate enough to rule out the possibility that device performance improvements do not originate from the presence of FE polarisation: the effects of poling unmodified devices were not studied; additionally, a control interlayer (such as a non-FE variant of the P(VDF) family) was not used to test whether ferroelectric effects are the root of device performance. As well as this, the effects on the active layer morphology were not thoroughly investigated. Asadi *et al.* argued that by following the methods described in this paper, the resulting devices are improved not by the presence of the FE polarisation, instead that the P(VDF–TrFE) layer simply acts as a work function modifier at the metal–polymer interface, akin to materials such as LiF [188]. To demonstrate this, devices were fabricated with interlayers of P(VDF–TrFE), poly(trifluoroethylene) (PTrFE, a non-ferroelectric polymer), and LiF: the resulting devices showed that the 'poled' P(VDF–TrFE) devices behave similarly to the LiF-modified devices, exhibiting similar V_{oc} and a slightly reduced J_{sc}. The authors also comment that the poling method used in this work may be insufficient to induce full polarisation in the (PVDF–TrFE) layer: the poling process requires compensation charges on both sides of the ferroelectric layer and as the free charge carrier density in polymers is relatively low, it is questionable whether there will be requisite charge compensation from the polymer to induce full polarisation in the FE layer, especially in the dark. The authors also argue that, under illumination, free charges photogenerated in the polymer will screen the FE polarisation, negating any electric field generated in the active layer; however, it is questionable that the polymer free charge density could reach a sufficient level to screen the polarisation completely.

Yang *et al.* fabricated bilayer FE-OPVs containing a P(VDF–TrFE) interlayer between the donor and acceptor materials, as illustrated in Figure 1.18 b), aiming to modulate the energy levels of donor and acceptor. Although no data for a reference device (without the interlayer) was included, both positively and negatively poled devices were shown to have improved device characteristics compared to unpoled devices: increases in V_{oc} from 0.55 V to 0.67 V and increases in J_{sc} by 0.8 mA cm^{-2} for reverse bias poling. Poling also appeared to reduce J_0, implying suppression of charge recombination. The authors observed that, although the V_{oc} is higher than those typically obtained for a P3HT:PCBM device (either in bilayer or blend configuration), the V_{oc} produced by these devices is still much lower than the theoretical maximum V_{oc} ($\sim$ 1.5 V, accounting for D–A offset and non-ideal diode losses). The authors posit that this is due to the

low surface coverage of P(VDF–TrFE) on P3HT ($\sim$ 20 %) resulting from formation of nanoislands (as opposed to a continuous thin-film of FE polymer) on account of the large surface energy mismatch between P3HT and P(VDF–TrFE). However, this paper also suffers from lack of controls: data from non-FE-modified devices is not present, nor a device containing a non-FE interlayer.

FE-OPV devices containing a P3HT:P(VDF–TrFE):PCBM blend as an active layer have been reported by Nalwa *et al.*: the FE polymer was added to the D–A blend in fractions of 0, 5, 10, and 20 % by weight of P3HT, leading to an increase in PCE from 2.5 % to 3.9 % (for 10 % of P(VDF-TrFE) arising predominantly from an 18 % increase in J_{sc}, albeit with minimal increases in V_{oc} [187]. Positive poling (using the methods used by Yuan *et al.* was shown to have no significant influence on device performance, but negative poling was shown to degrade J_{sc}, V_{oc}, and FF for devices containing 5 and 10 % P(VDF–TrFE)), whilst unmodified and 20 % P(VDF–TrFE) devices remained unaffected. However, it was shown that applying a positive bias pulse to a device previously subjected to negative bias restored device performance, suggesting some form of switchable behaviour.

Control devices consisting of *i)* unmodified P3HT/PCBM bilayers, *ii)* P3HT/P(VDF–TrFE)/PCBM trilayers (illustrated in Figure 1.18b), and *iii)* P3HT:P(VDF–TrFE)/PCBM bilayers were tested as microstructural changes induced by the presence of the FE polymer may affect device performance. Although device *ii)* exhibited a slight reduction in PCE (from 0.8 to 0.7 %), it exhibited the greatest degree of PL quenching which was tentatively ascribed to increased dissociation of singlet excitons — the authors propose that the reduced J_{sc} may be attributed to the FE polymer acting as a physical barrier to D–A electron transfer; additionally, a slight increase in V_{oc} from 0.4 to 0.5 V was observed. Device *iii)* yielded an increase in PCE from 0.8 to 1.3 % with much improved EQE. Although controls in this work should have included using a non-ferroelectric polymer in the blend to verify that ferroelectric effects are responsible for device enhancement, the results presented are of much interest.

Finally, to address some of the concerns raised by Asadi *et al.* in [188], Yuan *et al.* investigated the effect of using crystalline (FE) and amorphous (non-FE) P(VDF–TrFE) in their FE-OPVs [189]. The crystallinity of the polymer was varied using different deposition techniques (spin-coating for amorphous films, Langmuir–Blodgett deposition for crystalline films) and different annealing regimes; the presence or absence of ferroelectricity in these films was confirmed by piezoresponse force microscopy (PFM). Using forward and reverse bias pulses on the devices, it was shown that much more marked changes in device performance occurred for devices containing the crystalline polymer

than for those containing the amorphous one: in the former case, negative poling led to decreases in J_{sc} and FF, whereas positive bias poling resulted in increases in J_{sc} and V_{oc} (as shown in Yuan's previous paper). Conversely, for amorphous P(VDF–TrFE), although positive and negative poling yielded similar outcomes, the differences in J–V curves were found to be much less significant and were attributed to small polarisation effects arising from partial crystallisation of some of the FE polymer layer during thermal annealing. Additionally, work was carried out to address the potential screening of the ferroelectric polarisation by free charges in the polymer: it was calculated that, assuming charges were to accumulate at the active layer:FE polymer interface (*i.e.* due to poor charge extraction), the active layer would need to be illuminated for 30 seconds to generate the requisite number of charges to screen the polarisation. This, in turn, would result in a steady decrease in device performance over that time; however, little variation in device performance was observed over a period of $\sim$ 350 hours, providing sufficient evidence to conclude that the polarisation is not screened in the device.

So far, there has been no investigation into the effects of incorporating FE materials into hPVs, although some investigation into the effect of piezoelectricity on device performance has been carried out for ZnO-based devices [190].

1.5.3 Ferroelectric Materials

Ferroelectricity has been observed in a diverse number of different materials and compounds: as the effect was initially observed in salts (such as potassium dihydrogen phosphate, $K(HO)_2PO_2$ and Rochelle's salt, $K(OOC)(CHOH)_2(COO)Na$), it was thought that hydrogen bonding was a prerequisite for it to exist. However, the the discovery of ferroelectricity in perovskite-based ceramics was a landmark in research, and this class of compounds has become the most widely used in FE applications such as capacitors and ferroelectric random access memory (FERAM). More recently, ferroelectric polymers such as P(VDF–TrFE) have been of much interest as these materials require far less temperature intensive processing than perovskite compounds; consequently, these materials have been earmarked for use in plastic electronics, including applications such as switchable organic FETs [191]. As ferroelectric materials also possess pyro- and piezoelectric properties (spontaneous polarisation with changes in temperature and mechanical stress respectively) as well as high dielectric permittivities, these materials are found in a wide variety of roles.

The perovskite oxide class encompasses a number of important compounds: lead zirconate titanate ($Pb(Zr_{1-x}Ti_x)O_3$, PZT); bismuth ferrite ($BiFeO_3$, BFO); lithium nio-

bate ($LiNbO_3$, LNO); barium titanate ($BaTiO_3$, BTO); potassium niobate tantalate ($K(Nb_{1-x}Ta_x)O_3$, KNT). In these systems, ferroelectric behaviour arises from polymorphs with non-centrosymmetric crystal structures. In the case of PZT, ferroelectricity arises due to ion displacement within the lattice: the structure consists of corner-sharing (TiO_6) octahedra which contain a central Ti^{4+} ion. Above the T_c, the central ion is positioned in a central position in the octahedron, and thus there is no net dipole; below T_c, however, the Ti ion may occupy two different sites, one towards the 'top' apical oxygen, and the other towards the 'bottom' oxygen. Although this displacement is only on the order of 0.1 Å, this displacement is sufficient to generate a dipole within the octahedron, and if this displacement occurs in multiple parallel octahedra, a net directional polarisation is induced [192].

1.5.3.1 Lead Zirconate Titanate

PZT was chosen as the inorganic interface modifier in this work: despite environmental concerns surrounding PZT due to its lead content, it is considered an extremely suitable material for this project given its strong ferroelectric properties, transparency to visible light, ease of processing, and relatively low crystallisation temperatures. PZT is a solid solution between ferroelectric $PbTiO_3$ (tetragonal, $P4mm$) and antiferroelectric $PbZrO_3$ (orthorhombic, $Pbam$) [193, 194] and encompasses a number of phases with different structural and polarisation characteristics, the formation of which depends on both the temperature and the Zr:Ti ratio[14] — the phase diagram for the material shown below in Figure 1.19. The two most important regimes for ferroelectric applications are the high T_c rhomobohedral phase ($F_{R(HT)}$) and the ferroelectric tetragonal phase (F_T). Also of interest is the morphotropic phase boundary which arises at the Zr:Ti ratio 0.52:0.48 (PZT 52/48), at which point the material possesses an extremely high dielectric constant and piezoelectric response: it is thought that this occurs due to local monoclinic distortions in the material [195, 196].

PZT has become one of the most important and widely used piezo- and ferroelectric materials in industry due to its wide range of composition-dependent properties: the material characteristics may be tuned either through changing the Zr:Ti ratio or by doping with elements such as La (forming $(Pb_{1-x}La_x)(Zr_{1-y}Ti_y)O_3$ (PLZT)); a comprehensive review of PZT dopants is given by Xu [199]. PZT thin-films may be deposited using a number of different methods such as sol-gel synthesis [200], hydrothermal growth [201],

[14] Typically, the Zr:Ti ratio is stated with the compound abbreviation, *e.g.* $Pb(Zr_{0.6}Ti_{0.4})O_3$ is contracted to PZT 60/40, $Pb(Zr_{0.2}Ti_{0.8})O_3$ to PZT 20/80 and so forth.

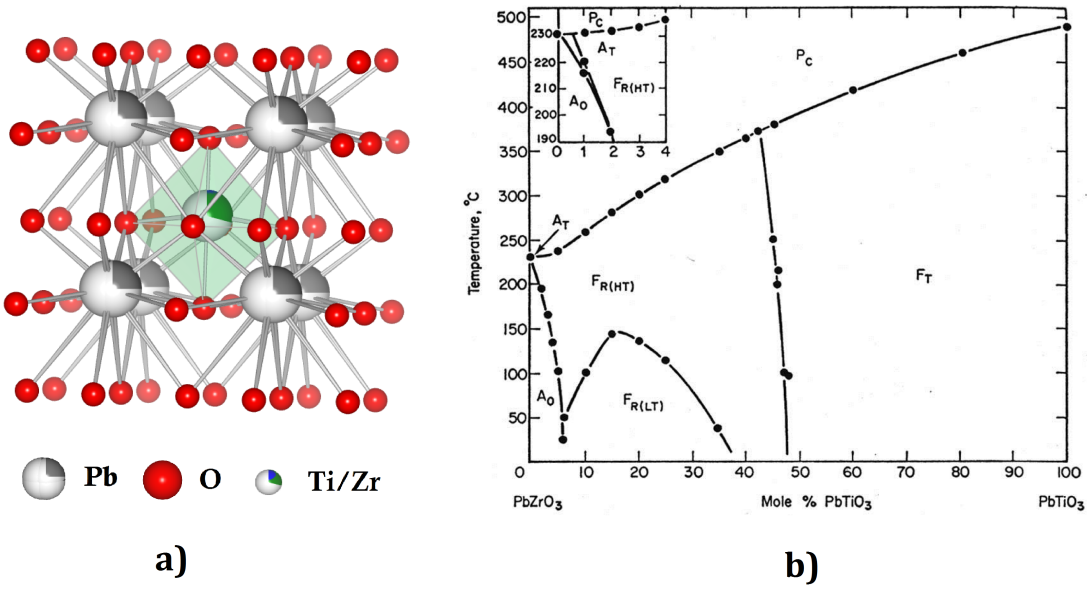

Figure 1.19 – a) Crystal structure of tetragonal $Pb(Zr_{0.3}Ti_{0.7})O_3$ showing the alternating layers of Pb and Ti/Zr. Crystal structure reproduced from structural parameters obtained from neutron diffraction studies by Frantti *et al.* [197], and structure was rendered using the VESTA programme [52]. b) solid solution phase diagram for PZT. P_c is the paraelectric cubic phase; A_T and A_O the antiferroelectric tetragonal and orthorhombic phases respectively; $F_{R(LT)}$ and $F_{R(HT)}$ the low temperature and high temperature rhombohedral phases respectively; F_T is the tetragonal ferroelectric phase. The morphotropic phase boundary between the orthorhombic and tetragonal forms exists for the compound PZT 52/48. Reproduced from [198].

sputtering [202], PLD [203], MOCVD [204], and molecular beam epitaxy [205]; a comprehensive overview of the different techniques and conditions used for the deposition of PZT thin-films is given by Izyumskaya *et al.* [206]. Sol-gel synthesis and metal-organic chemical vapour deposition (MOCVD) have been researched extensively for deposition of PZT thin-films: the sol-gel method is a relatively low-cost process which may be carried out in ambient conditions; MOCVD is one of the most common large-scale production techniques for thin-films and offers high deposition rates and excellent control over processing conditions. Generally, sol-gel-derived PZT films crystallise at a lower temperature than most other perovskite FE materials — Xu *et al.* reported the synthesis of crystalline PZT 52/48 by the sol-gel method using temperatures of no greater than 400 °C [207] using a sol-gel–hydrothermal treatment method. By using a conventional sol-gel process, PZT films can routinely be obtained using temperatures of 500 °C and generally require only a short annealing period to obtain a crystalline product [208], whereas materials such as BTO generally require higher temperatures (> 600 °C).

It has been observed that very thin films of PZT will, with sufficient thermal energy (*e.g.* during an annealing phase), form nanoislands which minimises the surface free energy of the substrate relative to a continuous layer of material [209] — this effect is of much interest for the fabrication of nanoscale devices, such as for capacitors for memory applications [210] if the islands are thick enough (both laterally and vertically with respect to the substrate) to exhibit ferroelectric effects and if they are distributed in a sufficiently ordered manner.

The versatility of PZT has allowed it to be employed in a large number of applications requiring it to be grown on a range of different substrates: epitaxial growth of PZT has been observed on substrates such as MgO, $SrTiO_3$, and $LaAlO_3$, and PZT is commonly grown on Pt-coated substrates for use in capacitors [206]. Although not widely researched, crystallisation of PZT on ITO [211] and ZnO [212] has been demonstrated; despite the relatively large lattice mismatch between ZnO and PZT (-22.3 % for the a-axis, +25.7 % for the c-axis), the use of ZnO as a growth buffer layer on Pt has been shown to enhance the ferroelectric properties of PZT 52/48 relative to those grown without it. There is growing interest in Metal–ZnO–FE (MFS) heterostructures which would be suitable for memory applications: coupling between the ferroelectric polarisation of materials such as PZT and BTO and the piezolectric properties of ZnO has been observed to generate polarisation phenomena at the interface between the two materials [213]. This coupling can create unique internal electric field variations and modulate the magnitude of the depletion layer in ZnO.

PZT possesses a wide band-gap, generally reported to lie between $\sim$ 3.45 eV (for $PbTiO_3$) and 3.70 eV (for $PbZrO_3$) with some outliers [215]: Moret *et al.* reported that, for PZT grown by MOCVD on $SrTiO_3$, the band gap remained constant over a range of PZT compositions at $\sim$ 3.6 eV [216]. Generally, the band gap of PZT will change for a single composition depending on the substrate, processing conditions, and deposition method. Due to the wide band-gap, PZT transmits well in the visible region of the electromagnetic spectrum and is thus suitable for the photovoltaic applications in this study. Although nominally an insulator, PZT does possess some conducting properties given that leakage current is observed to increase with decreasing film thickness for PZT capacitors: whilst acceptor impurities in PZT are generally compensated for by oxygen vacancies, a small fraction remain uncompensated and contribute to p-type conductivity in PZT [217]. For applications such as capacitors and FETs where PZT acts as a dielectric layer, minimising conduction in these films is of great importance as leakage currents must be minimised to produce efficient devices; however, in the case of photovoltaics, higher conductivity in PZT would be preferred to minimise current loss. Conduction mechanisms in PZT are thought to be both temperature- and field-dependent and have

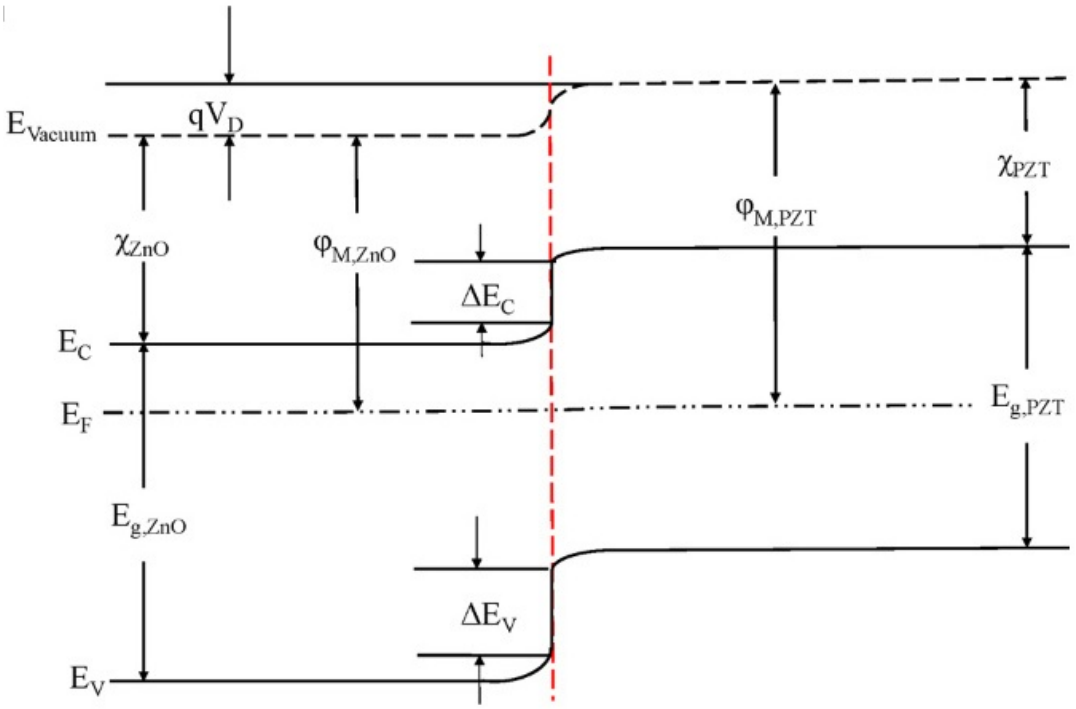

Figure 1.20 – Energy level schematic for a ZnO (left)/PZT (right) bilayer structure. E_{vacuum} is the vacuum level, qV_D the built-in potential due to work function difference between the two materials; χ the electron affinity; ϕ the work function; E_F the Fermi level; E_C and E_V the conduction and valence levels respectively; E_g the band gap; ΔE the band offset between the two materials. From [214], © IOP Publishing. Reproduced by permission of IOP Publishing. All rights reserved.

been studied extensively in Metal–Ferroelectric–Metal structures: these studies have also shown that the electrode properties are also key in determining conduction mechanisms through the structure [206, 218]; these include ohmic conductivity, Schottky (thermionic emission), Poole-Frenkel trap emission, Fowler–Nordheim tunneling, and space–charge-limited currents. Research by Zhou *et al.* into Pt–ZnO–PZT MFS heterostructures has shown interesting resistivity switching behaviour which tunes with voltage. Asymmetric current–voltage (I–V) characteristics were observed with the structures exhibiting diode-like behaviour: at low fields, ohmic conductivity is cited as the main transport mechanism, and at high fields, space–charge-limited current was thought to dominate in the high resistance regime, whereas the Fowler–Nordheim mechanism was found in the low resistance regime [214].

1.6 Experimental Materials

This section covers the properties of materials used in the fabrication of hPV devices in this study and compares them to widely used alternatives. This work was based on bilayer hPV devices with the structure ITO–ZnO–P3HT–M where ITO (Section 1.6.1) was employed as the transparent bottom electrode and P3HT (Section 1.6.2) as the polymeric donor material. The properties of ZnO have been covered extensively in Section 1.4.1.

1.6.1 TCO — Indium Tin Oxide

In this work, ITO was chosen as the bottom electrode for devices: ITO is a transparent conducting oxide (TCO), used extensively throughout industry as a contact material for electronic devices due to its high transparency, resilience to harsh processing conditions (such as temperatures > 200 °C which are used extensively in this work), and high conductivity. ITO is employed as a bottom electrode in the vast majority of OPV devices in both normal and inverted configurations (*i.e.* as either a hole or an electron collector respectively) — ITO has a high work-function (typically 4.5 eV [33], but values between 4.1 and 5.5 eV have been reported, depending on treatment [219]), making it suitable for both device architectures (in normal architecture, ITO transfers an electron to the lower-lying HOMO_A, whereas in inverted architecture, ITO may accept electrons from the higher-lying LUMO_A or CB_A). ITO is a solid solution of In_2O_3 and SnO_2, typically in a ratio of around 9:1, which crystallises in the cubic bixbyite structure (space group $Ia\bar{3}$) [220] and possesses a wide band-gap of ~ 4.0 eV and thus is highly transparent in the visible region. Both tin and oxygen vacancies contribute to the conductivity of ITO, thus highly crystalline material is not desirable for electronic applications. ITO is typically deposited by physical vapour deposition (PVD) or by sputtering.

Due to relatively high processing and materials costs, a suitable replacement for ITO has been sought after for several years, although none has yet supplanted it as the industry standard. Both inorganic and organic materials have been proposed, requiring less expensive raw materials and often those which may be deposited by solution processing routes, circumventing the high vacuum conditions used for ITO deposition. Fluorine-doped tin oxide (SnO_2:F, otherwise known at FTO) is a popular alternative to ITO and is used extensively in DSSCs, although FTO is generally less transparent to visible light; extensive research on doped ZnO has also been carried out, particularly focussing on Al:ZnO and Ga:ZnO (as discussed in Section 1.4.2.1) — the addition of these dopants vastly stabilises the somewhat erratic electronic properties of vanilla ZnO.

Another approach has been to use high work-function metals (Au [221] and Ag) as transparent electrodes — such films must either be ultrathin (< 10 nm), or non-continuous: for example, arrays of Ag NWs have been investigated in this capacity [222]. Park *et al.* have expanded on this concept by depositing multilayer 'sandwich' thin-films for use in photovoltaic, using M–ZnO:Ag:M–ZnO (M=Al or Ga) structures — by using a thin layer of metal between the two TCO materials, the conductivity may be enhanced whilst still maintaining acceptable film transparency [223].

In plastic electronics, the fabrication of flexible electronic devices is seen as a major goal — in such devices, inorganic materials are generally not mechanically stable enough (ITO electrodes, for example, are typically 150 – 200 nm thick), and thus there is a significant driving force for the development of all-organic devices, including electrodes which are typically inorganic: PEDOT:PSS [224] (often used as an EBL in OPVs) is the most commonly used polymer layer, although there are concerns about its chemical stability in the long term due to its acidity; carrier mobilities of organic electrodes tend to be much lower than for inorganic materials which may negatively influence device performance — as a result, much attention has been turned towards carbon nanotubes [225] and graphene [226] as their charge-carrying properties can be comparable to those of inorganic compounds; however, further developments in the synthesis and processing of these materials is required before they can begin to replace ITO.

1.6.2 Donor — P3HT

P3HT was used as the light-absorbing polymer in hPV devices in this study: this material is one of the most widely available, well understood, and versatile semiconducting polymers in the field, having been used in a multitude of applications — in addition to OPVs, P3HT has also been used in DSSCs [227] and in organic FETs [228]. P3HT has an energy gap of 1.9 eV and its hole mobilities on the order of 10^{-2} – 10^{-3} cm^{-2} V^{-1} s^{-1} [229]. Conjugation in semiconducting polymers occurs through delocalisation of π electrons along the carbon backbone, leading to the observed conductivity in these materials; the energy gap in these materials between the π-bonding and π^*-antibonding orbitals is created by a Peierls distortion[15], and thus these materials exhibit semiconducting rather than metal characteristics [230]. Charges are therefore mobile along the π-conjugated backbone of the polymer; more importantly, inter-chain electronic coupling allows charge hopping between polymer chains which gives rise to the high conductivities observed in

[15]Peierls' Theorem states that, "a one-dimensional, equally spaced chain with one electron is unstable", and thus such a chain will distort to minimise the ground state energy of electrons, leading to the creation of an energy gap.

appropriately packed conjugated polymers; as a result, the crystal packing (and therefore the degree of π–π-stacking and side-chain interaction) is key in governing the bulk conductivity of these polymers.

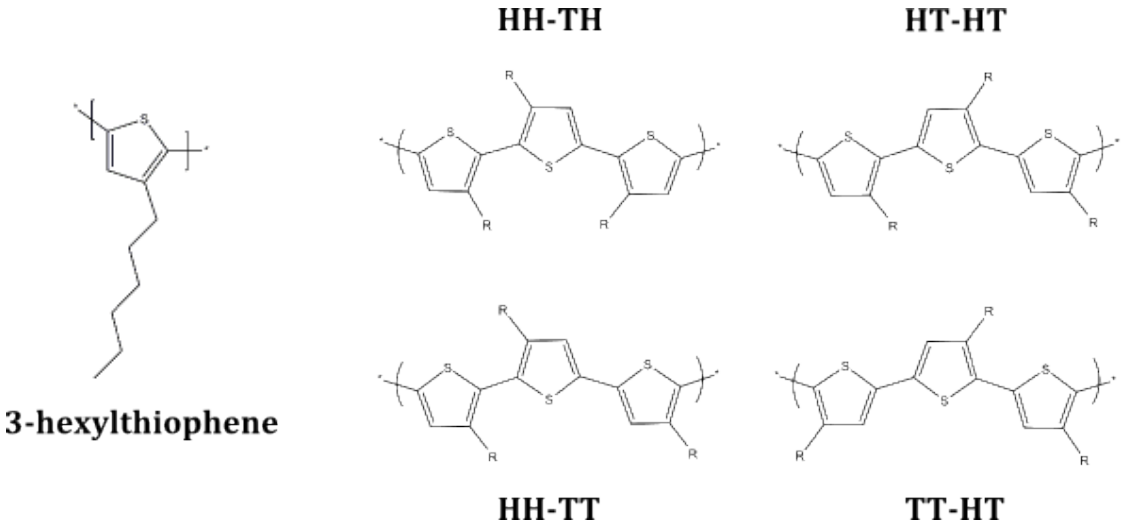

Figure 1.21 – 3-hexylthiophene residue and different trimer configurations for poly(3-alkylthiophene)s.

Due to the asymmetry of the 3-hexylthiophene monomer, three distinct dimer units may form (2,2', head–head (HH); 2,5', head–tail (HT); 5,5', tail–tail (TT)), which in turn gives rise to four trimer units (HT–HT; HH–TH; HH–TT; TT–HT): these are illustrated in Figure 1.21 [231]. The presence of non-HT coupling of thiophene residues in the polymer chain can lead to the adoption of non-planar conformations (due to steric interactions between side-chains) which, in turn, has a negative impact on its charge transport properties [232]. P3HT with high regioregularity has been observed to possess superior electronic properties to those with lesser degrees, as the HT coupling promotes formation of planar polymer conformations, increasing the conjugation along the polymer backbone, the degree of π–π stacking in the films, and the inter-chain transport characteristics [233].

The molecular weight, M_w, of a polymer will not only affect the mechanical and physical properties of the polymer (such as melting point and density), but also the electronic properties as it has a significant effect on the morphology of the film [234]. This is related to entanglement effects: smaller chain polymers are more easily able to reach low-energy conformations whereas longer chain polymers are more extensively entangled and therefore more constrained — as a result, a greater variation in morphology and crystal packing is observed with more extensive mixtures of crystalline and amorphous regions. Despite the greater degree of disorder and greater presence of amorphous material present for more entangled P3HT chains, charge transport in P3HT tends to be

much greater for higher molecular weight chains than lower ones, attributed to increased connectivity between grains with longer chain lengths [235].

Processing conditions may have a profound effect on the morphological properties of P3HT and, therefore, its electronic properties. P3HT may be deposited by a number of different methods including: spin-coating [236]; Langmuir-Blodgett deposition [237]; inkjet printing [238]; solid-state processing; electrodeposition [239]. Processing of P3HT generally proceeds through dissolution of the polymer in a suitable solvent (commonly xylene, chlorobenzene and derivatives thereof, and chloroform) followed by deposition: the morphology and microstructure depend heavily on the interactions between the polymer and solvent, especially the rate of solvent evaporation which can affect the crystallinity of the films — generally, slower evaporation of solvent allows a greater degree of the polymer to crystallise which may have a positive impact on charge transport [240, 241, 242].

1.7 Aims and Thesis Structure

In this study, a simple bilayer ZnO–P3HT system was chosen to investigate the effect of incorporation of an interlayer of PZT at the oxide:polymer interface on device performance. The inorganic interface modification route was chosen to nullify the surface defects of ZnO; moreover, the added ferroelectric functionality of the PZT may serve to further increase device performance.

There are two main parts to this thesis: firstly, in Chapters 3 & 4, PZT is grown on ZnO and characterised using a structural and compositional analysis techniques. In Chapter 3, the growth conditions for ZnO–PZT thin-films is optimised and the mechanism of growth discussed. In Chapter 4, the work focusses on growth of thin PZT films suitable for incorporation into hPV devices — this includes similar characterisation techniques, as well as detailed structural analysis of the film morphology. Secondly, in Chapter 5, the ZnO–PZT layers are incorporated into hPV devices. As well as observing changes in device performance with PZT modification, charge generation and lifetimes are probed to shed light on the role of PZT in these systems. The work in this thesis forms the basis for further research into PZT-modified OPV systems, especially with regards to investigating the effect of ferroelectric polarisation on charge generation and extraction.

References

[1] L. H. Hoddeson, "Interview with Dr. Russell Ohl, August 19th," 1976.

[2] R. S. Ohl, "Light-sensitive electric device," 1946.

[3] D. M. Chapin, C. S. Fuller, and G. L. Pearson, "Solar Energy Converting Apparatus," 1957.

[4] D. E. Carlson and C. R. Wronski, "Amorphous silicon solar cell," *Appl. Phys. Lett.* **28**(11), p. 671, 1976.

[5] W. Kruehler and J. Grabmaier, "Method for the manufacture of gallium arsenide thin film solar cells," 1987.

[6] J. Britt and C. Ferekides, "Thin-film CdS/CdTe solar cell with 15.8 % efficiency," *Appl. Phys. Lett.* **62**(22), pp. 2851–2852, 1993.

[7] "NREL Record Research Solar Cell Efficiencies, May 2014," 2014.

[8] C. J. Curtis, A. Miedaner, M. F. A. M. Van Hest, D. S. Ginley, and J. A. Nekuda, "Formation of copper-indium-selenide and/or copper-indium-gallium-selenide from indium selenide and copper selenide precursors; Patent No.: US 20090280598 A1," 2007.

[9] H. Tributsch, "Reaction of excited chlorophyll molecules at electrodes and in synthesis," *Photochem. Photobiol.* **16**, pp. 261–269, Jan. 1972.

[10] D. Kearns and M. Calvin, "Photovoltaic effect and photoconductivity in laminated organic systems," *J. Chem. Phys.* **29**(4), pp. 950–951, 1958.

[11] B. O'Regan and M. Grätzel, "A low-cost, high-efficiency solar-cell Based on dye-sensitized colloidal TiO_2 films," *Nature* **353**(6346), pp. 737–740, 1991.

[12] C. W. Tang, "2-Layer organic photovoltaic cell," *Appl. Phys. Lett.* **48**(2), pp. 183–185, 1986.

[13] R. Elsenbaumer, K. Jen, and R. Oboodi, "Processible and environmentally stable conducting polymers," *Synth. Met.* **15**, pp. 169–174, July 1986.

[14] B. Durlinger, "Case B: Environmental Impact of Photovoltaic Lighting," in *The Power of Design: Product Innovation in Sustainable Energy Technologies*, A. Reinders, J. C. Diehl, and H. Brezet, eds., ch. 4, pp. 253–262, John Wiley & Sons, Ltd., 2012.

[15] G. Carr, "Sunny Uplands - Alternative energy will no longer be alternative," *The World In 2013* , Nov. 2012.

[16] J. J. Benson-Smith and J. Nelson, "Organic donor–acceptor heterojunction solar cells," in *Nanostructured Photochem. Syst. Sol. Phot. Convers.*, M. Archer and A. J. Nozik, eds., ch. 7, pp. 453–501, Imperial College Press, London, 2008.

[17] J. Reid, "G24i Ships World's First Commercial Application of DSSC," 2009.

[18] V. M. Fthenakis, H. C. Kim, M. Held, M. Raugei, and J. Krones, "Update of PV energy payback times and life-cycle greenhouse emissions," in *24th Eur. Photovolt. Sol. Energy Conf.*, p. 4412, (Hamburg, Germany), 2009.

[19] A. Stoppato, "Life cycle assessment of photovoltaic electricity generation," *Energy* **33**(2), pp. 224–232, 2008.

[20] V. Fthenakis and H. Kim, "Photovoltaics: life-cycle analyses," *Sol. Energy* **85**, pp. 1609–1628, Aug. 2011.

[21] A. C. Veltkamp and M. J. de Wild-Scholten, "Dye sensitised solar cells for large-scale photovoltaics; the determination of environmental performances," in *Renew. Energy*, ECN Solar Energy, The Netherlands, (Makuhari Messe, Chiba, Japan), 2006.

[22] R. Garcia-Valverde, J. A. Cherni, and A. Urbina, "Life cycle analysis of organic photovoltaic technologies," *Prog. Photovoltaics* **18**(7), pp. 535–558, 2010.

[23] E. A. Alsema, "Energy pay-back time and CO_2 emissions of PV systems," *Prog. Photovoltaics Res. Appl.* **8**, pp. 17–25, Jan. 2000.

[24] E. A. Alsema, M. J. de Wild-Scholten, and V. M. Fthenakis, "Environmental impacts of PV electricity generation — a critical comparison of energy supply options," in *21st Eur. Photovolt. Sol. Energy Conf.*, (Dresden, Germany), 2006.

[25] M. A. Green, K. Emery, Y. Hishikawa, W. Warta, and E. D. Dunlop, "Solar cell efficiency tables (version 44)," *Prog. Photovoltaics Res. Appl.* **22**, pp. 701–710, July 2014.

[26] M. C. Scharber, D. Mühlbacher, M. Koppe, P. Denk, C. Waldauf, A. J. Heeger, and C. L. Brabec, "Design rules for donors in bulk-heterojunction solar cells — towards 10 % energy-conversion efficiency," *Adv. Mater.* **18**(6), p. 789, 2006.

[27] J. J. M. Halls, J. Cornil, D. A. dos Santos, R. Silbey, D. H. Hwang, A. B. Holmes, J.-L. Bredas, and R. H. Friend, "Charge- and energy-transfer processes at polymer/polymer interfaces: a joint experimental and theoretical study," *Phys. Rev. B* **60**(8), p. 5721, 1999.

[28] J. Nelson, *The Physics of Solar Cells*, Imperial College Press, London, 2003.

[29] T. M. Clarke and J. R. Durrant, "Charge photogeneration in organic solar cells," *Chem. Rev.* **110**(11), pp. 6736–6767, 2010.

[30] R. A. Marcus, "On the theory of oxidation–reduction reactions involving electron transfer. I," *J. Chem. Phys.* **24**, pp. 966–978, May 1956.

[31] J. E. Norton, J.-L. Brédas, J. Cornil, and V. Coropceanu, "Molecular understanding of organic solar cells: the challenges," *Acc. Chem. Res.* **42**, pp. 1691–9, Nov. 2009.

[32] F. C. Jamieson, E. B. Domingo, T. McCarthy-Ward, M. Heeney, N. Stingelin, and J. R. Durrant, "Fullerene crystallisation as a key driver of charge separation in polymer/fullerene bulk heterojunction solar cells," *Chem. Sci.* **3**(2), p. 485, 2012.

[33] Y. Park, V. Choong, Y. Gao, B. R. Hsieh, and C. W. Tang, "Work function of indium tin oxide transparent conductor measured by photoelectron spectroscopy," *Appl. Phys. Lett.* **68**(19), pp. 2699–2701, 1996.

[34] P. A. Tippler and R. A. Llewellyn, *Modern Physics*, W. H. Freeman, 3rd ed., 1999.

[35] J. B. Franklin, J. M. Downing, F. Giuliani, M. P. Ryan, and M. A. McLachlan, "Building on soft foundations: new possibilities for controlling hybrid photovoltaic architectures," *Adv. Energy Mater.* **2**, pp. 528–531, May 2012.

[36] S. Sista, Z. Hong, L.-M. Chen, and Y. Yang, "Tandem polymer photovoltaic cells — current status, challenges and future outlook," *Energy & Environ. Sci.* **4**(5), p. 1606, 2011.

[37] C.-C. Chen, W.-H. Chang, K. Yoshimura, K. Ohya, J. You, J. Gao, Z. Hong, and Y. Yang, "An efficient triple-junction polymer solar cell having a power conversion efficiency exceeding 11 %," *Adv. Mater.* **26**, pp. 5670–5677, July 2014.

[38] Z. M. Beiley and M. D. McGehee, "Modeling low cost hybrid tandem photovoltaics with the potential for efficiencies exceeding 20 %," *Energy & Environ. Sci.* **5**(11), p. 9173, 2012.

[39] A. G. Pattantyus-Abraham, I. J. Kramer, A. R. Barkhouse, X. Wang, G. Konstantatos, R. Debnath, L. Levina, I. Raabe, M. K. Nazeeruddin, M. Grätzel, and E. H. Sargent, "Depleted-heterojunction colloidal quantum dot solar cells," *ACS Nano* **4**(6), pp. 3374–3380, 2010.

[40] J.-C. Lee, W. Lee, S.-H. Han, T. G. Kim, and Y.-M. Sung, "Synthesis of hybrid solar cells using CdS nanowire array grown on conductive glass substrates," *Electrochem. commun.* **11**(1), pp. 231–234, 2009.

[41] H. J. Lee, J. H. Yum, H. C. Leventis, S. M. Zakeeruddin, S. A. Haque, P. Chen, S. I. Seok, M. Grätzel, and M. K. Nazeeruddin, "CdSe quantum dot-sensitized solar cells exceeding efficiency 1 % at full-sun intensity," *J. Phys. Chem. C* **112**(30), pp. 11600–11608, 2008.

[42] D. Verma, A. Ranga Rao, and V. Dutta, "Surfactant-free CdTe nanoparticles mixed MEH-PPV hybrid solar cell deposited by spin coating technique," *Sol. Energy Mater. Sol. Cells* **93**(9), pp. 1482–1487, 2009.

[43] S. Günes, K. P. Fritz, H. Neugebauer, N. S. Sariciftci, S. Kumar, and G. D. Scholes, "Hybrid solar cells using PbS nanoparticles," *Sol. Energy Mater. Sol. Cells* **91**(5), pp. 420–423, 2007.

[44] E. Arici, N. S. Sariciftci, and D. Meissner, "Hybrid solar cells based on nanoparticles of $CuInS_2$ in organic matrices," *Adv. Funct. Mater.* **13**(2), pp. 165–171, 2003.

[45] S. Dayal, N. Kopidakis, D. C. Olson, D. S. Ginley, and G. Rumbles, "Photovoltaic devices with a low band gap polymer and CdSe nanostructures exceeding 3 % efficiency," *Nano Lett.* **10**(1), pp. 239–242, 2010.

[46] F. Zhang, B. Sun, T. Song, X. Zhu, and S. Lee, "Air stable, efficient hybrid photovoltaic devices based on poly(3-hexylthiophene) and silicon nanostructures," *Chem. Mater.* **23**, pp. 2084–2090, 2011.

[47] D. C. Olson, J. Piris, R. T. Collins, S. E. Shaheen, and D. S. Ginley, "Hybrid photovoltaic devices of polymer and ZnO nanofiber composites," *Thin Solid Films* **496**(1), pp. 26–29, 2006.

[48] L. Wang, J. S. Ji, Y. J. Lin, and S. P. Rwei, "Novel poly(3-nonylthiophene)-TiO_2 hybrid materials for photovoltaic cells," *Synth. Met.* **155**(3), pp. 677–680, 2005.

[49] H. Morkoç and Ü. Özgür, *Zinc Oxide : Fundamentals, Materials and Device Technology*, Wiley-VCH, Weinheim, 2009.

[50] T. Yamashita, R. Hansson, and P. C. Hayes, "The relationships between microstructure and crystal structure in zincite solid solutions," *J. Mater. Sci.* **41**(17), pp. 5559–5568, 2006.

[51] J. K. Burdett, T. Hughbanks, G. J. Miller, J. W. Richardson, and J. V. Smith, "Structural-electronic relationships in inorganic solids: powder neutron diffraction studies of the rutile and anatase polymorphs of titanium dioxide at 15 and 295 K," *J. Am. Chem. Soc.* **109**(12), pp. 3639–3646, 1987.

[52] K. Momma and F. Izumi, "VESTA 3 for three-dimensional visualisation of crystal, volumetric, and morphology data," *J. Appl. Crystallogr.* **44**, pp. 1272–1276, 2011.

[53] N. N. Greenwood and A. Earnshaw, *Chemistry of the Elements*, Elsevier Butterworth-Heinemann, 2nd ed., 1998.

[54] J. Downing, M. P. Ryan, N. Stingelin, and M. A. McLachlan, "Solution processed hybrid photovoltaics: preparation of a standard ZnO template," *J. Photonics Energy* **1**(1), pp. 11117–11119, 2011.

[55] R. M. Hewlett, *Solution-processed zinc oxide layers for thin-film electronic and hybrid photovoltaic devices.* Early stage assessment, Imperial College London, London, 2011.

[56] P. D. Yang, H. Q. Yan, S. Mao, R. Russo, J. Johnson, R. Saykally, N. Morris, J. Pham, R. R. He, and H. J. Choi, "Controlled growth of ZnO nanowires and their optical properties," *Adv. Funct. Mater.* **12**(5), pp. 323–331, 2002.

[57] S. Peulon and D. Lincot, "Mechanistic study of cathodic electrodeposition of zinc oxide and zinc hydroxychloride films from oxygenated aqueous zinc chloride solutions," *J. Electrochem. Soc.* **145**(3), pp. 864–874, 1998.

[58] Y. Ma, C. P. Wong, X. T. Zeng, T. Yu, Y. Zhu, and Z. X. Shen, "Pulsed laser deposition of ZnO honeycomb structures on metal catalyst prepatterned Si substrates," *J. Phys. D. Appl. Phys.* **42**(6), p. 5417, 2009.

[59] P. X. Gao, Y. Ding, W. J. Mai, W. L. Hughes, C. S. Lao, and Z. L. Wang, "Conversion of zinc oxide nanobelts into superlattice-structured nanohelices," *Science* **309**(5741), pp. 1700–1704, 2005.

[60] R. M. Wang, Y. J. Xing, J. Xu, and D. P. Yu, "Fabrication and microstructure analysis on zinc oxide nanotubes," *New J. Phys.* **5**, p. 115, 2003.

[61] M. C. Newton, S. Firth, T. Matsuura, and P. A. Warburton, "Synthesis and characterisation of zinc oxide tetrapod nanocrystals," *Emag-Nano 2005 Imaging, Anal. Fabr. Nanoscale* **26**, pp. 251–255, 2006.

[62] Ü. Özgür, Y. I. Alivov, C. Liu, A. Teke, M. A. Reshchikov, S. Doğan, V. Avrutin, S.-J. Cho, and H. Morkoç, "A comprehensive review of ZnO materials and devices," *J. Appl. Phys.* **98**, p. 041301, Aug. 2005.

[63] D. Look, D. Reynolds, J. Sizelove, R. Jones, C. Litton, G. Cantwell, and W. Harsch, "Electrical properties of bulk ZnO," *Solid State Commun.* **105**, pp. 399–401, Feb. 1998.

[64] D. H. Levy, D. Freeman, S. F. Nelson, P. J. Cowdery-Corvan, and L. M. Irving, "Stable ZnO thin film transistors by fast open air atomic layer deposition," *Appl. Phys. Lett.* **92**(19), p. 2101, 2008.

[65] E. Fortunato, P. Barquinha, A. Pimentel, A. Gonçalves, A. Marques, L. Pereira, and R. Martins, "Recent advances in ZnO transparent thin film transistors," *Thin Solid Films* **487**(1-2), pp. 205–211, 2005.

[66] P. D. C. King and T. D. Veal, "Conductivity in transparent oxide semiconductors," *J. Phys. Condens. Matter* **23**, p. 4214, Aug. 2011.

[67] D. Look, H. Mosbacker, Y. Strzhemechny, and L. Brillson, "Effects of surface conduction on Hall-effect measurements in ZnO," *Superlattices Microstruct.* **38**, pp. 406–412, Oct. 2005.

[68] C. H. Swartz, "Transport and surface conductivity in ZnO," *J. Mater. Res.* **27**, pp. 2205–2213, May 2012.

[69] A. Janotti and C. G. Van de Walle, "Fundamentals of zinc oxide as a semiconductor," *Reports Prog. Phys.* **72**(12), p. 6501, 2009.

[70] P. A. Cox, *The electronic structure and chemistry of solids*, Oxford University Press, Oxford, 1987.

[71] A. Janotti and C. G. Van de Walle, "New insights into the role of native point defects in ZnO," *J. Cryst. Growth* **287**(1), p. 58, 2006.

[72] A. Janotti and C. G. Van de Walle, "Native point defects in ZnO," *Phys. Rev. B* **76**(16), p. 5202, 2007.

[73] S. J. Baik, J. H. Jang, C. H. Lee, W. Y. Cho, and K. S. Lim, "Highly textured and conductive undoped ZnO film using hydrogen post-treatment," *Appl. Phys. Lett.* **70**(26), p. 3516, 1997.

[74] H. Ishizakiz and N. Yamada, "Preparation of $Zn_{1-x}Mg_xO$ film by electrochemical reaction," *Electrochem. Solid State Lett.* **9**(11), pp. C178–C180, 2006.

[75] Y. I. Kim and R. Seshadri, "Optical properties of cation-substituted zinc oxide," *Inorg. Chem.* **47**(19), pp. 8437–8443, 2008.

[76] A. Ohtomo, M. Kawasaki, T. Koida, K. Masubuchi, H. Koinuma, Y. Sakurai, Y. Yoshida, T. Yasuda, and Y. Segawa, "$Mg_xZn_{1-x}O$ as a II–VI widegap semiconductor alloy," *Appl. Phys. Lett.* **72**(19), p. 2466, 1998.

[77] A. Janotti and C. Van de Walle, "Absolute deformation potentials and band alignment of wurtzite ZnO, MgO, and CdO," *Phys. Rev. B* **75**, p. 1201, Mar. 2007.

[78] T. Makino, Y. Segawa, M. Kawasaki, A. Ohtomo, R. Shiroki, K. Tamura, T. Yasuda, and H. Koinuma, "Band gap engineering based on $Mg_xZn_{1-x}O$ and $Cd_yZn_{1-y}O$ ternary alloy films," *Appl. Phys. Lett.* **78**, p. 1237, Feb. 2001.

[79] H. Ishizaki, M. Imaizumi, S. Matsuda, M. Izaki, and T. Ito, "Incorporation of boron in ZnO film from an aqueous solution containing zinc nitrate and dimethylamineborane by electrochemical reaction," *Thin Solid Films* **411**(1), pp. 65–68, 2002.

[80] M. Suchea, S. Christoulakis, N. Katsarakis, T. Kitsopoulos, and G. Kiriakidis, "Comparative study of zinc oxide and aluminum doped zinc oxide transparent thin films grown by direct current magnetron sputtering," *Thin Solid Films* **515**(16), pp. 6562–6566, 2007.

[81] J. Hu and R. G. Gordon, "Textured aluminum-doped zinc oxide thin films from atmospheric pressure chemical-vapor deposition," *J. Appl. Phys.* **71**(2), p. 880, 1992.

[82] H. J. Ko, Y. F. Chen, S. K. Hong, H. Wenisch, T. Yao, and D. C. Look, "Ga-doped ZnO films grown on GaN templates by plasma-assisted molecular-beam epitaxy," *Appl. Phys. Lett.* **77**(23), p. 3761, 2000.

[83] D. C. Look, "Electrical and optical properties of p-type ZnO," *Semicond. Sci. Technol.* **20**(4), pp. S55–S61, 2005.

[84] V. Avrutin, D. J. Silversmith, and H. Morkoc, "Doping asymmetry problem in ZnO: current status and outlook," *Proc. IEEE* **98**(7), pp. 1269–1280, 2010.

[85] M. Dutta, T. Ghosh, and D. Basak, "N Doping and Al–N co-doping in sol-gel ZnO films: studies of their structural, electrical, optical, and photoconductive properties," *J. Electron. Mater.* **38**(11), pp. 2335–2342, 2009.

[86] C. H. Park, S. B. Zhang, and S. H. Wei, "Origin of p-type doping difficulty in ZnO: the impurity perspective," *Phys. Rev. B* **66**(7), p. 3202, 2002.

[87] H. Li, L. K. Schirra, J. Shim, H. Cheun, B. Kippelen, O. L. A. Monti, and J.-L. Bredas, "Zinc oxide as a model transparent conducting oxide: a theoretical and experimental study of the impact of hydroxylation, vacancies, interstitials, and extrinsic doping on the electronic properties of the polar ZnO (*0002*) surface," *Chem. Mater.* **24**, pp. 3044–3055, Aug. 2012.

[88] M. W. Allen, C. H. Swartz, T. H. Myers, T. D. Veal, C. F. McConville, and S. M. Durbin, "Bulk transport measurements in ZnO: the effect of surface electron layers," *Phys. Rev. B* **81**(7), p. 5211, 2010.

[89] R. Schlesinger, Y. Xu, O. T. Hofmann, S. Winkler, J. Frisch, J. Niederhausen, A. Vollmer, S. Blumstengel, F. Henneberger, P. Rinke, M. Scheffler, and N. Koch, "Controlling the work function of ZnO and the energy-level alignment at the interface to organic semiconductors with a molecular electron acceptor," *Phys. Rev. B* **87**, p. 5311, Apr. 2013.

[90] P. Rinke, "ZnO based hybrid inorganic/organic interfaces (Seminar, Imperial College London, February 12th)," 2013.

[91] S. Kowalczyk, F. McFeely, L. Ley, V. Gritsyna, and D. Shirley, "The electronic structure of $SrTiO_3$ and some simple related oxides (MgO, Al_2O_3, SrO, TiO_2)," *Solid State Commun.* **23**, pp. 161–169, July 1977.

[92] L. Forro, O. Chauvet, D. Emin, L. Zuppiroli, H. Berger, and F. Lévy, "High mobility n-type charge carriers in large single crystals of anatase (TiO_2)," *J. Appl. Phys.* **75**, p. 633, Jan. 1994.

[93] J. Gilot, I. Barbu, M. M. Wienk, and R. A. J. Janssen, "The use of ZnO as optical spacer in polymer solar cells: theoretical and experimental study," *Appl. Phys. Lett.* **91**(11), p. 3520, 2007.

[94] B. V. Andersson, D. M. Huang, A. J. Moulé, and O. Inganäs, "An optical spacer is no panacea for light collection in organic solar cells," *Appl. Phys. Lett.* **94**(4), p. 3302, 2009.

[95] J. Owen, M. S. Son, K.-H. Yoo, B. D. Ahn, and S. Y. Lee, "Organic photovoltaic devices with Ga-doped ZnO electrode," *Appl. Phys. Lett.* **90**(3), p. 3512, 2007.

[96] V. Bhosle, J. T. Prater, F. Yang, D. Burk, S. R. Forrest, and J. Narayan, "Gallium-doped zinc oxide films as transparent electrodes for organic solar cell applications," *J. Appl. Phys.* **102**(2), p. 23501, 2007.

[97] G. B. Murdoch, S. Hinds, E. H. Sargent, S. W. Tsang, L. Mordoukhovski, and Z. H. Lu, "Aluminum doped zinc oxide for organic photovoltaics," *Appl. Phys. Lett.* **94**(21), p. 3301, 2009.

[98] S. Park, S. J. Tark, J. S. Lee, H. Lim, and D. Kim, "Effects of intrinsic ZnO buffer layer based on P3HT/PCBM organic solar cells with Al-doped ZnO electrode," *Sol. Energy Mater. Sol. Cells* **93**(6-7), pp. 1020–1023, 2009.

[99] L. Murphy, W. Hong, H. Aziz, and Y. Li, "Organic photovoltaics with thick active layers ($\sim$ 800 nm) using a high mobility polymer donor," *Sol. Energy Mater. Sol. Cells* **114**, pp. 71–81, July 2013.

[100] S. Schumann, R. Da Campo, B. Illy, A. C. Cruickshank, M. A. McLachlan, M. P. Ryan, D. J. Riley, D. W. McComb, and T. S. Jones, "Inverted organic photovoltaic devices with high efficiency and stability based on metal oxide charge extraction layers," *J. Mater. Chem.* **21**(7), pp. 2381–2386, 2011.

[101] A. Nardes, M. Kemerink, M. de Kok, E. Vinken, K. Maturova, and R. Janssen, "Conductivity, work function, and environmental stability of PEDOT:PSS thin films treated with sorbitol," *Org. Electron.* **9**, pp. 727–734, Oct. 2008.

[102] T. Umeda, T. Shirakawa, A. Fujii, and K. Yoshino, "Improvement of characteristics of organic photovoltaic devices composed of conducting polymer–fullerene systems by introduction of ZnO layer," *Jpn. J. Appl. Phys.* **42**, pp. 1475–1477, 2003.

[103] M. S. White, D. C. Olson, S. E. Shaheen, N. Kopidakis, and D. S. Ginley, "Inverted bulk-heterojunction organic photovoltaic device using a solution-derived ZnO underlayer," *Appl. Phys. Lett.* **89**(14), p. 3517, 2006.

[104] S. K. Hau, H.-L. Yip, N. S. Baek, J. Zou, K. O'Malley, and A. K.-Y. Jen, "Air-stable inverted flexible polymer solar cells using zinc oxide nanoparticles as an electron selective layer," *Appl. Phys. Lett.* **92**(25), p. 3301, 2008.

[105] R. Søndergaard, M. Helgesen, M. Jørgensen, and F. C. Krebs, "Fabrication of polymer solar cells using aqueous processing for all layers including the metal back electrode," *Adv. Energy Mater.* **1**(1), pp. 68–71, 2011.

[106] F. C. Krebs, S. A. Gevorgyan, and J. Alstrup, "A roll-to-roll process to flexible polymer solar cells: model studies, manufacture and operational stability studies," *J. Mater. Chem.* **19**(30), pp. 5442–5451, 2009.

[107] S. H. Eom, S. Senthilarasu, P. Uthirakumar, C.-H. Hong, Y.-S. Lee, J. Lim, S. C. Yoon, C. Lee, and S.-H. Lee, "Preparation and characterization of nano-scale ZnO as a buffer layer for inkjet printing of silver cathode in polymer solar cells," *Sol. Energy Mater. Sol. Cells* **92**(5), pp. 564–570, 2008.

[108] A. Manor, E. A. Katz, T. Tromholt, and F. C. Krebs, "Enhancing functionality of ZnO hole blocking layer in organic photovoltaics," *Sol. Energy Mater. Sol. Cells* **98**, pp. 491–493, Mar. 2012.

[109] S. K. Hau, H.-L. Yip, H. Ma, and A. K.-Y. Jen, "High performance ambient processed inverted polymer solar cells through interfacial modification with a fullerene self-assembled monolayer," *Appl. Phys. Lett.* **93**(23), p. 3304, 2008.

[110] H. L. Yip, S. K. Hau, N. S. Baek, H. Ma, and A. K. Y. Jen, "Polymer solar cells that use self-assembled-monolayer-modified ZnO/metals as cathodes," *Adv. Mater.* **20**(12), pp. 2376–2382, 2008.

[111] X. Ju, W. Feng, K. Varutt, T. Hori, A. Fujii, and M. Ozaki, "Fabrication of oriented ZnO nanopillar self-assemblies and their application for photovoltaic devices," *Nanotechnology* **19**(43), p. 5706, 2008.

[112] R. Thitima, C. Patcharee, S. Takashi, and Y. Susumu, "Efficient electron transfers in ZnO nanorod arrays with N719 dye for hybrid solar cells," *Solid. State. Electron.* **53**(2), pp. 176–180, 2009.

[113] N. Sekine, C.-H. Chou, W. L. Kwan, and Y. Yang, "ZnO nano-ridge structure and its application in inverted polymer solar cell," *Org. Electron.* **10**(8), pp. 1473–1477, 2009.

[114] M. D. Archer and A. J. Nozik, *Nanostructured and photoelectrochemical systems for solar photon conversion*, Imperial College Press, London, 2008.

[115] F. C. Krebs, Y. Thomann, R. Thomann, and J. W. Andreasen, "A simple nanostructured polymer/ZnO hybrid solar cell — preparation and operation in air," *Nanotechnology* **19**(42), p. 4013, 2008.

[116] E. D. Spoerke, M. T. Lloyd, E. M. McCready, D. C. Olson, Y.-J. Lee, and J. W. P. Hsu, "Improved performance of poly(3-hexylthiophene)/zinc oxide hybrid photovoltaics modified with interfacial nanocrystalline cadmium sulfide," *Appl. Phys. Lett.* **95**(21), p. 3506, 2009.

[117] C. Goh, S. R. Scully, and M. D. McGehee, "Effects of molecular interface modification in hybrid organic-inorganic photovoltaic cells," *J. Appl. Phys.* **101**(11), p. 114503, 2007.

[118] S. J. Wu, Q. D. Tai, and F. Yan, "Hybrid photovoltaic devices based on poly (3-hexylthiophene) and ordered electrospun ZnO nanofibers," *J. Phys. Chem. C* **114**(13), pp. 6197–6200, 2010.

[119] Q. Tai, X. Zhao, and F. Yan, "Hybrid solar cells based on poly(3-hexylthiophene) and electrospun TiO_2 nanofibers with effective interface modification," *J. Mater. Chem.* **20**(35), pp. 7366–7371, 2010.

[120] S. D. Oosterhout, M. M. Wienk, S. S. van Bavel, R. Thiedmann, L. Jan Anton Koster, J. Gilot, J. Loos, V. Schmidt, and R. A. J. Janssen, "The effect of three-dimensional morphology on the efficiency of hybrid polymer solar cells," *Nat. Mater.* **8**(10), pp. 818–824, 2009.

[121] Y. Vaynzof, D. Kabra, L. Zhao, P. K. H. Ho, A. T.-S. Wee, and R. H. Friend, "Improved photoinduced charge carriers separation in organic–inorganic hybrid photovoltaic devices," *Appl. Phys. Lett.* **97**(3), p. 3309, 2010.

[122] Y.-J. Lee, M. T. Lloyd, D. C. Olson, R. K. Grubbs, P. Lu, R. J. Davis, J. A. Voigt, and J. W. P. Hsu, "Optimization of ZnO nanorod array morphology for hybrid photovoltaic devices," *J. Phys. Chem. C* **113**(35), pp. 15778–15782, 2009.

[123] L. Baeten, B. Conings, J. D'Haen, C. De Dobbelaere, A. Hardy, J. V. Manca, and M. K. Van Bael, "Tuning the dimensions of ZnO nanorod arrays for application in hybrid photovoltaics," *ChemPhysChem* **13**, pp. 2777–83, Aug. 2012.

[124] J. Bouclé, H. J. Snaith, and N. C. Greenham, "Simple approach to hybrid polymer/porous metal oxide solar cells from solution-processed ZnO nanocrystals," *J. Phys. Chem. C* **114**(8), pp. 3664–3674, 2010.

[125] H. E. Unalan, P. Hiralal, D. Kuo, B. Parekh, G. Amaratunga, and M. Chhowalla, "Flexible organic photovoltaics from zinc oxide nanowires grown on transparent and conducting single walled carbon nanotube thin films," *J. Mater. Chem.* **18**(48), pp. 5909–5912, 2008.

[126] W. Fu, Y. Shi, W. Qiu, L. Wang, Y. Nan, M. Shi, H. Li, and H. Chen, "High efficiency hybrid solar cells using post-deposition ligand exchange by monothiols," *Phys. Chem. Chem. Phys.* **14**, pp. 12094–8, Sept. 2012.

[127] W. J. E. Beek, M. M. Wienk, and R. A. J. Janssen, "Hybrid solar cells from regioregular polythiophene and ZnO nanoparticles," *Adv. Funct. Mater.* **16**(8), pp. 1112–1116, 2006.

[128] W. J. E. Beek, M. M. Wienk, M. Kemerink, X. N. Yang, and R. A. J. Janssen, "Hybrid zinc oxide conjugated polymer bulk heterojunction solar cells," *J. Phys. Chem. B* **109**(19), pp. 9505–9516, 2005.

[129] P. A. C. Quist, W. J. E. Beek, M. M. Wienk, R. A. J. Janssen, T. J. Savenije, and L. D. A. Siebbeles, "Photogeneration and decay of charge carriers in hybrid bulk heterojunctions of ZnO nanoparticles and conjugated polymers," *J. Phys. Chem. B* **110**(21), pp. 10315–10321, 2006.

[130] C. Müller, T. A. M. Ferenczi, M. Campoy-Quiles, J. M. Frost, D. D. C. Bradley, P. Smith, N. Stingelin-Stutzmann, and J. Nelson, "Binary organic photovoltaic blends: a simple rationale for optimum compositions," *Adv. Mater.* **20**(18), p. 3510, 2008.

[131] L. J. A. Koster, W. J. van Strien, W. J. E. Beek, and P. W. M. Blom, "Device operation of conjugated polymer/zinc oxide bulk heterojunction solar cells," *Adv. Funct. Mater.* **17**(8), pp. 1297–1302, 2007.

[132] C. Pacholski, A. Kornowski, and H. Weller, "Self-assembly of ZnO: from nanodots to nanorods," *Angew. Chemie Int. Ed.* **41**(7), pp. 1188–1191, 2002.

[133] D. J. D. Moet, L. J. A. Koster, B. de Boer, and P. W. M. Blom, "Hybrid polymer solar cells from highly reactive diethylzinc: MDMO-PPV versus P3HT," *Chem. Mater.* **19**(24), pp. 5856–5861, 2007.

[134] A. J. Said, G. Poize, C. Martini, D. Ferry, W. Marine, S. Giorgio, F. Fages, J. Hocq, J. Bouclé, J. Nelson, J. R. Durrant, and J. Ackermann, "Hybrid bulk heterojunction solar cells based on P3HT and porphyrin-modified ZnO nanorods," *J. Phys. Chem. C* **114**(25), pp. 11273–11278, 2010.

[135] P. Suresh, P. Balaraju, S. K. Sharma, M. S. Roy, and G. D. Sharma, "Photovoltaic devices based on PPHT:ZnO and dye-sensitized PPHT:ZnO thin films," *Sol. Energy Mater. Sol. Cells* **92**(8), pp. 900–908, 2008.

[136] Q. Zheng, G. Fang, F. Cheng, H. Lei, W. Wang, P. Qin, and H. Zhou, "Hybrid graphene–ZnO nanocomposites as electron acceptor in polymer-based bulk-heterojunction organic photovoltaics," *J. Phys. D. Appl. Phys.* **45**, p. 5103, Nov. 2012.

[137] A. M. Peiro, P. Ravirajan, K. Govender, D. S. Boyle, P. O'Brien, D. D. C. Bradley, J. Nelson, and J. R. Durrant, "Hybrid polymer/metal oxide solar cells based on ZnO columnar structures," *J. Mater. Chem.* **16**(21), pp. 2088–2096, 2006.

[138] M. Q. Wang and X. G. Wang, "Electrodeposition zinc-oxide inverse opal and its application in hybrid photovoltaics," *Sol. Energy Mater. Sol. Cells* **92**(3), pp. 357–362, 2008.

[139] C. Xu, K. Yang, L. Huang, and H. Wang, "Vertically aligned ZnO nanodisks and their uses in bulk heterojunction solar cells," *J. Renew. Sustain. Energy* **2**(5), p. 53101, 2010.

[140] A. L. Briseno, T. W. Holcombe, A. I. Boukai, E. C. Garnett, S. W. Shelton, J. J. M. Frechet, and P. Yang, "Oligo- and polythiophene/ZnO hybrid nanowire solar cells," *Nano Lett.* **10**(1), pp. 334–340, 2009.

[141] Z. Y. Yin, S. X. Wu, X. Z. Zhou, X. Huang, Q. C. Zhang, F. Boey, and H. Zhang, "Electrochemical deposition of ZnO nanorods on transparent reduced graphene oxide electrodes for hybrid solar cells," *Small* **6**(2), pp. 307–312, 2010.

[142] G. K. Mor, O. K. Varghese, M. Paulose, and C. A. Grimes, "Transparent highly ordered TiO_2 nanotube arrays via anodization of titanium thin films," *Adv. Funct. Mater.* **15**(8), pp. 1291–1296, 2005.

[143] Y. X. Li, M. Zhang, M. Guo, and X. D. Wang, "Hydrothermal growth of well-aligned TiO_2 nanorod arrays: Dependence of morphology upon hydrothermal reaction conditions," *Rare Met.* **29**(3), pp. 286–291, 2010.

[144] Y. Y. Lin, C. W. Chen, T. H. Chu, W. F. Su, C. C. Lin, C. H. Ku, J. J. Wu, and C. H. Chen, "Nanostructured metal oxide/conjugated polymer hybrid solar cells by low temperature solution processes," *J. Mater. Chem.* **17**(43), pp. 4571–4576, 2007.

[145] D. C. Olson, Y. J. Lee, M. S. White, N. Kopidakis, S. E. Shaheen, D. S. Ginley, J. A. Voigt, and J. W. P. Hsu, "Effect of polymer processing on the performance of poly(3-hexylthiophene)/ZnO nanorod photovoltaic devices," *J. Phys. Chem. C* **111**(44), pp. 16640–16645, 2007.

[146] B. Conings, L. Baeten, H.-G. Boyen, D. Spoltore, J. DHaen, L. Grieten, P. Wagner, M. K. Van Bael, and J. V. Manca, "Influence of interface morphology onto the photovoltaic properties of nanopatterned ZnO/poly(3-hexylthiophene) hybrid solar cells: an impedance spectroscopy study," *J. Phys. Chem. C* **115**, pp. 16695–16700, Aug. 2011.

[147] C. S. Karthikeyan, M. Thelakkat, and M. Willert-Porada, "Different mesoporous titania films for solid-state dye sensitised solar cells," *Thin Solid Films* **511**, pp. 187–194, 2006.

[148] C. Tian, Z. Zhang, J. Hou, and N. Luo, "Surfactant/co-polymer template hydrothermal synthesis of thermally stable, mesoporous TiO_2 from $TiOSO_4$," *Mater. Lett.* **62**(1), pp. 77–80, 2008.

[149] K. M. Coakley, Y. X. Liu, M. D. McGehee, K. L. Frindell, and G. D. Stucky, "Infiltrating semiconducting polymers into self-assembled mesoporous titania films for photovoltaic applications," *Adv. Funct. Mater.* **13**(4), pp. 301–306, 2003.

[150] K. M. Coakley and M. D. McGehee, "Photovoltaic cells made from conjugated polymers infiltrated into mesoporous titania," *Appl. Phys. Lett.* **83**(16), pp. 3380–3382, 2003.

[151] D. C. Olson, Y. J. Lee, M. S. White, N. Kopidakis, S. E. Shaheen, D. S. Ginley, J. A. Voigt, and J. W. P. Hsu, "Effect of ZnO processing on the photovoltage of ZnO/poly(3-hexylthiophene) solar cells," *J. Phys. Chem. C* **112**(26), pp. 9544–9547, 2008.

[152] J. J. Uhlrich, D. C. Olson, J. W. P. Hsu, and T. F. Kuech, "Surface chemistry and surface electronic properties of ZnO single crystals and nanorods," *J. Vac. Sci. & Technol. A* **27**(2), pp. 328–335, 2009.

[153] N. O. V. Plank, M. E. Welland, J. L. MacManus-Driscoll, and L. Schmidt-Mende, "The backing layer dependence of open circuit voltage in ZnO/polymer composite solar cells," *Thin Solid Films* **516**(20), pp. 7218–7222, 2008.

[154] M. T. Lloyd, Y.-J. Lee, R. J. Davis, E. Fang, R. M. Fleming, J. W. P. Hsu, R. J. Kline, and M. F. Toney, "Improved efficiency in poly(3-hexylthiophene)/zinc oxide solar cells via lithium incorporation," *J. Phys. Chem. C* **113**(41), pp. 17608–17612, 2009.

[155] P. Ruankham, T. Sagawa, H. Sakaguchi, and S. Yoshikawa, "Vertically aligned ZnO nanorods doped with lithium for polymer solar cells: defect related photovoltaic properties," *J. Mater. Chem.* **21**(26), pp. 9710–9715, 2011.

[156] G. V. Rao, F. Säuberlich, and A. Klein, "Influence of Mg content on the band alignment at CdS/(Zn,Mg)O interfaces," *Appl. Phys. Lett.* **87**(3), p. 2101, 2005.

[157] D. C. Olson, S. E. Shaheen, M. S. White, W. J. Mitchell, M. F. A. M. van Hest, R. T. Collins, and D. S. Ginley, "Band-offset engineering for enhanced open-circuit voltage in polymer–oxide hybrid solar cells," *Adv. Funct. Mater.* **17**(2), pp. 264–269, 2007.

[158] M. Wang, J.-P. Sun, S. Suei, and I. G. Hill, "Optimizing the photovoltage of polymer/zinc oxide hybrid solar cells by calcium doping," *J. Appl. Phys.* **112**(4), p. 044511, 2012.

[159] S. Oh, T. Nagata, J. Volk, and Y. Wakayama, "Improving the performance of inorganic–organic hybrid photovoltaic devices by uniform ordering of ZnO nanorods and near-atmospheric pressure nitrogen plasma treatment," *J. Appl. Phys.* **113**(8), p. 083708, 2013.

[160] K. Noori and F. Giustino, "Ideal energy-level alignment at the ZnO/P3HT photovoltaic interface," *Adv. Funct. Mater.* **22**, pp. 5089–5095, Dec. 2012.

[161] P. Tiwana, P. Docampo, M. B. Johnston, H. J. Snaith, and L. M. Herz, "Electron mobility and injection dynamics in mesoporous ZnO, SnO_2, and TiO_2 Films used in dye-sensitized solar cells," *ACS Nano* **5**(6), pp. 5158–5166, 2011.

[162] J. Piris, N. Kopidakis, D. C. Olson, S. E. Shaheen, D. S. Ginley, and G. Rumbles, "The locus of free charge-carrier generation in solution-cast $Zn_{1-x}Mg_xO$/poly(3-hexylthiophene) bilayers for photovoltaic applications," *Adv. Funct. Mater.* **17**(18), pp. 3849–3857, 2007.

[163] S. Fukuzumi, "Development of bioinspired artificial photosynthetic systems," *Phys. Chem. Chem. Phys.* **10**(17), pp. 2283–2297, 2008.

[164] P. Ravirajan, A. M. Peiro, M. K. Nazeeruddin, M. Graetzel, D. D. C. Bradley, J. R. Durrant, and J. Nelson, "Hybrid polymer/zinc oxide photovoltaic devices with vertically oriented ZnO nanorods and an amphiphilic molecular interface layer," *J. Phys. Chem. B* **110**(15), pp. 7635–7639, 2006.

[165] T.-H. Lee, H.-J. Sue, and X. Cheng, "ZnO and conjugated polymer bulk heterojunction solar cells containing ZnO nanorod photoanode," *Nanotechnology* **22**(28), p. 5401, 2011.

[166] Y. Y. Lin, Y. Y. Lee, L. W. Chang, J. J. Wu, and C. W. Chen, "The influence of interface modifier on the performance of nanostructured ZnO/polymer hybrid solar cells," *Appl. Phys. Lett.* **94**(6), p. 3308, 2009.

[167] Y. Vaynzof, A. A. Bakulin, S. Gélinas, and R. H. Friend, "Direct observation of photoinduced bound charge-pair states at an organic–inorganic semiconductor interface," *Phys. Rev. Lett.* **108**, p. 6605, June 2012.

[168] K. Ogata, T. Hama, K. Hama, K. Koike, S. Sasa, M. Inoue, and M. Yano, "Characterization of alkanethiol/ZnO structures by X-ray photoelectron spectroscopy," *Appl. Surf. Sci.* **241**(1-2), pp. 146–149, 2005.

[169] T. C. Monson, M. T. Lloyd, D. C. Olson, Y.-J. Lee, and J. W. P. Hsu, "Photocurrent cnhancement in polythiophene- and alkanethiol-modified ZnO solar cells," *Adv. Mater.* **20**(24), pp. 4755–4759, 2008.

[170] M. T. Lloyd, R. P. Prasankumar, M. B. Sinclair, A. C. Mayer, D. C. Olson, and J. W. P. Hsu, "Impact of interfacial polymer morphology on photoexcitation dynamics and device performance in P3HT/ZnO heterojunctions," *J. Mater. Chem.* **19**(26), pp. 4609–4614, 2009.

[171] D. J. Baker, C. G. Allen, T. D. Berman, M. R. Bergren, J. M. Albin, D. C. Olson, E. C. Przekwas, M. S. White, D. S. Ginley, R. T. Collins, and T. E. Furtak, "Functionalized zinc oxide for improved organic photovoltaic systems," *Phys. Technol. Org. Semicond. Devices* **1115**, pp. 143–148, 2010.

[172] J. Weickert, F. Auras, T. Bein, and L. Schmidt-Mende, "Characterization of interfacial modifiers for hybrid solar cells," *J. Phys. Chem. C* **115**(30), pp. 15081–15088, 2011.

[173] J. Yu, T.-L. Shen, W.-H. Weng, Y.-C. Huang, C.-I. Huang, W.-F. Su, S.-P. Rwei, K.-C. Ho, and L. Wang, "Molecular design of interfacial modifiers for polymer–inorganic hybrid solar cells," *Adv. Energy Mater.* **2**(2), p. 245, 2011.

[174] J. A. Chang, J. H. Rhee, S. H. Im, Y. H. Lee, H.-j. Kim, S. I. Seok, M. K. Nazeeruddin, and M. Grätzel, "High-performance nanostructured inorganic–organic heterojunction solar cells," *Nano Lett.* **10**(7), pp. 2609–2612, 2010.

[175] M. S. White, D. C. Olson, N. Kopidakis, A. M. Nardes, D. S. Ginley, and J. J. Berry, "Control of charge separation by electric field manipulation in polymer-oxide hybrid organic photovoltaic bilayer devices," *Phys. Status Solidi a* **207**(5), pp. 1257–1265, 2010.

[176] P. Atienzar, T. Ishwara, B. N. Illy, M. P. Ryan, B. C. O'Regan, J. R. Durrant, and J. Nelson, "Control of photocurrent generation in polymer/ZnO nanorod solar cells by using a solution-processed TiO_2 overlayer," *J. Phys. Chem. Lett.* **1**(4), pp. 708–713, 2010.

[177] Y.-J. Lee, R. J. Davis, M. T. Lloyd, P. P. Provencio, R. P. Prasankumar, and J. W. P. Hsu, "Open-circuit voltage improvement in hybrid ZnO–polymer photovoltaic devices with oxide engineering," *IEEE J. Sel. Top. Quantum Electron.* **16**, pp. 1587–1594, Nov. 2010.

[178] J. F. Scott, "Applications of modern ferroelectrics," *Science* **315**, pp. 954–9, Feb. 2007.

[179] J. C. Burfoot, *Ferroelectrics: an introduction to the physical principles*, Van Nostrand, 1st ed., 1967.

[180] Z. Huang, Q. Zhang, and R. W. Whatmore, "Low temperature crystallization of lead zirconate titanate thin films by a sol-gel method," *J. Appl. Phys.* **85**, p. 7355, May 1999.

[181] D. D. Fong, G. B. Stephenson, S. K. Streiffer, J. A. Eastman, O. Auciello, P. H. Fuoss, and C. Thompson, "Ferroelectricity in ultrathin perovskite films.," *Science* **304**, pp. 1650–3, June 2004.

[182] B. Noheda and G. Catalan, "Symmetry Engineering and Size Effects in Ferroelectric Thin Films," in *Handbook of Advanced Dielectric, Piezoelectric and Ferroelectric Materials*, Z.-G. Ye, ed., ch. 25, pp. 756–786, Woodhead Publishing Ltd, 1st ed., 2008.

[183] H. Huang, "Solar energy: ferroelectric photovoltaics," *Nat. Photonics* **4**, pp. 134–135, Mar. 2010.

[184] S. Y. Yang, J. Seidel, S. J. Byrnes, P. Shafer, C.-H. Yang, M. D. Rossell, P. Yu, Y.-H. Chu, J. F. Scott, J. W. Ager, L. W. Martin, and R. Ramesh, "Above-bandgap voltages from ferroelectric photovoltaic devices," *Nat. Nanotechnol.* **5**, pp. 143–7, Feb. 2010.

[185] M. Qin, K. Yao, and Y. C. Liang, "High efficient photovoltaics in nanoscaled ferroelectric thin films," *Appl. Phys. Lett.* **93**(12), p. 2904, 2008.

[186] Y. Yuan, T. J. Reece, P. Sharma, S. Poddar, S. Ducharme, A. Gruverman, Y. Yang, and J. Huang, "Efficiency enhancement in organic solar cells with ferroelectric polymers," *Nat. Mater.* **10**(4), pp. 296–302, 2011.

[187] K. S. Nalwa, J. A. Carr, R. C. Mahadevapuram, H. K. Kodali, S. Bose, Y. Chen, J. W. Petrich, B. Ganapathysubramanian, and S. Chaudhary, "Enhanced charge separation in organic photovoltaic films doped with ferroelectric dipoles," *Energy & Environ. Sci.* **5**, pp. 7042–7049, 2012.

[188] K. Asadi, P. de Bruyn, P. W. M. Blom, and D. M. de Leeuw, "Origin of the efficiency enhancement in ferroelectric functionalized organic solar cells," *Appl. Phys. Lett.* **98**(18), pp. 3301–3303, 2011.

[189] Y. Yuan, P. Sharma, Z. Xiao, S. Poddar, A. Gruverman, S. Ducharme, and J. Huang, "Understanding the effect of ferroelectric polarization on power conversion efficiency of organic photovoltaic devices," *Energy & Environ. Sci.* , 2012.

[190] J. Briscoe, S. Shoaee, J. R. Durrant, and S. Dunn, "Piezoelectric enhancement of hybrid organic/inorganic photovoltaic device," *J. Phys. Conf. Ser.* **476**, p. 2009, Dec. 2013.

[191] R. C. G. Naber, C. Tanase, P. W. M. Blom, G. H. Gelinck, A. W. Marsman, F. J. Touwslager, S. Setayesh, and D. M. de Leeuw, "High-performance solution-processed polymer ferroelectric field-effect transistors," *Nat. Mater.* **4**, pp. 243–248, Feb. 2005.

[192] A. R. West, *Solid State Chemistry And Its Applications*, John Wiley & Sons, Ltd., 1st ed., 1984.

[193] A. K. Tagantsev, K. Vaideeswaran, S. B. Vakhrushev, A. V. Filimonov, R. G. Burkovsky, A. Shaganov, D. Andronikova, A. I. Rudskoy, A. Q. R. Baron, H. Uchiyama, D. Chernyshov, A. Bosak, Z. Ujma, K. Roleder, A. Majchrowski, J.-H. Ko, and N. Setter, "The origin of antiferroelectricity in $PbZrO_3$," *Nat. Commun.* **4**, p. 2229, July 2013.

[194] J. A. Rodriguez, A. Etxeberria, L. González, and A. Maiti, "Structural and electronic properties of $PbTiO_3$, $PbZrO_3$, and $PbZr_{0.5}Ti_{0.5}O_3$: first-principles density-functional studies," *J. Chem. Phys.* **117**, p. 2699, Aug. 2002.

[195] S. A. Mabud, "The morphotropic phase boundary in PZT solid solutions," *J. Appl. Crystallogr.* **13**, pp. 211–216, June 1980.

[196] R. Guo, L. Cross, S.-E. Park, B. Noheda, D. Cox, and G. Shirane, "Origin of the high piezoelectric response in $PbZr_{1-x}Ti_xO_3$," *Phys. Rev. Lett.* **84**, pp. 5423–5426, June 2000.

[197] J. Frantti, J. Lappalainen, S. Eriksson, V. Lantto, S. Nishio, M. Kakihana, S. Ivanov, and H. k. Rundlöf, "Neutron Diffraction Studies of $Pb(Zr_xTi_{1-x})O_3$ Ceramics," *Jpn. J. Appl. Phys.* **39**, pp. 5697–5703, Sept. 2000.

[198] B. Jaffe, W. R. Cook, and H. Jaffe, *Piezoelectric Ceramics*, Academic Press London and New York, 1971.

[199] Y. Xu, *Ferroelectric Materials and Their Applications*, Elsevier Science Ltd., 1st ed., 1991.

[200] Q. Zhang, R. W. Whatmore, Z. Huang, and E. M. Vickers, "Low temperature formation of sol-gel derived ferroelectric lead zirconate titanate ($Pb(Zr_xTi_{1-x})O_3$, x = 0.3) thin films," *J. Phys. IV Fr.* **08**, pp. Pr9–79–Pr9–82, Dec. 1998.

[201] K. Shimomura, T. Tsurumi, Y. Ohba, and M. Daimon, "Preparation of lead zirconate titanate thin film by hydrothermal method," *Jpn. J. Appl. Phys.* **30**, pp. 2174–2177, Sept. 1991.

[202] A. Okada, "Electrical properties of lead-zirconate–lead-titanate ferroelectric thin films and their composition analysis by Auger electron spectroscopy," *J. Appl. Phys.* **49**, p. 4495, Aug. 1978.

[203] T. Zhu, L. Lu, and M. Lai, "Pulsed laser deposition of lead–zirconate–titanate thin films and multilayered heterostructures," *Appl. Phys. A* **81**, pp. 701–714, Apr. 2005.

[204] R. Ramesh, S. Aggarwal, and O. Auciello, "Science and technology of ferroelectric films and heterostructures for non-volatile ferroelectric memories," *Mater. Sci. Eng. R Reports* **32**, pp. 191–236, Apr. 2001.

[205] N. Izyumskaya, V. Avrutin, X. Gu, Ü. Özgür, B. Xiao, T. D. Kang, H. Lee, and H. Morkoç, "Growth of high-quality $Pb(Zr_xTi_{1-x})O_3$ films by peroxide MBE and their optical and structural characteristics," *MRS Proc.* **966**, pp. 0966–T11–17, Feb. 2006.

[206] N. Izyumskaya, Y. I. Alivov, S. J. Cho, H. Morkoç, H. Lee, and Y. S. Kang, "Processing, structure, properties, and applications of PZT thin films," *Crit. Rev. Solid State Mater. Sci.* **32**, pp. 111–202, July 2007.

[207] H. Xu, T. Kiyomoto, Y. Morikawa, M. Okuyama, and C. Lin, "Hydrothermal transformation of gel $Pb(Zr_{0.52}, Ti_{0.48})O_3$ thin films into perovskite phase at low temperature of 160 °C," *Jpn. J. Appl. Phys.* **37**, pp. L809–L811, July 1998.

[208] Q. Zhang and R. W. Whatmore, "Sol-gel PZT and Mn-doped PZT thin films for pyroelectric applications," *J. Phys. D. Appl. Phys.* **34**(15), p. 2296, 2001.

[209] W. T. Lee, E. K. H. Salje, and M. T. Dove, "Effect of surface relaxations on the equilibrium growth morphology of crystals: platelet formation," *J. Phys. Condens. Matter* **11**, pp. 7385–7410, Sept. 1999.

[210] I. Szafraniak-Wiza, M. Alexe, and M. Hesse, "Nanosized Ferroelectric Crystals," in *Handbook of Advanced Dielectric, Piezoelectric and Ferroelectric Materials*, Z.-G. Ye, ed., ch. 20, pp. 600–664, Woodhead Publishing Ltd, 1st ed., 2008.

[211] C. C. A. Barron, M. McLachlan, Q. Zhang, and D. W. McComb, "Ferroelectric three-dimensionally ordered macroporous thin films," *Integr. Ferroelectr.* **92**(1), pp. 43–52, 2007.

[212] X. Wang, Y. Wang, J. Yin, and Z. Liu, "Enhanced ferroelectric properties of $Pb(Zr_{0.52}Ti_{0.48})O_3$ films on $Pt/TiO_2/SiO_2/Si(001)$ using ZnO buffer layer," *Scr. Mater.* **46**, pp. 783–787, June 2002.

[213] V. M. Voora, T. Hofmann, M. Brandt, M. Lorenz, M. Grundmann, N. Ashkenov, H. Schmidt, N. Ianno, and M. Schubert, "Interface polarization coupling in piezoelectric–semiconductor ferroelectric heterostructures," *Phys. Rev. B* **81**, p. 5307, May 2010.

[214] M.-X. Zhou, Z.-W. Li, B. Chen, J.-G. Wan, and J.-M. Liu, "Tunable resistive switching behaviour in ferroelectric–ZnO bilayer films," *J. Phys. D. Appl. Phys.* **46**, p. 5304, Apr. 2013.

[215] C. H. Peng, J.-F. Chang, and S. B. Desu, "Optical properties of PZT, PLZT, and PNZT thin films," *MRS Proc.* **243**, p. 21, Feb. 1991.

[216] M. P. Moret, M. A. C. Devillers, K. Wörhoff, and P. K. Larsen, "Optical properties of $PbTiO_3$, $PbZr_xTi_{1-x}O_3$, and $PbZrO_3$ films deposited by metalorganic chemical vapor on $SrTiO_3$," *J. Appl. Phys.* **92**, p. 468, July 2002.

[217] D. J. Wouters, G. J. Willems, and H. E. Maes, "Electrical conductivity in ferroelectric thin films," *Microelectron. Eng.* **29**, pp. 249–256, Dec. 1995.

[218] P. Juan, H. Chou, and J. Lee, "The effect of electrode material on the electrical conduction of metal-$Pb(Zr_{0.53}Ti_{0.47})O_3$-metal thin film capacitors," *Microelectron. Reliab.* **45**, pp. 1003–1006, May 2005.

[219] F. Nüesch, L. J. Rothberg, E. W. Forsythe, Q. T. Le, and Y. Gao, "A photoelectron spectroscopy study on the indium tin oxide treatment by acids and bases," *Appl. Phys. Lett.* **74**, p. 880, Feb. 1999.

[220] M. Quaas, C. Eggs, and H. Wulff, "Structural studies of ITO thin films with the Rietveld method," *Thin Solid Films* **332**, pp. 277–281, Nov. 1998.

[221] H. M. Stec, R. J. Williams, T. S. Jones, and R. A. Hatton, "Ultrathin transparent Au electrodes for organic photovoltaics fabricated using a mixed mono-molecular nucleation layer," *Adv. Funct. Mater.* **21**(9), p. 1709, 2011.

[222] L. Hu, H. S. Kim, J.-Y. Lee, P. Peumans, and Y. Cui, "Scalable coating and properties of transparent, flexible, silver nanowire electrodes," *ACS Nano* **4**, pp. 2955–63, May 2010.

[223] H.-K. Park, J.-W. Kang, S.-I. Na, D.-Y. Kim, and H.-K. Kim, "Characteristics of indium-free GZO/Ag/GZO and AZO/Ag/AZO multilayer electrode grown by dual target DC sputtering at room temperature for low-cost organic photovoltaics," *Sol. Energy Mater. Sol. Cells* **93**(11), pp. 1994–2002, 2009.

[224] F. L. Zhang, M. Johansson, M. R. Andersson, J. C. Hummelen, and O. Inganas, "Polymer photovoltaic cells with conducting polymer anodes," *Adv. Mater.* **14**(9), pp. 662–665, 2002.

[225] M. W. Rowell, M. A. Topinka, M. D. McGehee, H. J. Prall, G. Dennler, N. S. Sariciftci, L. B. Hu, and G. Gruner, "Organic solar cells with carbon nanotube network electrodes," *Appl. Phys. Lett.* **88**(23), p. 3506, 2006.

[226] X. Wang, L. Zhi, and K. Müllen, "Transparent, conductive graphene electrodes for dye-sensitized solar cells," *Nano Lett.* **8**(1), pp. 323–327, 2007.

[227] W. Zhang, R. Zhu, F. Li, Q. Wang, and B. Liu, "High-performance solid-state organic dye sensitized solar cells with P3HT as hole transporter," *J. Phys. Chem. C* **115**, pp. 7038–7043, Apr. 2011.

[228] M. Mas-Torrent, D. den Boer, M. Durkut, P. Hadley, and A. P. H. J. Schenning, "Field effect transistors based on poly(3-hexylthiophene) at different length scales," *Nanotechnology* **15**, pp. S265–S269, Apr. 2004.

[229] M. Brinkmann, "Structure and morphology control in thin films of regioregular poly(3-hexylthiophene)," *J. Polym. Sci. Part B Polym. Phys.* **49**, pp. 1218–1233, Sept. 2011.

[230] S. A. Jenekhe, "A class of narrow-band-gap semiconducting polymers," *Nature* **322**, pp. 345–347, July 1986.

[231] M. Jaiswal and R. Menon, "Polymer electronic materials: a review of charge transport," *Polym. Int.* **55**, pp. 1371–1384, Dec. 2006.

[232] R. D. McCullough, "The chemistry of conducting polythiophenes," *Adv. Mater.* **10**, pp. 93–116, Jan. 1998.

[233] H. Sirringhaus, P. J. Brown, R. H. Friend, M. M. Nielsen, K. Bechgaard, B. M. W. Langeveld-Voss, A. J. H. Spiering, R. A. J. Janssen, E. W. Meijer, P. Herwig, and D. M. de Leeuw, "Two-dimensional charge transport in self-organized, high-mobility conjugated polymers," *Nature* **401**, pp. 685–688, Oct. 1999.

[234] R. J. Kline and M. D. McGehee, "Morphology and charge transport in conjugated polymers," *J. Macromol. Sci. Part C Polym. Rev.* **46**, pp. 27–45, Jan. 2006.

[235] F. P. V. Koch, J. Rivnay, S. Foster, C. Müller, J. M. Downing, E. Buchaca-Domingo, P. Westacott, L. Yu, M. Yuan, M. Baklar, Z. Fei, C. Luscombe, M. A. McLachlan, M. Heeney, G. Rumbles, C. Silva, A. Salleo, J. Nelson, P. Smith, and N. Stingelin, "The impact of molecular weight on microstructure and charge transport in semicrystalline polymer semiconductorspoly(3-hexylthiophene), a model study," *Prog. Polym. Sci.* **38**, pp. 1978–1989, Dec. 2013.

[236] C.-C. Chang, C.-L. Pai, W.-C. Chen, and S. A. Jenekhe, "Spin coating of conjugated polymers for electronic and optoelectronic applications," *Thin Solid Films* **479**, pp. 254–260, May 2005.

[237] S. K. Sharma, R. Singhal, B. D. Malhotra, N. Sehgal, and A. Kumar, "Lactose biosensor based on Langmuir-Blodgett films of poly(3-hexyl thiophene)," *Biosens. Bioelectron.* **20**, pp. 651–7, Oct. 2004.

[238] S. P. Speakman, G. G. Rozenberg, K. J. Clay, W. I. Milne, A. Ille, I. A. Gardner, E. Bresler, and J. H. Steinke, "High performance organic semiconducting thin films: ink jet printed polythiophene (rr-P3HT)," *Org. Electron.* **2**, pp. 65–73, Sept. 2001.

[239] E. L. Ratcliff, J. L. Jenkins, K. Nebesny, and N. R. Armstrong, "Electrodeposited, "textured" poly(3-hexyl-thiophene) (e-P3HT) Films for photovoltaic applications," *Chem. Mater.* **20**, pp. 5796–5806, Sept. 2008.

[240] D. H. Kim, Y. Jang, Y. D. Park, and K. Cho, "Controlled one-dimensional nanostructures in poly(3-hexylthiophene) thin film for high-performance organic field-effect transistors," *J. Phys. Chem. B* **110**(32), pp. 15763–8, 2006.

[241] J.-F. Chang, B. Sun, D. W. Breiby, M. M. Nielsen, T. I. Sölling, M. Giles, I. McCulloch, and H. Sirringhaus, "Enhanced mobility of poly(3-hexylthiophene) transistors by spin-coating from high-boiling-point solvents," *Chem. Mater.* **16**, pp. 4772–4776, Nov. 2004.

[242] G. Li, Y. Yao, H. Yang, V. Shrotriya, G. Yang, and Y. Yang, ""Solvent annealing" effect in polymer solar cells based on poly(3-hexylthiophene) and methanofullerenes," *Adv. Funct. Mater.* **17**, pp. 1636–1644, July 2007.

Chapter 2

Experimental Methods

In the first part of this chapter, the synthetic methods and processing conditions used for depositing the materials used in this study — namely ZnO, lead zirconate titanate (PZT), and poly(3-hexylthiophene) (P3HT) — are described, including general background information on the techniques.

The second half of the chapter focusses on the characterisation techniques used to analyse the materials properties of these layers and the hybrid photovoltaic (hPV) devices fabricated from them. This is broken down into several sections encompassing: *i)* physical and structural characterisation *ii)* compositional characterisation; *iii)* optoelectronic characterisation of materials, both in the context of the materials themselves and in terms of device dynamics; *iv)* fabrication and testing of hPV devices. Additional procedural details are given in the relevant sections in subsequent chapters.

2.1 Substrate Preparation

The materials used in this work were deposited on different substrates — glass (diamond cut from VWR soda lime microscope slides), glass coated with a thin-film of patterned "device grade" indium tin oxide (ITO, PsiOtec Ltd., 12 x 12 x 1 mm, 12 x 8 mm active area, 12 – 16 Ω sq^{-1}), and SiO_2/Si wafers (Crystal GmbH). The cleaning method for these was the same: firstly, the substrates were rinsed and ultrasonicated for 8 minutes in acetone. These were subsequently removed from solution and rubbed with an absorbent pad to remove traces of photoresist and other contaminants, before being sonicated in acetone for a further 8 minutes. Lastly, the substrates were transferred to a beaker containing IPA and ultrasonicated for 10 minutes before being dried using N_2 gas.

2.2 Materials Processing

This section covers the growth methods used for synthesis of ZnO and PZT thin-films and the processing of P3HT for device fabrication and optoelectronic characterisation.

2.2.1 Oxide Synthesis Routes

ZnO films were processed using two methods, sol-gel deposition and spray pyrolysis, whilst the sol-gel method alone was used for growth of PZT films. These routes were chosen on the basis that they require relatively low temperatures (although it should be noted that the temperatures used in this study are higher than ideal for OPV fabrication) and may be carried out in ambient conditions from solution.

2.2.1.1 The Sol-gel Method

A sol-gel is a biphasic molecular precursor solution from which a solid material may be grown consisting of *i)* a liquid gel matrix which acts as the solvent, and *ii)* a solid phase of the precursor species which may be formed through colloidal aggregation or condensation to form a long-range network (known as a sol) [1]. Typically, the precursor is an organometallic or metal chloride dissolved in a suitable solvent which leads to formation of colloidal particles by condensation or hydrolysis reactions, creating a network of the metal oxide connected by bridging oxo- (M–O–M) or hydroxo- (M–(OH)–M) bonds.

The concentration of both the precursor material and solution additives are crucial in determining the characteristics of the sol-gel, *e.g.* chemical stability, viscosity, and particle size; effects such as particle flocculation or particle growth due to continued condensation reactions with the sol may be effectively inhibited by tuning the pH or by adding a complexing agent. For thin-film growth, a sol-gel must be applied to a substrate (most commonly by spin-coating, although other methods such as dip-coating are also used) and dried, leading to densification of the film and, in some cases, decomposition of the precursor to form the product. During the drying stage, the solvent is thermally extracted from the precursor film. The rate at which this occurs can have a significant effect on the microstructure of the resulting film as fast solvent extraction can result in the formation of pores. In most cases, a final processing step is required to complete the transformation of the film from precursor to product: in this work, both ZnO and PZT thin-films were annealed to complete oxide formation. The methods for ZnO and PZT deposition in this work are outlined in Section 2.2.2.1 and Section 2.2.3.1 respectively.

2.2.1.2 Spray Pyrolysis

Spray pyrolysis has become a popular method for preparing dense thin-films of inorganic materials due to the requirement of a very basic setup, the short time required to produce the films, and the potential for scaling the technique to large areas. In this method, a simple solution of a suitable metal precursor (such as acetate, chloride, or nitrate) with a relatively low decomposition temperature is made using a suitable low-boiling point solvent. This is subsequently sprayed onto a heated substrate using an aerosol; the heat from the substrate causes the evaporation of the solution droplets and pyrolyses the precursor, leading to the crystallisation of the oxide on the substrate. SP is a popular technique for producing dense, crystalline inorganic thin-films as it may be carried out under ambient conditions, involves simple starting materials, allows for rapid production of large volumes of material, may be applied to a wide range of materials, and may easily be modified to incorporate dopants in the precursor solution. However, due to the number of mechanical and chemical variables involved in the process, the films produced by this method may show high variability: mechanical variables include substrate temperature, spray height, spray rate, droplet size, spray time and number of spray cycles. Among the chemical variables which may be controlled are solution concentration, carrier solvent properties, and precursor decomposition temperature [2]. As such, automated systems are becoming more popular as a way of attaining more control over the processing conditions, leading to greater batch-to-batch and sample-to-sample repeatability.

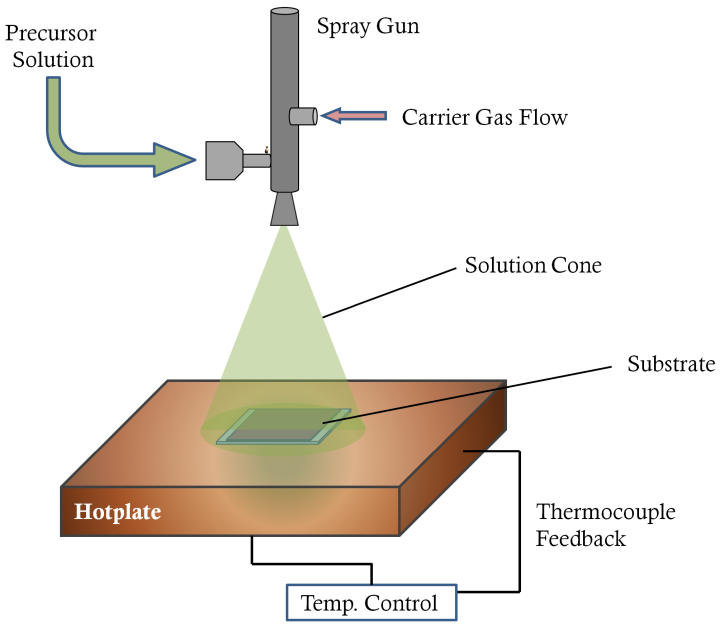

Figure 2.1 – Schematic diagram of typical spray pyrolysis setup.

2.2.2 ZnO Synthesis

2.2.2.1 Sol-gel

Sol-gel-derived ZnO films (SG-Z) were used in this work as a substrate for PZT growth and as an acceptor layer for bilayer ZnO–P3HT and ZnO–PZT–P3HT devices. The sol-gel method used in this work was originally outlined by Ohyama [3, 4] and optimised by Downing [5] to produce films to be used as seed layers for ZnO nanorod growth, and employs zinc acetate dihydrate ($Zn(ac)_2{\cdot}2H_2O$)[1] as the precursor compound. The films produced by this method have been well characterised and have been shown to produce working hPV devices [6]; as such, they were considered to be an ideal testbed material for this study.

This particular route is widely used due to the ease of preparing both the sol-gel and the thin-films, as well as the stability of the sol-gel over time due to the presence of a chelating ligand. The sol-gel is produced as follows: $Zn(ac)_2{\cdot}2H_2O$ was weighed and placed into a volumetric flask; to this, 2-aminoethanol was added in a 1:1 molar ratio to Zn^{2+} — 2-aminoethanol is a bidentate ligand (coordinating via both its hydroxyl and amine groups) which stabilises the metal ions in the sol-gel and inhibits the condensation of $Zn(OH)_2$ agglomerates. The solution was then made up with 2-methoxyethanol, sonicated for 10 minutes, and stirred for a further 30 minutes until all the zinc acetate had dissolved, leaving a transparent, yellow-tinged sol-gel with a concentration of 0.75 M Zn^{2+}.

Thin-films were made from the $Zn(ac)_2$ sol-gel by spin-coating: a substrate was loaded into a Chemat KW–4A spin coater, and the sol-gel dispensed to cover the substrate using a syringe fitted with a 0.2 μm poly(tetrafluoroethylene) (PTFE) filter. The substrates were spun in two stages: firstly, a 'loading' stage at 600 rpm for 10 seconds to spread the solution evenly across the substrate surface, then at 2000 rpm for a further 45 seconds. After the spin cycle was finished, the underside was cleaned with acetone and the substrate heated on a hotplate at 350 °C for 8 minutes to dry the film and to initiate decomposition of the zinc precursor. Subsequent coating stages were also carried out — in total, 3 coatings were used as standard in this work, leading to a final film thickness of $\sim$ 140 nm and highly orientated in the (*002*) direction. After the final drying step, the substrates were loaded directly into a preheated Carbolite DAF 11/1 box furnace at 450 °C. The thin-films were annealed for between 5 and 60 minutes to complete decomposition of the acetate and to improve the crystallinity of the films. After annealing, the furnace was switched off and the samples left inside to cool.

[1] 'ac' is the abbreviated form of the acetate group, $^{-}OOCCH_3$. Although $Zn(ac)_2{\cdot}2H_2O$ was the exact starting material used, the water of crystallisation will henceforth be omitted for brevity.

2.2.2.2 Spray Pyrolysis

The method used in this work is derived from work by Bashir [7], using a precursor solution consisting of $Zn(ac)_2{\cdot}H_2O$ dissolved in methanol. The mechanism of ZnO thin-film formation using this method has been posited to be dependent on the pyrolysis temperature [8]: at high temperatures (> 400 °C), not only does the carrier solvent evaporate in flight, but pyrolysis of the metal precursor also occurs before it reaches the substrate, resulting in non-uniform grain size. At lower temperatures, however (350 – 400 °C), the carrier solvent evaporates in flight, but the precursor species lands on the substrate where the pyrolysis of the material takes place. This affects the microstructure of the films, including their grain size and orientation which may, in turn, affect their electronic properties.

Substrates were placed onto a hotplate heated to 400 °C. The precursor solution was prepared by dissolving $Zn(ac)_2{\cdot}2H_2O$ in MeOH by ultrasonicating the solution for 1 hour. This was then was sprayed onto the heated substrate using an Iwata Revolution spray gun (fluid nozzle: 0.5 mm; needle: 0.5 mm): compressed air set at a pressure of 0.5 bar was used as the carrier gas, and the deposition height was set at 20 cm for all samples. The deposition was carried out using a repeated spraying/drying cycle: the substrates were sprayed for 10 s, followed by a 'drying' time of 45 s. A short spray time was used to minimise cooling of the substrate during the deposition, and the long 'drying' time to allow for pyrolysis of the metal precursor as well as ensuring that the substrate had heated back up to the indicated temperature. After the final drying step, the substrates were removed from the hotplate and left to cool. Some films were annealed using a Carbolite MTF 12/48/250 tube furnace pre-heated to 450 °C.

2.2.3 PZT Synthesis

For the deposition of PZT, a solution-based route was chosen — although vacuum methods such as PLD offer greater control in terms of film thickness and morphology, health concerns around using lead-based materials in such a system made such a route unfeasible. As discussed previously in Section 1.5.3.1, the Zr:Ti ratio of PZT is important in determining both the structural and physical properties of the material — Figure 1.19 in the previous chapter illustrates the changes in structure that occur when moving from $PbZrO_3$ (PZO) through to $PbTiO_3$ (PTO). In this work, $Pb(Zr_{0.30}Ti_{0.70})O_3$ (PZT 30/70) was chosen as the as the composition lies in the middle of the tetragonal region, such that any variations in the Zr:Ti ratio which may arise from processing are less likely to lead to structural changes in the material.

2.2.3.1 PZT Sol-gel Chemistry

A general overview of sol-gels is given in Section 2.2.1.1. The procedure used for the synthesis of the PZT 30/70 sol-gel was developed by Zhang [9, 10, 11] - this precursor consists of a mixture of Ti and Zr alkoxides and lead acetate in an acetic acid/alcoholic medium. The structure and chemistry of this particular sol-gel are fairly complex: in this system, the alkoxide groups of the Ti and Zr species are replaced with chelating acetate ligands, drastically increasing the gelation time of the solution by stabilising it with respect to hydrolysis. As a result, chain-like particles of metal oxo acetate species (terminated with alkoxy groups) form and grow slowly in solution over time; in addition, it has been established that the size of these particles may have an effect on the orientation of the thin-films derived from the sol-gel. Detailed studies and kinetic modelling of this PZT sol-gel system are presented and discussed in a series of papers by Zhang, Huang, *et al.* [12, 13, 14] and are beyond the scope of this study.

The sol-gel used in this work was provided by Dr Q. Zhang (Cranfield University), produced by the following method: $Pb(OAc)_2{\cdot}3H_2O$ was mixed with a stoichiometric amount of the bidentate ligand methanolamine and dissolved in methanol by gentle heating at 50 °C. Separately, $Zr(O^iPr)_4$ (70 % in ^{n}PrOH) and $Ti(O^nBu)_4$ were mixed in the ratio of 3:7, followed by the addition of acetic acid (AcOH) in the ratio of (Ti+Zr):AcOH = 1:2. After dilution with EtOH, the mixture was stirred at room temperature for 1 hour. Subsequently, the two metal precursor solutions were mixed together and stirred for a further 2 hours, after which acetic acid was added, such that the pH $\approx$ 3.4. The solution was passed through a 0.2 μm filter and, to complete the process, a small amount of ethylene glycol (EG) was added to increase the solution viscosity. The final concentration of this stock sol-gel is 0.4 M (relating to the concentration of the Zr/Ti species); it should be noted that the actual molar ratio of Pb:(Ti+Zr) is close to 1.1:1. This excess of Pb is used due to its volatility and loss from the films during heating: as perovskite PZT can only tolerate a $\sim$ 2 % loss of Pb in the tetragonal structure, it is vital that this loss is compensated for [15].

2.2.3.2 Sol-gel Deposition

Thin-films of PZT 30/70 were made by the following method: a substrate was loaded into a Chemat KW–4A spin-coater, and a sufficient volume of filtered PZT sol-gel (using a 0.2 μm PTFE filter) was loaded onto the substrate using an Eppendorf pipette — for a 12 mm x 12 mm substrate, a solution volume of 70 μl was used. Immediately after loading, the substrate was spun at a speed of 3000 rpm for 40 s, resulting in the formation of

a thin-film[2]. The substrate was removed, the underside cleaned with ^{i}PrOH, and placed on a hotplate set at 200 °C for 45 s to remove any remaining solvent. The substrates were then loaded into a Carbolite MTF 12/58/250 tube furnace and heated at different ramp rates (from at temperature to 1 °C min^{-1}) to the desired set-point of 480 °C $\leq T \leq$ 600 °C. The substrates were held at this temperature for between 5 and 60 minutes before being allowed to cool back to room temperature. In Chapters 4 & 5, the concentration of the PZT sol-gel was varied from 0.4 M to 0.001 M (with respect to [Zr+Ti]) to tune the thickness of the thin-films: this was carried out by diluting the sol-gel with a mixture of dried MeOH and acetic acid with a pH $\sim$ 3.4, the same as that of the stock PZT sol-gel.

Whilst both ZnO and PZT thin-films are prepared by sol-gel routes, different pathways govern the film-formation process: ZnO crystallises directly from the precursor during the drying stage; however, in the case of PZT, the drying phase does not yield the perovskite phase directly, instead forming an amorphous pyrochlore phase. This phase possesses two forms, depending on the drying temperature used and the ambient conditions: one is $Pb_2(Zr,Ti)_2O_6$, a relatively unstable, oxygen-deficient compound which converts rapidly into the perovskite phase with sufficient thermal energy input; the other is the Pb-deficient $Pb_2(Zr,Ti)_2O_7$ which is much more stable and converts far more slowly — this phase is one of the most common impurities for PZT prepared by this method [16, 17]. Generally, it has been found that drying films in an inert atmosphere can promote formation of the oxygen-deficient phase to promote perovksite formation; additionally, using a sol-gel containing an excess of Pb^{2+} — as is the case in this study — can also favour it.

Studies by Szafraniak-Wiza *et al.* have been carried out into the growth of PZT nanoislands: these structures may be obtained by annealing very thin films of PZT with sufficient thermal energy to activate reorganisation of the material — this process is driven by minimisation of the surface free energy at the PZT–substrate interface [18, 19]. Although such nanostructures are potentially useful for a number of applications, full surface coverage of ZnO by PZT is desired in this work; as such, careful control of both the annealing temperature and time is required to prevent the break-up of the thin PZT layers. Island formation has been studied for PZT films on $SrTiO_3$ annealed between 600 – 1100 °C for times between 5 minutes and 10 hours and was observed to produce irregular structures at lower temperatures (650 °C), whereas more ordered structures were observed at higher temperatures ($\geq$ 800 °C) [20]. The annealing temperatures used in this work are much lower than those reported for the formation of nanoislands, but

[2]This spin-coating regime is noticeably different to that used for ZnO deposition: due to the different fluid properties of the respective sol-gels (such as viscosity), different regimes are required to deposit thin-films from these solutions.

to this point no studies have been carried out on nanoisland formation in ITO/PZT or ZnO/PZT heterostructures. Therefore, care must taken to ensure that the film does not break up: to address this, this study aims to achieve crystallisation of PZT in the desired phase whilst minimising the thermal energy input through use of lower temperatures and shorter annealing times.

2.2.4 P3HT Processing

P3HT was used as the donor material for oxide:polymer bilayer hPV devices. The processing conditions, particularly the solvent used to cast P3HT, are important in determining the morphological properties of the polymer thin-films, which also have a significant influence on the transport properties. Although no comprehensive study has been carried out to determine the best solvent to use in the fabrication of ZnO/P3HT hPV devices, there has been much research dedicated to P3HT processing for organic field-effect transistors (OFETs) and for the P3HT:PCBM blend system used in OPVs. In a study by Chang *et al.* into the effect of casting solvent on P3HT OFET mobility, a range of different solvents with different boiling points (BP) were used: chloroform (BP = 61.2 °C); thiophene (BP = 84 °C); xylene (BP = 138.5 °C); cyclohexylbenzene (CHB, BP = 239 °C); 1,2,4–trichlorobenzene (TCB, BP = 214.4 °C) [21]. It was found that, whilst P3HT easily dissolved in chloroform, thiophene, and TCB, its solubility is relatively poor in xylene and TCB and constant heating is required to prevent gelation of solution and formation of aggregates.

Using spin-coating, higher BP solvents such as xylene and TCB have been shown to produce OFETs with higher mobilities: lower BP solvents tend to evaporate too quickly during the spinning process, preventing crystallisation and therefore reducing the device mobilities. Films derived from TCB solutions produced devices with the best mobilities, followed by xylene: xylene produces slightly lower quality (less uniform) films due to the effects of polymer aggregation. Similar trends have been reproduced in a number of separate studies [22].

P3HT thin-films in this study were deposited by spin-coating from either xylene or chlorobenzene solutions: xylene was chosen due to its high BP and high crystallinity of the resulting thin-films of lower molecular weight polymer (Merck, M_w 60 kg mol^{-1}), whereas CB was found to be more suited to those with higher molecular weights (Department of Chemistry, M_w 84.7 kg mol^{-1} [23]). To create a polymer solution, P3HT was weighed and placed in a glass vial, followed by solvent addition using a micropipette. In this work, solutions were made with concentrations ranging from 5 – 45 mg ml^{-1}.

For processing the xylene solutions, the vials were then heated to 85 °C on a hotplate for 1 hour and the solutions kept heated throughout the whole deposition process to ensure full dissolution of the polymer. For CB solutions, the polymer was stirred and heated at 55 °C for 12 hours. Prior to deposition, the solution was heated to 85 °C for 30 minutes and held at this temperature throughout the process. For spin-coating, a substrate was loaded into a Chemat KW–4A spin-coater and the substrate covered with the hot solution using a micropipette, followed by spinning at 1500 rpm for 30 s.

2.3 Physical and Strucutral Characterisation

The films produced in this work were subjected to a number of structural characterisation techniques to evaluate key properties including the thickness (profilometry), crystal structure (X-ray diffraction), and microstructure (AFM and TEM). Brief outlines of these techniques and the instrumental setups used are given below.

2.3.1 Profilometry

Film thickness may be evaluated using a range of methods including optical or physical means. Contact profilometry falls into the latter category and was used to measure the thickness of both oxide and polymer thin-films. In this study a Veeco Dektak 150 was used to evaluate film thickness: this apparatus is equipped with a diamond stylus (tip radius of 5 μm) which is lowered until it makes contact with the surface with a constant force (in this case, between 1.0 and 10.0 mg). The stylus is then moved in a straight line across the surface for a specified distance, tracking changes in the stylus height. If the stylus is dragged across a step in the film, the relative change in step height can be measured by evaluating the film heights at the top and bottom of the step. To measure film thickness, a section of the underlying substrate must be exposed to create such step; additionally, the two regions must be sufficiently smooth to allow for an accurate assessment of the change in heights.

To prepare films for contact profilometry, a step in the film between the sample material and substrate must be created. In this study, this was carried out in three different ways depending on the sample material: *i)* creation of a scratch in a deposited film by using a scalpel blade — this is most effective for polymer films which are mechanically less stable than oxides; *ii)* etching the top layer of a sample using a suitable orthogonal etching agent with respect to the substrate — for P3HT, a solvent such as toluene would normally be effective, whilst 2 M NaOH or HCl could be used to etch ZnO without damaging the underlying glass or ITO; *iii)* for films which are more mechanically stable, it is possible to create a steps during processing - in the case of spin-coating, a small

area of the substrate may be masked by using Kapton tape prior to film deposition. This creates a region of bare substrate which can be used as a reference area for profilometry measurements. It should be noted that the presence of the masking agent can affect the spin-coating process, leading to build-up of material at the tape edge and can affect the removal of fluid from the surface. As such, the film thickness at this interface will not be representative of the film thickness of the unmasked film; however, by using a longer scan across the deposited material region of the substrate (*i.e.* to a large distance from the masked area) it is possible to acquire an acceptable measure of the film thickness, although the uncertainty in the final values will be greater than for films which do not use this method.

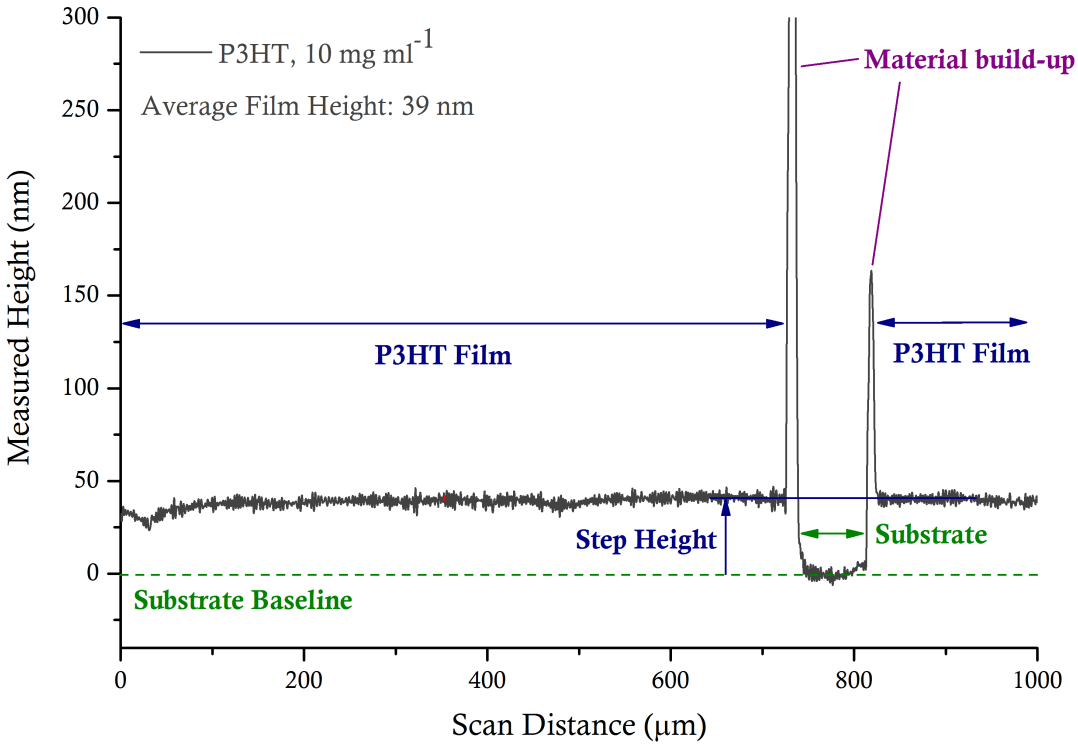

Figure 2.2 – Film height calculation for a P3HT film spin-coated from a 10 mg ml^{-1} solution (using chlorobenzene as a solvent) on glass. The step in the film was created by using a scalpel blade. The data were acquired for a scan length of 1000 μm at a velocity of 20 μm s^{-1}; a constant contact force of 1.5 mg was used. The substrate region (shown in green) was used as a reference area to level the data and subsequently set to zero-height; the step height was then calculated from the two remaining P3HT material regions (shown in blue). The material build-up regions either side of the reference area occurred during the scratching process and were excluded from the step height calculation. The measurement yielded an average film height of 39 nm (with a standard deviation of 3 nm).

To evaluate film thickness, measurements were carried out on a minimum of two separate samples; for each sample, line profiles were acquired in at least 6 different areas

across the step region. To calculate the average film height for a single scan, the line profiles were levelled by using a flat area of the sample — usually the substrate — as a reference to correct for sample tilt and scanner bow effects; the reference area is then set to zero height and the step height of the film calculated. A sample calculation of film step height calculation is given in Figure 2.2.

2.3.2 X-Ray Diffraction

X-ray diffraction (XRD) has become one of the primary analytical techniques in solid-state chemistry. It allows for non-destructive analysis of a material's crystal structure, provides data from which a large amount of structural information may be derived for a given material, and is extremely versatile, both in terms of the materials that may be studied by this technique and in the different types of measurement that may be carried out. In this study, XRD was used to verify the crystallisation of materials in the correct phase, to assess preferred crystallographic orientation of the films, and the approximate crystallite size.

To carry out XRD, a crystalline sample is irradiated with monochromated X-rays and the angles and intensities of the diffracted beam measured. The technique is underpinned by Bragg's Law, given in Equation 2.1:

$$n\lambda = 2d_{hkl}\ \sin\theta_{hkl} \tag{2.1}$$

where λ is the wavelength of incident radiation; d_{hkl} is the separation between lattice planes; $2sin\theta_{hkl}$ is the scattering angle at which the intensity maximum is observed [24]. When a sample with an ordered structure is irradiated with X-rays, the incident radiation interacts with electrons in the sample, leading to elastic diffraction of the beam. An ordered sample contains defined sets of lattice planes, described by Miller indices in the form ($h\ k\ l$), which have a defined interplanar d-spacing: as these spacings are of a similar order to the wavelength of the inbound radiation, the planes may act as a grating leading to diffraction of the X-ray beam. Whilst most of the diffracted radiation cancels through destructive interference, in specific directions the interference is constructive, leading to maxima in the diffracted beam intensity at certain angles. A diffractometer therefore measures the diffracted beam intensity with changing angular dependence, usually expressed in terms of 2θ. As each different ($h\ k\ l$) lattice plane present in a crystalline structure satisfies Bragg's Law at a specific value of θ, each structure will generate a unique diffraction pattern and the d-spacing information acquired allows for indexing of the structure and determination of lattice parameters [25].

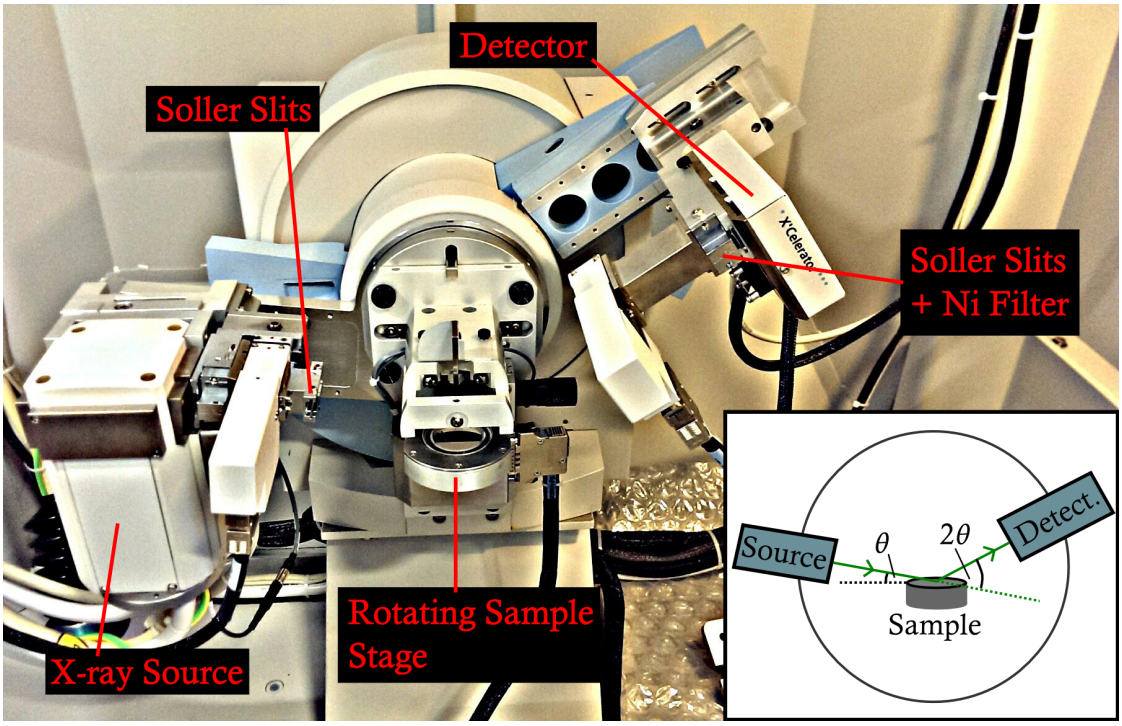

Figure 2.3 – Photograph of the Panalytical X'Pert Pro setup used in this work. **Inset**: schematic representation of the angular relationship between the X-ray source and the detector. Based on [26].

XRD patterns were obtained using two instruments: a Bruker D2 Phaser and a Panalytical X'Pert Pro (shown in Figure 2.3). Both instruments are equipped with a Cu X-ray source: an accelerated beam of electrons is fired at the metal, leading to ionisation of $1s$ electrons. To fill this core hole, either a $2p \rightarrow 1s$ transition will occur, generating Kα_1 (1.5405 Å) and Kα_2 (1.5444 Å) radiation[3]; a $3p \rightarrow 1s$ transition generates K$_\beta$ radiation which is filtered using a Ni filter. The Bruker D2 Phaser generates X-rays using a tension of 30 kV and a current of 10 mA; all samples were acquired using a step-size of 0.033° 2θ and a time-per-step of 0.7 s. The Panalytical X'pert Pro operates at a tension of 40 kV and 40 mA, and is equipped with 0.04 rad Soller slits to minimise background radiation. Data were acquired using a step-size of 0.033° 2θ. Thin-film samples were mounted and levelled using a hand-press, and subsequently rotated during the measurement at a speed of 60 rpm. Powder samples were loaded onto a sample holder, levelled with a clean glass side, and not spun during measurement.

Scherrer analysis was used to estimate crystallite sizes in the thin-films. The Scherrer

[3]Kα_1 and Kα_2 (with wavelengths separated by ~ 0.004 Å) due to the fact that the $2p$ electron may be either a spin-$^1/_2$ or a spin-$^3/_2$

Equation describes the size-dependent contributions to diffraction peak broadening from the crystallites [27] and is given as follows.

$$d = \frac{K\lambda}{(\beta_{meas} - \beta_{ins})cos\theta} \tag{2.2}$$

where d is the crystallite size (in Å), K a shape factor (this varies from $\sim 0.7 - 1.3$; where detailed crystallite information is not known, 0.9 is usually a good approximation [28]), λ the X-ray wavelength, β_{meas} the FWHM of the sample peak (in radians), β_{ins} the measured peak broadening due to the instrument, and θ the Bragg angle of the peak. β_{ins} can be obtained by using a single crystal standard, such as Si — for a perfect crystal, the peak broadening due to the crystallite should tend to 0, thus the peak broadening observed in the standard can be assumed to arise solely from the instrumental setup. There are two main caveats associated with Scherrer calculation: firstly, that the method is generally limited to particles smaller than 100 nm, and secondly that it provides a lower-bound estimate for the crystallite size and that further peak broadening contributions, such as strain, may not be taken into account [29].

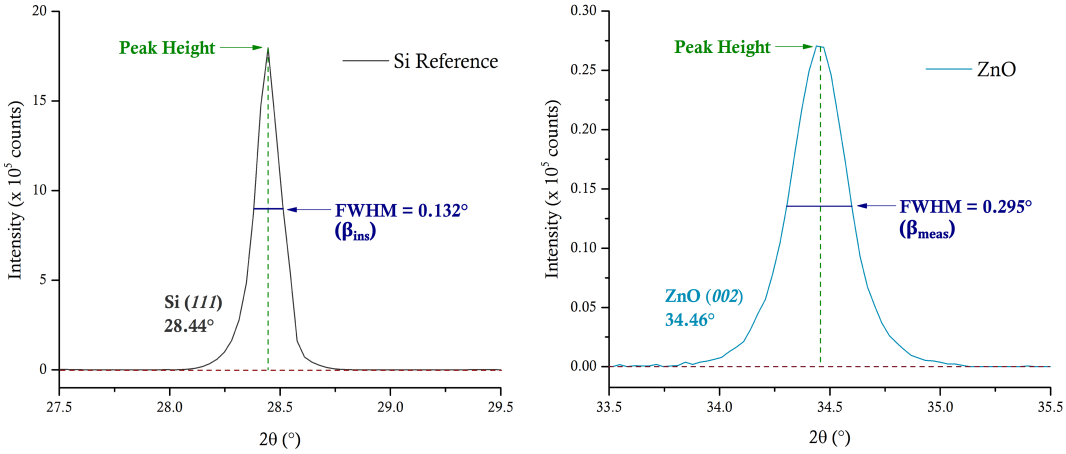

Figure 2.4 – Full width at half maximum (FWHM) calculation for Scherrer analysis. The XRD pattern on the left shows a single crystal Si (*111*) peak used to determine the instrumental broadening (β_{ins}) of the apparatus. The right-hand XRD pattern was acquired for a sol-gel-derived ZnO film on glass and displays the (*002*) peak of the material. Background modelling was carried out using a Sonneveld-Visser algorithm prior to calculation of the FWHM. Here, the (*002*)-orientated ZnO crystallite size was determined to be 51 nm, using a K value of 0.9.

In this work, Scherrer measurements were conducted as follows: to calculate β_{ins}, a diffraction pattern for a Si standard was acquired using the same instrumental setup and scan parameters (step size and per-step scan time). For ZnO, the Si (*111*) peak was used as this falls at a 2θ value of 28.44° which lies close to the (*100*), (*002*), and (*101*) peaks of

ZnO. Calculation of the FWHM for the peaks of both the standard and the sample was carried out using the Panalytical X'pert Software suite by applying a Sonneveld-Visser background subtraction to the raw XRD data; this was followed by a measurement of the peak height to determine the half maximum position and, subsequently, the FWHM. An example of this peak measurement is given in Figure 2.4. The crystallite size values quoted in this study were averaged between at least 3 samples.

2.3.3 Transmission Electron Microscopy

Transmission electron microscopy (TEM) can be used to examine the cross-sectional microstructure of a thin-film with very high resolution — in this work, it was used to identify the structure of ZnO and ZnO–PZT thin-films and to help elucidate the growth mechanisms of these materials. In TEM, a beam of electrons is accelerated towards a sample. As the electrons interact with the material, an image is produced which can be detected by the instrument [30]. Its operation is analogous to that of an optical light microscope; however, given the small de Broglie wavelength of the electrons, much higher resolution is possible. Sample preparation is of vital importance in TEM as an extremely thin sample is required, typically on the order of $\sim$ 100 nm: in this work, cross-sections were cut out of bulk thin-films using the focussed ion beam lift-out method [31].

The main component of a transmission electron microscope is the column, illustrated in Figure 2.5: after loading the sample into the microscope, the column is pumped down to high vacuum. The electron beam is generated by applying an accelerating voltage (on the order of 100 – 200 kV) between a metal tip (usually tungsten) and an anode. The beam is passed through a set of magnetic lenses — the condenser, the objective, and the projector. The condenser is a set of lenses and apertures used to reduce the beam diameter and offers effective control of the spot size and beam convergence; additionally, this also controls the fraction of the beam incident on the specimen which can have an impact on the intensity of illumination. The beam then passes into the objective system which generates an initial (inverted) image of the sample: as the quality of the final image depends on the quality of the initial image, the role of the objective system in imaging is crucial. The projector system then allows magnification of the final image which is subsequently captured using a phosphor screen or a CCD detector.

Image contrast in TEM depends on the interaction between the electron beam and the sample: the electron beam may be unaffected by the sample, whilst in other cases scattering (both elastic and inelastic) may occur. The effective cross-section of an atom depends on the square of its radius, thus heavier atoms scatter the electron beam moreso than lighter ones, leading to distinct regional contrast in the final image — imaging in this mode is referred to as bright field. It should also be noted that sample thickness

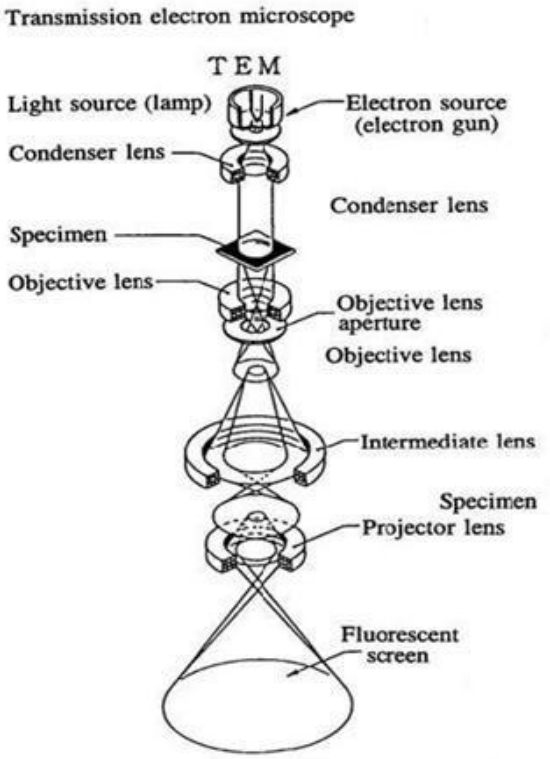

Figure 2.5 – Schematic diagram of a typical TEM column, reproduced from the JEOL 2000FX handbook.

can also play a role in contrast (thicker areas of a sample will create more scattering events and therefore will appear darker), and thus can add an extra layer of complexity to image analysis. Bright field imaging was considered to be well suited to this work, especially given the differences in atomic mass between Pb and Zn. The TEM images in this work were acquired using an FEI Titan 80/300 with accelerating voltages of 300 kV. After acquisition, the images were processed using the programme Digital Micrograph.

2.3.4 Atomic Force Microscopy

Atomic force microscopy (AFM) is a powerful, non-destructive technique which can be used to image surface structure with very high resolution. In this regard, it is comparable to scanning electron microscopy (SEM); however, whilst SEM provides a two-dimensional image with height-related contrast and excellent depth-of-field, AFM can generate a true three-dimensional map of a surface including detailed height information — this can subsequently be used in quantitative surface analysis [32]. Additionally, there is a myriad of different AFM techniques which may be used in analysis of different surface

properties (*e.g.* conductive AFM to measure local current-voltage characteristics [33]), or in functionalisation of a surface (modified AFMs have been used in nanolithography [34]). In this work, tapping mode (intermittent contact) AFM was used to characterise the surfaces of ZnO and ZnO–P3HT thin-films, generating topography (height), amplitude error, and phase offset maps. In Section 4.4.1, quantitative analysis of AFM data was used extensively to describe the surface structure of these films. These studies were carried out using a Bruker Multimode Nanoscope AFM.

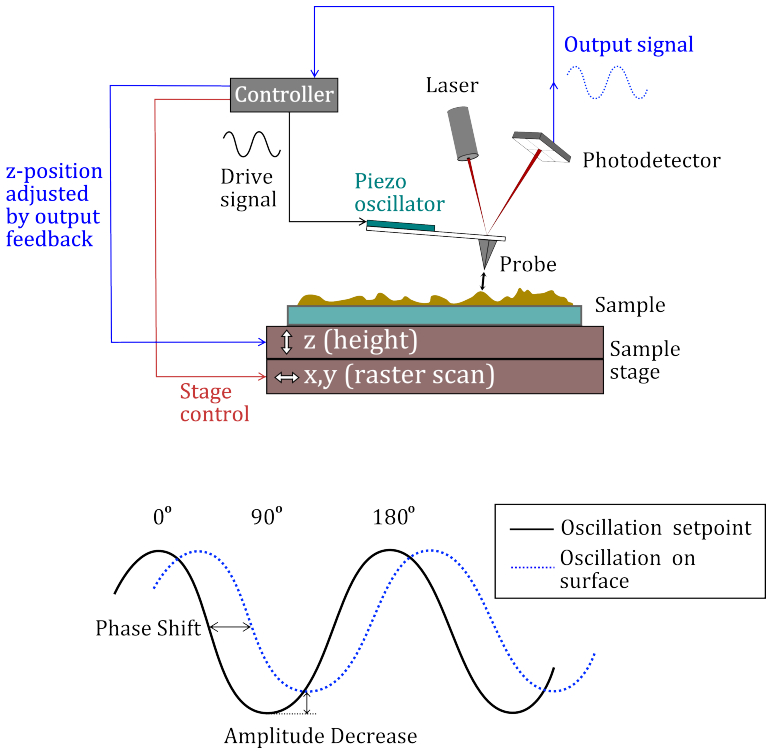

Figure 2.6 – **Top**: a schematic diagram of a typical tapping mode AFM setup: the probe is oscillated at a set amplitude, whilst the sample is rastered in the x-y directions underneath it. The probe makes intermittent contact with the sample resulting in oscillation in the cantilever deflection; by measuring this against the input oscillation, the forces acting on the probe may be measured [32]. **Bottom**: representation of the amplitude offset caused by interaction of the vibrating probe when engaged with a sample.

A representation of an AFM operating in tapping mode is given in Figure 2.6. The instrument in this study is a sample scanning microscope, *i.e.* the AFM probe is fixed whilst the sample is mounted on a moving stage: the high-precision control in x, y, and z directions required by the technique is achieved by changing the applied voltage across piezoelectric components [35]. The AFM probes used in this work (Bruker OTESPA, resonance frequency 300 kHz) consist of a rectangular, Sb-doped-Si cantilever which posses a sharp tip with a length of 15 – 20 μm and a radius of 8 nm. In this mode of

operation, the cantilever oscillates at just below its resonant frequency with the tip making intermittent contact with the surface. Interactions between the tip and the sample surface dampen the oscillation amplitude; consequently, the AFM feedback mechanisms adjust the height of the stage to attempt to maintain a constant oscillation amplitude, thus providing a measure of sample height. Deflection of the probe is measured using a laser which reflects off the cantilever into a 4-sector photodetector, thus allowing detection of both vertical and lateral deflection. A more in-depth description of atomic force microscope setups is given in [32].

In addition to the height maps generated in tapping mode AFM, phase offset images are also often acquired. Due to the attractive forces between the tip and the sample, contact between the two causes an offset in the phase of the oscillation (illustrated in Figure 2.6). The phase shift depends on a number of factors, predominantly the adhesiveness of a surface (as well as height contributions) [36]; as such, different materials can exhibit different offsets in phase depending on their physical properties, and biphasic systems — especially in the case of soft materials — often show significant phase contrast. Due to the height contribution to the phase, deriving quantitative data from phase images can be difficult; however, it can be useful for identifying phase separation in materials systems.

In this study, 0.75 x 0.75 (512 lines), 2 x 2 (512 lines), and 15 x 15 μm (1024 lines) scans were acquired using scan rates between 0.5 and 1 Hz. Cantilever tuning was carried out automatically using the AFM software; typically, images were acquired using a drive amplitude of around 75 mV and an amplitude setpoint of 180 mV. Images were processed using the Gwyddion software suite [37]. The images in this work have been corrected for background effects using a polynomial subtraction and line corrected. Additionally, surface reconstruction to take into account tip effects were applied to the images using the tip parameters supplied by the manufacturer.

Film roughness parameters were derived from all AFM height scans acquired in this study. Roughness is a useful quantity which is routinely derived from AFM data and can often be correlated with material properties: for example, increased roughening of a surface can lead to an increase in light scattering. The roughness parameters R_a (arithmetic) and R_{RMS} (root-mean-squared) for the film series were derived from the Z-height scans. These describe the deviation of the height of a film from a mean plane and are given by:

$$R_a = \frac{1}{n}\sum_{i=1}^{n} |y_i| \tag{2.3}$$

$$R_{RMS} = \sqrt{\frac{1}{n}\sum_{i=1}^{n} {y_i}^2} \tag{2.4}$$

where y_i is the height of the i^{th} point relative to the mean line and n the number of points [32]. These two measures of roughness are fairly similar although R_{RMS} is always larger than R_a for a given sample; R_{RMS} is also more sensitive to outlying data points.

2.4 Compositional Characterisation

The composition of ZnO–PZT films was probed in both the surface and bulk regions by using X-ray photoelectron spectroscopy (XPS) and time-of-flight secondary ion mass spectrometry (ToF-SIMS) respectively. As it is harder to assume direct control of many processing variables in solution processing *cf.* vacuum deposition, these techniques were employed to monitor the uniformity of composition across the samples made in this work. Additionally, such characterisation can aid in the elucidation of material growth mechanisms.

2.4.1 X-Ray Photoelectron Spectroscopy

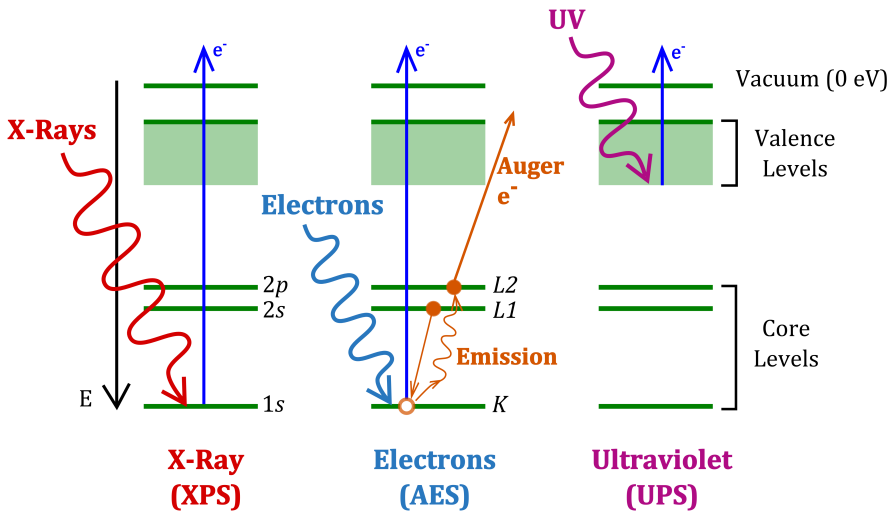

Figure 2.7 – Energy-level representations for the emission of electrons in X-ray, Auger, and Ultraviolet photoelectron spectroscopy. Diagram drawn with reference to [38].

Photoelectron spectroscopy (PES) is an important tool in surface analysis for determining material characteristics including elemental composition, oxidation state, and

electronic properties. In this work, XPS was used to determine the surface composition of ZnO–PZT thin-films; whilst ultraviolet photoelectron spectroscopy (UPS) was also considered to probe the surface electronic properties of these films, it was found that the PZT-modified films built up excessive amounts of surface charge, thus leading to significant distortion of results.

The technique is based on the photoelectric effect — when a material absorbs incident high energy radiation such as X-rays or UV light, it ejects electrons from the surface (also described as photoelectrons) which are detected in PES. The kinetic energy (E_{kin}) of these photoelectrons can be related to the binding energy of the atoms from whence they came by the application of the energy conservation principle:

$$E_{kin} = h\nu - E_B + \phi \tag{2.5}$$

where $h\nu$ is the photon energy, E_B the binding energy of the electron in the solid, and ϕ is the Fermi energy of the material[4]. The two main variants of PES are XPS, mainly used for probing chemical composition with hard X-rays, and UPS, which is used to characterise the valence levels of a material using ultraviolet radiation. Auger electron spectroscopy (AES), is also used extensively as a complementary technique to XPS — Auger electrons[5] give similar information to photoelectrons generated in XPS, but the smaller spot size allows identification of fine surface features [39]. A representation of the mechanisms of electron ejection in XPS, AES, and UPS is given in Figure 2.7.

PES is used to probe the top 1 – 12 nm of a sample; whilst the interaction volume created by the incident radiation may be on the order of micrometres, only electrons at the surface will escape to vacuum — those ejected deeper within the material are trapped before reaching the surfac. Whilst PES is a surface technique, depth profiling may be carried out by etching the material to create a cross-section which may then be analysed. Traditionally, PES is a technique carried out under ultra-high vacuum (UHV, $p < 10^{-7}$ mbar) as the detector is set at some distance from the sample and the presence of gases in the chamber will lead to further scattering of the photoelectrons. However, recent developments have seen the manufacture of PES systems which are able to operate under ambient conditions — this is particularly useful for studying materials which are processed under ambient conditions as UHV may cause changes in the surface such as

[4] E_B is measured with respect to the Fermi level of the material; in practice, the sample is electrically connected to the spectrometer, thus it is measured with respect to the Fermi level of the spectrometer.

[5] When a core electron is ionised from an atom, an electron from a higher lying shell drops into the hole, releasing radiation with characteristic energy. Auger electrons are generated when this emitted radiation ionises a second electron from the atom.

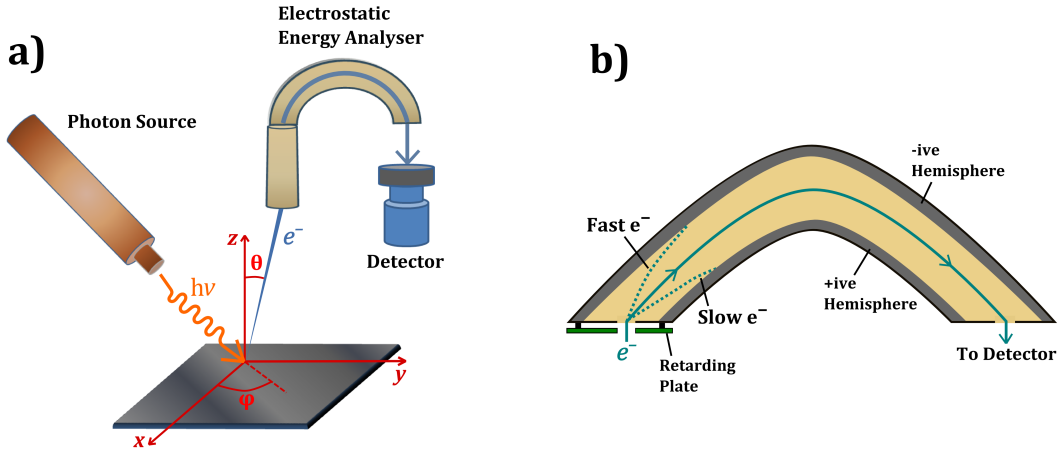

Figure 2.8 – a) A typical angle-resolved photoelectron spectroscopy setup; b) diagram of an electrostatic energy analyser, used in the collection and kinetic energy measurement of photoelectrons.

removal of adsorbate or other species within the material. The samples are prepared for PES by mounting onto a metal stub with a small square of carbon tape and creating a conductive pathway from the film to the stub using silver paint. Prior to analysis, samples for PES were kept in the dark in a dry N_2 atmosphere.

XPS is an extremely important surface analysis technique in materials science. By analysing a sample over a wide range of energies, characteristic peaks for the major components of a material can be identified and the relative atomic ratios calculated by fitting the peak areas, thus giving an accurate measure of surface composition. Higher resolution scans focussing on characteristic atomic peaks allows for analysis of their chemical environments and can yield information such as oxidation state and the nature of chemical bonding: for example, in analysing the O 1s peaks for a ZnO sample, the resulting peaks often contain several components (in the case of oxygen, species such as oxide (–O) and hydroxyl (–OH) bonds may form), each possessing a slightly different binding energy [40]. These components can be fit by using Gaussian–Lorentzian models, and the relative ratios of each component can be determined, provided the resolution of the instrument is high enough.

In this study, XPS was carried out using Mg Kα radiation ($h\nu$ = 1253.6 eV) under a vacuum of 4 $\times$ 10^{-10} mbar. Photoelectrons were detected using a semi-spherical channeltron with a pass energy of 5 eV. Data fitting and analysis was carried out using CasaXPS software: to calculate the elemental ratios from the full XPS spectrum, the spectrum was calibrated and fitted with a background; subsequently, the elemental peaks were assigned based on known reference core lines — and example of this is presented in Figure 2.9. Composition was obtained by calculating the peak areas obtained by

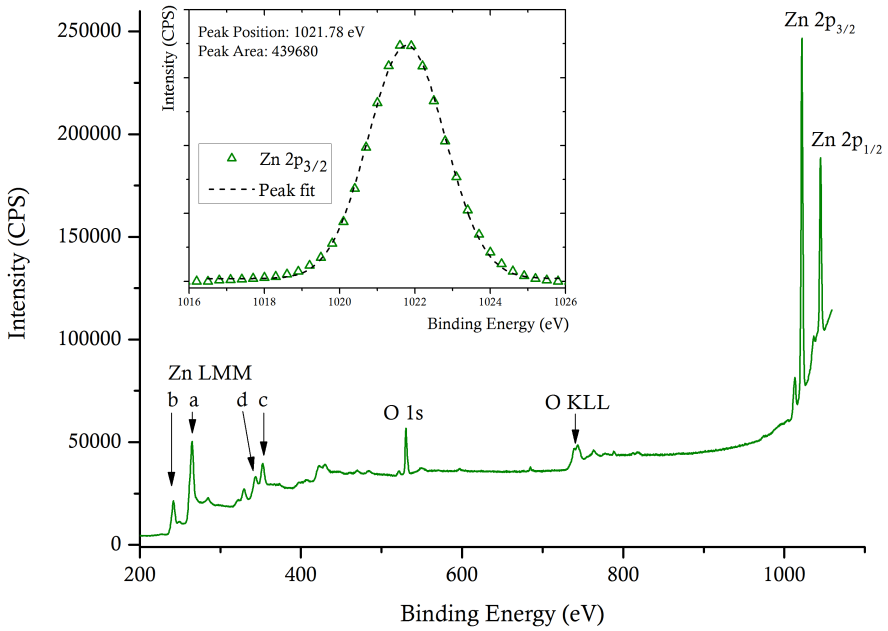

Figure 2.9 – A wide scan X-ray photoelectron energy spectrum acquired for a spray-pyrolysed ZnO film on ITO using Mg K_α radiation. Characteristic O and Zn peaks have been assigned. **Inset**: Gaussian peak fitting for the Zn $2p_{3/2}$ core line — note that this fitting has been carried out on background subtracted data.

Gaussian–Lorentzian fitting for the different elemental components, and correcting the values using known atomic sensitivity factors. It should be noted that the elemental ratios derived by this method are relative rather than absolute measures of compositon; however, comparison of elemental ratios can be extremely useful in the analysis of oxide materials.

2.4.2 Time-of-Flight Secondary Ion Mass Spectrometry

ToF-SIMS is a technique for compositional analysis which uses an ion beam to remove atoms from the surface of a sample, followed by their extraction towards a detector: as such, this is a destructive technique. Additionally, the apparatus requires ultra-high vacuum conditions to increase the mean free path of the liberated ions and to prevent loss of material through collisions with foreign species in the analysis chamber. Here, ToF-SIMS was used to analyse the composition of ZnO–PZT thin-films as a function of depth. Whilst ToF-SIMS does not provide an absolute quantitative measure of the sample composition, the changes in composition of an elemental signal through the sample can provide a lot of information on film structure and growth.

ToF-SIMS, also known as static SIMS, relies on the principle that ions with the same energy but different mass travel at different velocities; the mass of the ions generated from

the sample is measured by the time taken for an ion to travel from the sample surface to the detector — the time-of-flight in this work was measured from the short pulse of the primary ion beam (< 1 ns) [41, 42]. This gives an extremely accurate mass resolution as well as detection limits in the parts-per-million range; additionally, the technique can offer sub-micron lateral resolution if tightly focussed ion beams are used [43].

For this study, ZnO and PZT thin-films were grown on Si wafers and depth profiling was carried out using an Ion-Tof GmbH TOF.SIMS^5 instrument. A dual-beam setup was employed for depth profiling: this uses a short pulse Cs^+ sputtering beam and a 25 keV Bi^+ analytical beam, both of which are angled at 45° to the substrate are pulsed in an alternating sequence during depth profile analysis — this allows for acquisition of data with nanometre-scale depth resolution. Additionally, a low energy electron beam is directed at the target area to prevent a build up of charge on the sample surface. In the mode of operation used in this work, the sputtering beam erodes the sample to generate a crater with the analytical beam focussed in the centre to avoid analysis of the edges. Generally, this method generates secondary CsM^+ ions, although monoatomic ions can also be generated; unless otherwise stated, the elemental signals acquired in this work were derived from the Cs-bonded species. After sputtering, an extraction field of 2 kV was applied to draw the ions into the ToF analyser; these are subsequently focussed towards an ion mirror which reflects the ions downwards into the detector.

2.5 Optoelectronic Characterisation

Optical characterisation methods were used in this study to probe characteristics of ZnO–PZT thin-films relevant to their operation in hPV devices: UV-vis spectroscopy was used to calculate ZnO band gaps and to evaluate film transparency, whereas photoluminescence (PL) and transient absorption spectroscopy (TAS) were used to analyse charge dynamics at the ZnO–PZT–P3HT interface.

2.5.1 UV-visible Transmission Spectroscopy

Ultraviolet–visible spectroscopy (UV–vis) was used in this study to calculate material band gaps, estimate film thickness, and determine optical transmission for both oxide and polymer materials. This was carried out using a Bentham 2000 Series Spectrometer which passes a beam from a halogen light source through a pair of diffraction gratings to achieve monochromation. The beam is subsequently collimated to achieve a defined spot-size and directed through the sample towards a Si photodetector which tracks changes in the incoming light intensity. Optical transmission (expressed in T%) is calculated from a background scan which measures the beam signal strength over the same wavelength

range in the absence of a sample. Transmission of light is affected by a number of factors such as reflection from a material's surface, scattering or reflection of light at interfaces, scattering of light due to charge carriers, and electronic excitation [44].

The transmission of a material is related to the absorbance by the Beer-Lambert law. For a transmission percentage, *T(%)*, the absorbance (α) is given:

$$T(\%) = 100\ \frac{I}{I_0} = 100\ e^{-\sigma l N} \tag{2.6}$$

$$\alpha = -\left(ln\ \frac{I}{I_0}\right) \tag{2.7}$$

I/I_0 is the ratio of the transmitted intensity to the incident intensity of radiation, σ an absorption and scattering cross-section, l the path length, and N the concentration of the attenuating medium [45]. It should be noted that absorbance is sometimes calculated in decibels (dB) using a base 10 relation which can sometimes lead to confusion.

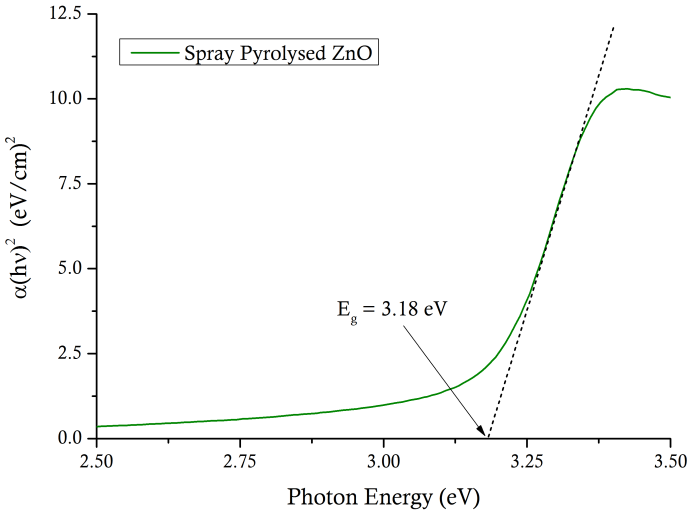

Figure 2.10 – Tauc plot for calculation of the direct band gap of a 60 nm-thick film of spray-pyrolysed ZnO on glass.

The band gap of ZnO was calculated using the Tauc method [46]: for a direct band gap material such as ZnO [47], the absorbance is approximately related to the band gap (E_g) by:

$$\alpha = \frac{A^*\sqrt{h\nu - E_g}}{h\nu} \tag{2.8}$$

A^* is a material-dependent factor. By plotting $(\alpha h\nu)^2$ vs hν, the band gap can be estimated by extrapolating the slope of the curve to the x-axis, with the intercept equal to E_g.

2.5.1.1 Thickness Evaluation

The thickness of spray-pyrolysed ZnO thin-films was evaluated from their UV-vis absorption spectra. The absorption coefficient, γ, of a material is related to its transmittance by [48]:

$$\gamma t = -ln\left(\frac{T}{1-R}\right) \tag{2.9}$$

where t is the material thickness and R the reflectance. Given the very low thicknesses of ZnO in this work, the changes in reflectance were assumed to be negligible within this range ($<$ 100 nm), thus yielding the relation:

$$t = \frac{\alpha(\lambda)}{\gamma(\lambda)} \tag{2.10}$$

In this work, γ was measured using ellipsometry (evaluated at 368 nm, the band-edge of ZnO), as well as the thickness. The thickness values for these films derived from the UV-vis absorbance were in agreement with those obtained from ellipsometry; subsequent profilometry measurements also yielded similar values. Whilst only valid within a small range of thicknesses, this method was used to measure the thickness distribution of thin-films deposited using the same processing conditions and routine (*i.e.* towards a single target thickness).

2.5.2 Photoluminescence Spectroscopy

Photoluminescence (PL) spectroscopy is a versatile technique which can be used to measure the electronic properties of materials through photoexcitation and subsequent observation of radiative decay. In this study, PL was used in two ways: firstly to provide a qualitative comparison between the defect signatures in ZnO (for both unmodified and PZT-modified films); secondly, charge generation in D–A polymer:oxide systems may be probed by exciting the donor polymer and monitoring the subsequent PL emission — changes in PL emission can be related to changes in exciton quenching dynamics.

Photoexcitation of a material from a singlet ground state produces an excited state. The decay of the excited state may proceed by several pathways: vibrational (non-emissive) relaxation, radiative decay from a singlet excited state (fluorescence), and radiative decay from a triplet excited state (phosphorescence). Additionally, resonant

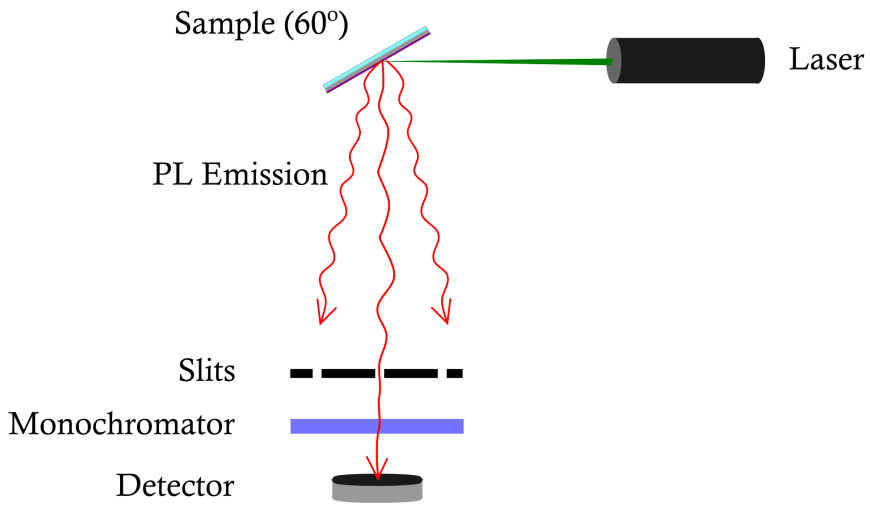

Figure 2.11 – Representation of a typical PL emission spectroscopy setup.

radiation may also occur in which a photon of a particular wavelength is absorbed and re-emitted on an extremely short (nanosecond) timescale. As the energy of the emission is characteristic of the energy level of the excited state, this allows for quantification of the electronic properties of materials if data is acquired using high resolution apparatus [49]. In this work, two PL experiments were carried out as follows:

Probing Oxide Defects: in ZnO and ZnO–PZT thin-films, the defects in ZnO were probed by exciting the ZnO with an above-band gap energy of 320 nm (3.87 eV) and PL emission scanned in the range 350 – 650 nm. In semiconductors, the most intense primary emission band corresponds to emission from the conduction band of the material, whereas emission at below band gap energies is generally indicative of material defects. Although the experiments used were not able to provide quantitative data on the ZnO defects, qualitative comparison between ZnO and ZnO–PZT thin-films yields information on the relative defect density, as well as the general location of defect levels in the mid-gap [50].

Measuring Exciton Quenching: for films with a donor–acceptor heterojunction, it is possible to probe charge generation dynamics in the donor material using PL. In this work, the effect of PZT modification on charge generation in P3HT was probed by exciting the P3HT (550 nm, 2.25 eV) and scanning for emission in the range 575 – 850 nm. On excitation of the polymer, excitons are generated which may decay radiatively; however, if excitons dissociate into their respective polarons before undergoing radiative decay, no emission occurs. Therefore, a decrease in PL intensity from a reference (neat) P3HT

film indicates a degree of exciton quenching and thus charge generation in a film [51].

A typical representation of a PL instrumental apparatus is given in Figure 2.11. In this work, an Horiba Fluorolog-3 equipped with a HgXe probe source was used to measure films for both of the aforementioned experiments. After acquisition of the raw data, corrections for film absorption were made by measuring the absorbance of each thin-film at the excitation wavelength of the film using UV-vis spectroscopy.

2.5.3 Transient Absorption Spectroscopy

Transient absorption spectroscopy (TAS) is a powerful technique for probing charge dynamics in materials down to the picosecond regime and has become an important tool for analysing and understanding OPV operation. TAS is a time-resolved pump–probe technique in which the sample is irradiated with a short burst of monochromatic light (pump) and a second pulse at a different wavelength (probe) is used for measuring the absorption of the sample after excitation. Excitation of the P3HT in this work generates excitons which may dissociate at the donor–acceptor interface to yield free charge polarons. By probing the population of free hole polarons in the P3HT over time, their decay can be measured which yields quantitative information on recombination in these materials — the faster the polaron decay signal, the greater the degree of free charge recombination. It is believed that signals from charge-transfer states and free hole polarons are indistinguishable, and thus the polaron lifetime takes into account contributions from both geminate and non-geminate recombination mechanisms [52].

In this work ZnO–PZT–P3HT films were excited using 1 ns laser pulses (at $\sim 30\ \mu\text{J cm}^{-2}$) with a pump wavelength of 510 nm. A probe wavelength of 980 nm was selected to detect hole polarons in the P3HT [53], generated using a monochromated quartz halogen lamp.

Usually, TAS data is plotted as change in absorbance (or optical density, ΔOD), calculated using the Beer-Lambert law given in Equation 2.6. The number of polarons per cm^2 (n_p) present in the active layer after excitation is given by Equation 2.11:

$$n_p = \frac{\Delta OD}{\epsilon\, 1000}\, N_A \tag{2.11}$$

where N_A is Avogadro's number. To calculate the efficiency of excitation (η, *i.e.* the ratio of generated polarons to incident photons (n_i), ${}^{n_p}/_{n_i}$:

$$n_i = \frac{E\lambda_{ex}}{hc} \tag{2.12}$$

$$\eta = \frac{n_p}{n_i} = \frac{\Delta OD\, hc}{\epsilon\, 1000E\, \lambda_{ex}}\, N_A \tag{2.13}$$

where λ_{ex} is the excitation wavelength.

2.6 Hybrid Photovoltaics

This section covers the fabrication process and testing of bilayer hPV devices incorporating the ZnO–(PZT)–P3HT active layer. Data derived from these devices is presented in Chapter 5.

2.6.1 Device Fabrication

Bilayer devices with the structure ITO–ZnO–(PZT)–P3HT–MoO_3–Ag were fabricated in a multi-stage process: firstly, the patterned ITO substrates were cleaned using the procedure outlined in Section 2.1[6]; after ZnO deposition (Section 2.2.2), a small area of the ITO at the edge of the film was exposed by etching with dilute HCl, followed by rinsing and drying. This area was then masked using a small piece of Kapton tape (heat resistant to 250 °C) prior to PZT deposition to prevent the exposed ITO from coming into contact with the sol-gel. After PZT deposition (Section 2.2.3), the polymer layer was deposited as outlined in Section 2.2.4 and the an area of ITO exposed by removing the polymer with a cotton swab impregnated with toluene.

The device structure was completed by evaporating MoO_3/Ag top contacts using a Kurt J. Lesker thermal evaporator. A laser-cut mask was employed during deposition for patterning the contacts. Prior to device testing, small quantities of silver paint were applied to the non-active edges (*i.e.* outside of the ITO pattern on the substrate) of the top contacts and to the exposed area of ITO (bottom contact) to ensure a good electrical contact between the pins in the testing unit and the device. Before testing, the devices were loaded into testing chambers inside a glovebox, sealing them in a N_2 environment.

[6]Whilst UV–O_3 treatment of ITO is often used in device fabrication, this step was omitted in this study. Although the treatment confers increased hydrophilicity to the surface, the introduction of O^{2-} ions into the ITO surface increases the work function of ITO and lowers surface conductivity. Whilst this has been shown to improve hole injection in organic light-emitting diodes [54], the increase in work function increases the gap to the work function of ZnO [55] which, in the case of hPVs, may create an energetic barrier at this interface and inhibit charge collection; therefore, in this work this step was omitted as an Ohmic contact between ITO and ZnO was desired.

2.6.2 Solar Cell J–V Testing

The hPV devices were characterised by measuring their J–V characteristics in the dark and under illumination. This was carried out using by connecting the devices to a Keithley 2420 SourceMeter and using a Keithley Oriel Solar Simulator equipped with an AM 1.5G filter as a light source. Before device testing, the solar simulator was calibrated using a Si photodiode to adjust the incident light intensity to 100 mW cm^{-2}.

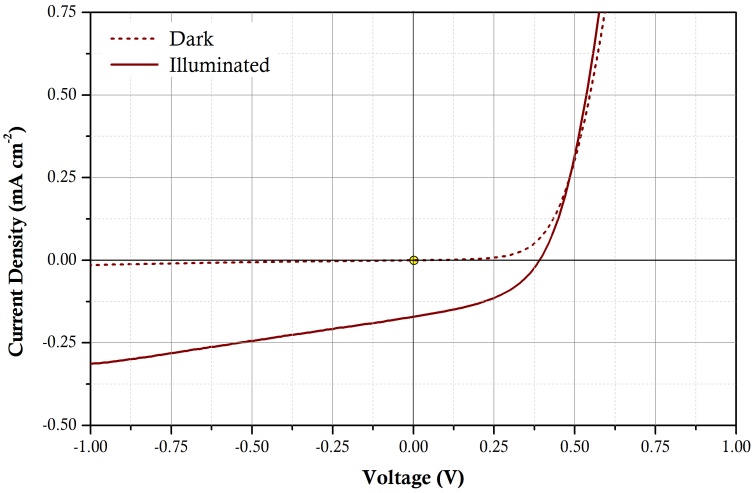

Figure 2.12 – Dark and illuminated (100 mW cm^{-2}) J–V curves obtained for a ZnO–P3HT based bilayer hPV device.

Typically, J–V curves were acquired by sweeping the device voltage from -1.5 – +1.5 V (step size 0.015 V); the devices were connected to the source meter such that under reverse bias the voltage appeared in the 3^{rd} quadrant, moving into the 1^{st} quadrant under forward bias: this is illustrated in Figure 2.12. For each sample, 3 measurements were taken: firstly under dark conditions, then under illumination, and lastly a second dark scan was taken after illumination to monitor changes in J–V behaviour.

Under illumination, devices were typically irradiated with light for less than 2 minutes in total. However, tests were carried out to investigate changes in device performance with prolonged illumination (up to 30 minutes). The four main solar cell characteristics (defined in Section 1.3.1) — short-circuit current density (J_{sc}), open-circuit voltage (V_{oc}), fill-factor (FF), and power conversion efficiency (PCE) — were calculated automatically by the data acquisition programme on completion of the measurements. Additionally, series and shunt resistances were calculated under dark conditions: shunt resistance may be derived from the inverse of the slope of the J–V curve under saturation in the reverse bias regime (typically at -3 V), whilst series resistance may be similarly calculated by the same method at the forward bias saturation point (typically +3 V).

References

[1] L. L. Hench and J. K. West, "The sol-gel process," *Chem. Rev.* **90**, pp. 33–72, Jan. 1990.

[2] P. S. Patil, "Versatility of chemical spray pyrolysis technique," *Mater. Chem. Phys.* **59**, pp. 185–198, June 1999.

[3] M. Ohyama, H. Kozuka, T. Yoko, and S. Sakka, "Preparation of ZnO films with preferential orientation by sol-gel method," *J. Ceram. Soc. Japan* **104**(1208), pp. 296–300, 1996.

[4] M. Ohyama, H. Kouzuka, and T. Yoko, "Sol-gel preparation of ZnO films with extremely preferred orientation along (*002*) plane from zinc acetate solution," *Thin Solid Films* **306**, pp. 78–85, Aug. 1997.

[5] J. Downing, M. P. Ryan, N. Stingelin, and M. A. McLachlan, "Solution processed hybrid photovoltaics: preparation of a standard ZnO template," *J. Photonics Energy* **1**(1), pp. 11117–11119, 2011.

[6] J. M. Downing, *Control and Characterisation of Metal Oxide/Polymer Morphologies for Hybrid Photovoltaic Devices.* Doctor of Philosophy, Imperial College London, 2013.

[7] A. Bashir, P. H. Wobkenberg, J. Smith, J. M. Ball, G. Adamopoulos, D. D. C. Bradley, and T. D. Anthopoulos, "High-performance zinc oxide transistors and circuits fabricated by spray pyrolysis in ambient atmosphere," *Adv. Mater.* **21**(21), p. 2226, 2009.

[8] M. Krunks and E. Mellikov, "Zinc oxide thin films by the spray pyrolysis method," *Thin Solid Films* **270**(1-2), pp. 33–36, 1995.

[9] Q. Zhang, R. W. Whatmore, Z. Huang, and E. M. Vickers, "Low temperature formation of sol-gel derived ferroelectric lead zirconate titanate ($Pb(Zr_xTi_{1-x})O_3$, x = 0.3) thin films," *J. Phys. IV Fr.* **08**, pp. Pr9–79–Pr9–82, Dec. 1998.

[10] Q. Zhang, Z. Huang, M. Vickers, and R. Whatmore, "Effect of the particle size in PZT precursor sols on the orientation of the thin films," *J. Eur. Ceram. Soc.* **19**, pp. 1417–1421, June 1999.

[11] Q. Zhang and R. W. Whatmore, "Sol-gel PZT and Mn-doped PZT thin films for pyroelectric applications," *J. Phys. D. Appl. Phys.* **34**(15), p. 2296, 2001.

[12] Q. Zhang, M. Vickers, A. Patel, and R. Whatmore, "Determination of particle size and shape during the hydrolysis of $Pb(Zr_{0.3}Ti_{0.7})O_3$ precursor solutions," *J. Sol-Gel Sci. Technol.* **11**, pp. 141–152, July 1998.

[13] Q. Zhang, Z. Huang, and R. Whatmore, "Studies of lead zirconate titanate sol ageing part I: factors affecting particle growth," *J. Sol-Gel Sci. Technol.* **23**, pp. 135–144, Feb. 2002.

[14] Z. Huang, Q. Zhang, and R. Whatmore, "Studies of lead zirconate titanate sol aging part II: particle growth mechanisms and kinetics," *J. Sol-Gel Sci. Technol.* **24**, pp. 49–55, May 2002.

[15] M. J. Lefevre, J. S. Speck, R. W. Schwartz, D. Dimos, and S. J. Lockwood, "Microstructural development in sol-gel derived lead zirconate titanate thin films: the role of precursor stoichiometry and processing environment," *J. Mater. Res.* **11**, pp. 2076–2084, Jan. 1996.

[16] K. G. Brooks, I. M. Reaney, R. Klissurska, Y. Huang, L. Bursill, and N. Setter, "Orientation of rapid thermally annealed lead zirconate titanate thin films on (*111*) Pt substrates," *J. Mater. Res.* **9**, pp. 2540–2553, Mar. 1994.

[17] I. M. Reaney, D. V. Taylor, and K. G. Brooks, "Ferroelectric PZT thin films by sol-gel deposition," *J. Sol-Gel Sci. Technol.* **13**, pp. 813–820, Jan. 1998.

[18] I. Szafraniak, C. Harnagea, R. Scholz, S. Bhattacharyya, D. Hesse, and M. Alexe, "Ferroelectric epitaxial nanocrystals obtained by a self-patterning method," *Appl. Phys. Lett.* **83**, p. 2211, Sept. 2003.

[19] M. Dawber, I. Szafraniak, M. Alexe, and J. F. Scott, "Self-patterning of arrays of ferroelectric capacitors: description by theory of substrate mediated strain interactions," *J. Phys. Condens. Matter* **15**, pp. L667–L671, Nov. 2003.

[20] I. Szafraniak-Wiza, M. Alexe, and M. Hesse, "Nanosized Ferroelectric Crystals," in *Handbook of Advanced Dielectric, Piezoelectric and Ferroelectric Materials*, Z.-G. Ye, ed., ch. 20, pp. 600–664, Woodhead Publishing Ltd, 1st ed., 2008.

[21] J.-F. Chang, B. Sun, D. W. Breiby, M. M. Nielsen, T. I. Sölling, M. Giles, I. McCulloch, and H. Sirringhaus, "Enhanced mobility of poly(3-hexylthiophene) transistors by spin-coating from high-boiling-point solvents," *Chem. Mater.* **16**, pp. 4772–4776, Nov. 2004.

[22] M. Surin, P. Leclère, R. Lazzaroni, J. D. Yuen, G. Wang, D. Moses, A. J. Heeger, S. Cho, and K. Lee, "Relationship between the microscopic morphology and the charge transport properties in poly(3-hexylthiophene) field-effect transistors," *J. Appl. Phys.* **100**(3), p. 033712, 2006.

[23] J. H. Bannock, S. H. Krishnadasan, A. M. Nightingale, C. P. Yau, K. Khaw, D. Burkitt, J. J. M. Halls, M. Heeney, and J. C. de Mello, "Continuous synthesis of device-grade semiconducting polymers in droplet-based microreactors," *Adv. Funct. Mater.* **23**, pp. 2123–2129, May 2013.

[24] L. E. Smart and E. A. Moore, *Solid State Chemistry: An Introduction*, CRC Press, 4th ed., 2012.

[25] A. R. West, *Solid State Chemistry And Its Applications*, John Wiley & Sons, Ltd., 1st ed., 1984.

[26] J. Grebenkemper, "Powder X-ray Diffraction."

[27] P. Scherrer, "Betimmung der Grösse und der inneren Struktur von Kolloidteilchen mittels Röntgenstrahlen," *Göttinger Nachrichten Gesell.* **2**, pp. 98–100, 1918.

[28] B. D. Cullity, *Elements of X-Ray Diffraction*, Prentice Hall, 3rd ed., 2001.

[29] U. Holzwarth and N. Gibson, "The Scherrer equation versus the 'Debye-Scherrer equation'," *Nat. Nanotechnol.* **6**, p. 534, Sept. 2011.

[30] D. B. Williams and C. B. Carter, *Transmission Electron Microscopy: A Textbook for Materials Science, Volume 3*, Springer Science & Business Media, 2009.

[31] L. A. Giannuzzi, J. L. Drown, S. R. Brown, R. B. Irwin, and F. A. Stevie, "Applications of the FIB lift-out technique for TEM specimen preparation.," *Microsc. Res. Tech.* **41**, pp. 285–90, May 1998.

[32] P. Eaton and P. West, *Atomic Force Microscopy*, Oxford University Press, Oxford, 1st ed., 2010.

[33] M. Guide, X.-D. Dang, and T.-Q. Nguyen, "Nanoscale characterization of tetrabenzoporphyrin and fullerene-based solar cells by photoconductive atomic force microscopy," *Adv. Mater.* **23**(20), p. 2313, 2011.

[34] J. Park and H. Lee, "Effect of surface functional groups on nanostructure fabrication using AFM lithography," *Mater. Sci. Eng. C* **24**, pp. 311–314, Jan. 2004.

[35] C. Canale, B. Torre, D. Ricci, and P. C. Braga, "Recognizing and avoiding artifacts in atomic force microscopy imaging," *Methods Mol. Biol.* **736**, pp. 31–43, Jan. 2011.

[36] R. Garcia, C. Gómez, N. Martinez, S. Patil, C. Dietz, and R. Magerle, "Identification of nanoscale dissipation processes by dynamic atomic force microscopy," *Phys. Rev. Lett.* **97**, p. 6103, July 2006.

[37] D. Nečas and P. Klapetek, "Gwyddion: an open-source software for SPM data analysis," *Cent. Eur. J. Phys.* **10**(1), pp. 181–188, 2012.

[38] L. Scuderio, "WSU: `http://public.wsu.edu/~scudiero/`."

[39] G. Attard and C. Barnes, *Surfaces*, Oxford University Press, 1998.

[40] H. Li, L. K. Schirra, J. Shim, H. Cheun, B. Kippelen, O. L. A. Monti, and J.-L. Bredas, "Zinc oxide as a model transparent conducting oxide: a theoretical and experimental study of the impact of hydroxylation, vacancies, interstitials, and extrinsic doping on the electronic properties of the polar ZnO (*0002*) surface," *Chem. Mater.* **24**, pp. 3044–3055, Aug. 2012.

[41] A. Adriaens, L. Van Vaeck, and F. Adams, "Static secondary ion mass spectrometry (S-SIMS) Part 2: material science applications," *Mass Spectrom. Rev.* **18**(1), pp. 48–81, 1999.

[42] A. Benninghoven, "Chemical analysis of inorganic and organic surfaces and thin films by static time-of-flight secondary ion Mass spectrometry (TOF-SIMS)," *Angew. Chemie Int. Ed.* **33**, pp. 1023–1043, June 1994.

[43] H. Téllez, A. Aguadero, J. Druce, M. Burriel, S. Fearn, T. Ishihara, D. S. McPhail, and J. A. Kilner, "New perspectives in the surface analysis of energy materials by combined time-of-flight secondary ion mass spectrometry (ToF-SIMS) and high sensitivity low-energy ion scattering (HS-LEIS)," *J. Anal. At. Spectrom.* **29**, p. 1361, May 2014.

[44] B. Clark, *UV Spectroscopy: Techniques, Instrumentation and Data Handling*, Springer Science & Business Media, 1993.

[45] D. F. Swinehart, "The Beer-Lambert law," *J. Chem. Educ.* **39**, p. 333, July 1962.

[46] J. Tauc, R. Grigorovici, and A. Vancu, "Optical properties and electronic structure of amorphous germanium," *Phys. status solidi* **15**(2), pp. 627–637, 1966.

[47] H. E. Belghiti, T. Pauporté, and D. Lincot, "Mechanistic study of ZnO nanorod array electrodeposition," *Phys. status solidi* **205**, pp. 2360–2364, Oct. 2008.

[48] V. Srikant and D. R. Clarke, "On the optical band gap of zinc oxide," *J. Appl. Phys.* **83**(10), pp. 5447–5451, 1998.

[49] M. Klessinger and J. Michl, *Excited states and photochemistry of organic molecules*, VCH, 1995.

[50] D. Zhang, Q. Wang, and Z. Xue, "Photoluminescence of ZnO films excited with light of different wavelength," *Appl. Surf. Sci.* **207**, pp. 20–25, Feb. 2003.

[51] W. J. E. Beek, M. M. Wienk, M. Kemerink, X. N. Yang, and R. A. J. Janssen, "Hybrid zinc oxide conjugated polymer bulk heterojunction solar cells," *J. Phys. Chem. B* **109**(19), pp. 9505–9516, 2005.

[52] T. M. Clarke and J. R. Durrant, "Charge photogeneration in organic solar cells," *Chem. Rev.* **110**(11), pp. 6736–6767, 2010.

[53] T. M. Clarke, A. M. Ballantyne, J. Nelson, D. D. C. Bradley, and J. R. Durrant, "Free energy control of charge photogeneration in polythiophene/fullerene solar cells: the influence of thermal annealing on P3HT/PCBM blends," *Adv. Funct. Mater.* **18**, pp. 4029–4035, Dec. 2008.

[54] W. Song, S. So, D. Wang, Y. Qiu, and L. Cao, "Angle dependent X-ray photoemission study on UV–ozone treatments of indium tin oxide," *Appl. Surf. Sci.* **177**, pp. 158–164, June 2001.

[55] P. Destruel, H. Bock, I. Séguy, P. Jolinat, M. Oukachmih, and E. Bedel-Pereira, "Influence of indium tin oxide treatment using UV–ozone and argon plasma on the photovoltaic parameters of devices based on organic discotic materials," *Polym. Int.* **55**(6), pp. 601–607, 2006.

Chapter 3

Growth and Structure of Sol-gel-derived PZT Films on ZnO

3.1 Introduction

In this chapter, a study into the growth of sol-gel-derived lead zirconate titanate (PZT) thin-films on indium tin oxide (ITO) and ZnO is reported. A limited number of papers have been published on the growth of ZnO–PZT structures: the use of ZnO as a 'bridging' growth layer for epitaxial growth of PZT 52/48 by pulsed laser deposition (PLD) has been reported by Chen *et al.* [1]; a similar study had also been carried out previously by Wang [2]. In both cases, the presence of the ZnO buffer layer led to an increase in capacitor performance due to changes in the preferred orientation in the ZnO–PZT film, as well as a reduction in fatigue properties. Recently, there has been interest in ferroelectric (FE) oxide–ZnO heterostructures which exploit the polarisation coupling between the switchable FE polarisation and the piezoelectric polarisation of ZnO [3]: Zhou *et al.* reported the sol-gel deposition of PZT 52/48 on ZnO for this purpose, showing crystallisation of the former in the desired FE phase [4]; however, this report carries little in the way of materials characterisation beyond X-ray diffraction (XRD) and UV-vis spectroscopy.

Given the limited available literature on the growth of ZnO–PZT bilayers, initial experiments were carried out into ITO–PZT thin-films for two main reasons: firstly the growth of PZT on ITO is well-documented and provides a reference point for the growth of ZnO–PZT films; secondly, ITO was considered to be an appropriate test substrate for growth given the batch-to-batch similarity between as-purchased ITO units. The effect of the annealing conditions on the crystal structure of ITO–PZT thin-films was studied (for temperatures $< 600\,^{\circ}\mathrm{C}$) and subsequently these were used as a guide and comparison for the investigation into ZnO–PZT growth. The growth mechanism for ITO–PZT films

has been investigated by Roy *et al.* who propose that layer growth proceeds via formation of rosette structures: seeds of crystalline PZT form on the ITO from the pyrochlore precursor phase, initially growing in the direction normal to the substrate followed by rapid lateral growth. PbO has been cited as a key agent in this process, as growth of rosettes of perovskite is limited by the availability of PbO to the PZT precursor phase [5]. Other examples of ITO–PZT heterostructures include the growth of 3-dimensional ordered macroporous (3DOM) structures of PZT on ITO by sol-gel [6].

In this chapter, the growth of ZnO (both sol-gel-derived, Sol-Z, and spray-pyrolysed, SP-Z) used in this work is outlined and characterisation of the films' crystallinity and microstructure evaluated. The effect of annealing conditions was then investigated for both ITO–PZT and ZnO–PZT films using X-ray diffraction (XRD) and the microstructure of these films compared using atomic force microscopy (AFM). More in-depth characterisation of ZnO–PZT films was carried out using transmission electron microscopy (TEM) and the composition probed using time-of-flight secondary ion mass spectroscopy (ToF-SIMS).

3.2 Growth of ZnO

ZnO was prepared by two methods, namely spin-coating of a sol-gel precursor and by spray pyrolysis — the experimental procedures for these two techniques are outlined in Section 2.2.2. The sol-gel method was chosen due to prior experience with these films and due to the success found in employing these films in ZnO–P3HT (poly(3-hexylthiophene) hybrid photovoltaic (hPV) devices; spray pyrolysis offers a fast method for producing crystalline ZnO with reasonable thickness control. Moreover, a multitude of reports incorporating SP-Z films into electronic devices such as thin-film transistors [7] and hPVs [8, 9] have been published. In this section all experiments were carried out using soda-lime glass as substrates.

For analysis of XRD data, the ZnO peaks were compared against a standard ZnO reference, JCPDS reference 00-001-1136 (zincite). A comparison of ZnO peak positions for the films deposited in this work are shown in the Appendix (Table A.2). A simulated XRD plot for a reference ZnO powder is shown in Figure 3.1: the simulation (Cu Kα_1 radiation, step size 0.033°) was carried out through the Inorganic Crystal Structure Database (ICSD, FIZ Karlsruhe) using structural parameters determined by Kisi *et al.* from neutron diffraction on a ZnO powder sample [10].

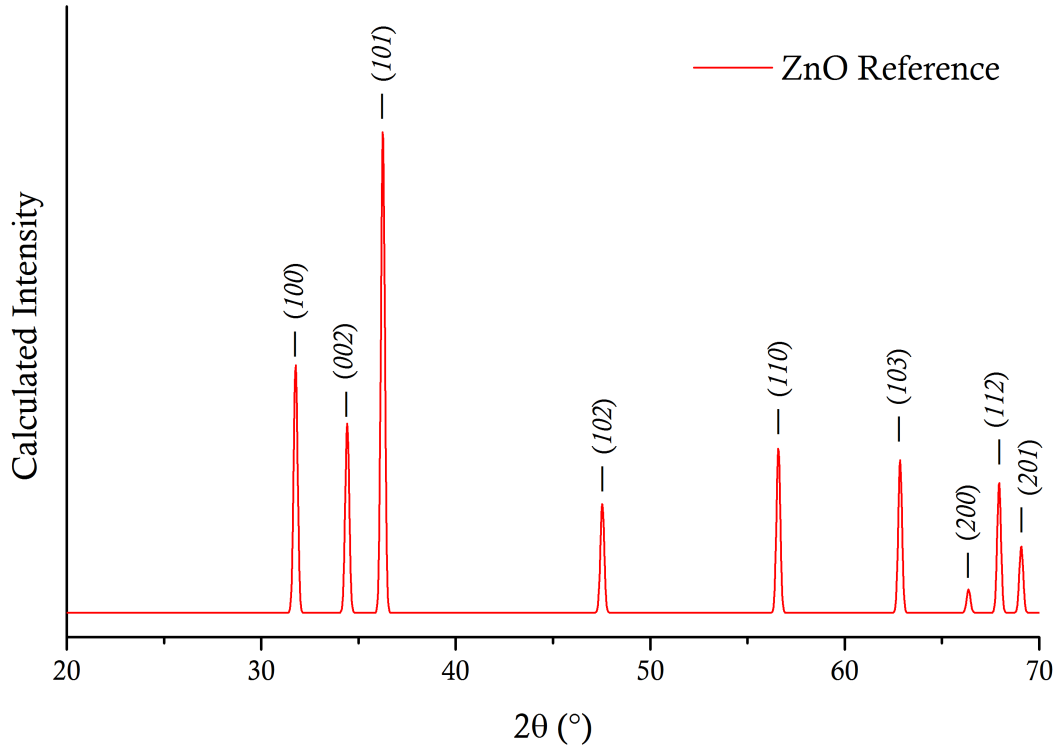

Figure 3.1 – Simulated XRD powder pattern for ZnO, calculated using Cu Kα_1 radiation (1.5406 Å) and a step size 0.033°. Pattern produced using the Inorganic Crystal Structure Database (ICSD, FIZ Karlsruhe); structural data used in the calculation was provided by [10]. Reference *d*-spacings and peak positions used in this work are given in Appendix Table A.2.

3.2.1 ZnO Growth from Sol-gel

Sol-Z films were synthesised using the method outlined by Downing *et al.* [11], as outlined in Section 2.2.2.1: a $Zn(ac)_2$ sol-gel with a concentration 0.75 M was spin-coated and dried at 300 °C for 10 minutes; this was repeated twice more followed by an annealing step at 450 °C to improve crystallinity. These processing conditions produced a crystalline ZnO thin-film with a thickness of $\sim$ 145 nm as measured using profilometry. The resulting films exhibit high transparency in the visible region ($>$ 80 %) and had previously been employed successfully as acceptor layers in hPV devices. All ZnO films exhibited a strong orientation preference in the (*002*) direction, *cf.* ZnO powder, in which the relative peak intensity (RPI) for this orientation is only $\sim$ 30 %.

As shown in the inset of Figure 3.2, annealing of the Sol-Z led to an increase in the intensity of the (*002*) peak which may be interpreted as an increase in crystallinity. There was no substantial change in the full width at half maximum (FWHM) with annealing, and thus little change in the crystallite size derived using the Scherrer equation (Equation 2.2) was measured — for films annealed for 1 hour, this was determined to

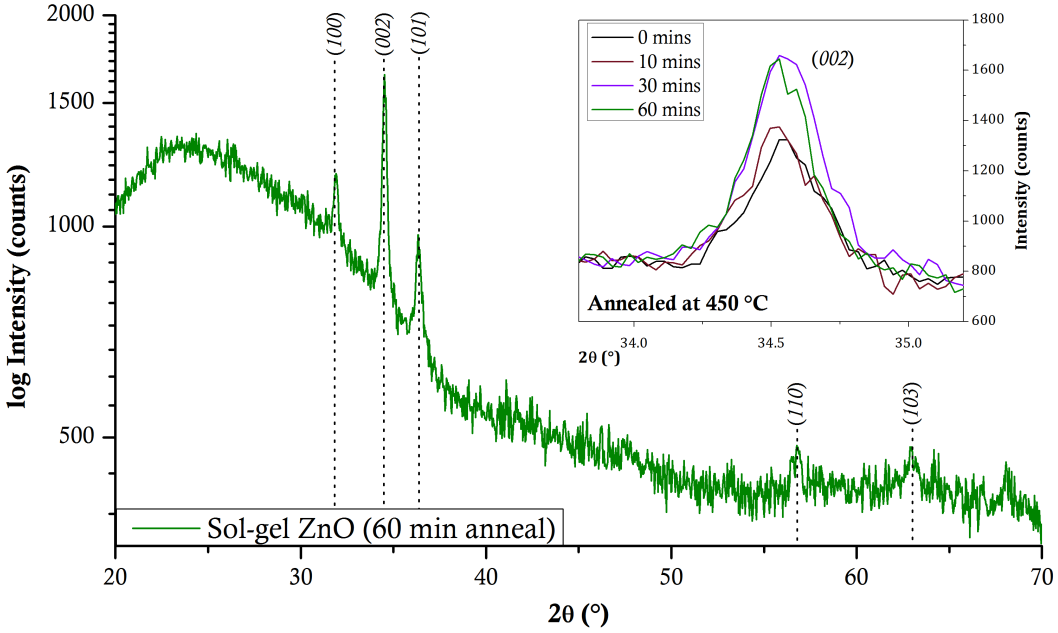

Figure 3.2 – XRD pattern for a Glass–Sol-Z thin-film annealed at 450 °C for 1 hour. **Inset:** small angular region containing showing the effects of annealing time on the (*002*) peak shape.

be ∼ 57 nm for the (*002*) orientation measured from three different samples; crystallite sizes for the (*100*) and (*101*) orientations were not determined due to the weak intensity of the diffraction peaks (as noted in Section 2.3.2, Scherrer analysis yields approximate measures of crystallite size). Scanning electron microscopy (SEM) images of films before and after annealing did not exhibit much discernible difference in topography, suggesting that the microstructure is 'set' during the spin-coating/drying phase: these are shown in Appendix Figure A.1. Growth of the Sol-Z films on ITO yielded similar diffraction patterns. More in-depth analysis of the microstructure of Sol-Z films is given below in Section 3.2.3.

3.2.2 ZnO Growth by Spray Pyrolysis

SP-Z thin-films were produced as detailed in Section 2.2.2.2: for these experiments, a 0.1 M precursor solution was sprayed onto substrates heated to 400 °C; the spraying height was fixed at 20 cm and the carrier gas pressure set at 2 bar. SP-Z films used to grow PZT layers were fabricated using an 8-cycle coating routine, each cycle consisting of 4 passes over the substrate (a total spray time of ∼ 7 s), followed by a 'drying' phase of 45 seconds to allow the substrate to heat back up to temperature. This spray routine yielded SP-Z films with a thickness of 67 ± 5 nm derived from UV-visible transmis-

sion spectroscopy (as outlined in Section 2.5.1.1), a value in good agreement with those obtained by profilometry ($\sim$ 60 nm).

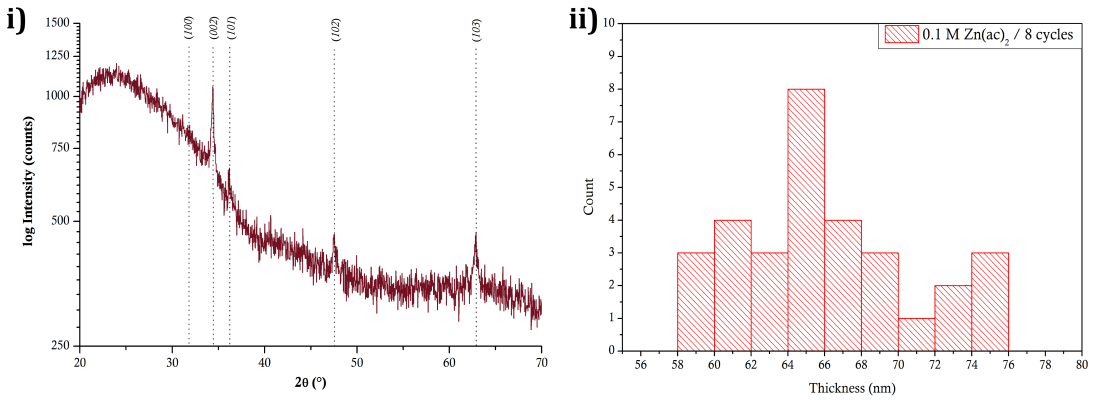

Figure 3.3 – *i)* XRD pattern for a Glass–SP-Z film grown at 400 °C using a 0.1 M $Zn(ac)_2$/MeOH precursor solution and a spray routine consisting of 8 coating cycles. *ii)* frequency distribution of film thicknesses for SP-Z films sprayed using the same processing routine. 30 films in total were analysed with a mean film thickness of 67 $\pm$ 5 nm.

As the spray routine was carried out by hand it was conceded that there would be a natural variation in some of the spraying parameters, particularly the spray height and the spray time. Changes in either of these of these would affect the amount of solution reaching the substrate, thereby influencing the film thickness. The thickness for 30 SP-Z films deposited using the same routine was evaluated using UV-vis, the results of which are displayed in Figure 3.3. The mean film thickness was calculated to be 67 nm, with variation from 58 to 76 nm ($\sigma = 5$ nm).

XRD data obtained for these films (in Figure 3.3) revealed that, like Sol-Z, the ZnO was orientated in the (*002*) direction, with Scherrer analysis of this peak from four different samples yielding an average crystallite size of $\sim$ 52 nm (values ranging from 48 nm to 66 nm). Given the relative thinness of the films, the ZnO peaks in the XRD data are fairly weak with the (*101*) orientation producing a very small peak and the (*100*) appearing to be absent altogether.

TEM micrographs were acquired for a cross-section of a SP-Z film: although these were taken a single region from a single film and thus cannot be taken as entirely representative the material, the data produced by this technique can be used to complement the other structural data obtained in this work. The micrographs show that spray pyrolysis yields dense ZnO films consisting of seemingly large but poorly defined grains leading to a fairly rough ZnO surface. The SP-Z grain boundaries in the images appear to be much less well-defined and sharp than those in the Sol-Z films, hindering the ex-

traction of meaningful grain sizes — approximate measurements yielded grains around 30 to 70 nm, values in the same order as those obtained from XRD data.

A thickness evaluation of the cross-section (by measuring the distance between the top and bottom ZnO interfaces in a direction normal to the substrate at $\sim$ 5 nm intervals across the micrographs) yielded an average value of 48 nm, a thickness of 10 nm lower than the thinnest SP-Z film as measured by UV-vis: whilst this measurement was only obtained from a single cross-section of an SP-Z film and cannot be considered to be representative of an entire substrate, it raises the question of the accuracy of the profilometry and UV-vis measurements which lend greater weight to the maximum film height values; given the roughness of the SP-Z films, this is likely to be somewhat greater than an average value of layer height. Compounding this, the discrepancy in roughness between ITO substrates (used for TEM images, RMS roughness of $\sim$ 3 nm for ITO) and the glass substrates used in in profilometry/UV-vis measurements (RMS roughness $<$ 1 nm) may also play a role in measurement of film thickness.

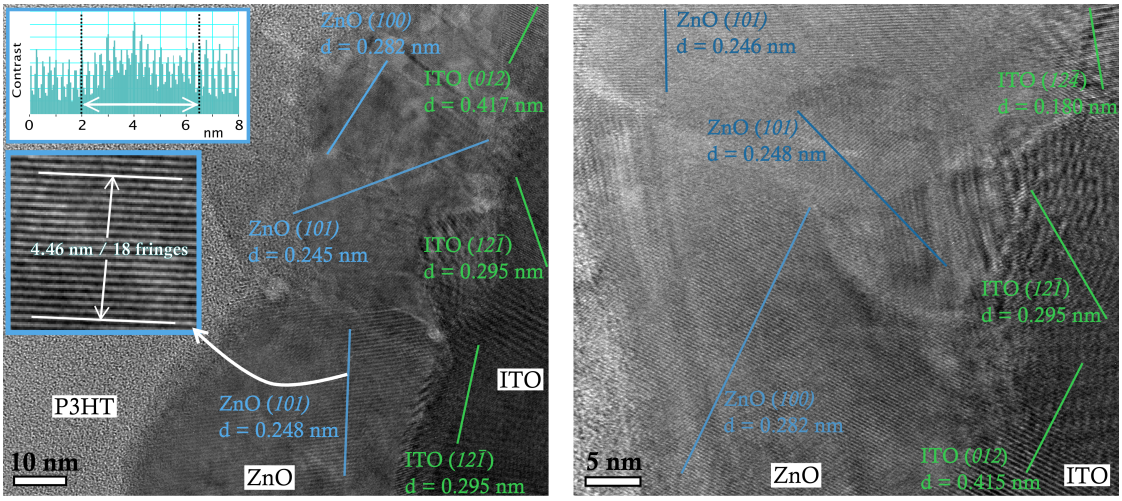

Figure 3.4 – High-resolution TEM images of an ITO–SP-Z–P3HT film obtained at **Left**: 200,000 x and **Right**: 410,000 x magnification, both with a beam energy of 300 kV. The images present lattice fringes with characteristic *d*-spacing of specific crystallographic orientations: the green lines indicate single crystallite regions of ITO, and blue for ZnO. The insets in the **Left** image show a magnified ZnO crystallite accompanied by 1-dimensional line profile of the micrograph and the calculation method for the *d*-spacing; in this case, the *d*-spacing corresponds to the (*101*) plane of ZnO.

Lastly, high-resolution TEM images exhibited lattice fringes in both the ITO and ZnO regions of the film, allowing for crystallographic analysis of the films; XRD-derived reference *d*-spacings used for this listed in Appendix Table A.1 for ITO in Appendix Table A.2 for ZnO. Both the ITO and ZnO films are highly polycrystalline; in the case of ZnO, the direction of the lattice fringes suggested that most of the ZnO crystallites are orientated with the c-axis pointing in the direction normal to the substrate (for example,

Figure 3.4 shows lattice fringes in a ZnO crystallite originating from the (*100*) plane of ZnO; the planes are stacked perpendicular to the substrate, indicating that the c-axis is also orientated in this direction), consistent with the strong preference for the (*002*) orientation seen in the XRD data.

3.2.3 Comparison of ZnO Microstructure

ZnO Type	Thickness [profilometry] (nm)	Thickness [UV-vis] (nm)	XRD Cryst. Size (nm)	R_a (nm)	R_{RMS} (nm)	R_{max} (nm)
Sol-Z	145	–	55	3.33	4.16	30.7
SP-Z	60	67	52	6.47	8.10	73.1

Table 3.1 – Structural parameters for sol-gel-derived and spray-pyrolysed ZnO thin-films (Sol-Z and SP-Z respectively). UV-vis thickness measurements were not carried out for the Sol-Z films as the method requires that the films are densely packed. Roughness parameters were derived from AFM topography measurements: R_a is the arithmetic roughness, R_{RMS} the root mean square roughness, and R_{max} the maximum recorded Z-value for the film. The mathematical basis for these quantities are given in Section 2.3.4.

As discussed above, growth of both SP-Z and Sol-Z films yielded crystallographically similar films on glass (*i.e.* with similar preferred orientation and Scherrer-derived crystallite size); however, growth on ITO led to a changes in the growth orientation of SP-Z. The microstructures of ITO–Sol-Z and ITO–SP-Z films are described and contrasted in this section: TEM and atomic force microscopy (AFM) were used for this purpose. Although differences in microstructure were not readily observed from the AFM data, from SEM images (shown in Appendix Figure A.1), the topography of the two films appears to be rather different — whilst the SP-Z grains appear to be fairly contiguous, the Sol-Z film appears to be much more broken up with small granular islands forming suggesting some degree of porosity.

Grain size and roughness parameters were obtained from AFM — these are displayed in Table 3.1 with thickness and XRD-derived crystallite size. The Sol-Z films were found to be markedly less rough than the SP-Z films, as shown in Table 3.1, the R_{RMS} being 4.16 nm for the former and 8.10 nm for the latter. For SP-Z films, the values for R_{max} (*i.e.* the maximum Z-height recorded) were comparable to the overall thickness of the films suggesting that they contain pinholes.

TEM micrographs of these films are shown in Figure 3.5: these images confirm that the Sol-Z films are not densely packed and possess a fairly complex microstructure. In comparison, the SP-Z layer deposited by this method consists of a single, continuous

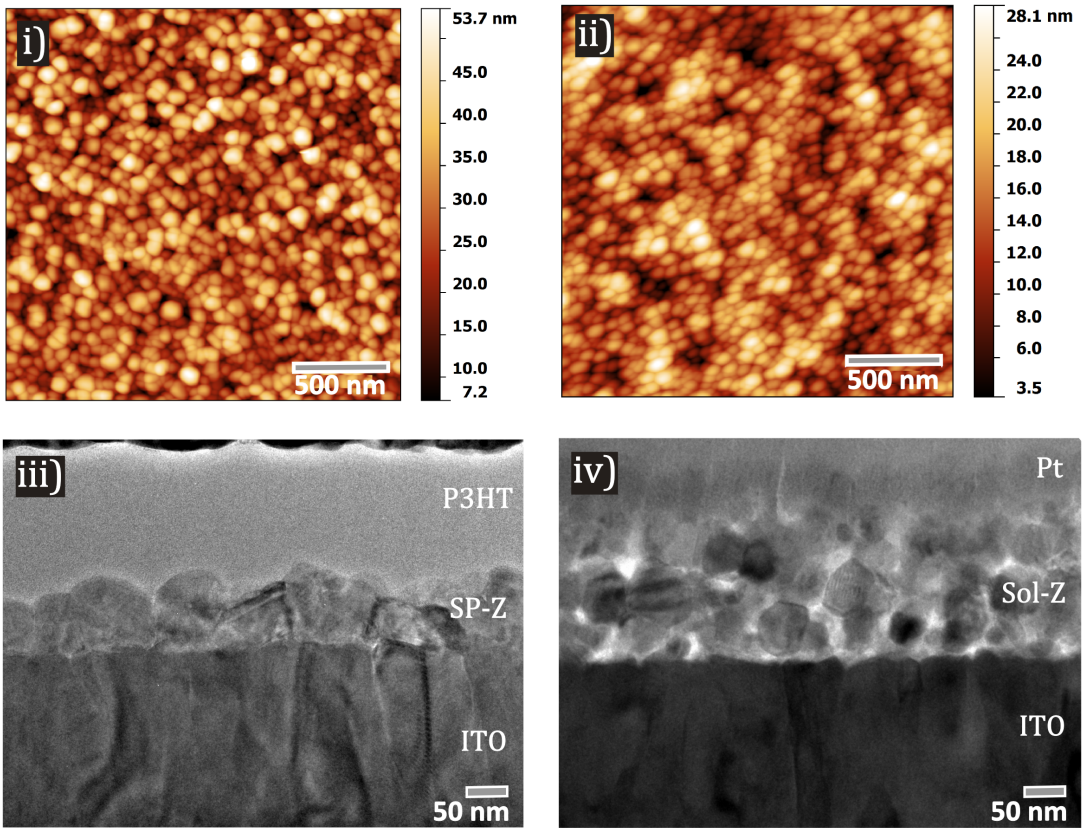

Figure 3.5 – *i)* and *ii)* 2 x 2 μm tapping-mode AFM height scans for SP-Z and Sol-Z films respectively. *iii)* TEM micrograph of an ITO–SP-Z–P3HT–Au film: sample preparation carried out by C. Burgess and image acquired by Dr C. McGilvery; *iv)* TEM micrograph for an ITO–Sol-Z–Pt thin-film prepared and imaged by Dr J. B. Gilchrist. Both images acquired at a magnification of 30,000 x.

layer with comparable grain sizes, although the distribution of grain sizes appears to be somewhat more varied than the more uniform Sol-Z films.

Despite the roughness of the SP-Z films compared to the Sol-Z, the former were considered to be more suitable substrates for investigating PZT growth due to their greater density and less complex microstructure. However, Sol-Z films were later used in Chapter 5 for hPV device fabrication — PZT had been shown to grow on Sol-Z films in an earlier study (a TEM micrograph of a Sol-Z–PZT film is shown in Appendix Figure B.1).

3.3 Growth of PZT Thin-Films from Sol-Gel

Thin-films of $Pb(Zr_{0.30}Ti_{0.70})O_3$ (PZT 30/70) were prepared using the sol-gel method outlined in Section 2.2.3. ITO-coated glass was initially used as a test substrate for PZT growth: although growth on glass was originally considered, annealing at temperatures

up to 600 °C failed to produce crystalline PZT — this has also been reported by Roy *et al.* [5]. Subsequently, similar growth conditions were used in ZnO–PZT experiments and the two compared. As a reference, a powder sample of PZT was synthesised by drying a small volume of the sol-gel, grinding it using an agate pestle and mortar, and heating it in an alumina crucible at 560 °C for 1 hour. The XRD pattern obtained for this sample (shown in Figure 3.6) was used as a guide in this work. These experiments aimed to produce crystalline PZT in the tetragonal phase whilst restricting the thermal energy input.

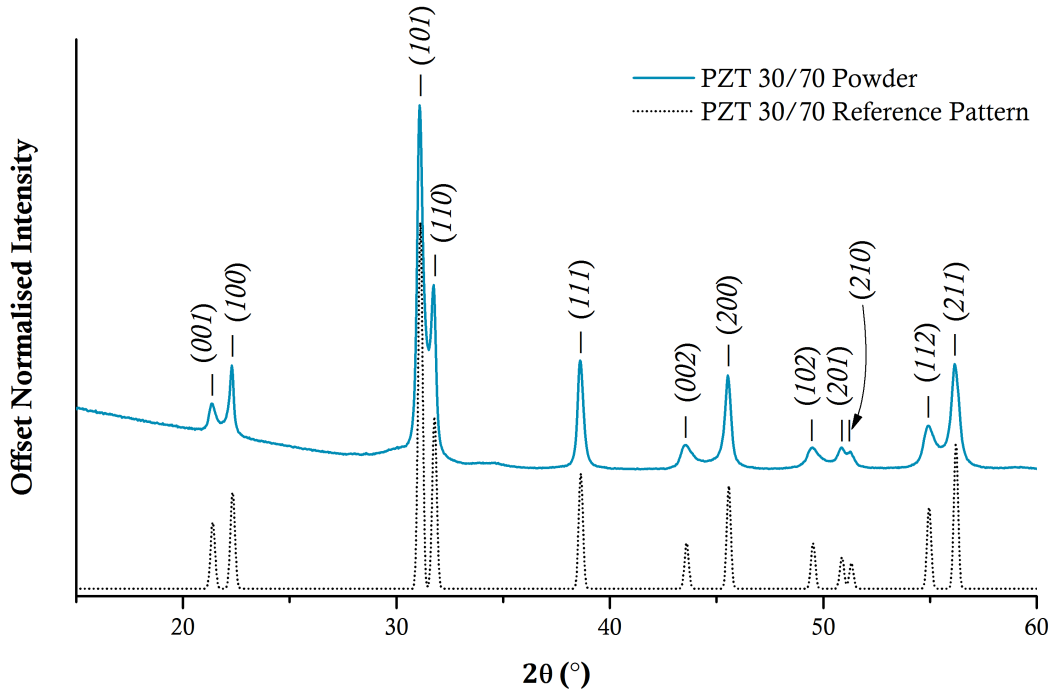

Figure 3.6 – X-ray powder diffraction pattern obtained for a sample of PZT 30/70 heated for 1 hour at 560 °C compared against a calculated reference pattern from [12]. The XRD pattern calculation was carried out using the Inorganic Crystal Structure Database (ICSD, FIZ Karlsruhe), simulated with Cu Kα_1 radiation and a step-size of 0.033°. Peak positions and corresponding *d*-spacings for the PZT powder made in this work are given in Appendix Table A.3.

The focus on using relatively low temperatures stems from a number of factors: firstly, low-temperature processing is desired in hPV fabrication (although the temperatures used in this work are admittedly higher than those considered to be ideal [13]); secondly, it was considered that prolonged heating at elevated temperatures could drive ion inter-diffusion at the oxide–oxide interfaces [14]; thirdly, the experiments in Chapter 4 focus on reducing the thickness of the PZT layer — lower temperatures were seen as important to prevent nanoisland formation in these films, as discussed in Sections 1.5.3.1 & 2.2.3.1. In this chapter, all PZT films were grown from sol-gel with a concentration of

0.4 M (with respect to the Ti/Zr content): the thickness of this layer was evaluated by profilometry of Si–PZT films, yielding a thickness value of 105 nm when processed under the same conditions. Although these films are much thicker than those used for interlayers (< 20 nm), films of this thickness were grown for ease of structural characterisation by conventional XRD techniques.

3.3.1 Growth of PZT on ITO

The experiments outlined in this section investigated the effect of annealing conditions (heating rate, temperature and time) on the crystallisation of PZT on ITO; all films were deposited using the same spin-coating conditions (3000 rpm for 40 s followed by drying at 200 °C for 45 seconds). Firstly, the annealing temperature was fixed at 500 °C and the heating rate changed between 1 °C min^{-1} and no ramp in which the samples were loaded into a preheated oven (henceforth abbreviated to PrH); the samples were annealed for 30 minutes and allowed to cool down to room temperature inside the furnace. The resulting XRD data were screened for changes in preferred crystallographic orientation and for the intermediate pyrochlore phase which typically yields very broad peaks in the range 29 – 30.5° [15] — although this peak is partially obscured by an ITO peak, it was still possible to identify this phase in the data.

Little difference in crystal structure was observed in films heated at 5, 10, 15 °C min^{-1}, and PrH; however, there was a marked change in preferred orientation of the PZT film when heated at 1 °C min^{-1}. In the former cases, a random orientation was observed, whereas films heated at 1 °C min^{-1} were highly orientated in the (*100*) direction as shown in Figure 3.7. Given the minimal differences between films annealed at 5, 10, 15 °C min^{-1}, and PrH, subsequent experiments investigated films annealed at PrH and 1 °C min^{-1} only.

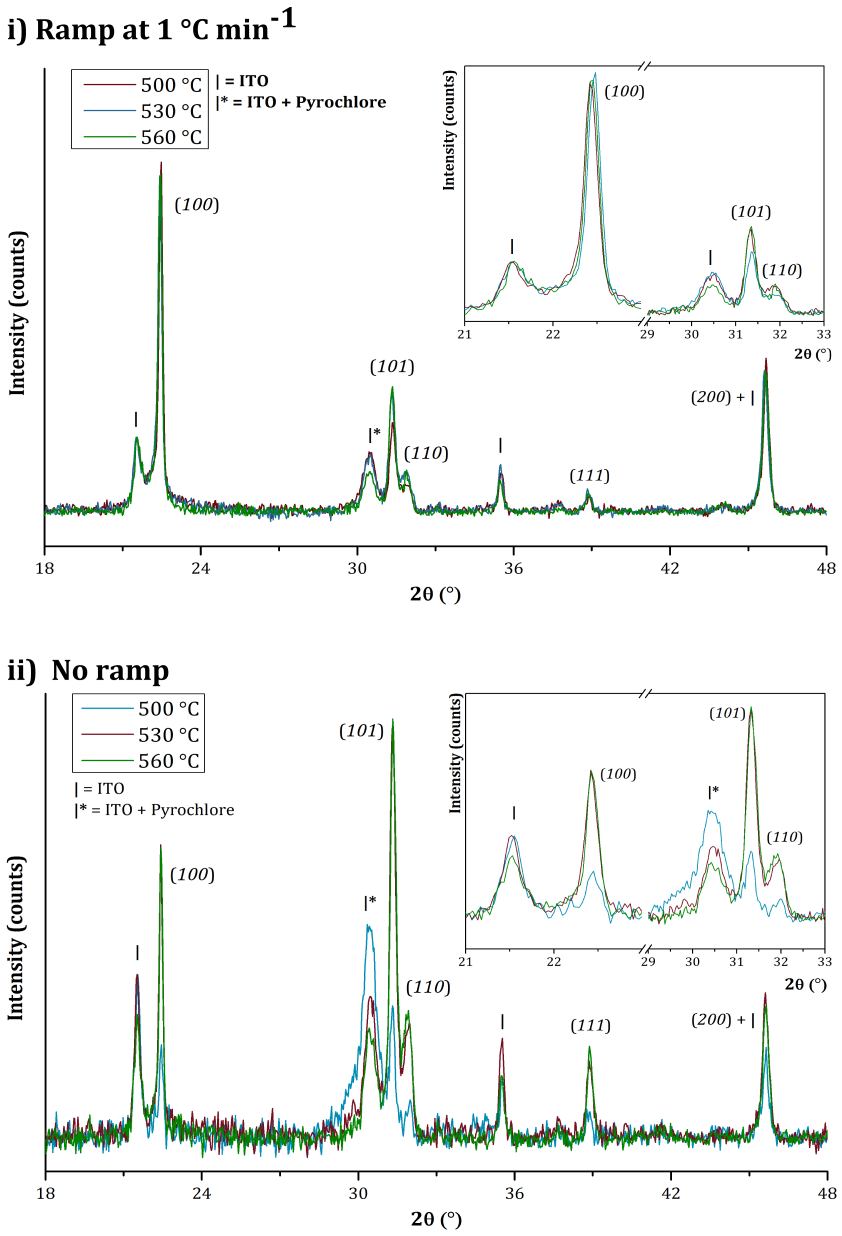

Figure 3.7 – Overlayed XRD patterns for ITO–PZT 30/70 (0.4 M sol-gel) thin-films annealed for 30 minutes at different temperatures with *i)* a ramp rate of 1 °C min^{-1}, and *ii)* no ramp (PrH). Inset in both sets of data is a small-angle region coinciding with the (*001*)/(*100*) and (*101*)/(*110*) peaks. The intensity of the (*200*) PZT peak is greater than expected as it is co-incident with a substrate peak. The displayed data in this figure has been corrected for background contributions using a Sonneveld–Visser algorithm [16] for clarity.

Next, the effect of varying the temperature from 500 – 560 °C was investigated: the XRD data from this is displayed in Figure 3.7. For all films, the annealing time was held constant at 30 minutes. For films heated at 1 °C min^{-1}, little change was observed in the XRD data: at all temperatures, the films exhibited a strong preference for the (*100*) orientation. Increasing the temperature to 560 °C led to a reduction in the pyrochlore signal, suggesting more extensive conversion of the intermediate to perovskite.

For the PrH annealed films, a random orientation was observed with greatest intensity in the (*101*) peak. Increasing temperature from 500 to 530 °C greatly increased the intensity of the XRD peaks, suggesting more complete crystallisation of PZT in the perovskite phase, whilst the XRD patterns between 530 and 560 °C films are relatively similar; comparing the angular region containing pyrochlore signal between the two films, it appears that increasing the temperature to 560 °C increases the degree of conversion from the intermediate to perovskite.

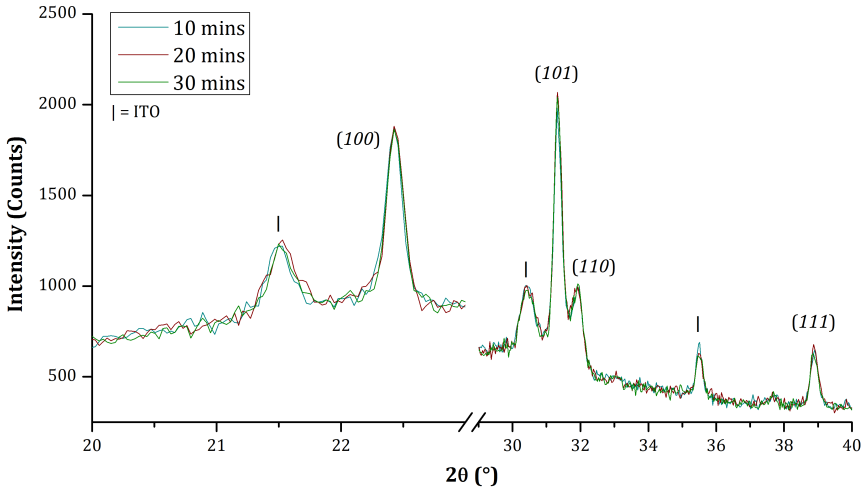

Figure 3.8 – Overlayed XRD patterns for ITO–PZT 30/70 (from 0.4 M sol-gel) thin-films annealed at 560 °C for different lengths of time with no temperature ramp. Figure shows two small-angle regions containing the (*001*)/(*100*) and (*101*)/(*110*) peaks respectively.

Lastly, films were annealed for different times at 500 °C and 560 °C (PrH). For the set at 500 °C, the films were annealed for times up to 1 hour: for heating times up to 30 minutes, the ITO peaks dominate the XRD patterns with observed PZT peaks being very weak — additionally, the data (shown in Appendix Figure A.3) show that the majority of the material still exists in the pyrochlore phase; however, at 40 minutes, the PZT peaks become much more intense with further increases in intensity observed at 60 minutes, along with concomitant reductions in pyrochlore signal. The XRD data for the 560 °C set are shown in Figure 3.8: little change was observed when increasing annealing time from 10 to 30 minutes suggesting that substantial conversion of pyrochlore to PZT occurs rapidly at this temperature, although more advanced crystallographic analysis techniques

such as grazing incidence XRD would be required to verify that full conversion had taken place.

3.3.2 PZT Growth on Spray-Pyrolysed ZnO

Investigation into the growth of PZT on SP-Z was carried out in a similar fashion to the ITO–PZT experiments detailed above: SP-Z films were deposited on glass followed by deposition of the PZT films from a 0.4 M sol-gel and subsequent annealing; as with the prior experiments, changes in temperature, heating rate, and time were made to the annealing regime and the effects probed using XRD. As the results from Section 3.3.1 showed, the ramp rate had a strong influence in determining the crystallographic orientation of PZT on ITO — slower ramping favouring a highly (*100*) orientated film, whilst more rapid annealing favoured a random orientation. As such, a similar experiment was carried out for SP-Z–PZT films, comparing films annealed with no ramp and at 1 °C min^{-1}.

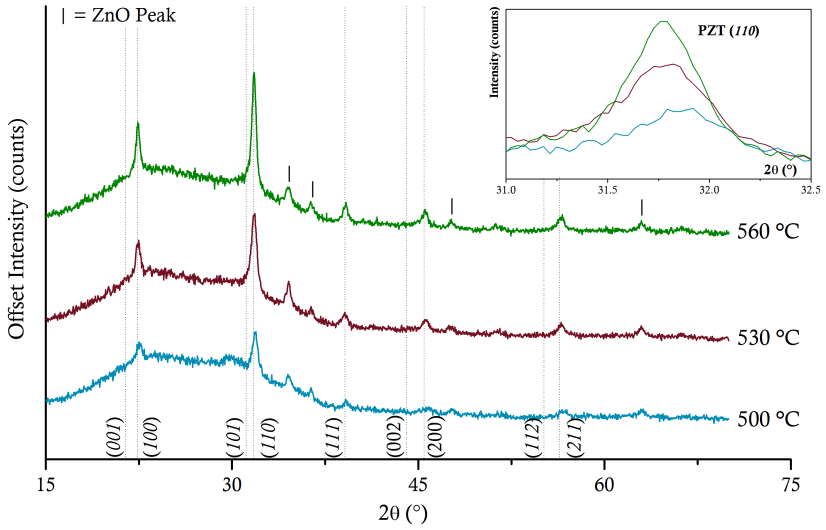

Figure 3.9 – Offset XRD patterns for SPZ–PZT (0.4 M) thin-films annealed for 30 minutes at different temperatures (no temperature ramp). Inset: a small-angle region showing the (*110*) peak (this regon would also contain the (*101*) peak.

In both cases, the films were annealed at 530 °C for 30 minutes: the data for these films is shown in Appendix Figure A.4. Surprisingly, the two XRD patterns for these films are almost identical with the (*110*) orientation producing the most intense peaks — as the peaks are quite broad (suggesting that the PZT crystallites are quite small), the tetragonal splitting cannot be resolved with this technique[1]. Whilst in the randomly

[1]Whilst this may give the PZT pattern the appearance of being a cubic structure, this highly unlikely

orientated PZT powder and ITO–PZT films the (*101*) is more intense than the (*110*), in the ZnO–PZT case this is reversed.

Following on from this, ZnO–PZT films were grown at different temperatures — 500, 530, and 560 °C — using a preheated furnace and annealing films for 30 minutes: the XRD data for this set is shown in Figure 3.9. A general increase in crystallinity was observed with increasing temperature, although there seemed to be no differences in the ratios between the different crystallographic orientations with changing temperature. However, at 500 °C there is a noticeable contribution from the pyrochlore phase which is observe to diminish at higher temperatures, indicating a more complete conversion of precursor material.

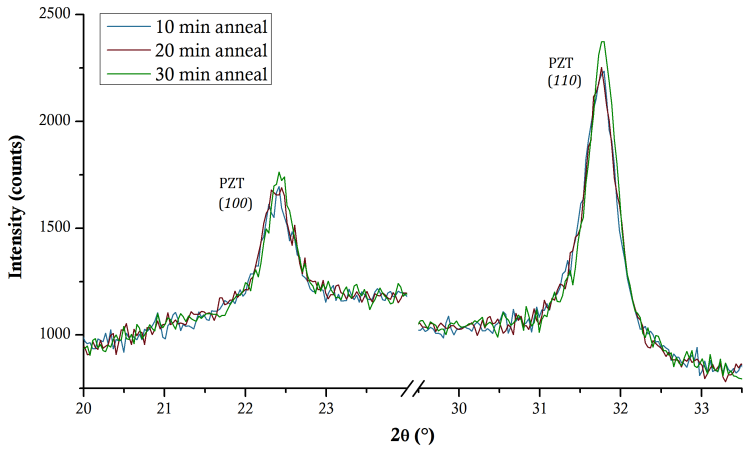

Figure 3.10 – Small-angle regions for XRD patterns of SP-Z–PZT thin-films annealed at 560 °C for different times (no temperature ramp). The first region focusses on the region containing (*001*)/(*100*) peaks, and the second contains the (*101*)/(*110*) peaks.

Lastly, after fixing the annealing temperature at 560 °C, the effect of annealing time was investigated — these results are presented in Figure 3.10. These data suggest that prolonged annealing does not have a great impact on the crystallographic characteristics of these films. No trace of the intermediate pyrochlore phase was observed in the XRD patterns, suggesting that most or all of the intermediate has been converted to crystalline PZT.

In Table 3.2, peak parameters derived from XRD patterns of PZT powder, ITO–PZT, and SP-Z–PZT samples are compared (all samples annealed at 560 °C with no temperature ramp; the powder reference sample was annealed for 1 hour, whereas the thin-films were annealed for 30 minutes).

given that cubic polymorphs of PZT have only been observed at high temperature. Similar XRD patterns

Peak	$(h\ k\ l)$	**PZT Powder**		**ITO–PZT** 1 °C min^{-1}		**ITO–PZT** PrH		**ZnO–PZT** PrH	
		2θ	RPI %	2θ	RPI %	2θ	RPI %	2θ	RPI %
1	(*0 0 1*)	21.38°	8	–	0	–	0	–	0
2	(*1 0 0*)	22.30°	20	22.44°	100	22.43°	65	22.43°	45
3	(*1 0 1*)	31.12°	100	31.34°	38	31.32°	100	–	–
4	(*1 1 0*)	31.74°	50	31.89°	14	31.93°	34	31.78°	100
5	(*1 1 1*)	38.61°	30	38.87°	5	38.85°	20	39.16°	16
6	(*0 0 2*)	43.54°	7	44.05°	4	–	0	–	0
7	(*2 0 0*)	45.53°	27	45.68°	42*	45.63°	34*	45.55	14
8	(*1 0 2*)	49.44°	6	–	0	–	0	–	0
9	(*2 0 1*)	50.93°	6	–	0	–	0	51.24°	6
10	(*1 1 2*)	54.96°	12	–	0	–	0	–	0
11	(*2 1 1*)	56.18°	30	56.39°	6	56.35°	24	56.52°	14

Table 3.2 – Comparison of XRD peak data between the PZT powder reference pattern and ITO–PZT and SP-Z–PZT (grown from 0.4 M sol-gel) thin-films annealed at 560 °C (no ramp) for 30 minutes. Asterisks (*) for the ITO–PZT sample indicate that the (*200*) peak coincides with an ITO peak and therefore its intensity cannot be ascribed solely to contributions from PZT. Although the between the ZnO (*100*) and the PZT (*110)* peaks occur at the same position (31.9°), the ZnO peak is discounted as insignificant given that it is barely detectable in the SP-Z reference scans. The (*101*) peak in the ZnO–PZT films does appear to be present, but cannot be accurately resolved due to the broadening of the (*110*), hence its peak parameters are not displayed here.

Crystallite sizes for the PZT peaks in ITO–PZT and ZnO–PZT films were derived using the Scherrer equation. In the case of ITO–PZT films, the crystallite sizes were similar for films annealed at 1 °C min^{-1} and with PrH: the (*100*) peak in both cases was extremely sharp and the derived crystallite size was much larger than the limit of the Scherrer equation (this is usually considered to be the case for crystallite sizes above $\sim$ 100 nm [18] due to the decrease in peak broadening contributions from the increasing crystallite size), whereas the (*101*) and (*111*) orientations exhibited broader peaks corresponding to relatively fine crystallite sizes of 55 – 70 nm. The ZnO–PZT films contained much smaller grains in all measurable orientations — (*100*), (*110*), and (*111*) — yielding crystallite sizes between 27 – 30 nm. This is discussed in more detail below in Section 3.4.

corresponding to tetragonal PZT have been reported in the literature [17].

3.3.3 Summary

PZT was successfully grown on ITO and ZnO substrates. For ITO–PZT films, annealing with fast heating rates yielded a randomly ordered film, whereas heating at 1 °C min^{-1} led to a preferential orientation in the (*100*) direction. For ZnO–PZT films, no such dependence on annealing conditions was observed with films annealed under all conditions yielding films with a preference for the (*110*) orientation, with a Scherrer equation-derived crystallite size of 27 – 30 nm. Further experiments into ZnO–PZT films were carried out using films annealed at 560 °C in a preheated furnace (no temperature ramp) based on the absence of detectable pyrochlore contributions in these films and the increased XRD peak intensity observed for these films.

3.4 Microstructure and Composition of ZnO–PZT Films

Sol-gel growth of PZT has been well-documented on a number of substrates: for example, PZT has been observed to form large (> 1 μm), single-crystalline rosette structures on ITO [19] whilst growth on platinised Si/SiO_2 tends to yield either rosette or columnar-type morphologies depending on the precursor pyrolysis and annealing conditions [20]. Film evolution has been described as a nucleation-controlled process relying on the formation of interfacial species (*e.g.* intermetallic Pt–Pb phases in the case of platinised substrates [21], or formation of layers of PbO on ITO which acts as a seed for the growth of (*100*)-orientated PZT crystallites) [5]. In the case of low seeding densities, film formation generally proceeds through rosette growth: after formation of a PZT seed, growth is controlled by availability of PbO at the pyrochlore/PZT interface; due to the low seeding densities, rosettes tend to be large, typically between 1 – 10 μm depending on the growth conditions used. At higher seeding densities, fine-grained (submicron) columnar structures are favoured. However, few reports exist detailing the growth of PZT on ZnO and the work in this section aims to shed light on the process using microstructural and compositional characterisation techniques.

3.4.1 Topography

Microstructural characterisation and compositional analysis of ZnO–PZT films was undertaken to shed light on the nature of the growth process — in this investigation, the films were annealed at 560 °C (PrH) for 20 minutes. Firstly, tapping mode AFM was used to characterise the sample topography; scans for both ITO–PZT and SP-Z–PZT films are displayed in Figure 3.11. From the large-area (15 x 15 μm) scans, it is clear that the microstructure of ZnO–PZT and ITO–PZT films are very different: the whilst

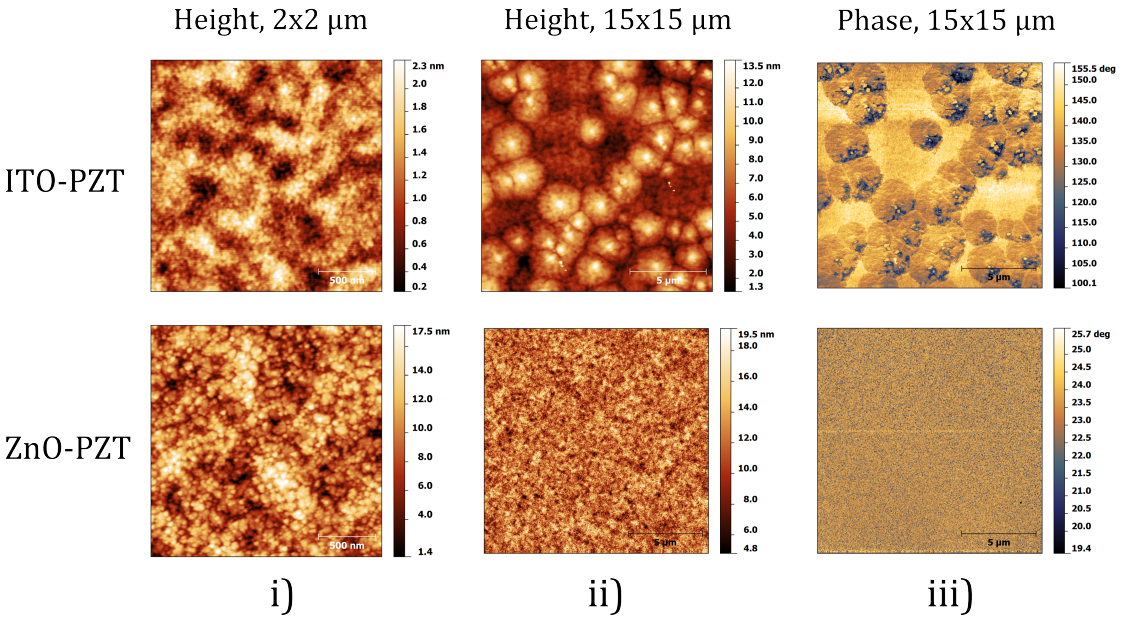

Figure 3.11 – Tapping mode AFM images comparing the topography of ITO–PZT (top row) and ZnO–PZT (bottom row) films. *i)* 2 x 2 μm height scans (ITO–PZT scan from granular region); *ii)* 15 x 15 μm height scans; *iii)* 15 x 15 μm phase scans. The corresponding phase scans acquired with *i)* are included in Appendix Figure A.5.

the ITO–PZT films clearly consist of large rosettes of $\sim 2-3$ μm in diameter surrounded by small, tightly packed grains, the ZnO–PZT structure appears to be quite uniform and does not appear to contain such large features as observed for ITO–PZT. It is unclear whether the ITO–PZT film is a mixed microstructure film of fully converted PZT (*i.e.* both the rosette and granular regions of the film consist of crystallised PZT) or a partially annealed film (due to erroneous underheating of the film): under these conditions, it would be expected that the film would have undergone full conversion to PZT [5, 22] and the XRD results showed no clear evidence for the presence of large quantities of pyrochlore.

The ZnO–PZT film consists of small, tightly packed grains: as a result, this leads to substantial peak broadening in the XRD data for these films. The application of PZT to the ZnO layer causes a significant decrease in R_{RMS} from 8.10 nm to 2.35 nm: a more detailed treatment of these films' topography is given in Section 4.4.1. Fine-grained sol-gel-derived PZT structures have been observed in the case of buffer-layer modified substrates, such as Ti-modified Pt [23] and TiO_2-modified ITO [24]: the perovskite seeding density is much greater on the Ti-containing layer than for the bare substrate, leading to a much more granular structure. From these results it may be posited that ZnO plays a similar role in promoting granular PZT growth, with the small grain size indicative of a high seeding density by ZnO.

3.4.2 Cross-Sectional Composition and Imaging

In the the literature, the choice of Ti and TiO_2 as seeding layers is seen as advantageous given that PZT contains Ti: incorporation of Ti from the buffer layer into the PZT structure may cause local variations in Zr:Ti ratio but if an appropriate PZT composition is chosen the material should still crystallise with the same crystal structure (*i.e.* if the composition lies in the middle of a crystallographic tolerance range). However, it is possible for Zn to be incorporated into the PZT structure [25, 26] which may affect its electrical and polarisation characteristics. Given the acidity of the PZT sol-gel (pH $\sim$ 3.4), some dissolution of ZnO may occur during the spin-coating process [27] which may cause a greater distribution of Zn within the PZT structure than would be expected from simple thermally activated diffusion. To test the effect of acid treatment on ZnO, a solution of acetic acid in MeOH with the same pH as the PZT sol-gel (3.4) was applied to SP-Z films using an identical process to PZT deposition. The resulting XRD and AFM showed little change in the crystallinity or the microstructure of the films suggesting that this did not incur significant changes in the ZnO structure Appendix Figure A.6. However, even a small degree of surface etching will lead to incorporation of Zn ions into solution, potentially leading to PZT doping.

To investigate this, ToF-SIMS and TEM were used to probe the cross-sectional composition and microstructure of the ZnO–PZT films: ToF-SIMS provides information on elemental composition as a function of sample depth and can indicate the extent to which Zn infiltrates the PZT layer, as well as any mixing of Pb, Ti, or Zr into ZnO; through TEM, the ZnO–PZT was imaged to determine the microstructure of the PZT layer and to identify regions which may contain secondary phases.

3.4.2.1 Time-of-Flight Secondary Ion Mass Spectrometry

ToF-SIMS data plots for ZnO and ZnO–PZT films on SiO_2/Si substrates are presented in Figure 3.12: as well as the elemental profiles shown here, profiles derived from isotopic variations of each species were also analysed. To assign material regions it was assumed that, for a sharp junction between two materials, the interface between them occurs at the point where the signal for each material drops to a value of 50 % of that of the bulk. This is illustrated in the Si/ZnO plot which yields a ZnO thickness of 61 nm, a value in good agreement with the profilometry and UV-vis measurements for ZnO given in Section 3.2. The ZnO–PZT film may be divided up into four distinct parts corresponding to bulk ZnO, the ZnO/PZT interface, bulk PZT, and a region of around 4 nm at the PZT surface. The total thickness of the PZT layer was shown to be around 107 nm, whereas the ZnO region is noticeably smaller than that obtained from ToF-SIMS

analysis of a Si/ZnO, as well as the profilometry and UV-vis measurements conducted earlier in this chapter. Whilst this may be partially attributed to the roughness of the ZnO layer (R_{RMS} = 8.10 nm for ITO–SPZ films), the micrographs in Figure 3.13 suggest that PZT modification does affect the microstructure of ZnO.

The interfacial region between the two materials is of particular interest: due to the acidic PZT processing conditions and the temperatures used, it was hypothesised that intermixing between the the constituent elements of PZT and ZnO may take place, with formation of secondary phases being a possible outcome. In the interfacial region, the elemental signal decay rates for PZT are not as high as would be expected for a sharp, flat interface (as for the Si/ZnO interface); however, this is likely to be a reflection of the interfacial roughness, as shown in the TEM data in the following section (Figure 3.13). Elemental intermixing in ToF-SIMS data is often accompanied by a 'diffusion tail', *i.e.* non linear decay in the elemental signal [28]; this is not present in any of the elemental signals here. Additionally, as Zn-doped PZT has previously been synthesised, there was a possibility that Zn could diffuse into the PZT bulk; however, the data for Zn (including its isotopes) showed no trace of diffusion tails.

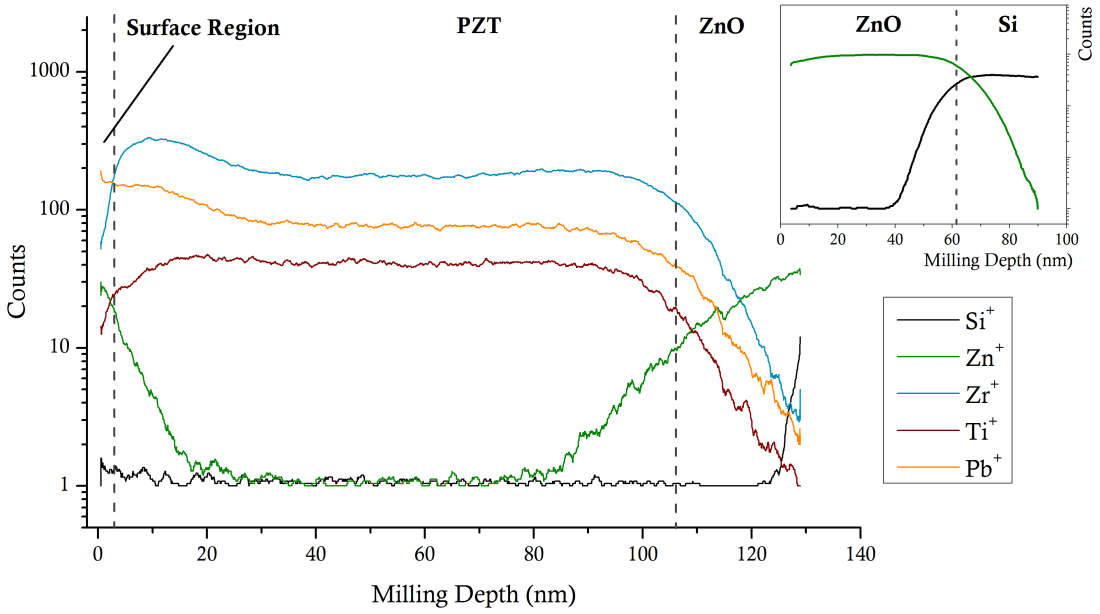

Figure 3.12 – ToF-SIMS depth profile for a Si/SiO_2/SP-Z/PZT film (560 °C, no ramp, 30 minutes). Inset is a plot for an Si/SiO_2/SP-Z film. All elemental signals except for Si are derived from the CsM^+ ion, where M = Zn, Zr, Ti, Pb. Depth was calibrated by profilometry of the crater created during the milling process: the crater was found to be ∼ 129 nm deep. Data acquired by Dr S. Fearn.

Whilst the elemental ratios between Pb, Zr, and Ti remain fairly constant in the bulk region of PZT, the top 20 nm of the film show a number of interesting features:

i) The elemental profiles for Pb, Zr, and Ti remain flat in the bulk. Each of the Pb, Zr, and Ti signals (including isotopic species) were observed to increase at a depth of around 35 nm with Zr and Ti signals reaching maxima at $\sim$ 15 nm deep: for Zr, this increase in signal corresponds to $\sim$ 80 % compared to a $\sim$ 55 % rise in Ti (these were derived from multiple isotopic profiles), suggesting a slight shift in composition in this region. The origin of this signal increase is uncertain, perhaps indicating an increase in material density.

ii) All isotopic species for Zr and Ti exhibit a sharp decline in signal intensity near the top of the film, starting at a depth of around 4 nm.

iii) The Pb signals increase at a depth of around 35 nm, as for Zr and Ti; however, rather than declining at the top of the film the signal increases throughout the surface region. Consequently, the data suggest that the PZT surface is Pb rich relative to Zr and Ti. Given that Pb evaporates from the surface during annealing of the PZT films due to its volatility, a population of excess Pb at the surface is not unexpected.

iv) The signals for Zn and its isotopes show that the element is excluded from the PZT bulk and does not diffuse into this region. However, these signals are observed to rise in the surface region, starting at a depth of $\sim$ 15 nm, reaching the 50 % value at a depth of 3 nm. Whilst this may be interpreted as evidence of discontinuities in the PZT layer, in such a case the Zn signal would not decay to zero. As such, it may be inferred that some Zn is subsumed from the ZnO layer during processing and preferentially segregates to the film surface during processing. Consequently, the surface region (top 3 nm) of the PZT film is predominantly populated by Pb and Zn, rather than by pure PZT.

The imaging data in the following section is used to complement these results, particularly in determining the structure of the interface between ZnO and PZT.

3.4.2.2 Transmission Electron Microscopy

Transmission electron micrographs comparing cross-sections of unmodified and PZT-modified SP-Z films are given in Figure 3.13: as stated previously, the micrographs were acquired from a single cross-section of a ZnO film and therefore cannot be assumed to be representative of a film; however, these data can be used to complement the other structural characterisation methods. From a visual comparison, it is clear that the PZT modification affects the thickness of the ZnO layer — this was also suggested in the ToF-SIMS data shown in Figure 3.12. Thickness measurements obtained from multiple

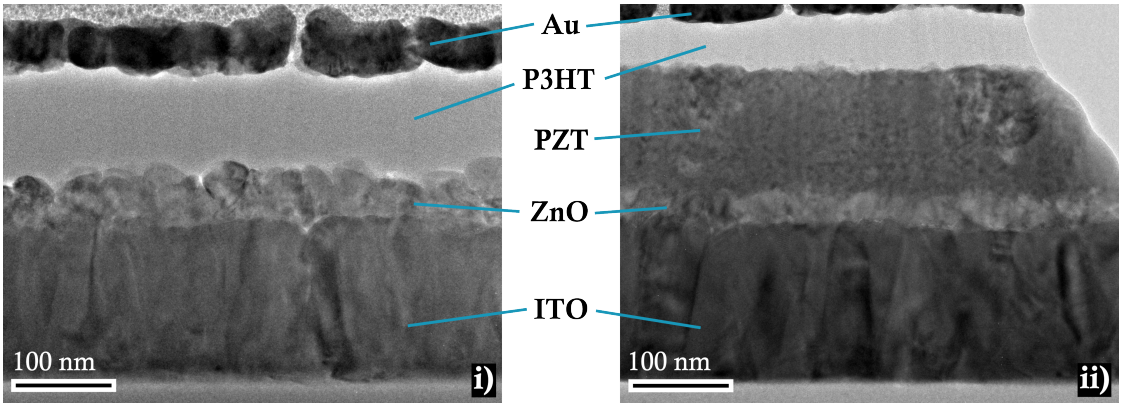

Figure 3.13 – Transmission electron micrographs acquired for *i)* unmodified and *ii)* 0.4 M PZT sol-gel modified thin-films with the structure ITO–SP-Z–(PZT)–P3HT–Au; the P3HT layer was used to provide clearer images of the surface of the oxide film. Micrographs were acquired at a magnification of 36,000 x with a beam energy of 300 kV. Imaging was carried out by Dr C. McGilvery; sample preparation was performed by C. Burgess and Dr J. B. Gilchrist.

micrographs yielded an average ZnO thickness of 34 nm compared to an unmodified SP-Z thickness of 48 nm (measured in Section 3.2.2). The thickness of the PZT region was measured by the same method, yielding a value of 136 nm — this value is greater than the measured thickness of PZT films on glass derived using profilometry (105 nm) and in the ToF-SIMS data (107 nm) although as the TEM cross-section is taken from a small region of the film (approximately 500 nm in length), this is not necessarily representative of the entire structure. In contrast, the ToF–SIMS data was derived from an area with dimensions on the order of 10^{-4} m. The PZT layer itself is dense and highly polycrystalline — this is consistent with the AFM data in Section 3.4.1 which showed the PZT consisting of small, tightly packed grains.

High resolution TEM was employed to investigate the interface between ZnO and PZT to assess the effect of PZT modification on the ZnO and to ascertain if any secondary phases were present in the region. In Figure 3.14, the high resolution micrographs show the ZnO region before and after PZT modification: it appears that, whilst the PZT modification does dissolve some of the ZnO from the top of the film, the bulk ZnO region bears close resemblance to that of the unmodified reference.

Micrographs of the PZT layer and the ZnO–PZT interface are shown in Figure 3.15. The PZT region is highly polycrystalline with most continuous regions of lattice fringes being between 5 and 20 nm in length: these crystallite orientations were assigned using XRD-derived *d*-spacings displayed in Appendix Table A.2 for ZnO and Appendix Table A.3 for PZT.

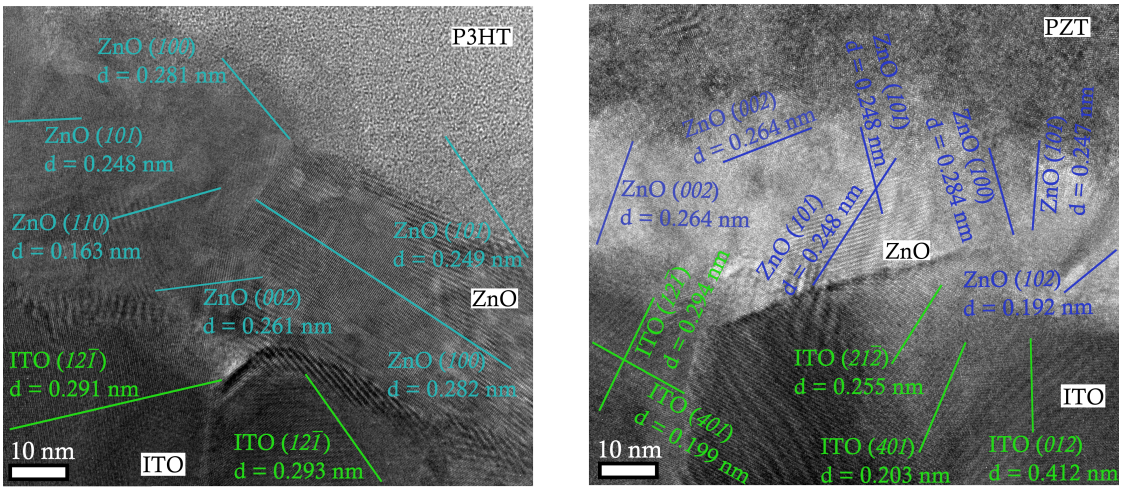

Figure 3.14 – High resolution transmission electron micrographs showing the effect of PZT modification on the ZnO layer: unmodified SP-Z (shown with its P3HT capping layer) is displayed on the left; the layer on the right was modified with 0.4 M PZT sol-gel. Crystallites assigned from their characteristic *d*-spacings are presented in green for ITO and blue for ZnO. Images were acquired at a magnification of 255,000 x and a beam energy of 300 kV. Imaging was carried out by Dr C. McGilvery; sample preparation was performed by C. Burgess and Dr J. B. Gilchrist.

Whilst it was speculated that an amorphous layer of material may form at the ZnO–PZT interface, the high-resolution TEM data shows that the structure possesses a crystalline–crystalline interface, as evidenced by the ubiquitousness of lattice fringes. From measurement of the *d*-spacing of the lattice fringes close to the interface (as shown in Figure 3.15), it appears that a secondary phase forms in this region: crystallites with lattice spacings of ~ 0.296 nm and ~ 0.303 nm do not correspond to either ZnO or PZT. Whilst the composition of this phase could not be ascertained in this experiment, one possible candidate is PbO, especially given the excess of lead in the PZT sol-gel as well as its role in converting the pyrochlore intermediate to crystalline PZT [5]. Formation of a PbO layer has been thought to nucleate (*100*) crystallites of PZT [29, 30] on a variety of substrates, thought to proceed through the tetragonal PbO (*001*) plane (d = 0.499 nm).

There are two main forms of PbO, litharge (tetragonal, $P4/nmm$) and massicot (orthorhombic, $Pbcm$), the former being a low temperature polymorph and transition from tetragonal to orthorhombic occurring at $\sim$ 580 °C [31]. Using standard XRD reference data (JCPDS 01-085-711 for litharge, JCPDS 01-077-1971 for massicot) it appears that the latter would be the more likely candidate as it possesses *d*-spacings of 0.307 nm (*111*) and 0.295 nm (*002*), where the (*111*) orientation is dominant in the powder form. Further supporting this, it has been observed that the presence of a variety of different elements such as Si, Ge, Se, and Mo in low concentrations (10 –

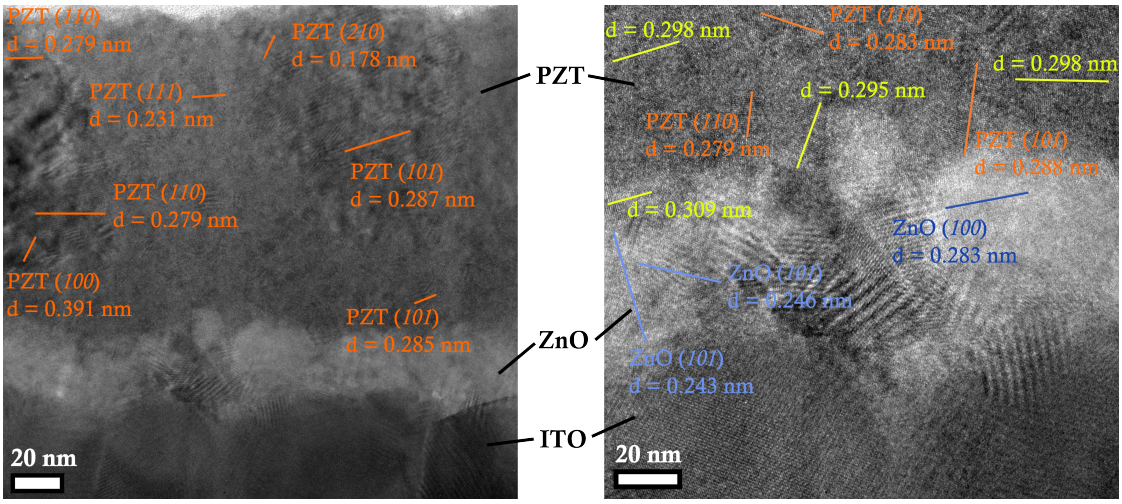

Figure 3.15 – High resolution transmission electron micrographs of **Left:** the bulk region of the PZT (magnification 100,000 x); **Right:**: the interfacial region between ZnO and PZT with lattice fringe *d*-spacings assigned for ZnO (blue), PZT (orange), and the secondary phase (yellow, discussed in the text). Images were acquired with a beam energy of 300 kV. Imaging was carried out by Dr C. McGilvery; sample preparation was performed by Dr J. B. Gilchrist.

100 ppm) stabilise the orthorhombic form of PbO [32] — whilst Zn was not tested in this experiment, it is conceivable that it could also play a similar role in the stabilisation of the orthorhombic phase. It was not determined the extent to which Zn was incorporated into this phase: it has been established that ZnO is sparingly soluble (< 5 %mol) in PbO [33]; Keester *et al.* succeeded in producing $Pb_{1-x}Zn_xO$ in which the Zn content was calculated to be extremely low (< 2 %mol), although high oxygen pressures were required in this process. The inhibition of tetragonal PbO formation would then appear to suppress the formation of a preferentially (*100*)-textured PZT film as the resulting ZnO–PZT structures are preferentially orientated in the (*110*) direction.

Further local compositional analysis such as energy-dispersive X-ray spectroscopy (EDX) may be employed to confirm the presence of PbO in these films. Imaging of the intermediate stages of film evolution would also be useful to understand whether the formation of the secondary phase is key in seeding growth of the PZT film — the XRD data suggest that PZT crystallises rapidly on ZnO (*cf.* ITO) and the formation of PbO on ZnO may play a key role in the growth process; additionally, if the phase is indeed PbO, investigation of prolonged annealing may show whether this phase diminishes with greater thermal energy input. Additionally, the presence of these phases may have an impact on the functional properties of the ZnO–PZT structure and may serve to counter polarisation in the material.

3.4.3 Summary

ZnO provides a high seeding density surface for the nucleation of PZT; as a result, the ZnO–PZT thin-films produced in this work consist of small, densely packed grains around 20 nm in diameter; this is in contrast to ITO–PZT thin-films in which growth proceeds via above-micron rosette formation. From cross-sectional imaging of these films, the PZT modification leads to microstructural changes in the ZnO layer, as well as a reduction of around 15 nm in its thickness: the data show that whilst the bulk region of PZT remains uncontaminated with Zn, there is a significant increase in the Zn signal at the top of the PZT film (a region of $\sim$ 3 nm), suggesting segregation of Zn etched by the sol-gel to the top of the film. The surface also appears to be lead-rich, given an increase in the Pb signals in this surface region. The absence of diffusion tails in the ToF-SIMS signals for Pb, Ti, Zr, and Zn at the ZnO–PZT interface suggest that there is no significant elemental mixing between the two materials, and that the slow decay in signal at this interface arises simply from the roughness of the interface. From analysis of high resolution TEM data, it appears that the ZnO–PZT interface is crystalline, with the *d*-spacing of crystallites in the PZT region suggesting the presence of a secondary phase. Whilst the composition of this phase was not analysed, one potential candidate is orthorhombic PbO (massicot) which has been shown to stabilise in the presence of trace metal impurities.

3.5 Conclusions

Growth of PZT on ZnO was found to yield dense, randomly orientated, highly polycrystalline thin-films with small grain sizes ($\sim$ 20 nm) at temperatures in the range 500 – 560 °C; films in subsequent experiments would be annealed at 560 °C based on the XRD data presented in this chapter. The growth of PZT on ZnO was found to differ substantially from growth on ITO which tends to favour large ($>$ 1 μm) rosette formation; the small grain size present in these films relates to a much greater seeding density offered by ZnO compared to ITO.

Compositional and microstructural analysis was carried out on the ZnO–PZT films using ToF-SIMS and TEM respectively: whilst growth of PZT on ZnO from sol-gel has previously been reported, no study of this interface has previously been published. From the compositional data, it was ascertained that Zn does not diffuse into the PZT bulk; however, it was observed that some Zn is subsumed from the ZnO substrate and segregates to the material surface (in a region of approximately 3 nm in depth). Moreover, modification with PZT was seen to reduce the thickness of the ZnO layer in both compositional and TEM data. From high-resolution TEM micrographs, it was determined

that a secondary phase may occur at the ZnO–PZT interface: although a full analysis of this region was not carried out, orthorhombic PbO (Massicot) is viewed as a likely candidate. Further study is needed to determine whether PbO plays a role in 'seeding' PZT on ZnO, as has previously been observed in the case of PZT growth on ITO. As there is interest in developing ZnO–PZT structures due to the polarisation coupling between the two materials [4, 34], the presence of a secondary phase should be taken into account in device development as its presence may have an impact on both the material's functional and contact properties.

References

[1] D. Y. Chen, T. E. Murphy, and J. D. Phillips, "Properties of ferroelectric Pb(Zr,Ti)O_3 thin-films on ZnO/Al_2O_3 (*0001*) epilayers," *Thin Solid Films* **491**(1-2), pp. 301–304, 2005.

[2] X. Wang, Y. Wang, J. Yin, and Z. Liu, "Enhanced ferroelectric properties of Pb($Zr_{0.52}Ti_{0.48}$)O_3 films on Pt/TiO_2/SiO_2/Si(*001*) using ZnO buffer layer," *Scr. Mater.* **46**, pp. 783–787, June 2002.

[3] V. M. Voora, T. Hofmann, M. Brandt, M. Lorenz, M. Grundmann, N. Ashkenov, H. Schmidt, N. Ianno, and M. Schubert, "Interface polarization coupling in piezoelectric–semiconductor ferroelectric heterostructures," *Phys. Rev. B* **81**, p. 5307, May 2010.

[4] M.-X. Zhou, Z.-W. Li, B. Chen, J.-G. Wan, and J.-M. Liu, "Tunable resistive switching behaviour in ferroelectric–ZnO bilayer films," *J. Phys. D. Appl. Phys.* **46**, p. 5304, Apr. 2013.

[5] S. S. Roy, H. Gleeson, C. P. Shaw, R. W. Whatmore, Z. Huang, Q. Zhang, and S. Dunn, "Growth and characterisation of lead zirconate titanate (30/70) on indium tin oxide coated glass for oxide ferroelectric-liquid crystal display application," *Integr. Ferroelectr.* **29**(3-4), pp. 189–213, 2000.

[6] M. A. McLachlan, D. W. McComb, M. P. Ryan, A. N. Morozovska, E. A. Eliseev, E. A. Payzant, S. Jesse, K. Seal, A. P. Baddorf, and S. V. Kalinin, "Probing local and global ferroelectric phase stability and polarization switching in ordered macroporous PZT," *Adv. Funct. Mater.* **21**(5), pp. 941–947, 2011.

[7] A. Bashir, P. H. Wobkenberg, J. Smith, J. M. Ball, G. Adamopoulos, D. D. C. Bradley, and T. D. Anthopoulos, "High-performance zinc oxide transistors and circuits fabricated by spray pyrolysis in ambient atmosphere," *Adv. Mater.* **21**(21), p. 2226, 2009.

[8] Y. Vaynzof, D. Kabra, L. Zhao, P. K. H. Ho, A. T.-S. Wee, and R. H. Friend, "Improved photoinduced charge carriers separation in organic–inorganic hybrid photovoltaic devices," *Appl. Phys. Lett.* **97**(3), p. 3309, 2010.

[9] N. O. V. Plank, M. E. Welland, J. L. MacManus-Driscoll, and L. Schmidt-Mende, "The backing layer dependence of open circuit voltage in ZnO/polymer composite solar cells," *Thin Solid Films* **516**(20), pp. 7218–7222, 2008.

[10] E. H. Kisi and M. M. Elcombe, "u parameters for the wurtzite structure of ZnS and ZnO using powder neutron diffraction," *Acta Crystallogr. C* **45**, pp. 1867–1870, Dec. 1989.

[11] J. Downing, M. P. Ryan, N. Stingelin, and M. A. McLachlan, "Solution processed hybrid photovoltaics: preparation of a standard ZnO template," *J. Photonics Energy* **1**(1), pp. 11117–11119, 2011.

[12] J. Frantti, J. Lappalainen, S. Eriksson, V. Lantto, S. Nishio, M. Kakihana, S. Ivanov, and H. k. Rundlöf, "Neutron Diffraction Studies of $Pb(Zr_xTi_{1-x})O_3$ Ceramics," *Jpn. J. Appl. Phys.* **39**, pp. 5697–5703, Sept. 2000.

[13] F. C. Krebs, Y. Thomann, R. Thomann, and J. W. Andreasen, "A simple nanostructured polymer/ZnO hybrid solar cell — preparation and operation in air," *Nanotechnology* **19**(42), p. 4013, 2008.

[14] R. S. Wang, Q. L. Gu, C. C. Ling, and H. C. Ong, "Studies of oxide/ZnO near-interfacial defects by photoluminescence and deep level transient spectroscopy," *Appl. Phys. Lett.* **92**, p. 2105, Jan. 2008.

[15] Z. Huang, Q. Zhang, and R. W. Whatmore, "Structural development in the early stages of annealing of sol-gel prepared lead zirconate titanate thin films," *J. Appl. Phys.* **86**, p. 1662, Aug. 1999.

[16] E. J. Sonneveld and J. W. Visser, "Automatic collection of powder data from photographs," *J. Appl. Crystallogr.* **8**, pp. 1–7, Feb. 1975.

[17] Q. Zhang, C. P. Shaw, Z. Huang, and R. W. Whatmore, "Sol-gel derived lead zirconate titanate thick films and their improved pyroelectric properties," *Integr. Ferroelectr.* **64**(1), pp. 207–216, 2004.

[18] U. Holzwarth and N. Gibson, "The Scherrer equation versus the 'Debye-Scherrer equation'," *Nat. Nanotechnol.* **6**, p. 534, Sept. 2011.

[19] Y. Ohya, T. Tanaka, and Y. Takahashi, "Dielectric properties of lead zirconate titanate thin film fabricated on In_2O_3:Sn substrate by sol-gel method," *Jpn. J. Appl. Phys.* **32**, pp. 4163–4167, Sept. 1993.

[20] S. A. Impey, Z. Huang, A. Patel, R. Beanland, N. M. Shorrocks, R. Watton, and R. W. Whatmore, "Microstructural characterization of sol-gel lead–zirconate–titanate thin films," *J. Appl. Phys.* **83**, p. 2202, Feb. 1998.

[21] Z. Huang, Q. Zhang, and R. W. Whatmore, "Low temperature crystallization of lead zirconate titanate thin films by a sol-gel method," *J. Appl. Phys.* **85**, p. 7355, May 1999.

[22] S. Dunn and R. Whatmore, "Substrate effects on domain structures of PZT 30/70 sol-gel films via PiezoAFM," *J. Eur. Ceram. Soc.* **22**(6), pp. 825–833, 2002.

[23] K. Aoki, Y. Fukuda, K. Numata, and A. Nishimura, "Effects of titanium buffer layer on lead–zirconate–titanate crystallization processes in sol-gel deposition technique," *Jpn. J. Appl. Phys.* **34**, pp. 192–195, Jan. 1995.

[24] C. P. Shaw, S. S. Roy, R. W. Whatmore, H. Gleeson, Z. Huang, Q. Zhang, and S. Dunn, "Growth and characterisation of lead zirconate titanate (30/70) thin films using TiO_2 seeding for oxide ferroelectric-liquid crystal display application," *Ferroelectrics* **256**, pp. 159–174, Jan. 2001.

[25] S. K. S. Parashar, R. N. P. Choudhary, and B. S. Murty, "Nanocrystalline Zn doped PZT synthesized by mechanical alloying," *Ferroelectrics* **325**, pp. 65–74, Sept. 2005.

[26] A. Dalakoti, A. Bandyopadhyay, and S. Bose, "Effect of Zn, Sr, and Y addition on electrical properties of PZT thin films," *J. Am. Ceram. Soc.* **89**, pp. 1140–1143, Mar. 2006.

[27] P. Delahay, M. Pourbaix, and P. Van Rysselberghe, "Potential-pH diagram of zinc and its applications to the study of zinc corrosion," *J. Electrochem. Soc.* **98**, p. 101, Mar. 1951.

[28] L. Qiao, T. C. Droubay, T. Varga, M. E. Bowden, V. Shutthanandan, Z. Zhu, T. C. Kaspar, and S. A. Chambers, "Epitaxial growth, structure, and intermixing at the $LaAlO_3/SrTiO_3$ interface as the film stoichiometry is varied," *Phys. Rev. B* **83**, p. 085408, Feb. 2011.

[29] S.-Y. Chen and I.-W. Chen, "Temperature–time texture transition of $Pb(Zr_{1-x}Ti_x)O_3$ thin films: I, role of Pb-rich intermediate phases," *J. Am. Ceram. Soc.* **77**, pp. 2332–2336, Sept. 1994.

[30] S.-Y. Chen and I.-W. Chen, "Temperature–time texture transition of $Pb(Zr_{1-x}Ti_x)O_3$ thin films: II, heat treatment and compositional effects," *J. Am. Ceram. Soc.* **77**, pp. 2337–2344, Sept. 1994.

[31] K. Keester and W. White, "Phase relations in the system PbO–ZnO–O at high oxygen pressures," *J. Inorg. Nucl. Chem.* **33**, pp. 3269–3284, Oct. 1971.

[32] W. Kwestroo, J. de Jonge, and P. Vromans, "Influence of impurities on the formation of red and yellow PbO," *J. Inorg. Nucl. Chem.* **29**, pp. 39–44, Jan. 1967.

[33] M. P. Bauleke and K. O. McDowell, "The system lead oxide–zinc oxide," *J. Am. Ceram. Soc.* **46**, pp. 243–243, May 1963.

[34] E. Cagin, D. Y. Chen, J. J. Siddiqui, and J. D. Phillips, "Hysteretic metal–ferroelectric–semiconductor capacitors based on PZT/ZnO heterostructures," *J. Phys. D. Appl. Phys.* **40**, pp. 2430–2434, Apr. 2007.

Chapter 4

Towards PZT Interlayers

4.1 Introduction

The work reported in Chapter 3 focussed on the growth of PZT thin-films $\sim$ 105 nm in thickness in order to understand growth processes and to facilitate characterisation of the material. However, interface modifiers in oxide:polymer hybrid photovoltaic (hPV) devices are usually rather thinner: molecular modification of the oxide surface is usually effected through the formation of self-assembled monolayers, whilst inorganic interlayers are generally found to be grown at thicknesses of less than 25 nm. This is especially important for PZT given the high resistivity of the material compared to other inorganic interface modifiers such as TiO_2 and CdS. Recently, there has been great interest in the growth of nanoscale ferroelectric structures such as ultrathin films and nanostructures [1, 2] and research into effects of reduced size on ferroelectric properties: whilst it had previously been thought that ferroelectric effects would diminish substantially at length scales below $\sim$ 20 nm, more recent studies have shown that they may persist in films as thin as ($\sim$ 1 nm) [3].

The aim of the work reported in this chapter is to grow continuous thin-films of PZT 30/70 on ZnO with thicknesses of $<$ 25 nm, such that they may be incorporated into hPV devices. It has been observed that perovskite films grown at small length scales may reorganise on the substrate to form non-continuous structures such as islands which are undesirable in the context of this work [4, 5]. Evaluation of these thin-films was carried out by topographical characterisation and subsequent microstructural analysis using atomic force microscopy (AFM). The surface and bulk composition were characterised through X-ray photoelectron spectroscopy (XPS) and time-of-flight secondary ion mass spectroscopy (ToF-SIMS). Although it was not possible to characterise the ferroelectric properties of these films in this work, details of how this may be carried out is outlined in Chapter 6, namely through the use of piezo-force microscopy (PFM).

4.2 Growth of PZT

Reduction of PZT thickness was achieved by changing the concentration of the precursor sol-gel and using the same processing conditions outlined in Chapter 3. To dilute the sol-gel, a solution of acetic acid in methanol with approximately the same pH as the stock sol-gel (pH 3.4) was used. The stock sol-gel (0.4 M Zr + Ti) was found to produce a thin-film of approximately 105 nm on quartz, as measured by profilometry. The dilution levels of this stock solution were subsequently selected based on the assumption of a linear relationship between concentration and thickness.

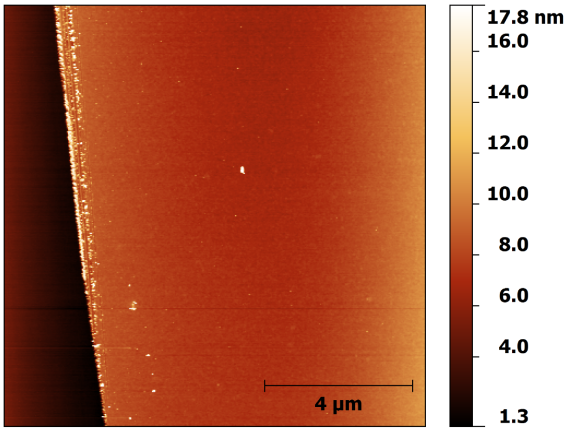

PZT Conc. (M)	$\frac{[\text{Sol}]}{[\text{Stock}]}$	Predicted Thickness (nm)	AFM Thickness (nm)
0.400 (stock)	1.0000	105*	102.0 ± 4.0
0.100	0.2500	26	17.4 ± 3.2
0.050	0.1250	13	10.8 ± 4.6
0.025	0.0625	7	6.4 ± 0.2
0.010	0.0250	3	3.9 ± 0.7
0.001	0.0025	< 1	—

Figure 4.1 – *Left:* Tapping mode AFM topography image for a scratched film derived from a 0.025 M PZT sol-gel deposited on Si/SiO_2: the thickness was evaluated by measuring the step height between the material and the exposed substrate. *Right:* table of thicknesses acquired for different PZT sol-gel concentrations.

Physical evaluation of PZT thickness was carried out by depositing the PZT sol-gel on very low roughness Si/SiO_2 substrates: although these thickness values are not directly transferrable to ZnO (due to roughness, differences in wetting *etc.*), they do provide a measure as to the amount of material deposited for different sol-gel concentrations using these conditions. However, PZT thin-films in this work are identified by the concentration of the sol-gel they are derived from as opposed to the thickness values measured here. After spin-coating at 3000 rpm and drying the films at 200 °C, the film was scratched in different locations using a scalpel then annealed at 560 °C for 30 minutes (no temperature ramp). Scratching the films before annealing was done as crystalline PZT is a hard material [6] and difficult to etch due to the high chemical resistance of the Zr–O bonds [7]. Although only a small proportion of the PZT will crystallise on Si/SiO_2 under these conditions, annealing these films was found to increase substantially the hardness of these films, thus film scratching was carried out before annealing when the film was in a

softer state. The height step in the film was then measured using tapping mode AFM: despite its limited scan range, AFM is much more sensitive to changes in height than profilometry. Measurements for films derived from 0.4 M PZT sol-gel yielded similar results by profilometry (105 ± 7 nm), but scans for thinner films exhibited poor signal-to-noise ratios. The topography images were levelled and corrected using Gwyddion [8], and the results are displayed in Figure 4.1.

As the 0.001 M sol-gel is a 'wash' modifier — *i.e.* not expected to form a continuous thin-film, rather just modifying the ZnO surface chemistry — its thickness could not be evaluated using this method. The film thicknesses are in good agreement with the predicted thicknesses (save for a thinner-than-expected 0.1 M film) and are of appropriate length scales for their intended application in hPVs.

4.2.1 XRD

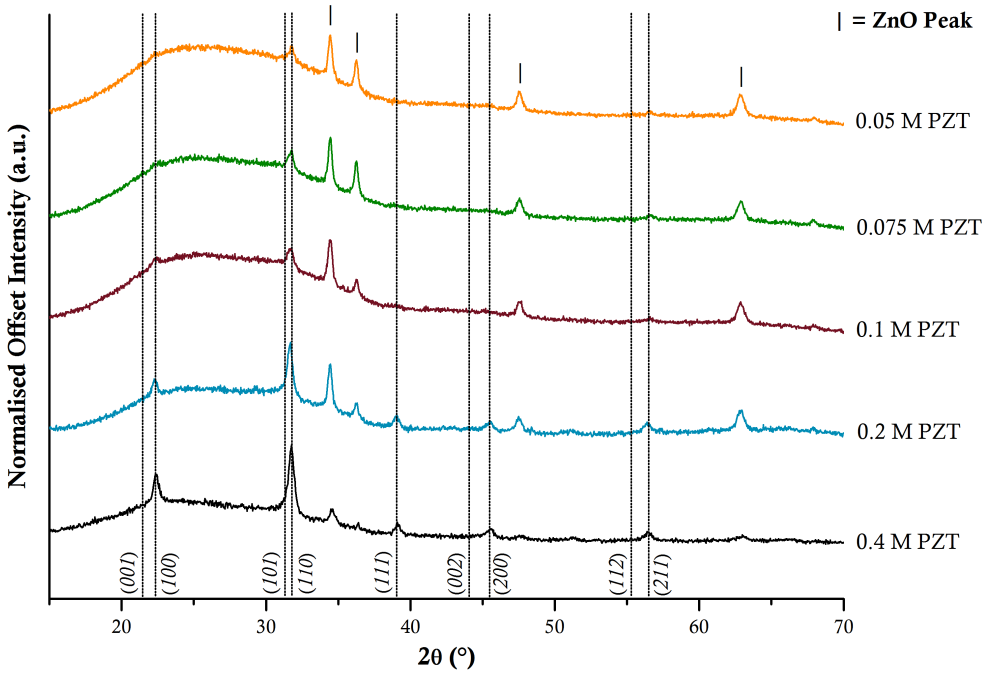

Figure 4.2 – Offset XRD patterns for SP-Z–PZT thin-films derived from PZT sol-gels of different concentration. All films were annealed under the same conditions: 560 °C in a preheated furnace, 20 mins.

As shown in Figure 4.2, PZT peaks were found to be present for diluted sol-gels down to 0.05 M (∼ 11 nm): at this point, only the (*110*) peak is visible. At more dilute concentrations, the resulting PZT layers were too thin for detection using the XRD apparatus. In contrast, films derived from diluted sol-gels were not observed to crystallise on ITO. It is likely that this is related to the differing perovskite seeding densities of ITO

and ZnO, as discussed in Section 3.4: in the case of ITO–PZT, the low seeding density combined with the reduced volume of precursor material (and, importantly, the local concentration of PbO [9]) inhibits rosette growth; however, in the case of ZnO–PZT, the high seeding density leads to fast crystallisation of PZT, even with the reduced material volume.

4.3 Composition

4.3.1 X-Ray Photoelectron Spectroscopy

XPS was used to probe both the surface composition of ZnO–PZT films and their surface chemistry through analysis of the O 1*s* core lines. In contrast to ToF–SIMS, the XPS was used to probe the material surface: although the incident X-rays may penetrate deep into the sample, only electrons originating from the first few nanometres of the surface will be able to escape, the others being subject to collisions with other atoms [10]. In this work, Al K_α radiation was used (1486.6 eV) to analyse the samples with a probe size of around 3 μm in diameter. The atomic percentages are calculated from fitting of the characteristic core lines in the XPS spectrum and determining the peak area, followed by correction for the specific elements using known atomic sensitivity factors. Data were collected for each ZnO–PZT film from two samples.

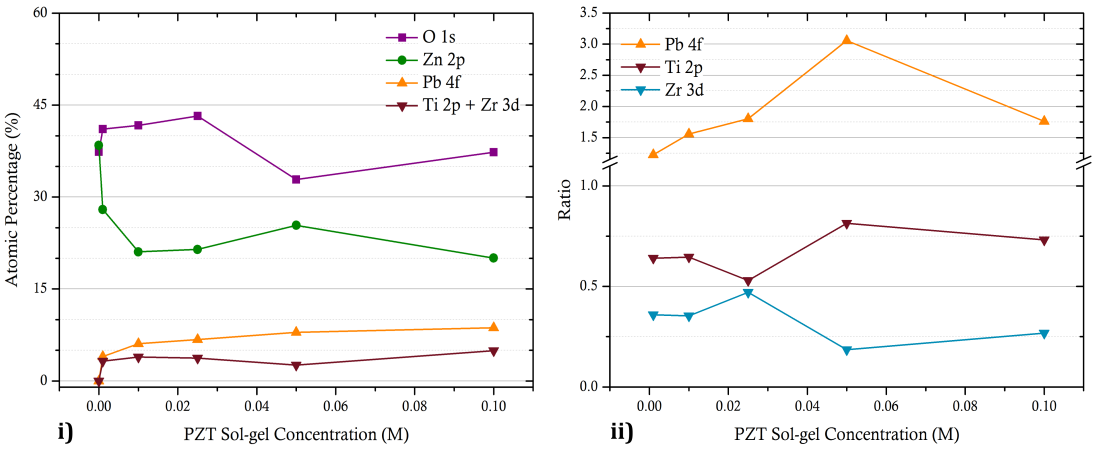

Figure 4.3 – *i)* Relative atomic percentage plots for the core lines of Pb, Ti, Zr, Zn, and O with changing PZT sol-gel concentration. *ii)* The relative ratios of Pb 4*s*, Ti 2*p*, and Zr 3*d* normalised to Ti + Zr = 1. Data acquired by Dr E. Ratcliff.

Relative atomic percentages of Zn, Pb, Ti, Zr, and O are shown in Figure 4.3, as well as the ratios between Pb, Ti, and Zr normalised such that Ti + Zr = 1. In the ideal case, it would be expected that the Pb:(Ti+Zr) ratio would be 1:1 and that the Zn signal

would decrease with increasing PZT sol-gel concentration as the PZT layer increases in thickness. However, the Pb:Ti:Zr ratios deviate from this expected behaviour — firstly, the actual ratio of the Zr:Ti ions varies from the expected $Zr_{0.3}Ti_{0.7}$. Whilst most of the films range from Zr = 0.19 to 0.36 (thus well within the tetragonal region of PZT phase behaviour), at 0.05 M the ratio is 0.47:0.53 which lies very close to the morphotropic phase boundary of PZT. As reported in [11], a depth-profile Auger electron spectroscopy (AES) study of sol-gel-derived PZT thin-films revealed that there are fluctuations in composition throughout the bulk, particularly at grain boundaries where Pb and Zr concentration tend to rise with decreases in Ti. However, given the relatively large spot size used in XPS (*i.e.* much larger than the grain size of the film), the results presented do not arise from grain boundary effects. This composition was observed in two separate PZT 0.05 M films; however, it should be noted that these films were from the same batch. From the ToF-SIMS data of a ZnO–PZT 0.4 M film in Section 3.4.2, the relative ratio of the Zr and Ti signals was observed to change close to the film surface, and it may be the case that there is the potential for significant composition variation in this region of ZnO–PZT films. However, a more comprehensive ToF-SIMS study would be required to verify this.

Another observation made from the ToF-SIMS data acquired from the 0.4 M PZT thin-film was that the Pb concentration appeared to increase near the surface due to the excess $Pb(OAc)_2$ used in the sol-gel. This is also reflected in these results: the thinnest PZT layer (0.001 M) is closest to the expected PZT stoichiometry (1.23:0.36:0.64) with the Pb %at tending towards 2.00 with increasing sol-gel concentration. The 0.05 M films yielded slightly higher Pb concentrations than the other films, with a Pb %at of 3.06 times the concentration of the Ti and Zr components.

The Zn $2p$ signal is observed to decrease on modification with PZT; however, it does not fall below the sum of the individual Pb $4f$, Ti $2p$, and Zr $3d$ signals, despite the increasing PZT thickness ($\sim$ 17 nm at 0.1 M). As shown in Figure 3.12 (Section 3.4.2), for a ZnO–PZT (0.4 M) film, a surface region of around 2 – 3 nm forms at the top of the film; additionally, the $CsZn^+$ signal was observed to increase at the film surface whilst being absent in the PZT bulk. Whilst this could possibly be attributed to island formation (*i.e.* the film surface contains distinct regions of both ZnO and PZT components) or discontinuity in the PZT film, the ToF-SIMS data on dense, continuous PZT layers in the previous chapter suggests that this surface Zn arises from chemical etching of ZnO by the sol-gel.

4.3.1.1 Surface Chemistry

The O 1*s* core line data shown in Figure 4.4 show the evolution of the the oxygen bonding in the film with increasing PZT sol-gel concentration. The unmodified ZnO film appears to consist of 3 components as outlined in [12]: the main O–Zn bond, O–Zn bonds affected by nearby defects, and surface HO–Zn groups. Modification with PZT yields a shift in the core line maximum to lower binding energy, centred around 530.8 eV, which corresponds to the energy of surface O–Pb bonds [13, 14]. Modification of ZnO with 0.001 M PZT leads to an immediate decline in the Zn hydroxyl signal; moreover, the Pb bonding dominates the O 1*s* shape. Although the 0.001 M modification should only modify the very top of the ZnO film, the relative drop in O–Zn contribution to the core line suggests that this modification affects a larger volume of the ZnO film. Whilst it is possible to derive quantitative data from O 1*s* core line fitting, due to the presence of up to 6 discrete components within a 5 eV range higher resolution data would be required in order to acquire significant species populations for these surfaces.

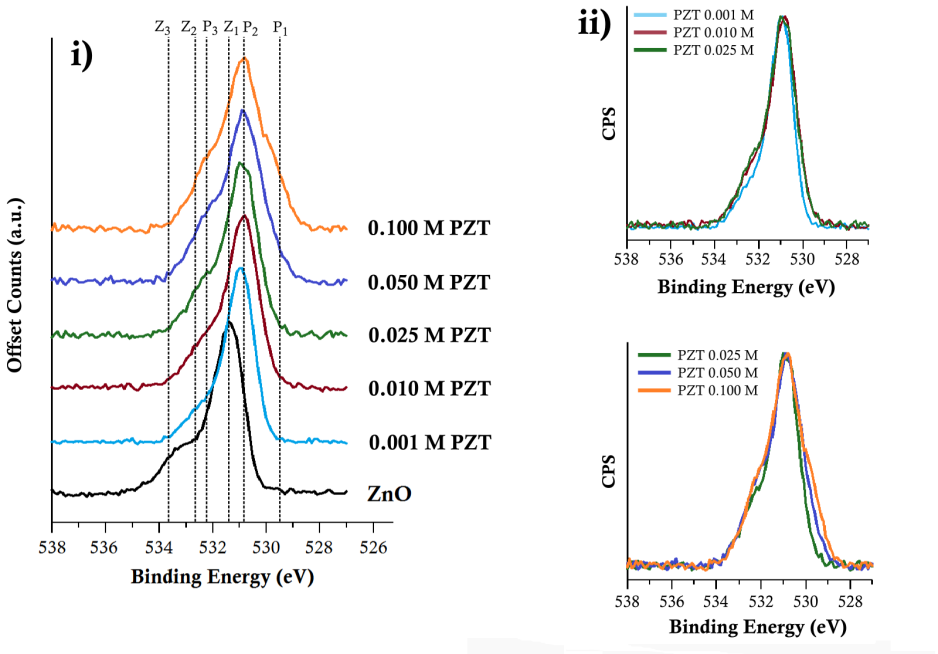

Figure 4.4 – O 1*s* core lines acquired by XPS for ITO–ZnO–PZT thin-films with different PZT sol-gel concentrations. *i)* displays the peaks as an offset stack, whilst plots the PZT modified samples together showing gradual broadening of the core line. The ZnO peak assignments in *i)* are as follows (from [12]: $\mathbf{Z}_1$ (531.4 eV), O–Zn bond; $\mathbf{Z}_2$ (532.6 eV), O–Zn bond close to lattice defects; $\mathbf{Z}_3$ (533.7 eV), HO–Zn surface groups. The contributions from Pb are (from [13]): $\mathbf{P}_1$ (529.5 eV), O–Pb; $\mathbf{P}_2$ (530.8 eV), O–Pb surface species; $\mathbf{P}_3$ (532.2 eV), HO–Pb surface species. Data acquired by Dr E. Ratcliff.

The data suggest that there an increasingly large contribution to the O 1*s* core line arising from HO–Pb groups. As discussed in Section 1.4.1.3.2, the presence of HO–Zn

bonding can be detrimental to device performance due to the unfavourable electronic interaction between the hydroxyl groups and the polymer; whilst modification of ZnO with PZT removes the HO–Zn population, it is not known how differing degrees of hydroxyl termination of PZT would affect the PZT:polymer interaction and the resulting conformation of the organic material — further investigations into this area are required.

4.3.2 Time-of-Flight Secondary Ion Mass Spectrometry

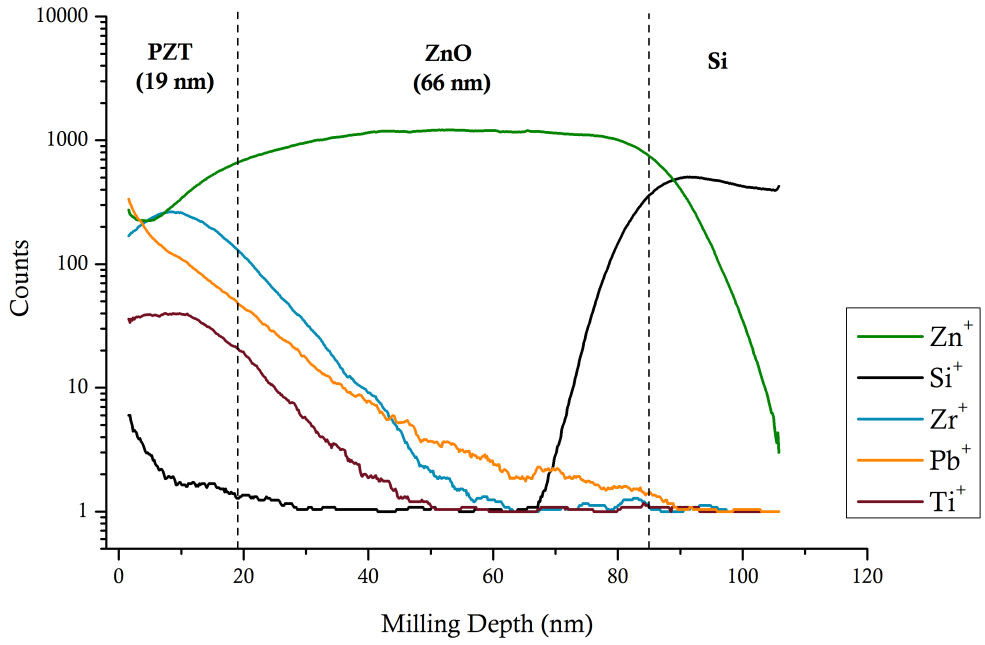

Figure 4.5 – ToF-SIMS depth profile for an ITO–ZnO–PZT (0.05 M sol-gel) thin-film, featuring three distinct material regions (PZT, ZnO, and Si). The different material regions were demarcated at the point where elemental signals drop to 50 % of their maximum value. All elemental signals except for Si are derived from the CsM^+ ion, where M = Zn, Zr, Ti, Pb. Depth was calibrated by profilometry of the crater created during the milling process — the total film depth was found to be 106 nm. Data acquired by Dr S. Fearn.

ToF-SIMS data was acquired for a single 0.05 M PZT film as a complement to the XPS data above and compared with the composition and imaging data obtained from a ZnO–PZT 0.4 M thin-film given in Section 3.4.2. Whilst the thickness measurements in Figure 4.1 show that 0.05 M of PZT should deposit approximately 11 nm of material, from the ToF-SIMS data the PZT is seen to affect approximately the top 20 nm of the film: this is likely a reflection of the high surface roughness of the spray pyrolysed ZnO layers (R_{RMS} 8.10 nm). A number of observations can be made from these data:

i) The Si^+ signal shown in Figure 4.5 increases near the surface of the film; whilst this may indicate some degree of contamination, this rise was only observed for the Si^+ signal and not for its isotopes. Moreover, given that the observed signal in this region was about 2 orders of magnitude lower than the Si maximum, it is likely that this is an artifact.

ii) The Pb signals for all isotopes exhibit a much different profile to Ti and Zr as they do not possess maxima. The signals exhibit similar behaviour to Ti and Zr when moving from the ZnO to the PZT region; however, the signal does not level off in the same fashion and at a distance of $\sim$ 2 nm from the film surface there is a sharp upturn in the signal spanning an order of magnitude. This indicates that the film surface here is Pb-rich, as was determined by both the XPS data and from the ToF-SIMS data for the 0.4 M PZT film.

iii) The Zn signals are not observed to diminish to zero in the PZT region, as was the case for the thick 0.4 M PZT film on ZnO. Whilst this may be due to discontinuity in the PZT film, it is likely that this is simply a reflection of the roughness of the ZnO–PZT interface, particularly when taking into account the XPS results in the previous section and the absence of a significant population of Zn–O bonds in the O 1*s* signals. The ZnO signals are observed to decline in the PZT region, reaching a minimum at a depth of around 4 nm before increasing in the surface region of the film; this again indicates segregation of Zn to the top of the film as the signal would be expected to drop towards zero otherwise.

4.3.3 Summary

Both surface and bulk compositions of the ZnO–PZT thin-film series were probed using XPS and ToF-SIMS respectively. From the XPS data, excess Pb and Zn are shown to be present at the surface in all films with the atomic concentration of Pb increasing with increasing sol-gel concentration: this is not unexpected given that the precursor sol-gel contains an excess of Pb to account for loss during annealing. From the O 1*s* core lines, PZT modification removes the HO-Zn groups from the surface which are known to be detrimental to device performance, although HO-Pb groups were observed to increase with increasing PZT thickness. The ToF-SIMS data obtained for the ZnO–PZT 0.05 M film corroborates the findings of the XPS data, showing that the PZT surface is Pb rich; additionally, as was the case for the 0.4 M PZT film, there is evidence of Zn etching and segregation to the surface region of the film.

4.4 Microstructure

Microstructural analysis of the ITO–ZnO–PZT series was carried out using AFM. This technique was used to characterise the grain structure of the films and to track the evolution of the film microstructure with increasing PZT layer thickness. Power spectral density (PSD) analysis of the AFM topography films was used to provide a comprehensive description of the grain structure — the results are discussed with reference to the TEM data presented in Section 3.4.2.2.

4.4.1 Topography

Tapping mode AFM was used to characterise the ITO–ZnO–PZT thin-films, yielding topographical (Z-height), phase offset, and amplitude error maps — a brief description of AFM and the equipment used in these experiments is given in Section 2.3.4. Height and phase scans (2 x 2 μm) for the PZT film series are displayed in Figure 4.6. 0.75 x 0.75 μm and 15 x 15 μm scans were also acquired.

There are clear differences in morphology between the ZnO and highest concentration of PZT (0.4 M) — the ZnO surface possesses a large distribution of grain sizes and a rough surface ($R_{RMS} = 8.10$ nm); in contrast, films modified with 0.4 M PZT (~ 105 nm) of PZT are much less rough and consist of smaller grains. Grain size analysis of AFM data may be carried out using algorithms such as watershed and thresholding to obtain quantitative population distributions: in this case, the watershed method was used to derive the grain sizes from the amplitude error plots given the clear marking of grain boundaries in these images. Given the relatively small size of the grains — especially in the PZT case — effective segmentation of the grains in the images was somewhat limited and thus the derived grain distributions are only approximate. From the distributions shown in Appendix Figure B.2, the ZnO film exhibited a wide range of grain sizes from around 10 to 50 nm (mean grain size 48 nm), whereas in the case of the ZnO–PZT (0.4 M) film distribution was rather less diffuse (the mean grain size being 28 nm) — these are comparable to the approximate crystallite sizes derived from XRD data by the Scherrer method in Section 3.2.3.

From the AFM images, there is little evidence of island formation in these films from either the topography scans or from the contrast in phase images — if distinct regions of ZnO and PZT were present on a film surface, it would be expected that this would result in a more phase-contrasted image. Given that there are significant differences in roughness between the relatively flat Nb:$SrTiO_3$ substrates used for PZT nanoisland growth in [5] and the rough ZnO growth materials used in this work, this is not wholly

unsurprising. Furthermore, as ZnO is less chemically stable to the processing conditions used in PZT deposition than Nb:$SrTiO_3$, it could be expected that chemical changes in ZnO play a role in the promotion of PZT growth — chemical changes to the ZnO surface would likely preclude the formation of island structures or distinct separation between the two materials. This conclusion is also suggested by the XPS data in Section 4.3.1.1 as a discontinuous layer PZT or ZnO would be expected to present more equal populations of O–Pb and O–Zn bonds in the O 1*s* core-lines which is not observed.

The roughness parameters for the ITO–ZnO–PZT thin-film series are given in Table 4.1 as well as the maximum height value recorded for the films (R_{max})[1]. The parameters were derived from 15 x 15 μm height scans to include as many surface features as possible into the calculation — statistical quantities derived from smaller scans may be influenced heavily by local undulations in the film.

PZT Concentration (M)	R_a (nm)	R_{rms} (nm)	R_{max} (nm)
ITO	2.14	2.71	27.93
0.000	6.47	8.10	73.11
0.001	5.80	7.30	74.10
0.010	5.90	7.41	72.15
0.025	6.53	8.17	57.14
0.050	3.34	4.24	58.49
0.400	1.85	2.35	32.27

Table 4.1 – Roughness parameters derived from tapping-mode AFM height scans (15 x 15 μm) for SP-Z–PZT thin-films on ITO.

The data show that the films undergo 'smoothing' with increasing PZT layer thickness. Within this trend, an increasing roughness is observed at 0.025 M *cf.* the 0.001 and 0.01 M modified films — from a visual comparison with the AFM topography images, it could be posited that this marks the onset on discrete PZT layer formation. The application of PZT clearly has an influence on the grain structure of the films (as shown in Section 3.4.2.2), illustrated by modification with the 0.001 M PZT sol-gel — although this modification should only chemically alter the ZnO surface rather than forming a discrete PZT layer, a decrease in film roughness is seen and the grain size distribution analyses show a general enlargening of the grains. To verify the role of PZT in chemical modification of the ZnO, ZnO films were treated with a methanol/acetic acid

[1] R_{max} was used to check the films for pinholes: if its value is similar to the measured thickness for a film, it is likely that the films contain pinholes which can be detrimental to hPV performance.

solution with the same pH as the PZT sol-gel using the same conditions as with PZT modification — these results are presented in Appendix Figure A.6. Although the RMS roughness in the acid modified films is reduced from 4.95 to 3.95 nm, significant changes in microstructure and grain size are not observed suggesting that the presence the PZT precursor materials chemically drive the change in grain structure.

From the R_{max} values, it can also be concluded that, as well as generally smoothing the film surface, PZT modification also helps to eliminate pinholes as the values decrease with increasing PZT sol-gel concentration. At 0.025 M, the R_{max} value is lower than the sum of the lowest measured ZnO thickness and the estimated thickness of the 0.025 M PZT thin-film, suggesting that PZT helps to 'fill-in' the film which may help to reduce leakage current in devices by eliminating contact between polymer and the bottom electrode.

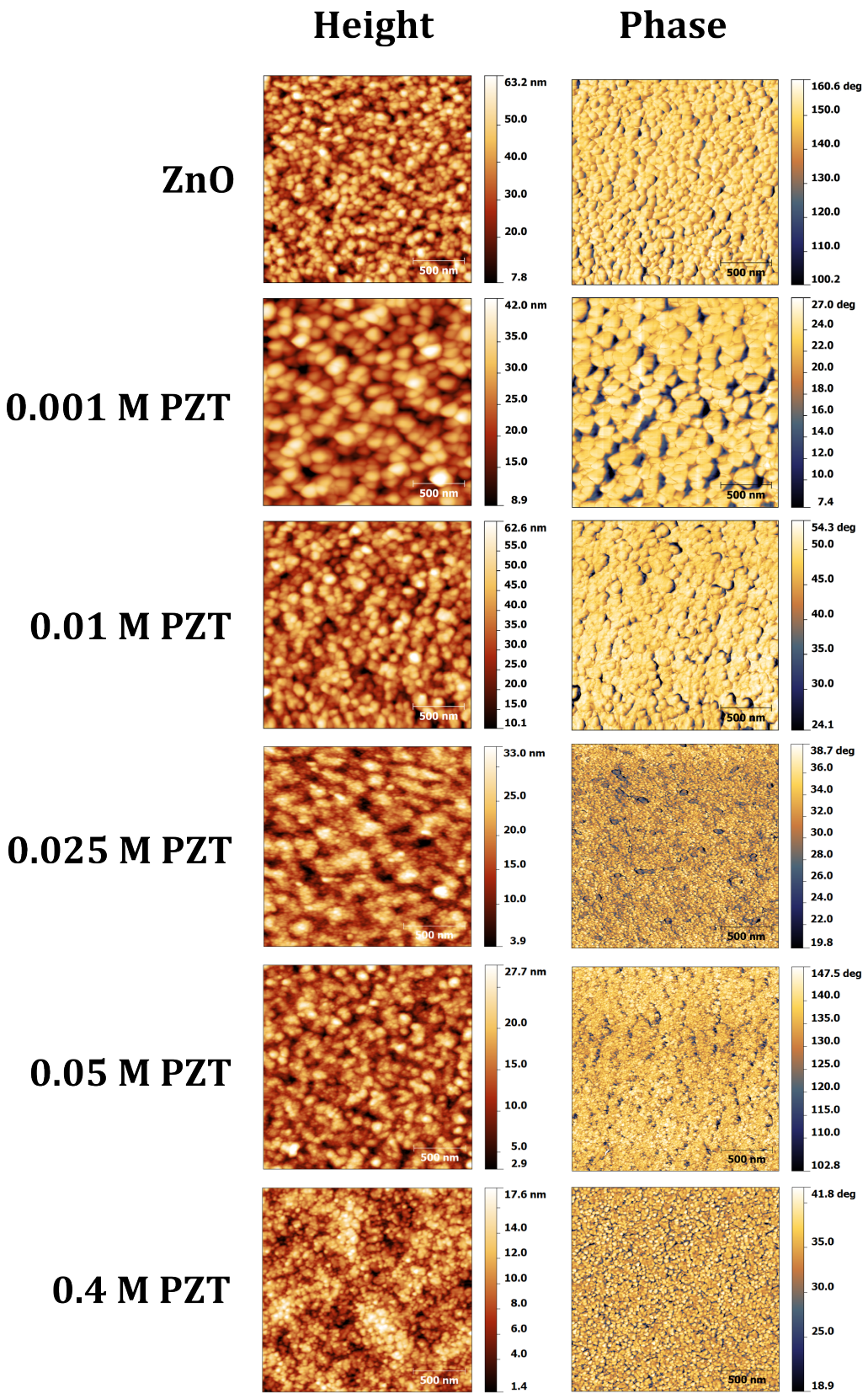

Figure 4.6 – 2 x 2 μm topography (Z) and phase scans for the ITO–ZnO–PZT thin-film series prepared with different PZT sol-gel concentrations, acquired using tapping mode AFM.

4.4.1.1 Fractal Analysis

Whilst roughness quantification can be extremely useful and may be correlated with a number of material properties, it is a general quantity solely derived from the height values of a film and excludes lateral relations between values and cannot be used in a description of surface structure. For example, this study shows a general decrease in roughness with increasing PZT sol-gel concentration; however, the roughness parameters only take into account the height deviation of a film and samples with very different morphologies may possess the same height values [15]. Moreover, the roughness parameters commonly used have been observed to depend on the sampling intervals of the instruments used to measure the samples [16, 17].

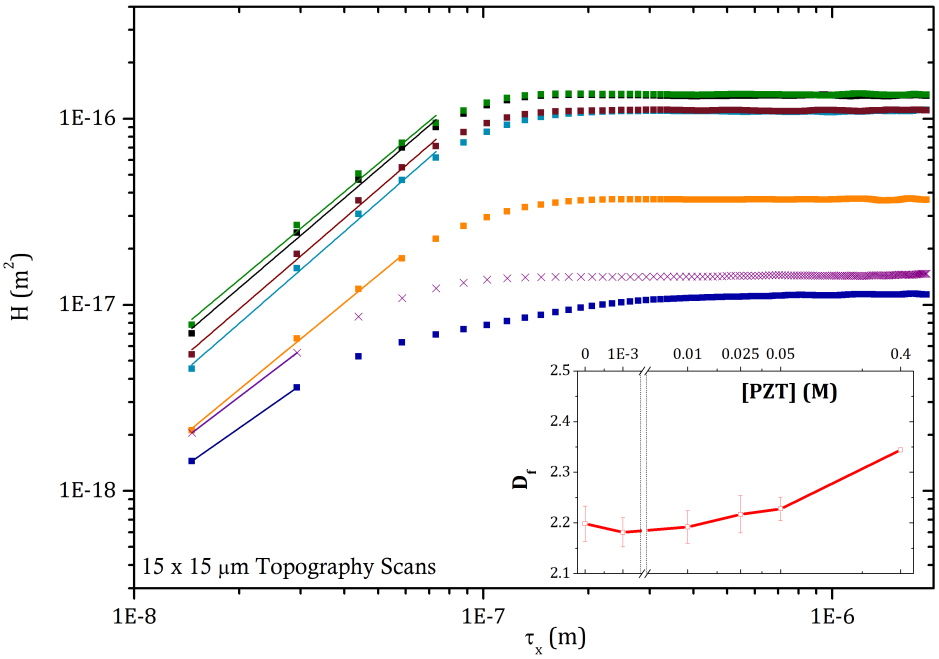

Figure 4.7 – Height-height correlation function (HHCF) plots derived from AFM topography scans (15 x 15 μm) and fits from which D_f is derived. **Inset:** variation of D_f with changing PZT sol-gel concentration.

Recently, fractal descriptions of thin-film surfaces have been used to describe their topographical structure [15, 18, 19]. Fractals allude to the fractured pieces of an object which combine to form a whole; the key feature of a fractal object is the concept of self-similarity, sometimes referred to as scale invariance, in that segments of an object are approximately similar to the object — as such, zooming in on a fractal image leads to no novel detail as the fractal pattern exists at multiple length scales[2] [20]. Whilst a

[2]Whilst exact self-similarity is a feature of some fractals, it is not a requirement of a fractal object: in many cases, a fractal has to be rescaled anisotropically to fulfill this criterion. This is referred to as

line, a plane, and a cube possess integer dimensionality of 1, 2, and 3 respectively, fractal objects possess non-integer dimensionality — this is quantified by the fractal dimension (D_f) which, in simple terms, describes how a fractal object fills space. A thin-film surface possesses a dimensionality $2 \leq D_f \leq 3$, with an increasing value corresponding to increasing surface complexity.

A number of methods exist for evaluating the fractal dimension of a surface from AFM topography data, including the area-perimeter [21] and variational methods [22]. The structure function method has previously been employed successfully in the fractal analysis of PZT [23] and ITO [16] thin-films: from the AFM height measurements consisting of a two-dimensional data field of size NxM (where N and M are the numbers of rows and columns), the one-dimensional height-height correlation function (HHCF) may be derived from the following by considering only the profiles along the fast scanning x-axis [24]:

$$H_x(\tau_x) = \frac{1}{N(M-m)} \sum_{l=1}^{N} \sum_{n=1}^{M-m} (z_{n+m,l} - z_{n,l})^2 \tag{4.1}$$

$$m = \tau_x/\Delta_x \ , \ n = \tau_y/\Delta_y$$

$$\tau_x = x_1 - x_2 \ , \ \tau_y = y_1 - y_2$$

thus the function is evaluated in τ_x where Δ_x is the sampling interval. As such, the HHCF describes the statistical relationship between two points on the surface. From the HHCF, D_f (in terms of deviation from a 2-dimensional plane) may be evaluated from the roughness exponent, α, using $D_f = 2 + (1 - \alpha)$. Below the 'knee' of the HHCF, the function scales with $r^{2\alpha}$, thus D_f may be evaluated by taking the slope of the log-log plot of the HHCF, as illustrated in Figure 4.7 [16].

Typically, increasing D_f in thin-films is indicative of increasing surface roughness [25]; however, in this case, the opposite trend is observed. This is most likely related to the changing morphology of the films with PZT modification: the addition of this layer leads to an increase in the film complexity despite the overall smoothing of the surface — from a visual inspection of the AFM height images, the thick (0.4 M) PZT thin-film consists of small, tightly packed grains with local undulations arising from the ZnO morphology; additionally, as discussed later in this chapter, the film also contains larger, multi-grain structures.

Whilst D_f should theoretically be constant at any length scale, the data in Table 4.2 show that there were discrepancies in D_f taken from 2 x 2 μm and 15 x 15 μm scans of up

self-affinity and is thought to be a characteristic of many polycrystalline, thin-film surfaces.

[PZT] (M)	Fractal Dimension 2 x 2 μm	15 x 15 μm	R_a (nm)	R_{RMS} (nm)
ITO	2.17	2.29	2.14	2.71
0.000	2.12	2.16	6.47	8.10
0.001	2.08	2.15	5.80	7.30
0.010	2.10	2.16	5.90	7.41
0.025	2.12	2.18	6.53	8.17
0.050	2.17	2.23	3.34	4.24
0.400	2.32	2.32	1.85	2.35

Table 4.2 – Fractal dimensions for ITO–ZnO–PZT thin-films calculated from the HHCF of AFM topography data. Roughness parameters (for 15 x 15 μm scans) are given for comparison.

to 0.09. These discrepancies are likely to arise from irregular features in the film which appear more frequently with increasing scan area [23] — this may be a reflection of the material growth process, resulting in local inhomogeneities in the surface structure [26], whereas a more homogeneous surface should yield a constant D_f over a wide scan range. As such, in the context of this study, D_f is a useful complement to the standard roughness quantities; in future studies, correlation of functional properties to both the roughness parameters and D_f may be made.

4.4.1.2 Power Spectral Density Function Analysis

Further structural information may be derived from the AFM data, in particular different structural components of the thin-film. As mentioned previously, direct measurement of grain-sizes through watershed segmentation algorithms did not provide a quantitatively accurate measure of grain size for these films, although they were useful for providing an approximate guide to the grain size distributions. However, it is possible to derive the length scales of correlated structures (including grains and larger structures) from other means, one of which is through analysis of power spectral density (PSD) functions [27, 28].

The PSD function is derived from the autocorrelation function (similar to the height-height correlation function given in Equation 4.1) and is essentially a decomposition of the surface height profile into its spatial wavelengths and describes both the surface roughness (much like the parameters R_a and R_{RMS}), but also information on the lateral components of this variation [29, 30]. The two-dimensional autocorrelation function

$G(\tau_x, \tau_y)$ is given:

$$G(\tau_x, \tau_y) = \int \int_{-\infty}^{\infty} z_1 z_2 \; w(z_1, z_2, \tau_x, \tau_y) \; \mathrm{d}z_1 \; \mathrm{d}z_2 \tag{4.2}$$

From this, the two-dimensional power spectral density function $W(K_x, K_y)$ may be expressed in terms of a Fourier transform:

$$W(K_x, K_y) = \frac{1}{4\pi} \int \int_{-\infty}^{\infty} G(\tau_x, \tau_y) \; e^{-i(K_x \tau_x + K_y \tau_y)} \; \mathrm{d}\tau_x \; \mathrm{d}\tau_y \tag{4.3}$$

As with the HHCF in Section 4.4.1.1, topographical AFM data is evaluated in one dimension along the fast scanning axis. This can then be evaluated using a fast Fourier transform:

$$W_{1D}(K_x) = \frac{2\pi}{NMh} \sum_{j=0}^{N} \left| \frac{h}{2\pi} \sum_{k=0}^{N} z_{kj} \; e^{-(K_x k h)} \right|^2 \tag{4.4}$$

This describes the 'standard' PSD function; however, it is also possible to derive the radial PSD (R-PSD), an angularly integrated two-dimensional function expressed as a function of radial frequency:

$$W_r(K) = \int_0^{2\pi} W(K \cos\phi, K \sin\phi) K \mathrm{d}\phi \tag{4.5}$$

Whilst the R-PSD is similar in nature to the PSD, it takes into account the correlation heights for all angles, thus providing a more complete correlation map of the data; as such, the R-PSD spectra were used to evaluate the ITO–ZnO–PZT films in this work. It has been noted that there are two widely used definitions of the PSD function in the literature, one of which scales with L^{-2} and the other with L^{-3}: this yields functions with units (length)^4 and (length)^3 respectively. As discussed in [28] and [31], the former definition of the PSD function results in it no longer being associated with roughness and thus the latter definition is used in this study.

The R-PSD spectrum contains information on both the film roughness (σ) and correlation length (τ): the former is equivalent to R_{RMS} (as calculated from an entire film), but applied to a single, discrete component — the PSD spectrum-derived value for σ is now used as a standard measure of microroughness [32]. τ is a measure of mean structure size and can apply both to individual grains and to larger, multigrain components. The main advantage of PSD spectrum analysis is that it allows for the identification of multiple components in films and quantification of their individual structural contributions such as roughness. This in contrast to standard roughness parameters which consider only the whole film; additionally, whilst grain-marking techniques (as outlined above)

may provide good approximations of grain size distributions, it is much harder to identify correlated structures with this method.

In preparation for extraction of the R-PSD data, raw AFM height scans were corrected for background using a 2nd-order polynomial and line corrected in both X and Y axes. Subsequently, the surface was reconstructed using an erosion algorithm to remove tip uncertainty effects — this was carried out using a tip model (pyramidal, 90° rotated tip, apex radius 8 nm, slope 54.7°. Subsequently, the R-PSD spectra were derived from the AFM height data using Gwyddion [8] — in calculating the R-PSD, the edges of the scans were omitted as these regions (particularly at the edges of the y-axis) can easily become distorted due to scanner artifacts [33].

4.4.1.2.1 Surface Models

Comprehensive surface structure models have been proposed to evaluate thin-films from their PSD spectra, in particular in [17] (metal fluoride coatings on fused silica and CaF_2 substrates) and in [34] (Gd_2O_3 films on quartz). In these papers, the PSD spectra analysed were derived by averaging data acquired over different scan sizes[3] to provide a single PSD spectrum covering a larger spectral range than its components. The models used in this paper consist of three components: *i)* a fractal model accounting for the substrate influences, given by:

$$W_{fr}(k) = \frac{F}{k^{v+1}} \tag{4.6}$$

where F is the spectral strength and v the spectral index relating to the fractal dimension of the surface. Next, the PSD contribution arising from the pure film was evaluated using the K-correlation model [35] (also known as the ABC model) from which the roughness and correlation lengths may be derived:

$$W_{ABC}(k) = \frac{A}{(1 + B^2 f^2)^{(C+1)/2}} \tag{4.7}$$

$$\sigma_{ABC} = \sqrt{\frac{2\pi A}{B^2(C-1)}} \quad \text{and} \quad \tau_{ABC} = \sqrt{\frac{(C-1)^2 B^2}{2\pi^2 C}}$$

where A determines the PSD at small f values, B the position of the 'knee' in the function, and C the function at high f values and is greater than 2. Lastly, as the ABC model alone

[3]This required partial overlap of spatial-frequency ranges of the individual curves and that the power spectral densities in the overlapping region were of the same order of magnitude.

does not account for superstructures which may appear in the low frequency range of the spectra, these were modelled using a shifted Gaussian model. Although the model used in these reported works was to fit a standard PSD, in this work, a function appropriate to the R-PSD spectra was used (where k_{sgs} is the frequency shift of the Gaussian):

$$W_{sgs}(k) = 1/2\ \sigma_{sgs}^2 \tau_{sgs}^2\ (k - k_{sgs})\ e^{(-1/4\,(k-k_{sgs})^2\ \tau_{sgs}^2)} \tag{4.8}$$

4.4.1.2.2 R-PSD Fitting

Firstly, PSD spectra derived from AFM topography scans with sizes 0.75 x 0.75, 2 x 2, and 15 x 15 μm were averaged to yield a single spectrum for each of the films analysed in this work, as outlined above in Section 4.4.1.2.1. In initial fits of the R-PSD spectra, whilst the fractal component fit appropriately to the high frequency range, the K-correlation model was found to be inadequate as the decay observed in the 5 x 10^7 to the 5 x 10^8 m^{-1} range was more rapid than could be attained in fitting. Whilst the models given in [16] and [17] consider the K-correlation as a description of the 'pure film' independent of the substrate, in these works, the materials systems were rather less complex consisting of substrate and coating components; in this case, the film consists of the substrate (glass), the ITO coating, ZnO, and finally the PZT modification. It was found that the best fits consisted of fitting the high frequency component with the fractal mode (Equation 4.6 and using multiple shifted Gaussian functions to model the remainder of the film (Equation 4.8). An example of the fit and its components is given in Figure 4.8. Fitting was carried out using the Origin software suite which employs a Levenberg-Marquadt algorithm to carry out a least squares fitting to the data.

It must be noted that, given the complexity of the film structures used in this work, that assignation of the derived parameters to specific components is not particularly straightforward. From the data below, it seems that the presence of ITO adds an extra layer of complexity to the interpretation of results; ultimately, the decision to continue the study into films containing the ITO layer was made for two reasons: firstly, as ITO is an essential component in devices, the data would reflect applied structures; secondly, as the ITO layer was shown to influence the grain structure of the SP-Z layer (compared to glass) in Section 3.2.2, analysing systems based on ITO–ZnO structures would be of greater use to this work. However, it is acknowledged that comparison to a set of films omitting the ITO layer would be required to increase the certainty of the assignments made in this work.

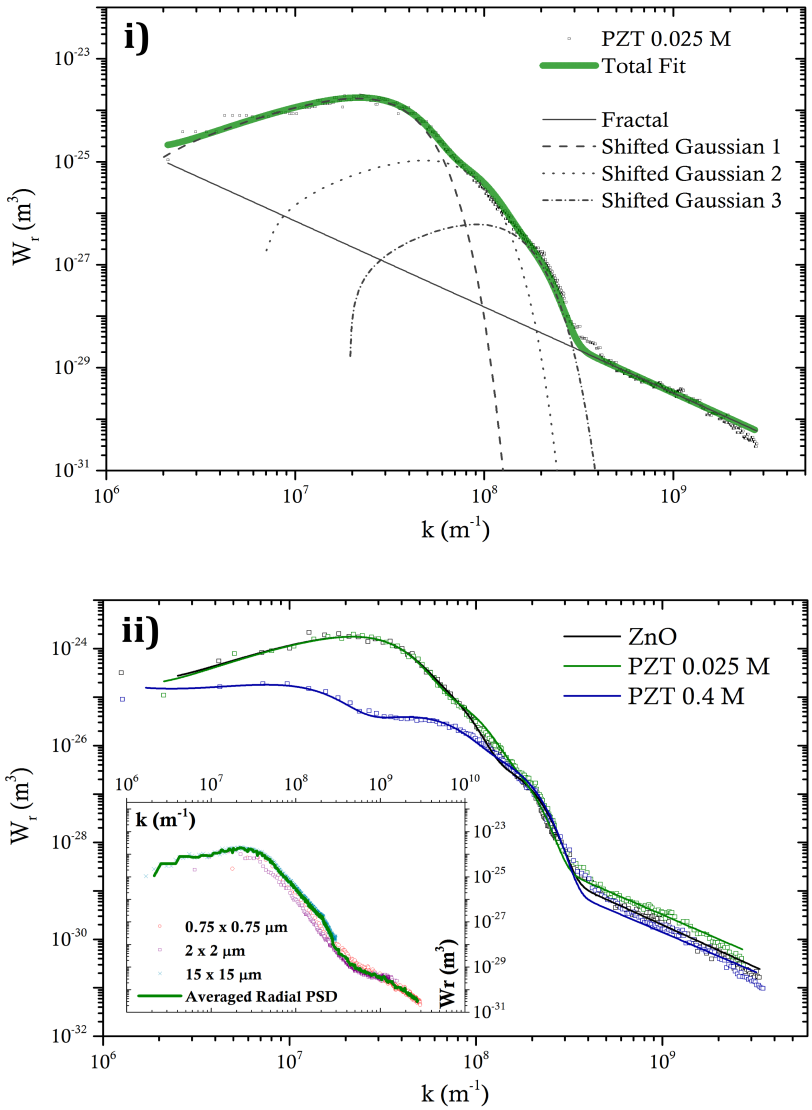

Figure 4.8 – *Top:* total fit and individual components for the R-PSD spectrum of an ITO–ZnO–PZT (0.025 M) thin-film derived from AFM topography (Z) data. *Bottom:* Comparison and fits for R-PSD spectra of thin-films modified with PZT sol-gels of differing concentration. Inset: R-PSD spectra obtained for 0.025 M sample using different scan AFM scan sizes and their combination to form a single R-PSD covering a wider frequency range.

The results of the R-PSD spectra fittings are given in Table 4.3 alongside the roughness parameters and fractal dimensions derived in Sections 4.4.1 & 4.4.1.1 respectively. Each film required fitting with 2 – 4 shifted Gaussian functions: in Table 4.3, Gaussian I corresponds to a PZT superstructure, Gaussian II to a ZnO component, and Gaussians III and IV to components with similar τ values present in all films. The PZT superstructure appears as a 'hump' in the lower frequency range of the R-PSD as shown for the 0.4 M example in Figure 4.8 and is first detected in the 0.05 M sample. Columnar PZT

structures have been observed to form on substrates such as Pt/Si [36] and it is likely that such structures could likewise grow on ZnO; whilst, it was not possible to identify distinct columns in the TEM cross-sections of SP-Z–PZT (0.4 M) films (discussed in Section 3.4.2.2), previous experiments into the ZnO–PZT system (not detailed in this study) showed that columns of PZT form on sol-gel-derived ZnO films when annealing the films under similar conditions — such a micrograph is displayed in Appendix B.1. As the PZT layer grown on the SP-Z films is more densely packed, it may be the case that these columns are present in these film with less well-defined superstructure boundaries.

Gaussian II was assigned to large ZnO grains, given that no such component was found in ITO or in the 0.4 M PZT case — these grains appear to be the most significant contributors to the film roughness. This component is affected by PZT modification — as noted previously, modification with 0.001 M PZT sol-gel leads to an enlargening of the ZnO grains and a slight decrease in roughness; this is reflected in an increase in correlation length from 71.8 to 80.8 nm. At 0.01 M and 0.025 M, the correlation lengths for this component match those observed for unmodified ZnO, whereas at 0.05 M this is reduced to 54.6 nm and the component is not present in the 0.4 M film. There is an increase in the roughness of this component at 0.025 M, whilst at 0.05 M this is much reduced from 7.53 to 2.43 nm — a similar observation was made for the R_{RMS} values, and it is possible that this marks the onset of discrete PZT layer formation.

Gaussians III and IV are more difficult to assign directly, given that they appear in each layer of the thin-film. It is possible that the ITO grains seed ZnO grains of similar sizes, leading to the wide distribution of grain sizes as derived from watershed analysis outlined earlier. τ_3 remains fairly consistent in magnitude through the PZT concentration series, as opposed to the ZnO component of Gaussian II — whilst there is a slight decrease from 40.0 nm to around 36.5 nm in the films modified with higher PZT concentrations, it is present in all the films. It is not certain whether, at the higher PZT concentrations, this quantity corresponds to some larger grains of PZT or whether it corresponds to film undulations due to the ZnO layer.

Gaussian IV presents only small variations across the film series. Whilst this is the dominant component for the 0.4 M PZT thin-film in terms of grain size, due to its co-incidence with ITO and ZnO components, unfortunately it cannot be used to measure the onset of PZT evolution in these films.

The fractal component of the model did not show substantial variation from film to film; the spectral index (related to the fractal dimension of the substrate) possessed a limited range from 0.59 to 0.69; however, the fitting of this region was not always satisfactory and the fitting model of this section requires further refinement.

Samples	**Standard Roughness** 15 x 15 μm			**D_f (HHCF)**		**Fractal Model**		**Gauss I** **PZT S. Struc.**		**Gauss II** **ZnO**		**Gauss III** **Mixed**		**Gauss IV** **Mixed**	
[PZT] (M)	R_a (nm)	R_{RMS} (nm)	R_{max} (nm)	2 x 2 μm	15 x 15 μm	K 10^{-16} m	v	σ_1 (nm)	τ_1 (nm)	σ_2 (nm)	τ_2 (nm)	σ_3 (nm)	τ_3 (nm)	σ_4 (nm)	τ_4 (nm)
ITO	2.14	2.71	27.93	2.17	2.34	13.3	0.65	–	–	–	–	2.52	39.8	0.94	19.5
0 (SP-Z)	6.47	8.10	73.11	2.12	2.16	7.39	0.63	–	–	7.14	71.8	3.72	40.0	0.92	18.7
0.001	5.80	7.30	74.10	2.06	2.15	8.0	0.59	–	–	6.93	80.8	2.31	41.5	0.84	18.0
0.010	5.90	7.41	72.15	2.10	2.16	35.1	0.69	–	–	6.96	69.0	2.46	36.7	0.73	15.9
0.025	6.53	8.17	57.14	2.12	2.18	34.6	0.67	–	–	7.53	69.9	2.70	34.0	0.85	19.7
0.050	3.34	4.24	58.49	2.17	2.23	3.1	0.61	3.26	106.6	2.43	54.6	5.00	36.2	0.47	16.8
0.400	1.85	2.35	32.27	2.32	2.40	10.5	0.68	1.65	144.0	–	–	1.49	36.5	0.90	17.3

Table 4.3 – All structural parameters derived from topographical AFM data. For the R-PSD spectra fits, Gaussian I corresponds to PZT superstructural contributions, Gaussian II is a ZnO contribution, whilst Gaussians III and IV are assigned to different components in the respective films.

4.4.1.2.3 Discussion

Given the complexity of the ITO–ZnO–PZT thin-films, the fitting model used in the previous section offers a reasonable description of the surface. The presence of PZT superstructures was not directly corroborated by inspection of the TEM data for these films; however, columnar PZT has been shown to form on Sol-Z films and it is likely that they too exist in the SP-Z case, albeit more tightly packed. Although further imaging is required in order to verify the model, the method does offer a non-destructive analytical technique for analysis of film microstructure. As TEM is a technique requiring time-intensive processing, it is difficult to acquire large volumes of data (*e.g.* for a series of films, such as the set investigated in this chapter) and to repeat experiments; in contrast, whilst not a perfect model, the R-PSD function method allows for the analysis of a large volume of data in a reasonably short space of time, as well as yielding quantitative information for each component. Additionally, AFM allows for the analysis of much larger areas which may be much more representative of a thin-film than a single cross-section.

Further validation of this system is needed, however. Firstly, the fractal component of the model did not always fit appropriately; secondly, the system could be reduced in complexity by removing the ITO component to deconvolute the system and increase the certainty in peak assignation; thirdly, using a more uniform and less complex ZnO layer (such as those deposited by techniques such as pulsed laser or atomic layer deposition) would also reduce the film complexity which the rough spray pyrolysed layers provide in this study. On top of this, by employing a greater range of PZT concentrations a fuller description of the evolution of the PZT layer could be made, particularly in terms of aspects such as layer formation and superstructure onset.

Ultimately, the structural parameters derived here may correlate well with the functional properties of PZT, especially in terms of ferroelectricity. One potential future experiment (outlined in Chapter 6) involves local ferroelectric characterisation of the ITO–ZnO–PZT film series using piezoforce microscopy (PFM) — it is likely that the microstructural characteristics derived here influence the polarisation characteristics of the film.

4.4.2 Summary

The microstructure of the ZnO–PZT system was evaluated using quantitative analysis of AFM data, namely through fractal analysis and the fitting of R-PSD functions. Increasing the thickness of PZT led to an increase in fractal dimension from 2.12 to 2.32, indicating an increase in topographical complexity. Whilst the R-PSDF fitting model used to evaluate these films requires refinement, the evolution of the PZT microstructure with increasing thickness was tracked through changes in the roughness and correlation size of each component. At PZT sol-gel concentrations above 0.05 M, a superstructural PZT component appears; it is likely that these corresponds to the formation of PZT

columns which have been observed to form on ZnO layers. This method of evaluation may be used for a number of different film systems and allow for quantitative analysis of microstructural characteristics whilst only requiring a small number of time-consuming TEM cross-sections to validate the model.

4.5 Conclusions

PZT layers were grown on ZnO with thicknesses appropriate for use as interlayers in hybrid photovolatic devices. This was achieved through dilution of a precursor sol-gel: in this study, sol-gel concentrations were varied from from 0.001 M to 0.05 M (0.4 M being the stock concentration of the PZT), yielding films up to 11 nm thick (as measure by AFM of PZT films on Si substrates). Compositional analysis was carried out using ToF-SIMS (bulk) and XPS (surface): the data show that the surfaces contain an excess of Pb, thus the films deviate from the expected stoichiometry between Pb:Ti:Zr; this is thought to arise due to the excess Pb added to the PZT sol-gel to compensate for loss during heating. From the analysis of XPS O 1s core lines, the evolution of the surface chemistry from ZnO to PZT was monitored, showing that even at an extremely low modifier concentration of 0.001 M, the HO–Zn groups are eliminated — these have been previously cited as being detrimental to device performance.

Topographical and microstructural characterisation was carried out using AFM: from these results and the XPS data it could be inferred that islands of PZT do not form using this modification process. Surface characteristics were derived, showing that, overall, film roughness decreases with increasing PZT thickness; using the HHCF method, the fractal dimension of the films was shown to increase with increasing PZT thickness indicating an increase in morphological complexity, despite the decreasing roughness.

Further evaluation of the microstructure was carried out by fitting the R-PSD function curves of the films to a surface model. From this, the microstructural evolution of the film could be determined to some degree, although the complexity of the ITO–ZnO–PZT layer structure introduces some uncertainty in the assignment of film components. The data suggest that PZT superstructures with correlation lengths of > 100 nm form at sol-gel concentrations of 0.05 M and above; it is thought that these superstructures correspond to polycrystalline column formations in the PZT film. Whilst this analytical model requires some refinement, the results show that it has much potential in the characterisation of film structure, in particular for large data sets as it is a much less time and labour-intensive technique than TEM. These results set up future experiments into the effect of reduced PZT size on polarisation characteristics which may be measured using PFM — this is outlined in Chapter 6.

References

[1] A. Gruverman and A. Kholkin, "Nanoscale ferroelectrics: processing, characterization and future trends," *Reports Prog. Phys.* **69**, pp. 2443–2474, Aug. 2006.

[2] J. F. Scott, "Ferroelectric Nanostructures for Device Applications," in *Handbook of Advanced Dielectric, Piezoelectric and Ferroelectric Materials*, Z.-G. Ye, ed., ch. 18, pp. 541–569, Woodhead Publishing Ltd, 1st ed., 2008.

[3] N. Izyumskaya, Y. I. Alivov, S. J. Cho, H. Morkoç, H. Lee, and Y. S. Kang, "Processing, structure, properties, and applications of PZT thin films," *Crit. Rev. Solid State Mater. Sci.* **32**, pp. 111–202, July 2007.

[4] W. T. Lee, E. K. H. Salje, and M. T. Dove, "Effect of surface relaxations on the equilibrium growth morphology of crystals: platelet formation," *J. Phys. Condens. Matter* **11**, pp. 7385–7410, Sept. 1999.

[5] I. Szafraniak, C. Harnagea, R. Scholz, S. Bhattacharyya, D. Hesse, and M. Alexe, "Ferroelectric epitaxial nanocrystals obtained by a self-patterning method," *Appl. Phys. Lett.* **83**, p. 2211, Sept. 2003.

[6] X. H. Xu, P. Gu, R. Jiang, G. Zhao, L. Wen, and J. R. Chu, "Characterization of mechanical properties of PZT thin film by nanoindentation," in *2006 1st IEEE Int. Conf. Nano/Micro Eng. Mol. Syst.*, pp. 56–60, IEEE, Jan. 2006.

[7] Kelu Zheng, Jian Lu, and Jiaru Chu, "Study on wet-etching of PZT thin film," in *Dig. Pap. Microprocess. Nanotechnol. 2003. 2003 Int. Microprocess. Nanotechnol. Conf.*, pp. 248–249, Japan Soc. of Appl. Phys, 2003.

[8] D. Nečas and P. Klapetek, "Gwyddion: an open-source software for SPM data analysis," *Cent. Eur. J. Phys.* **10**(1), pp. 181–188, 2012.

[9] S. S. Roy, H. Gleeson, C. P. Shaw, R. W. Whatmore, Z. Huang, Q. Zhang, and S. Dunn, "Growth and characterisation of lead zirconate titanate (30/70) on indium tin oxide coated glass for oxide ferroelectric-liquid crystal display application," *Integr. Ferroelectr.* **29**(3-4), pp. 189–213, 2000.

[10] G. Attard and C. Barnes, *Surfaces*, Oxford University Press, 1998.

[11] S. A. Impey, Z. Huang, A. Patel, R. Beanland, N. M. Shorrocks, R. Watton, and R. W. Whatmore, "Microstructural characterization of sol-gel lead–zirconate–titanate thin films," *J. Appl. Phys.* **83**, p. 2202, Feb. 1998.

[12] H. Li, L. K. Schirra, J. Shim, H. Cheun, B. Kippelen, O. L. A. Monti, and J.-L. Bredas, "Zinc oxide as a model transparent conducting oxide: a theoretical and

experimental study of the impact of hydroxylation, vacancies, interstitials, and extrinsic doping on the electronic properties of the polar ZnO (*0002*) surface," *Chem. Mater.* **24**, pp. 3044–3055, Aug. 2012.

[13] N. Wakiya, K. Kuroyanagi, Y. Xuan, K. Shinozaki, and N. Mizutani, "An XPS study of the nucleation and growth behavior of an epitaxial Pb(Zr,Ti)O_3/MgO(*100*) thin film prepared by MOCVD," *Thin Solid Films* **372**, pp. 156–162, Sept. 2000.

[14] B.-D. Qu, Y.-G. Wang, W.-L. Zhong, K.-M. Wang, and Z.-L. Wang, "Surface analysis of $PbTiO_3$ films prepared by the sol-gel method," *J. Appl. Phys.* **71**, p. 3467, Apr. 1992.

[15] H. Assender, V. Bliznyuk, and K. Porfyrakis, "How surface topography relates to materials' properties," *Science* **297**, pp. 973–6, Aug. 2002.

[16] D. Raoufi, A. Kiasatpour, H. R. Fallah, and A. S. H. Rozatian, "Surface characterization and microstructure of ITO thin films at different annealing temperatures," *Appl. Surf. Sci.* **253**(23), pp. 9085–9090, 2007.

[17] J. Ferré-Borrull, A. Duparre, and E. Quesnel, "Procedure to characterize microroughness of optical thin films: application to ion-beam-sputtered vacuum–ultraviolet coatings," *Appl. Opt.* **40**(13), p. 2190, 2001.

[18] W. Zahn and A. Zösch, "Characterization of thin-film surfaces by fractal geometry," *Fresenius. J. Anal. Chem.* **358**, pp. 119–121, May 1997.

[19] P. I. Oden, A. Majumdar, B. Bhushan, A. Padmanabhan, and J. J. Graham, "AFM imaging, roughness analysis and contact mechanics of magnetic tape and head surfaces," *J. Tribol.* **114**, p. 666, Oct. 1992.

[20] B. B. Mandelbrot, "Self-affine fractals and fractal dimension," *Phys. Scr.* **32**, pp. 257–260, Oct. 1985.

[21] L. Vázquez, R. Salvarezza, P. Ocón, P. Herrasti, J. Vara, and A. Arvia, "Self-affine fractal electrodeposited gold surfaces: characterization by scanning tunneling microscopy," *Phys. Rev. E* **49**, pp. 1507–1511, Feb. 1994.

[22] L. Spanos and E. A. Irene, "Investigation of roughened silicon surfaces using fractal analysis. I. Two-dimensional variation method," *J. Vac. Sci. & Technol. A Vacuum, Surfaces, Film.* **12**, p. 2646, Sept. 1994.

[23] Y.-R. Jeng, P.-C. Tsai, and T.-H. Fang, "Nanomeasurement and fractal analysis of PZT ferroelectric thin films by atomic force microscopy," *Microelectron. Eng.* **65**, pp. 406–415, May 2003.

[24] V. Ioannou-Sougleridis, V. Constantoudis, M. Alexe, R. Scholz, G. Vellianitis, and A. Dimoulas, "Effects on surface morphology of epitaxial Y_2O_3 layers on Si (*001*) after postgrowth annealing," *Thin Solid Films* **468**, pp. 303–309, Dec. 2004.

[25] T.-H. Fang, S.-R. Jian, and D.-S. Chuu, "Nanotribology and fractal analysis of ZnO thin films using scanning probe microscopy," *J. Phys. D. Appl. Phys.* **36**, pp. 878–883, Apr. 2003.

[26] T. Li and K. Park, "Fractal analysis of pharmaceutical particles by atomic force microscopy.," *Pharm. Res.* **15**, pp. 1222–32, Aug. 1998.

[27] S. Karan and B. Mallik, "Power spectral density analysis and photoconducting behavior in copper(II) phthalocyanine nanostructured thin films," *Phys. Chem. Chem. Phys.* **10**, pp. 6751–61, Dec. 2008.

[28] S. J. Fang, S. Haplepete, W. Chen, C. R. Helms, and H. Edwards, "Analyzing atomic force microscopy images using spectral methods," *J. Appl. Phys.* **82**, p. 5891, Dec. 1997.

[29] M. M. Iazykov, *Growth of pentacene on parylene and on BCB for organic transistors application, and DNA-based nanostructures studied by Amplitude Modulation Atomic Force Microscopy in air and in liquids.* Doctor of Philosophy, Université de Lyon / University Taras Chevchenko de Kyiv, 2011.

[30] J. M. Elson and J. M. Bennett, "Calculation of the power spectral density from surface profile data," *Appl. Opt.* **34**, pp. 201–8, Jan. 1995.

[31] S. D. Halepete, H. C. Lin, S. J. Fang, and C. R. Helms, "Analyzing atomic force micrographs using spectral methods," *MRS Proc.* **386**, p. 383, Feb. 1995.

[32] D. J. Janeczko, "Power spectrum standard for surface roughness: part I," in *33rd Annu. Tech. Symp.*, J. C. Stover, ed., pp. 175–183, International Society for Optics and Photonics, Jan. 1990.

[33] C. Canale, B. Torre, D. Ricci, and P. C. Braga, "Recognizing and avoiding artifacts in atomic force microscopy imaging," *Methods Mol. Biol.* **736**, pp. 31–43, Jan. 2011.

[34] N. Sahoo, S. Thakur, and R. Tokas, "Fractals and superstructures in gadolinia thin film morphology: influence of process variables on their characteristic parameters," *Thin Solid Films* **503**, pp. 85–95, May 2006.

[35] G. Palasantzas, "Roughness spectrum and surface width of self-affine fractal surfaces via the K-correlation model," *Phys. Rev. B* **48**, pp. 14472–14478, Nov. 1993.

[36] I. Pintilie, I. Pasuk, G. A. Ibanescu, R. Negrea, C. Chirila, E. Vasile, and L. Pintilie, "The impact of the Pb(Zr,Ti)O_3–ZnO interface quality on the hysteretic properties of a metal–ferroelectric–semiconductor structure," *J. Appl. Phys.* **112**(10), p. 4103, 2012.

Chapter 5

Incorporation of PZT into Hybrid Photovoltaic Devices

5.1 Introduction

In this chapter, an investigation into the incorporation of PZT into ZnO–P3HT (poly(3-hexylthiophene)) based hybrid photovoltaic (hPV) devices is reported. As covered in Section 1.4.3, inorganic interracial modifiers such as TiO_x and CdS have been shown to improve the performance of ZnO:polymer hPVs and in this work, PZT layers are incorporated at the oxide:polymer interface for the first time.

To evaluate the influence of PZT in the operation of the ZnO–(PZT)–P3HT system, photoluminescence spectroscopy (PL) and transient absorption spectroscopy (TAS) were used to probe the charge generation and recombination characteristics respectively at the oxide:polymer interface. Subsequently, hPV devices containing these layers were fabricated and tested to assess their overall impact on solar cell performance. This study provides the framework for further investigations into the effect of ferroelectric polarisation on hPV devices.

5.2 Electronic Characterisation of ZnO

As discussed in Section 1.4.1, the defect chemistry of ZnO is both extensive and sensitive to synthetic methods and processing conditions; as a result, ZnO is a highly variable material in terms of its optoelectronic properties. Given that the PZT growth experiments outlined in Chapters 3 & 4 had been carried out using spray-pyrolysed ZnO (SP-Z) as growth substrates, it was initially decided to carry out the work detailed in this chapter using these films. However, initial current density–voltage characterisation of SP-Z-based inverted bilayer hPV devices (device structure: ITO/SP-Z/P3HT/Ag) suggested that the ITO was collecting holes and the top contact electrons, *i.e.* that the

device was operating as a 'normal' rather than an inverted device (J–V data shown in Appendix Figure C.1), an unusual observation given that ZnO is a strongly n-type material. After eliminating the possibility of equipment malfunction or incorrect setup of the J–V testing rig, it was hypothesised that the defects in ZnO were interfering with the device operation; therefore, SP-Z films were characterised using PL spectroscopy and compared to sol-gel-derived ZnO films (Sol-Z) which had previously been successfully incorporated in hPV devices. Additionally, the effect of annealing SP-Z at 450 °C for 1 hour was measured — these being the same conditions used to anneal Sol-Z films.

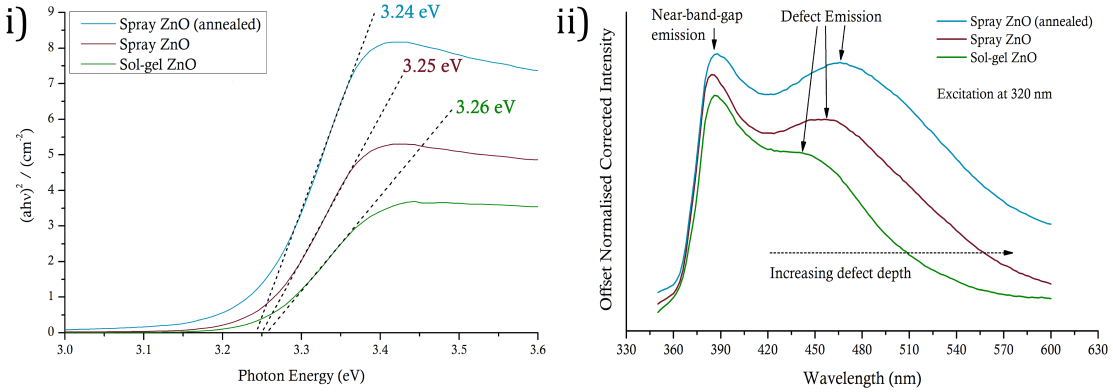

Figure 5.1 – *(i)* Tauc plot illustrating the calculation of direct band gaps for different Glass–ZnO films. *ii)* PL spectra for Glass–ZnO films (offset stacking, normalised spectra). The films were probed using an exciting laser at 320 nm and a scanning range of 350 – 600 nm. PL intensity was corrected using absorption value acquired at the excitation wavelength.

Band gaps for the different ZnO types (deposited on glass) were calculated from UV-vis spectroscopy using the Tauc method, as illustrated in Figure 5.1 — the method is described in Section 2.5.1. The band gap was not observed to vary significantly between films: 3.24 eV for Sol-Z, 3.25 eV for SP-Z, and 3.26 eV for annealed SP-Z — this is likely to be within the error of the technique. These values are lower than the commonly cited value of 3.3 eV for bulk ZnO: this is often observed in ZnO thin-films and is attributed to the presence of n-type defects [1]. It is unclear from these results alone whether the band gap changes observed here arise from defects, or perhaps other optical effects such as scattering.

To probe the ZnO defects, PL spectroscopy was used: the film was excited using a wavelength of 320 nm and the subsequent scan for emissions ranging from 350 – 600 nm — the resulting data (corrected for absorption) is displayed in Figure 5.1. The data show distinct differences in defect emission between the three films. Sol-Z presents the lowest degree of defect emission (centred $\sim$ 440 nm); in the unannealed SP-Z film, the defect peak is larger and shifted to longer wavelengths (centred at $\sim$ 455 nm). Annealing the SP-Z film further increases the defect emission and shifts the peak to even longer wavelengths (centred at $\sim$ 465 nm). Although identification of the specific defects requires higher resolution spectroscopy, qualitatively this signifies a shift of defects deeper into the band

gap: it is possible that in the SP-Z films (both as deposited and annealed), these provide an alternative conduction pathway through the mid-gap of ZnO.

5.3 Charge Generation and Recombination

In OPV systems, understanding interfacial processes is crucial for designing efficient devices. Whilst these processes are often reflected in the device performance, it can be difficult to ascribe them with certainty. As such, alternative methods such as the complementary techniques PL and TAS are widely used to isolate and identify interfacial effects. In this context, PL can be used to investigate processes at the donor–acceptor (D–A) interface by exciting the polymer: this generates excitons which either decay through radiative processes or by dissociation at the heterojunction which can ultimately lead to charge generation. In a D–A system, the degree of luminescence quenching is an indicator of efficient exciton dissociation. TAS is a pump–probe method used to characterise charge recombination in these systems; by exciting the polymer in a D–A system and scanning at a characteristic wavelength for charge polarons, the lifetime of these separated charges can be evaluated.

For the following studies, the ZnO–(PZT)–P3HT films were deposited on glass. ZnO (both SP-Z and Sol-Z) and PZT were deposited as reported in Chapter 3. On top of this, a 10 mg ml^{-1} solution of P3HT in chlorobenzene was spin-coated to produce a polymer film with a thickness of $\sim$ 40 nm as measured by profilometry.

5.3.1 Photoluminescence Spectroscopy Studies

Here, PL studies were carried out to evaluate: *i)* differences in charge generation between SP-Z and Sol-Z films; *ii)* the effect of PZT modification on defects in ZnO films; *iii)* the effect of PZT modification on charge generation in the ZnO–P3HT system. The three ZnO films evaluated in Section 5.2 — as deposited SP-Z, annealed SP-Z, and Sol-Z — were used in these studies. For PZT-modified films, PZT was spin-coated from a 0.05 M sol-gel (the molar concentration referring to the combined concentration of the Zr/Ti component), dried at 200 °C, then annealed at 560 °C for 30 minutes (loaded into a preheated oven) as outlined in Section 3.3.2.

5.3.1.1 ZnO–P3HT

Charge generation was measured in ZnO–P3HT films (with Sol-Z, SP-Z, and annealed SP-Z) by exciting the polymer layer at a wavelength of 550 nm. The results for Sol-Z–P3HT films (with as-cast and annealed P3HT) are shown below in Figure 5.2. For the Sol-Z–P3HT films, luminescence quenching is clearly observed: this yields around a 30 %

decrease in PL intensity. Assuming a perfectly flat ZnO–P3HT interface and a P3HT exciton diffusion length of 8.5 nm [2], for a 40 nm P3HT film, only $\sim$ 21 % of excitons can be expected to reach the heterojunction (assuming that all the excitons generated within L_{ex} of the interface reach it) — however, the Sol-Z–P3HT is not a perfectly flat interface (Sol-Z RMS roughness is $\sim$ 4.2 nm), thus it is expected that a greater number of excitons will be susceptible to quenching.

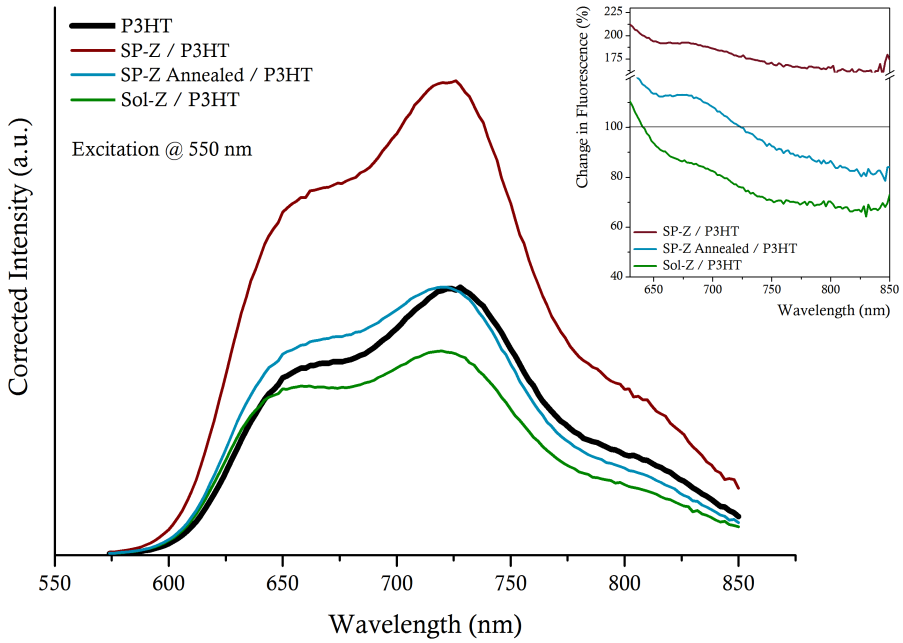

Figure 5.2 – Absorption corrected PL spectra for ZnO–P3HT thin-films on glass. The polymer was excited using a wavelength of 550 nm, followed by a scan for emission between 575 – 850 nm. The solid black line corresponds to neat P3HT on glass. Inset: the change in PL intensity as a percentage relative to the neat Glass–P3HT reference.

For the SP-Z and annealed SP-Z films, significant degrees of PL quenching were not observed; in fact, in the case of as-deposited SP-Z, a large increase in PL intensity was recorded. These results are discussed in greater detail below in Section 5.3.2.

5.3.1.2 ZnO–PZT–P3HT

The effect of PZT modification was investigated on both the defect chemistry of the oxide layers (through excitation of ZnO) and in the context of charge generation in the oxide:polymer heterojunction (through excitation of P3HT): datasets for both of these cases is presented in Figure 5.3. The PZT sol-gel concentration used in these studies was 0.05 M which yields an $\sim$ 11 nm thin-film on an Si/SiO_2 surface under these processing conditions.

From the PL spectra, it can be ascertained that PZT modification only effects a

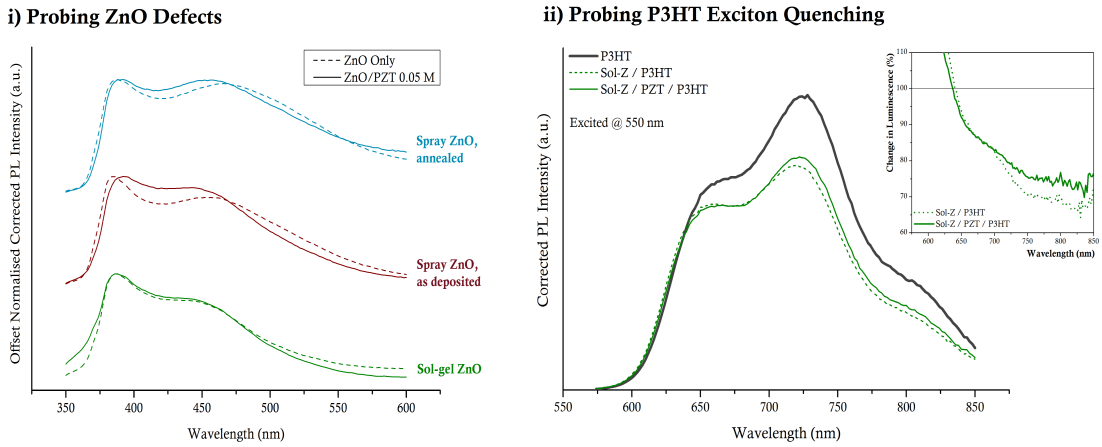

Figure 5.3 – *i)* Stacked absorption-corrected and normalised PL spectra comparing Sol-Z, SP-Z, and annealed SP-Z before (dashed lines) and after modification with 0.05 M of PZT (solid lines). The ZnO was excited at 320 nm and emissions scanned in the range 350 – 650 nm. *ii)* PL spectra for Sol-Z–P3HT films, with and without 0.05 M PZT (dashed line is unmodified ZnO, solid line for ZnO–PZT–P3HT). The bold line is the PL spectra for a neat Glass–P3HT film. In these data, the polymer was excited using a wavelength of 550 nm, followed by a scan for emission between 575 – 850 nm. Inset is the percentage change in luminescence relative to the neat P3HT.

small change in the defect characteristics of ZnO: in the case of Sol-Z, the PL profile is almost identical in both the modified and unmodified cases. For the SP-Z films, the defect emission appears to be slightly blue shifted in the PZT-modified films for the as-deposited SP-Z film, the PL profile is very similar to that of the Sol-Z–PZT film, albeit with greater defect emission (peak around 445 nm). For the annealed SP-Z–PZT film, the defect emission peak is centred around 455 nm, although this is blueshifted from $\sim$ 465 nm in the unmodified case; for both of the SP-Z films, it appears that the PZT processing conditions promote the shift of defects towards the conduction band, whereas the conditions used for SP-Z annealing promoted a shift in defects to deeper levels.

The PL data for Sol-Z–PZT–P3HT (Figure 5.3) yielded a slight decrease in luminescence quenching compared to the unmodified case. As was the case for SP-Z–P3HT films, no quenching was observed on PZT modification of SP-Z films (Appendix Figure C.3).

5.3.2 Discussion

Beek *et al.* observed increases in PL intensity in certain cases in their study of nanocrystalline ZnO:P3HT bulk heterojunction films and posited that the overall luminescence intensity in this system consists of contributions not only from exciton quenching, but also from luminescence arising from disordering of the polymer chains (although this claim was not investigated experimentally) [3]; as such, it was concluded that a quantitative measures of exciton dissociation cannot be derived from PL measurements on

ZnO:polymer systems — *i.e.* from these results, it would be erroneous to conclude that a 30 % decrease in PL intensity corresponds to quenching of 30 % of the excitons generated in these films. As discussed in Section 1.4.1.3, the defect chemistry of ZnO — especially at the surface — is highly sensitive to processing conditions and therefore it can be expected that there may be substantial differences in the defect populations of Sol-Z and SP-Z films; this in turn may affect the surface energy of the material and subsequently the ordering of the polymer on the oxide surface. However, further studies would be required to test this hypothesis — these are outlined in future work (Chapter 6). Ultimately, while this does not necessarily preclude the possibility of exciton quenching in these systems, the extent to which it occurs cannot be directly ascertained from these data. Likewise, although luminescence quenching was observed in Sol-Z–P3HT films both with and without PZT, this is not a straightforward quantitative measure of charge generation in these films.

The hypothesis that the defect levels in these SP-Z films effectively prevent them from acting as acceptor layers is supported by the PL data. Additionally, annealing of the films was not observed to change the defect emission favourably. It was concluded thus that subsequent experiments (TAS and hPV fabrication and testing) should be carried out using Sol-Z films. Despite the lack of success in fabricating SP-Z-based solar cells in this work, these layers have been successfully incorporated into working hPV devices in other reports [4, 5]: given the large number of variables in the deposition of these films, it is likely that some small changes to the spraying procedure will affect defect density and/or type. Other routes may be explored to improve the suitability of these layers to this application, such as inclusion of additives in the precursor solution — N-doping of ZnO (using atomic layer deposition) has been shown to reduce defect density and improve hPV performance [6], whilst the addition of poly(vinyl pyrrolidone) (PVP) has been investigated to stabilise defects in the synthesis of colloidal ZnO [7].

5.3.3 Transient Absorption Spectroscopy

TAS is used to study charge recombination in organic D–A systems. Typically, this is carried out by exciting the polymer (pump) — in this case using a wavelength of 510 nm to generate charges in P3HT — and measuring the signal over time from the resulting hole polarons in the film (probe) using a known wavelength, 980 nm in this case [8]. For this study, Sol-Z–PZT–P3HT films on glass were fabricated using methods outlined previously. The PZT sol-gel concentration was varied between 0.4 M and 0.001 M: in this section, results from 0.05 M and 0.01 M concentrations are presented in Figure 5.4. For all films, the P3HT thickness was $\sim$ 40 nm, deposited by spin-coating from chlorobenzene.

The polaron yield in the PZT-modified films was noticeably lower than for the Sol-Z/P3HT reference. Although the PL data suggest that the presence of PZT does not have a significant effect on exciton quenching, the decrease in yield may be attributed to the increased resistance of PZT relative to ZnO. However, the hole lifetime was greatly

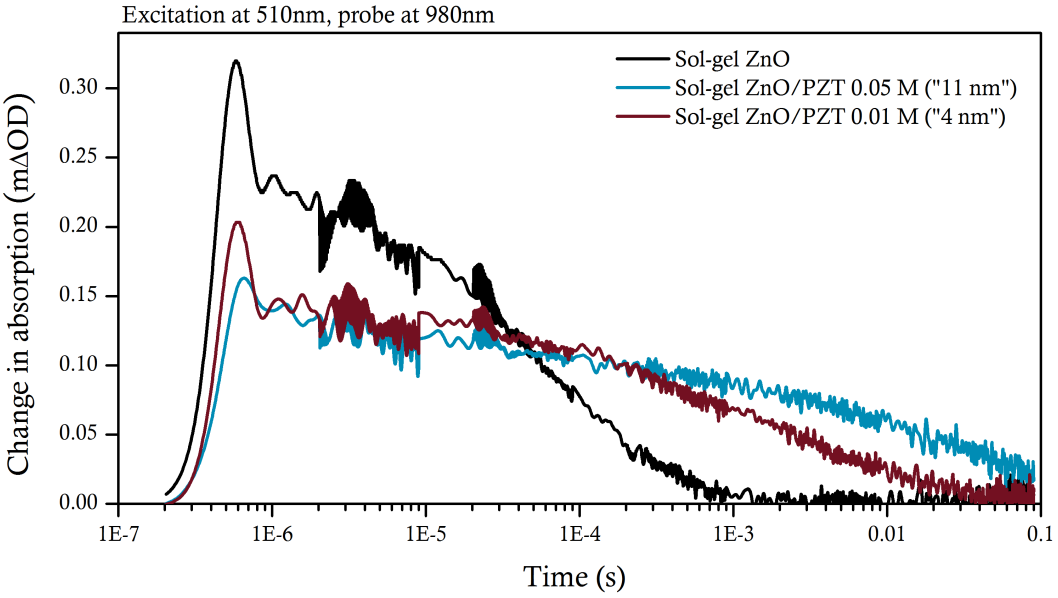

Figure 5.4 – Absorption-corrected TAS data for Sol-Z/(PZT)/P3HT films on glass. The P3HT was excited by pumping at 510 nm, whilst the hole polaron decay was measured at 980 nm. PZT concentrations of 0.05 M (11 nm of material on a flat surface) and 0.01 M (4 nm of material on a flat surface) were used. Data acquired by K. Prashanthan [9].

increased with PZT modification: for unmodified ZnO, the hole half-life was calculated to be 15 μs, whereas values of 162 μs and 2 ms were obtained for 0.025 M and 0.05 M of PZT respectively. A slight increase in polaron half-life (around 3-fold) was also observed in modification of ZnO with 0.001 M of PZT (data shown in Appendix Figure C.4), a very dilute solution corresponding to a sub-nanometre layer of material. Charge lifetimes of this magnitude have previously been observed in the case of dye-modified ZnO nanorods which exhibited a long lifetime of 6 ms [10] and in TiO_2-modified ZnO nanorods (8 ms) [11]. Increased hole lifetime in these systems is considered to be indicative of suppressed recombination pathways: in this case, it is hypothesised that the presence of PZT presents a physical barrier at the ZnO–P3HT interface which spatially separates electron and hole polarons and prevents them from undergoing non-geminate recombination.

5.3.4 Summary

PL was used to analyse the defects in ZnO films deposited by different processes, namely sol-gel and spray pyrolysis. These data showed that the deposition method and processing conditions significantly affect the defects in these films: the defects in Sol-Z appeared to be shallower than those observed in SP-Z, and the defect emission in the former was less intense. Subsequent modification with PZT did not have a significant effect on the defect emission in ZnO.

Subsequently, PL was used to probe charge generation in ZnO–(PZT)–P3HT films through excitation of P3HT. Luminescence quenching was observed in Sol-Z–P3HT films with and without PZT modification relative to neat P3HT, suggesting that charges were being generated at the polymer:oxide interface. However, no luminescence quenching was observed in SP-Z or SP-Z–PZT films; although this does not necessarily preclude the possibility of charge generation in these systems, it was decided that subsequent experiments be carried out solely on Sol-Z and Sol-Z–PZT films.

TAS data was then used to probe charge lifetime in the Sol-Z–PZT system using different concentrations of PZT. The presence of PZT was observed to increase the hole polaron lifetimes from 15 μs (unmodified ZnO) to up to 2 ms for 0.05 M PZT. These increased hole lifetimes were attributed to suppression of non-geminate recombination pathways by PZT.

5.4 Device Fabrication and Testing

5.4.1 Design and Fabrication

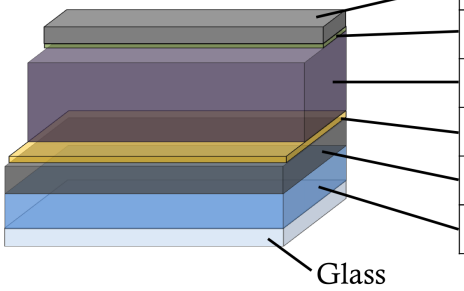

Layer	Function	Origin	Thickness
Ag	Contact	Evaporation	80 nm
MoO3	Top Contact	Evaporation	10 nm
P3HT	Donor	Spin-coating	435 nm
PZT	Interface Modifier	Sol-gel	~ 0 – 11 nm
ZnO	Acceptor	Sol-gel	145 nm
ITO	Bottom Contact	Psiotec Ltd.	160 nm

Figure 5.5 – Schematic diagram of hPV design with table containing processing details and thicknesses of each layer.

The effect of PZT modification on Sol-Z–P3HT devices was measured through fabrication of hPV devices and measuring their J–V characteristics under dark and illuminated conditions. In these experiments, PZT modification was carried out using sol-gels of different concentrations: 0.05 M (11 nm), 0.01 M (4 nm), and 0.001 M (< 1 nm)[1]. Given the wide band gap of PZT and perovskite ferroelectric materials in general (> 3.2 eV) [12], it was not expected that PZT would contribute much to device photovoltage: control devices without P3HT generated negligible photocurrent. A proposed flat energy band structure of the oxide:polymer interface is given in Figure 5.6.

In this study, inverted bilayer hPV devices were fabricated such that during operation the bottom ITO contact would collect electrons and the Ag top contact holes. The devices fabricated in this work were designed to maximise the shunt resistance and minimise contact resistance, short-circuit pathways, and leakage current; as a result, any trends in device performance would be predominantly influenced by processes occurring at the oxide:polymer interface. To this end, the following design points were taken into consideration:

i) Reasonably thick ZnO layer (> 100 nm) without pinholes to prevent direct contact of polymer with ITO.

[1]The PZT thicknesses were measured for films deposited on smooth Si/SiO_2 substrates; given the roughness of Sol-Z films and the porosity of the structure, it is expected that the actual PZT layer thickness will be slightly reduced, hence PZT sol-gel concentrations will be used to differentiate between films as opposed to thickness.

ii) Thick polymer layer: although better device performances (especially in terms of J_{sc}) can be achieved with thinner polymer layers, thicker layers help to eliminate short-circuit pathways.

iii) MoO_3/Ag top contacts: MoO_3 has been shown to improve device performance in OPVs and it has been observed that devices with these layers are relatively insensitive to the metal contact used [13]. The mechanism by which MoO_3 improves OPVs has been substantially revised in recent years: it has been established that it is predominantly an n-type material that improves devices not by electron-blocking, but by pinning the HOMO of the polymer to its work function resulting in an Ohmic contact and allowing efficient charge injection from polymer to oxide [14, 15]. By using Ohmic contacts, the resulting device V_{oc} will be determined by interfacial processes (with the maximum V_{oc} being determined by D_{HOMO}–A_{CB} offset) rather than by the built-in voltage between the contacts [16].

Fabrication of bilayer hPVs was carried out as follows: Sol-Z films were deposited on clean ITO substrates as outlined in Section 3.2 using 3 coats of 0.75 M $Zn(ac)_2$ sol-gel before annealing at 450 °C for 1 hour. A small area of ITO was masked using Kapton tape before PZT was deposited by spin-coating a sol-gel of concentrations 0.05 M (approximately 11 nm), 0.01 M (approximately 4 nm), and 0.001 M (< 1 nm), dried at 200 °C and annealed at 560 °C for 30 minutes (substrates loaded into preheated oven) and allowed to cool back to room temperature. High regioregularity, microfluidic flow reactor-derived P3HT (M_n 54,500 g mol^{-1}, PDI 1.55) [17] was stirred in chlorobenzene for at least 12 hours at 50 °C until dissolved to form a solution with a concentration of 45 mg ml^{-1}. Prior to deposition, the solution was heated to 75 °C and spin-coated at 1500 rpm for 45 seconds; this resulted in a polymer film of approximately 435 nm as measured by profilometry. Chlorobenzene was used to remove polymer covering the masked area of ITO; the ZnO in this area was also etched using 2 M HCl to expose the ITO bottom contact. Devices were completed as per the procedure in Section 2.6.1: top contacts consisting of 10 nm of MoO_3 followed by 80 nm of Ag were thermally evaporated onto the substrates using a shadow mask, yielding 6 contacts per substrate each with an area of 0.045 cm^2. Before device testing, a small quantity of Ag paste was applied to both top and bottom contacts to ensure a good electrical contact between the measuring equipment and the device.

J–V characteristics were measured as outlined in Section 2.6.2 using voltage sweeps from -1.5 to +1.5 V (from reverse to forward bias). Dark curves were acquired before and after device illumination; devices were illuminated by a Keithley Solar Simulator set at 100 mW cm^{-2} (AM 1.5) calibrated using a Si photodiode.

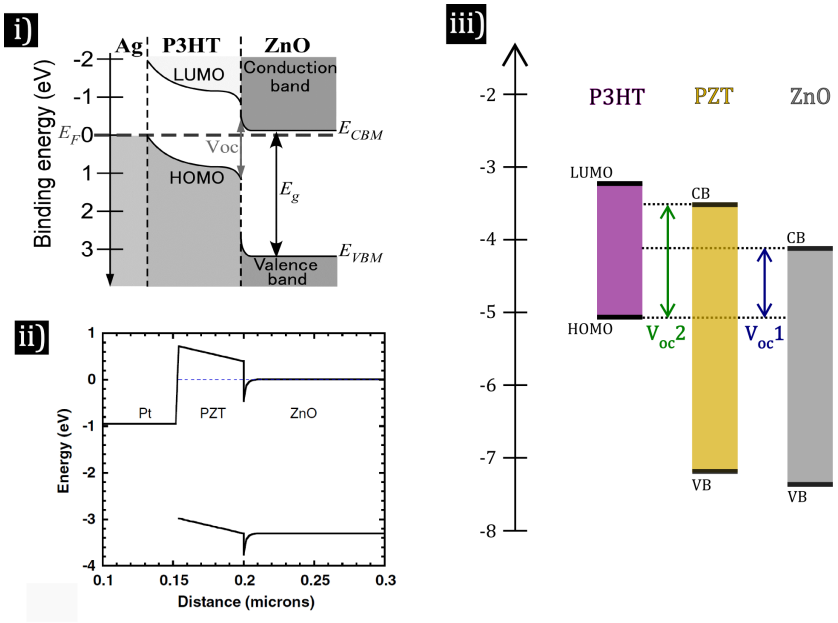

Figure 5.6 – Energy level diagrams for: *i)* the ZnO–P3HT system, reprinted with permission from [18], ©2013, AIP Publishing LLC.; *ii)* Pt–PZT–ZnO in a M–I–M structure (*N.B.* energy levels for PZT 52/48), from [19] ©IOP Publishing, reproduced by permission of IOP Publishing; *iii)* simple flat-band representation omitting band-bending of the ZnO–PZT–P3HT system showing the maximum V_{oc} for ZnO–P3HT ($V_{oc}1$) and ZnO–PZT–P3HT ($V_{oc}2$).

5.4.2 Device Performance

The unmodified ZnO devices exhibited somewhat poorer J–V characteristics than expected: in terms of V_{oc}, $\sim$ 0.30 V had been observed for hPV devices made from Sol-Z [20], compared to 0.16 V observed in this study; from the literature, V_{oc} values of 0.3 – 0.5 V can be expected from this system [21]. From the J–V curves given in Figure 5.7, the leakage current is very high in spite of the presence of both thick ZnO and polymer layers: this is reflected in the low FF values for these films (Table 5.1). Although the source of the leakage current is unclear, there are a number of possibilities: despite the relatively thick ZnO layer and the seeming absence of pinholes, the porous nature of the microstructure may present opportunities for direct contact between the polymer and the ITO; another possibility is if the ZnO surface contains a high density of electron traps which act as charge recombination centres [22].

Modification of Sol-Z films with all concentrations of PZT led to increases in device performance. At 0.001 M ($<$ 1 nm), the leakage current was greatly reduced, reflected in the improved fill-factors; increasing the PZT sol-gel concentration further reduced leakage current with both 0.01 M ($\sim$ 4 nm) and 0.05 M ($\sim$ 11 nm) exhibiting similar J–V curve gradients in the reverse bias regime. Shunt resistance (R_{sh}), calculated from

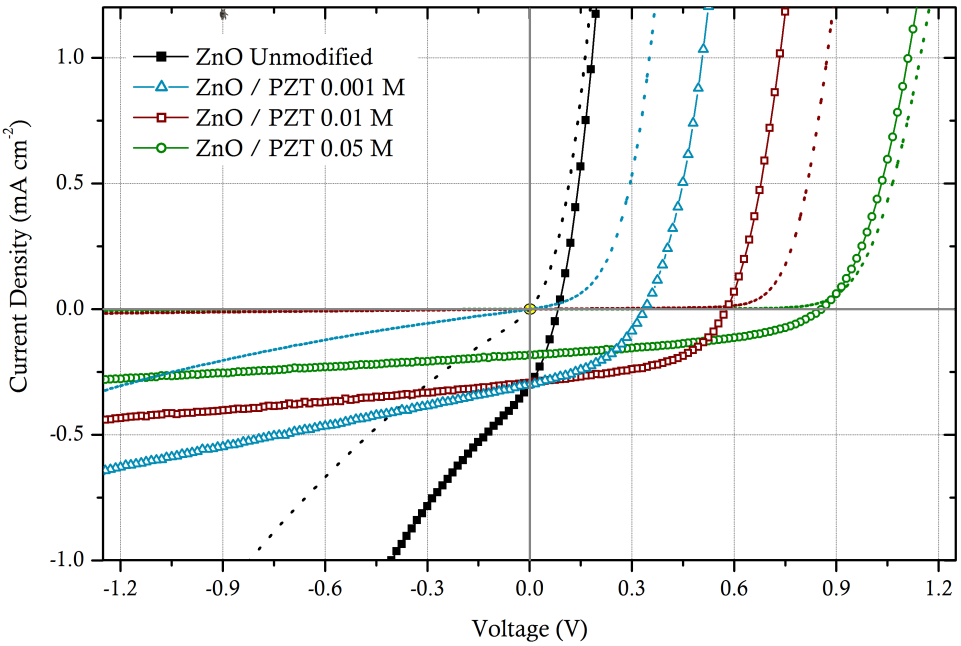

Figure 5.7 – J–V curves obtained for inverted ZnO–P3HT hPV devices with PZT interlayers derived from different concentrations of sol-gel. Illuminated curves (line and symbol plots) acquired under AM 1.5 conditions at 100 mW cm^{-2}; dark J–V curves (dotted lines) obtained after illumination are also presented.

the slope of the J–V curve under reverse bias, was seen to increase with increasing PZT concentration which would account for the observed decrease in leakage current; series resistance (R_s) values were also derived from the J–V curves in the forward bias region and showed an increase with increasing PZT concentration, to be expected given the insulating nature of PZT — both of these are listed in Table 5.1).

In terms of J_{sc}, the figures were comparable for 0.001 M and 0.01 M, agreeing with data in Section 5.3.1.2 showing that the presence of PZT did not have a great effect on charge generation. At 0.05 M, the J_{sc} is somewhat lower than for the reference devices (0.163 mA cm^{-2} compared to 0.233 mA cm^{-2}); this correlates with the TAS data which showed a decline in hole polaron yield in PZT-modified films. Although the PL data suggested that annealing P3HT in PZT-modified devices may improve exciton quenching, this processing step did not lead to a marked change in device characteristics; all data reported in this section is derived from devices with as-cast P3HT.

The presence of PZT enhanced the V_{oc} in all cases, up to 0.734 V for 0.05 M: this is comparable to the highest V_{oc} values reported for bulk ZnO–P3HT devices in the literature [23, 24, 25] and optimised nanocrystalline ZnO:P3HT BHJ devices [26, 27]. It is possible that increasing the thickness of the PZT layer further may lead to greater gains in V_{oc}, although the decreasing J_{sc} will limit this — devices with 0.1 M of PZT ($\sim$ 17 nm) exhibited negligible photocurrent.

[PZT Sol] (M)	J_{sc} (mA cm^{-2})	V_{oc} (V)	FF	PCE %	R_s Ω·cm^2	R_{sh} kΩ·cm^2
0	0.233 (0.304)	0.162 (0.131)	0.302 (0.344)	0.012 (0.014)	34	0.18
0.001	0.273 (0.301)	0.299 (0.338)	0.350 (0.422)	0.027 (0.043)	42	2.16
0.01	0.284 (0.293)	0.540 (0.578)	0.476 (0.503)	0.073 (0.085)	51	49.46
0.05	0.163 (0.182)	0.734 (0.856)	0.408 (0.4367)	0.050 (0.068)	87	123.75

Table 5.1 – Solar cell performance (AM 1.5 solar illumination) for ZnO–P3HT devices modified with PZT sol-gels of different concentrations. The average device values are presented first with the highest-performing pixels (by PCE) given in brackets. All devices illuminated for < 2 minutes.

The device performance values given in Table 5.1 were derived from pixels across 3 substrates at each PZT concentration with each averaged value derived from at least 4 device pixels. However, many of the pixels did not display rectifying behaviour (deemed to be 'dead') and therefore could not be used for evaluation. Pixel-to-pixel variation in device performance may be accounted for by a number of factors: firstly, the filling of these films with polymer may vary from film to film; secondly, the coating of the ZnO with PZT will be much less uniform than for a more planar film. Given the substantial changes in device performance with each concentration of PZT, these local variations in interlayer thickness can substantially affect the repeatability in device performance. As such, it would be beneficial to repeat these experiments using low roughness ZnO films (such as those deposited by methods such as atomic layer or pulsed laser deposition — ALD and PLD respectively) and a more complete range of PZT concentrations to optimise this system.

5.4.2.1 Effect of Illumination

Whilst ZnO–P3HT hPV devices have been shown to operate effectively, prolonged illumination generally leads to a rapid decrease in J–V characteristics, especially the V_{oc} [28] (in this paper, devices ceased to function after 50 minutes of constant illumination); indeed, many groups use UV filters to measure ZnO-based cells [29]. This has been ascribed to the electronic properties of ZnO (given that polymers are generally not observed to undergo degradation on such a short timescale) — UV light excites electrons into the ZnO conduction band (CB) which initially leads to trap filling. However, prolonged illumination further populates the CB and as the carrier density increases, the ZnO takes

on more conducting behaviour leading to disappearance of photovoltaic behaviour [30].

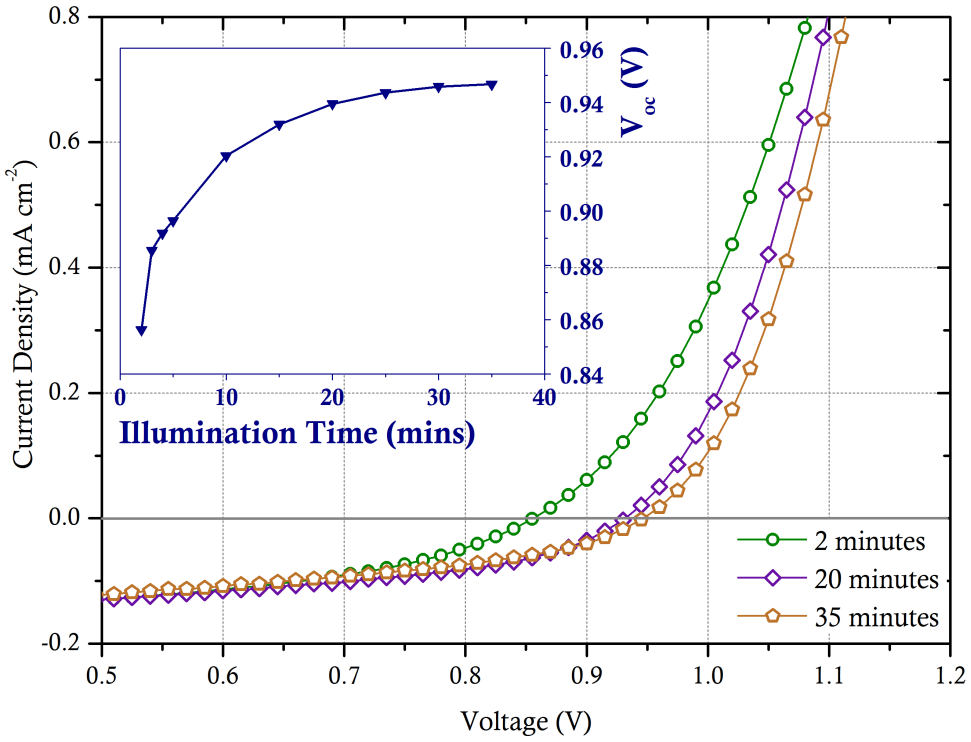

Figure 5.8 – J–V curves acquired at different time intervals for a device modified with 0.05 M PZT sol-gel under constant AM 1.5 illumination (100 mW cm^{-2}).

Conversely, the PZT-modified devices exhibited good stability under prolonged illumination and, as shown in Figure 5.8, the V_{oc} was observed to increase significantly over the course of 35 minutes — from 0.856 to 0.947 V for this particular pixel. This is the highest known V_{oc} value reported for ZnO–P3HT devices at the time of writing. Similar effects were observed for 0.01 M films: an increase from 0.578 to 0.714 V was observed over a 10 minute period. Devices modified with 0.001 M of PZT exhibited somewhat mixed results with the performance of some pixels declining with time and some exhibiting slight increases in V_{oc}, probably due to incomplete coating of the sample with the sol-gel. Whilst the V_{oc} was observed to stabilise under prolonged illumination, the J_{sc} and Fill Factor declined slightly after around 10 minutes of illumination, thought to be due to thermal effects or degradation of the polymer.

The V_{oc} of a solar cell, derived from the relationship between a diode and a photovoltage, is given thus [31]:

$$V_{oc} = \frac{nkT}{q} \ln\left(\frac{J_{sc}}{J_0} + 1\right) \tag{5.1}$$

As J_0 is a measure of the current which may be extracted from a device, V_{oc} is therefore strongly affected by recombination as it depends on the ratio $^{J_{sc}}/_{J_0}$. The increases in V_{oc} observed here are likely due to reductions in trap-assisted recombination: as the ZnO is illuminated, electrons are excited from the VB to the CB by UV irradiation which act to fill electron trap defects. Similar effects have been observed for OPV devices using ZnO interlayers in which device performance increases with illumination time [32]: in these cases, the ZnO is not part of the active layer, and thus the increase in layer conductivity does not have a perceptible effect on charge generation. The presence of PZT prevents the subsequent degradation of performance associated with increasing ZnO conductivity, thus these devices maintain their photovoltage. This is discussed in more detail in Section 5.4.3.

[PZT Sol] (M)	Illumination (mins)	J_{sc} (mA cm^{-2})	V_{oc} (V)	FF	PCE %
0.05	2	0.182	0.856	0.437	0.068
	5	0.184	0.896	0.461	0.075
	10	0.185	0.920	0.435	0.074
	20	0.181	0.940	0.404	0.069
	35	0.178	0.947	0.392	0.066
0.01	1	0.293	0.578	0.503	0.085
	6	0.312	0.679	0.515	0.109
	9	0.313	0.714	0.526	0.118

Table 5.2 – Solar cell characteristics for PZT-modified hPV devices under prolonged illumination at 100 mW cm^{-2} (AM 1.5). The values presented were acquired for single device pixels.

5.4.3 Discussion

The increases in V_{oc} observed for the PZT-modified devices can be attributed to both reduced interfacial recombination (as shown by the TAS data) and reduced trap-assisted recombination due to prolonged device illumination, as discussed above.

Table 5.3 compares the modification presented in this work with reports of other modifiers. The most comparable result presented is that for Mg-doped ZnO in which a voltage of > 0.90 V was reported: in this case, the doping changed the band gap of ZnO, raising the conduction band and therefore increasing the A_{CB}–D_{HOMO} offset, leading to the voltage rise (it should also be noted that Mg incorporation is likely to change the defect chemistry in ZnO). It is hypothesised that the high V_{oc} observed in this work is predominantly due to three factors: *i)* reduction in leakage current; *ii)* suppression of interfacial recombination; *iii)* enhancement of the depletion length in ZnO; *iv)* alteration

Modifier	Modifier Details	ZnO Structure	V_{oc} (V)	Hole $t_{1/2}$	Ref.
PZT	0.05 M	Bilayer	0.947	2 ms	-
CdS	20 nm	Bilayer	0.604	-	[33]
TiO_x	5 nm	Bilayer	0.604	-	[34]
Mg	Bulk, 35 %at	Bilayer	$\sim$ 0.900	-	[25]
TiO_2	$TiCl_4$ 0.05 M	Nanorod	0.320	8 ms	[11]
N	Surface	Nanorod	0.710	-	[23]
Z907	Dye	Nanorod	$\sim$ 0.250	6 ms	[10]

Table 5.3 – Review of the effect of different ZnO modifiers on V_{oc} and charge lifetime of ZnO–P3HT hPV devices.

of the heterojunction band structure by PZT.

Reduction in Leakage Current: the PZT modification results in a noticeable reduction in leakage current observed in the reverse bias region of the J–V data. This can be attributed to improvements in R_{sh} which were observed to increase with increasing PZT thickness; this may be a result of PZT "filling in" the ZnO layer and preventing contact between polymer and the ITO bottom contact — this was suggested by the topography data in Section 4.4.1. However, other surface modification techniques such as the nitrogen plasma used by Oh *et al.* have been shown to increase V_{oc} in devices without affecting the ZnO morphology [23], *i.e.* these improvements could not be attributed to removing pinholes in the ZnO films; Lee *et al.* have also proposed that modification of ZnO with thin TiO_x layers may also suppress current leakage by passivating ZnO surface defects [35]. Therefore, it is likely that — whilst PZT modification does eliminate physical leakage pathways — the leakage current is also reduced through changing the ZnO defect chemistry.

Suppression of Recombination: the hole lifetime data derived from TAS suggests that interfacial recombination is suppressed in PZT modified devices. However, in references [11] (TiO_2 modification of ZnO nanorods) and [10] (dye modification of ZnO nanorods), similarly long hole lifetimes were reported, yet the reported V_{oc} values were low. This suggests that this explanation alone is insufficient to account for the voltage observed in these devices[2].

Depletion Length in ZnO: The maximum attainable V_{oc} in the ZnO–P3HT system

[2]In both of these reports, the contacts would appear to be Ohmic (ITO and PEDOT:PSS/Au), thus the V_{oc} should be limited by the active layer rather than built-in voltage across the contacts of the device.

has been measured to be approximately 1.5 V [18], considering : in this study, the authors cite the short depletion in ZnO created by the interface with P3HT as one of the main reasons for V_{oc} losses. As reported by White *et al.*, the presence of a thin layer of TiO_x was calculated to stabilise the internal electric field in ZnO with increasing distance from the interface. Given the observation that the V_{oc} of PZT-modified ZnO devices do not degrade with illumination, it can be inferred that the presence of PZT acts to maintain the depletion zone in ZnO, despite the increasing population of the CB. It has been shown that polarisation coupling can occur between ZnO (piezoelectric) and PZT (ferroelectric) which may influence depletion in the ZnO layer [36] although further studies on PZT switching are required to investigate this effect in the context of hPV devices.

Effect of PZT on Band Structure: It is possible that the presence of PZT alters the device band structure[3]. In the case of CdS modification of ZnO–P3HT devices, the CB_{CdS} lies 0.3 eV above that of ZnO; the presence of CdS improved the V_{oc} in these devices by 0.3 V. In a study on Pt–PZT–ZnO M–I–M structures, it was proposed that the PZT CB lies above that of ZnO at $\sim$ 3.5 eV [19]. The increased separation in energy between the polymer HOMO and the oxide conduction band may account for the increased V_{oc}, although electronic characterisation of the PZT is required to determine its band structure in these films.

From these results, it is clear that PZT enhances the performance of ZnO-based hPV devices. Although the role of ferroelectricity in device performance was not established in these experiments, they set the foundations for investigations into the incorporation of poled PZT layers into hPV devices which may potentially effect further performance gains; regardless, the improvement of the V_{oc} close to 1 V in these devices is encouraging. By combining PZT-modification with established routes for improving the J_{sc} — through the transfer of this work into nanostructured arrays and/or the incorporation of acceptor interfacial modifiers such as PCBA [5] or designed conjugated molecules [37] — it may be possible to produce much higher performance hPV devices than have been reported to this point.

5.5 Conclusions

From PL and device testing, it was concluded that spray-pyrolysed ZnO films were unsuitable for hPV fabrication and subsequent experiments were carried out using sol-gel-derived ZnO. PL and TAS were used to probe charge generation and recombination in ZnO–PZT–P3HT films revealing that, whilst PZT modification has little effect on

[3]Unfortunately, it was not possible to verify this experimentally: attempted ultraviolet photoelectron spectroscopy (UPS) measurements on ZnO–PZT films were unsuccessful due to sample charging.

charge generation, the lifetime of separated hole polarons is greatly enhanced from 15 μs to 2 ms, suggesting reduction in interfacial geminate recombination.

Subsequent hPV device testing revealed that PZT greatly enhances the V_{oc}, although in some cases the J_{sc} was reduced due to increased series resistance. It was found that, unlike unmodified ZnO–P3HT devices, prolonged illumination did not lead to a rapid reduction in device performance, instead increasing the V_{oc}. In the case of modification with 0.05 M of PZT, saturation of the V_{oc} at 0.947 V was achieved after 35 minutes of illumination, suggesting complete filling of electron traps in ZnO [38]. This V_{oc} value is currently the highest reported for ZnO–P3HT devices. It is posited that the enhancement in V_{oc} arises from a number of factors including suppressed recombination, enhanced depletion in ZnO due to PZT modification, and the position of the PZT CB leading to augmentation of the D_{HOMO}–A_{CB} offset which determines the maximum V_{oc} that a device may attain.

Although the role of piezo- and ferroelectric effects were not established, this study provides the basis for future investigation. Moreover, these results show that PZT modification is an effective route for enhancing V_{oc} and subsequent integration with established methods for enhancing J_{sc} may provide a route towards the creation of high performance hPVs.

References

[1] V. Srikant and D. R. Clarke, "On the optical band gap of zinc oxide," *J. Appl. Phys.* **83**(10), pp. 5447–5451, 1998.

[2] P. E. Shaw, A. Ruseckas, and I. D. W. Samuel, "Exciton diffusion measurements in poly(3-hexylthiophene)," *Adv. Mater.* **20**(18), p. 3516, 2008.

[3] W. J. E. Beek, M. M. Wienk, and R. A. J. Janssen, "Hybrid solar cells from regioregular polythiophene and ZnO nanoparticles," *Adv. Funct. Mater.* **16**(8), pp. 1112–1116, 2006.

[4] N. O. V. Plank, M. E. Welland, J. L. MacManus-Driscoll, and L. Schmidt-Mende, "The backing layer dependence of open circuit voltage in ZnO/polymer composite solar cells," *Thin Solid Films* **516**(20), pp. 7218–7222, 2008.

[5] Y. Vaynzof, D. Kabra, L. Zhao, P. K. H. Ho, A. T.-S. Wee, and R. H. Friend, "Improved photoinduced charge carriers separation in organic–inorganic hybrid photovoltaic devices," *Appl. Phys. Lett.* **97**(3), p. 3309, 2010.

[6] K. P. Musselman, S. Albert-Seifried, R. L. Z. Hoye, A. Sadhanala, D. Munoz-Rojas, J. L. MacManus-Driscoll, and R. H. Friend, "Improved exciton dissociation at semiconducting polymer:ZnO donor:acceptor interfaces via nitrogen doping of ZnO," *Adv. Funct. Mater.* **24**, pp. 3562–3570, Mar. 2014.

[7] T. Gutul, E. Rusu, N. Condur, V. Ursaki, E. Goncearenco, and P. Vlazan, "Preparation of poly(N-vinylpyrrolidone)-stabilized ZnO colloid nanoparticles.," *Beilstein J. Nanotechnol.* **5**, pp. 402–6, Jan. 2014.

[8] T. M. Clarke, A. M. Ballantyne, J. Nelson, D. D. C. Bradley, and J. R. Durrant, "Free energy control of charge photogeneration in polythiophene/fullerene solar cells: the influence of thermal annealing on P3HT/PCBM blends," *Adv. Funct. Mater.* **18**, pp. 4029–4035, Dec. 2008.

[9] K. Prashanthan, *Transient Absorption Studies on Hybrid Metal Oxide/Polymer Solar Cells.* MRes Dissertation, Imperial College London, 2012.

[10] P. Ravirajan, A. M. Peiro, M. K. Nazeeruddin, M. Graetzel, D. D. C. Bradley, J. R. Durrant, and J. Nelson, "Hybrid polymer/zinc oxide photovoltaic devices with vertically oriented ZnO nanorods and an amphiphilic molecular interface layer," *J. Phys. Chem. B* **110**(15), pp. 7635–7639, 2006.

[11] P. Atienzar, T. Ishwara, B. N. Illy, M. P. Ryan, B. C. O'Regan, J. R. Durrant, and J. Nelson, "Control of photocurrent generation in polymer/ZnO nanorod solar cells by using a solution-processed TiO_2 overlayer," *J. Phys. Chem. Lett.* **1**(4), pp. 708–713, 2010.

[12] D. Tiwari and S. Dunn, "Photochemistry on a polarisable semi-conductor: what do we understand today?," *J. Mater. Sci.* **44**, pp. 5063–5079, Apr. 2009.

[13] C. Tao, S. Ruan, X. Zhang, G. Xie, L. Shen, X. Kong, W. Dong, C. Liu, and W. Chen, "Performance improvement of inverted polymer solar cells with different top electrodes by introducing a MoO_3 buffer layer," *Appl. Phys. Lett.* **93**, p. 3307, Nov. 2008.

[14] M. Kröger, S. Hamwi, J. Meyer, T. Riedl, W. Kowalsky, and A. Kahn, "Role of the deep-lying electronic states of MoO_3 in the enhancement of hole-injection in organic thin films," *Appl. Phys. Lett.* **95**, p. 3301, Sept. 2009.

[15] M. T. Greiner, M. G. Helander, W.-M. Tang, Z.-B. Wang, J. Qiu, and Z.-H. Lu, "Universal energy-level alignment of molecules on metal oxides," *Nat. Mater.* **11**, pp. 76–81, 2011.

[16] V. D. Mihailetchi, P. W. M. Blom, J. C. Hummelen, and M. T. Rispens, "Cathode dependence of the open-circuit voltage of polymer:fullerene bulk heterojunction solar cells," *J. Appl. Phys.* **94**, p. 6849, Oct. 2003.

[17] J. H. Bannock, S. H. Krishnadasan, A. M. Nightingale, C. P. Yau, K. Khaw, D. Burkitt, J. J. M. Halls, M. Heeney, and J. C. de Mello, "Continuous synthesis of device-grade semiconducting polymers in droplet-based microreactors," *Adv. Funct. Mater.* **23**, pp. 2123–2129, May 2013.

[18] T. Nagata, S. Oh, Y. Yamashita, H. Yoshikawa, N. Ikeno, K. Kobayashi, T. Chikyow, and Y. Wakayama, "Photoelectron spectroscopic study of band alignment of polymer/ZnO photovoltaic device structure," *Appl. Phys. Lett.* **102**(4), p. 3302, 2013.

[19] E. Cagin, D. Y. Chen, J. J. Siddiqui, and J. D. Phillips, "Hysteretic metal–ferroelectric–semiconductor capacitors based on PZT/ZnO heterostructures," *J. Phys. D. Appl. Phys.* **40**, pp. 2430–2434, Apr. 2007.

[20] J. M. Downing, *Control and Characterisation of Metal Oxide/Polymer Morphologies for Hybrid Photovoltaic Devices.* Doctor of Philosophy, Imperial College London, 2013.

[21] J. Huang, Z. Yin, and Q. Zheng, "Applications of ZnO in organic and hybrid solar cells," *Energy & Environ. Sci.* **4**, p. 3861, Sept. 2011.

[22] S. Shao, K. Zheng, T. Pullerits, and F. Zhang, "Enhanced performance of inverted polymer solar cells by using poly(ethylene oxide)-modified ZnO as an electron transport layer," *ACS Appl. Mater. Interfaces* **5**, pp. 380–5, Jan. 2013.

[23] S. Oh, T. Nagata, J. Volk, and Y. Wakayama, "Improving the performance of inorganic–organic hybrid photovoltaic devices by uniform ordering of ZnO nanorods

and near-atmospheric pressure nitrogen plasma treatment," *J. Appl. Phys.* **113**(8), p. 083708, 2013.

[24] M. Wang, J.-P. Sun, S. Suei, and I. G. Hill, "Optimizing the photovoltage of polymer/zinc oxide hybrid solar cells by calcium doping," *J. Appl. Phys.* **112**(4), p. 044511, 2012.

[25] D. C. Olson, S. E. Shaheen, M. S. White, W. J. Mitchell, M. F. A. M. van Hest, R. T. Collins, and D. S. Ginley, "Band-offset engineering for enhanced open-circuit voltage in polymer–oxide hybrid solar cells," *Adv. Funct. Mater.* **17**(2), pp. 264–269, 2007.

[26] D. J. D. Moet, L. J. A. Koster, B. de Boer, and P. W. M. Blom, "Hybrid polymer solar cells from highly reactive diethylzinc: MDMO-PPV versus P3HT," *Chem. Mater.* **19**(24), pp. 5856–5861, 2007.

[27] S. D. Oosterhout, M. M. Wienk, S. S. van Bavel, R. Thiedmann, L. Jan Anton Koster, J. Gilot, J. Loos, V. Schmidt, and R. A. J. Janssen, "The effect of three-dimensional morphology on the efficiency of hybrid polymer solar cells," *Nat. Mater.* **8**(10), pp. 818–824, 2009.

[28] N. C. Das and P. E. Sokol, "Hybrid photovoltaic devices from regioregular polythiophene and ZnO nanoparticles composites," *Renew. Energy* **35**, pp. 2683–2688, Dec. 2010.

[29] L. J. A. Koster, W. J. van Strien, W. J. E. Beek, and P. W. M. Blom, "Device operation of conjugated polymer/zinc oxide bulk heterojunction solar cells," *Adv. Funct. Mater.* **17**(8), pp. 1297–1302, 2007.

[30] P. A. C. Quist, W. J. E. Beek, M. M. Wienk, R. A. J. Janssen, T. J. Savenije, and L. D. A. Siebbeles, "Photogeneration and decay of charge carriers in hybrid bulk heterojunctions of ZnO nanoparticles and conjugated polymers," *J. Phys. Chem. B* **110**(21), pp. 10315–10321, 2006.

[31] J. Nelson, *The Physics of Solar Cells*, Imperial College Press, London, 2003.

[32] C. E. Small, S. Chen, J. Subbiah, C. M. Amb, S.-W. Tsang, T.-H. Lai, J. R. Reynolds, and F. So, "High-efficiency inverted dithienogermole-thienopyrrolodione-based polymer solar cells," *Nat. Photonics* **6**, pp. 115–120, Feb. 2012.

[33] E. D. Spoerke, M. T. Lloyd, E. M. McCready, D. C. Olson, Y.-J. Lee, and J. W. P. Hsu, "Improved performance of poly(3-hexylthiophene)/zinc oxide hybrid photovoltaics modified with interfacial nanocrystalline cadmium sulfide," *Appl. Phys. Lett.* **95**(21), p. 3506, 2009.

[34] M. S. White, D. C. Olson, N. Kopidakis, A. M. Nardes, D. S. Ginley, and J. J. Berry, "Control of charge separation by electric field manipulation in polymer-oxide hybrid organic photovoltaic bilayer devices," *Phys. Status Solidi a* **207**(5), pp. 1257–1265, 2010.

[35] Y.-J. Lee, R. J. Davis, M. T. Lloyd, P. P. Provencio, R. P. Prasankumar, and J. W. P. Hsu, "Open-circuit voltage improvement in hybrid ZnO–polymer photovoltaic devices with oxide engineering," *IEEE J. Sel. Top. Quantum Electron.* **16**, pp. 1587–1594, Nov. 2010.

[36] M.-X. Zhou, Z.-W. Li, B. Chen, J.-G. Wan, and J.-M. Liu, "Tunable resistive switching behaviour in ferroelectric–ZnO bilayer films," *J. Phys. D. Appl. Phys.* **46**, p. 5304, Apr. 2013.

[37] J. Yu, T.-L. Shen, W.-H. Weng, Y.-C. Huang, C.-I. Huang, W.-F. Su, S.-P. Rwei, K.-C. Ho, and L. Wang, "Molecular design of interfacial modifiers for polymer–inorganic hybrid solar cells," *Adv. Energy Mater.* **2**(2), p. 245, 2011.

[38] G. Ackbar, "It's no longer a trap," 1983.

Chapter 6

Summary and Future Work

6.1 Summary of Work

The aim of this thesis has been to improve the device performance of ZnO–P3HT hybrid photovoltaic (hPV devices) using the ferroelectric (FE) oxide lead zirconate titanate (PZT), opening the door to further research into the effects of FE polarisation on device performance. In Chapters 3 & 4, the work focussed on the growth of PZT on ZnO, especially in terms of microstructural and compositional characterisation. In the former, the growth of PZT on ZnO was optimised, establishing that PZT crystallises with a random orientation on ZnO in the temperature range used for this work (500 – 560 °C). The microstructure and composition of these films was determined; whilst it was found that some etching of Zn occurs during processing, the Zn is not incorporated into the PZT bulk, instead segregating to the top of the layer. The growth of PZT was found to proceed with a high seeding density on ZnO, leading to dense films with small (5 – 20 nm), tightly packed grains. Cross-sectional imaging revealed the presence of a secondary phase at the ZnO–PZT at the interface; whilst the composition of this was not ascertained, a likely candidate is orthorhombic PbO — PbO has previously been shown to influence PZT growth on other substrates such as ITO and Pt. Further studies are required to show the impact of these impurities on ferroelectric behaviour.

In Chapter 4, the results of the previous chapter were extended to PZT thin-films with reduced thickness. From compositional data, it was ascertained that excess Pb segregates to the surface of the PZT, likely forming a secondary phase; additionally, the change in the surface chemistry as a function of PZT thickness was recorded. The topography of the ZnO–PZT were characterised extensively using atomic force microscopy (AFM) showing that PZT island formation does not occur; additionally, power spectral density function analysis was used to derive structural correlation lengths for different components in the thin-films and the evolution of the ZnO–PZT microstructure with increasing PZT thickness was tracked. Although the model used requires some refinement, this is potentially a very useful tool for monitoring microstructural change using a non-destructive method as it circumvents the need for high volumes of cross-sectional

TEM data which requires a much longer time to prepare and image.

In Chapter 5, PZT was incorporated in hPV devices. PZT interlayers were shown to improve the open-circuit voltage (V_{oc}) of the devices substantially, leading to an overall increase in efficiency; additionally, unlike typical ZnO:P3HT devices, the solar cell characteristics of these devices improved with prolonged exposure to light. The V_{oc} was observed to reach a maximum value of 0.947 V (from 0.16 V for the unmodified film) with a PZT layer derived from a 0.05 M sol-gel: this is the highest V_{oc} value achieved by a ZnO–P3HT hybrid device at the time of writing. The origins of this large increase in V_{oc} can be partially attributed to the greatly increased charge lifetime, as determined by transient absorption spectroscopy, indicating a reduction in interfacial charge recombination. However, it is posited that the offset between the conduction band of the acceptor and the HOMO of the donor is increased with PZT modification, increasing the maximum attainable V_{oc} of the device which would also contribute to this large voltage increase.

6.2 Future Work

The work presented in this thesis provides the framework for a number of different avenues of research into both the ZnO–PZT system and into further hybrid and organic photovoltaic research. As well as photovoltaic applications, there are other applications which may exploit the polarisation coupling between the two materials — this has been demonstrated for ZnO–PZT-based capacitor systems [1], but may also be extended to other piezoelectric applications.

6.2.1 Further Materials Characterisation

Although this study includes a a broad range of structural characterisation of the ZnO–PZT films, there are a number of experiments available which would supply a greater understanding of the system. Two areas are of particular interest: firstly, analysing the PZT 'surface region' (as shown by the time-of-flight secondary ion mass spectrometry data in Section 3.12) and identifying the non-PZT phases present in this region; secondly, local FE characterisation of ZnO–PZT thin-films, particularly at lower PZT length scales to determine the critical thickness of the PZT layers in this system.

6.2.1.1 Grazing-incidence X-ray Diffraction Studies

In conventional XRD, the radiation incident on the sample typically penetrates on the order of millimetres and the resulting diffraction patterns are representative of the bulk crystallography. In this work, XRD characterisation of the PZT interlayers became increasingly difficult with decreasing thickness; additionally, the compositional analysis

of these films showed possible segregation of Pb and Zn to the surface. Grazing-incidence X-ray diffraction (GIXRD) can be used to probe the crystallography of the surface: this can be especially useful if secondary phases are present in this region; additionally, differences in surface structure to the bulk may be reflected in the results. A typical GIXRD instrumental setup is given in Figure 6.1 — typically very low glancing angles are used ($\sim 1°$), requiring a very well collimated and highly focussed, intense X-ray beam, usually achieved through the use of monochromator crystals (such as Ge) [2].

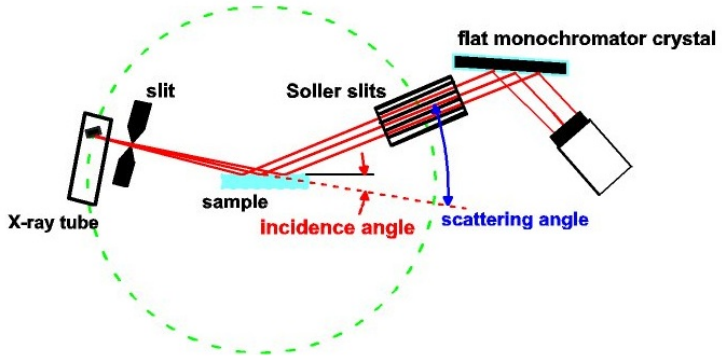

Figure 6.1 – Representation of GIXRD apparatus. Reproduced from [3]: image courtesy of the Helmholtz Zentrum Dresden Rossendorf (HZDR).

GIXRD has previously been used to investigate ultrathin PZT thin-films [4]. In the context of this work, the technique could be used in three ways: firstly, to identify crystallisation of PZT with decreasing film thickness to determine the point at which PZT no longer crystallises in the tetragonal phase; secondly, to probe the crystallinity of Pb and Zn impurity phases present at the PZT surface — these studies could be used to fine-tune the optimisation of annealing conditions and determine whether prolonged heating leads to a decrease in the presence of these impurities or whether the presence of Zn stabilises them; thirdly, GIXRD can be used to probe the crystal structure of polymers such as P3HT [5]. Differences in surface chemistry lead to differences in polymer ordering on a surface which may influence device performance [6]: by depositing thin layers (< 10 nm) of P3HT on ZnO and ZnO–PZT surfaces, any changes in interfacial polymeric ordering could be ascertained using this method — this method has previously been used to study polymer conformation on ZnO and Li-doped ZnO thin-films [7].

6.2.1.2 Scanning Probe Microscopy Techniques

Scanning probe microscopy encompasses a plethora of techniques which may be carried out using the same basic apparatus: this includes atomic force microscopy which was used extensively in Chapters 3 & 4 to image the topography of ZnO–PZT thin-films. With the appropriate modifications and equipment, investigation of properties such as

piezoresponse and local conductivity may be carried out [8] which would provide useful insights into the functional behaviour of ZnO–PZT system.

6.2.1.2.1 Ferroelectric Characterisation

The ZnO–PZT thin-films in this work did not exhibit discernible tetragonal peak splitting: although FE behaviour has been reported for ZnO–PZT films with similar XRD patterns [9], FE characterisation of the films in this work would be required to unambiguously determine that they do crystallise in the tetragonal phase. Moreover, determination of the FE properties of these films is a prerequisite to carrying out studies into the effects of permanent polarisation in hPV devices.

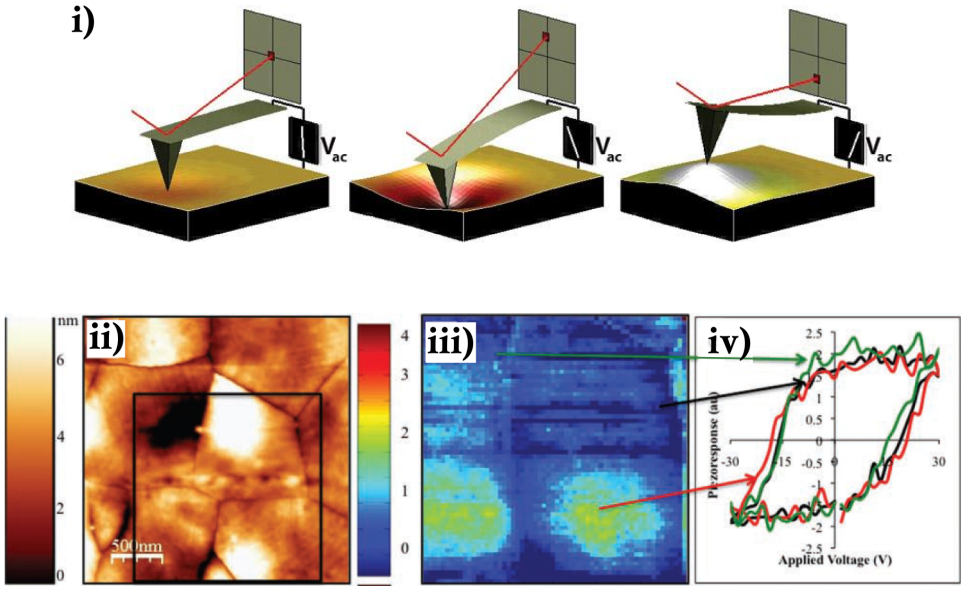

Figure 6.2 – *i)* illustration of the response of a piezoelectric sample to the applied AC bias of a PFM tip. Image reproduced from [10], originally by Dr S. Jesse (Oak Ridge National Laboratory). *ii)* topographical AFM image of a PZT rosette grown on ITO; *iii)* and *iv)* are the corresponding piezoforce response data acquired by SS-PFM. *iv)* shows the piezoelectric hysteresis loops acquired in different regions of the sample. Images reproduced with permission from [11].

Characterisation of FE properties is often conducted through the fabrication of Metal–Insulator–Metal structures and measurement of capacitance–voltage (C–V) characteristics. However, at reduced length scales of the FE material, designing capacitors which produce adequate signal-to-noise ratios in these measurements becomes increasingly difficult as the thickness of the film is reduced; additionally, it is expected that leakage current across the device will increase with decreasing thickness, further hindering measurement. An alternative method to this is the use of piezoresponse force microscopy (PFM): this technique, along with the spatially resolved switching spec-

troscopy PFM (SS-PFM) variation, has been used to characterise PZT films, notably in the verification of the ferroelectric properties of 3-dimensional nanostructures possessing grain sizes with comparable size to those used in this work [11].

The experimental setup for PFM is similar to that of AFM, outlined in Section 2.3.4, although sample grounding and conductive probes are required; unlike capacitors, a conductive top contact is not required, thus imaging could be carried out on the ITO–ZnO–PZT structures synthesised in this work. In operation, the polarisation response of the surface to an AC bias of the tip is measured, allowing imaging of ferroelectric domains [12]. SS-PFM allows acquisition of polarisation hysteresis loops across a surface, from which the FE switching characteristics can be derived. Additionally, this can be mapped as a function of position, thus allowing local variations in FE properties to be determined. This technique provide extremely useful data on the FE behaviour of the ZnO–PZT structures with changing thickness and could be used to determine the critical thickness of the PZT films. Additionally, a comparison between ZnO, ZnO–PZT, and a similar PZT film grown on a non-piezoelectric material (for example, TiO_2 provides a similarly high seeding density for PZT [13]) may yield insights into the polarisation coupling between ZnO and PZT.

6.2.1.2.2 Conducting AFM Studies

Conducting AFM (C-AFM) is an extension of AFM in which conventional topographical imaging is conducted whilst the current between the tip and the sample (negatively biased) is measured — for this, as with PFM, conductive probes are required. In addition to the current maps, current–voltage (I–V) characteristics may be recorded in a single location [14]. This technique may be used to investigate the conductivity of the ZnO–PZT thin-films and could be used to determine the extent to which PZT modification limits charge transport in a device.

C-AFM has also been used to acquire local I–V loops in bulk-heterojunction OPV devices to correlate film conductivity with the film morphology [15]. A comparison in the C-AFM scans of ZnO–P3HT and ZnO–PZT–P3HT films could be helpful in analysis of the role of PZT in hPV devices; moreover, this technique could be implemented as part of the proposed study into PZT poling in hPVs presented in Section 6.2.2.2.

6.2.2 Photovoltaics

This study has provided the basis for further research into the origins of enhancement of device performance by PZT which ultimately aims to elucidate whether FE polarisation does indeed affect the performance of either organic or hybrid photovoltaic systems, or whether this is a consequence of the other properties of the materials. The following proposed experiments build off the work in this thesis and aim address these outstanding points.

6.2.2.1 Optimisation of ZnO–PZT Devices

Whilst the work in Chapter 5 showed that PZT modification had a substantial positive impact on hPV device performance, further work needs to be carried out to elucidate the relation between PZT thickness and device performance: given the high resistivity of PZT, a balance needs to be found between the short-circuit current density (J_{sc}) and the open-circuit voltage (V_{oc}). Given the roughness and microstructural complexity of the sol-gel-derived ZnO thin-films, a more systematic study could be carried out by substituting these with ZnO deposited using more controlled conditions using methods such as chemical vapour deposition (CVD), pulsed laser deposition (PLD), or atomic layer deposition (ALD). Additionally, a more extensive range of PZT sol-gel concentrations could be employed, *e.g.* films with thickness from 0 – 20 nm with 2 nm intervals would lead to effective optimisation of the system, as well as providing good quality films for the experiments outlined in Section 6.2.1.2.

6.2.2.2 Ferroelectric Effects in hPVs

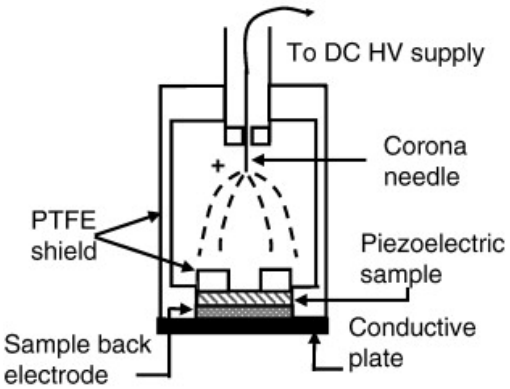

Figure 6.3 – Illustration of corona poling of a ferroelectric material. Reproduced from [16], ©2008 with permission from Elsevier.

The overarching motivation for incorporation of PZT into ZnO–P3HT devices was the investigation into FE effects on hPV devices, as well as a potential subsequent extension to OPV systems. One of the main findings in the original set of FE-OPV reports by Yuan *et al.* was tunability of the device through poling of the FE polymer [17, 18]. However, it has been argued that, using the methodology outlined in these papers, poling of the FE layer is unlikely [19]: poling was carried out using large voltage pulses through a fully fabricated device, whereas it has been argued that the active layer components of the solar cell may screen this charge, thus rendering the applied electric field insufficient to induce permanent polarisation in the FE polymer.

To unambiguously demonstrate the effects of poling on device performance, it is

proposed that the ZnO–PZT–P3HT devices are used, but rather than attempting to pole a completed device, the PZT layer is poled before the deposition of the polymer layer. One such method of poling these layers is corona poling [16]: this only requires that the sample is grounded via a bottom contact, whereas direct contact poling requires contacts above and below the FE layer. Corona poling uses a needle through which a high DC potential is applied, resulting in ionisation of surrounding air molecules; the electric charge from the needle is directed at the sample surface, creating an electric field. After poling the ITO–ZnO–PZT layers, device fabrication would proceed similarly to the methods used in this work; the spontaneous polarisation should remain if processing temperatures are held below the Curie temperature of the PZT films. Whilst this method precludes tuning of the polarisation of the same device, trends between differently poled layers from the same batch should yield discernible trends in data.

This methodology could also be extended to inverted OPV systems, using the ITO–ZnO–PZT layers as bottom contacts for P3HT:PCBM active layers — although the results of this thesis show that the presence of PZT is beneficial to the ZnO:P3HT system through enhancement of the open-circuit voltage (V_{oc}) which would not be observed to the same extent in an organic active layer system, it would provide further evidence as to the role of FE polarisation on device performance.

6.2.2.3 Improving Short-Circuit Current Density

Regardless of whether the FE properties of PZT influence device performance, the substantial V_{oc} improvement on modification of ZnO shows that PZT modification of the ZnO:P3HT interface is a viable route towards creating higher performance hPVs. These devices are still limited by low short circuit current density (J_{sc}), however, and steps to improve exciton harvesting in these devices is required. Improving the internal quantum efficiency of the devices could be achieved by modifying the ZnO–PZT layers with a self-assembled monolayer of phenyl-C_{61}-butyric acid (PCBA), as reported in [20] and [21]. As well as this, standard methods exist for increasing the interfacial area of hPV devices, predominantly through using ZnO nanostructures such as nanowires and nanorods which aim to increase the number of excitons which may reach the donor–acceptor heterojunction. Thin, conformal coatings of materials have been demonstrated on ZnO using techniques such as atomic layer deposition [22]; thin coatings of PZT have been achieved using this method [23], as well as through techniques such as liquid source misted chemical deposition which has been used to coat ZnO–Pd nanowires [24]. If similar V_{oc} increases are observed in interface-modified ZnO nanostructure devices as for the devices in this study, similar gains in device efficiency are to be expected.

References

[1] E. Cagin, D. Y. Chen, J. J. Siddiqui, and J. D. Phillips, "Hysteretic metal–ferroelectric–semiconductor capacitors based on PZT/ZnO heterostructures," *J. Phys. D. Appl. Phys.* **40**, pp. 2430–2434, Apr. 2007.

[2] R. Feidenhans'l, "Surface structure determination by X-ray diffraction," *Surf. Sci. Rep.* **10**, pp. 105–188, May 1989.

[3] A. Kolitsch, "Method of grazing incidence (GI-XRD), `http://www.hzdr.de/db/Cms?pOid=11644&pNid=0`," 2014.

[4] K. Vojisavljević, G. Branković, T. Srećković, A. Rečnik, and Z. Branković, "Preparation of ultrathin PZT films by a chemical solution deposition method from a polymeric citrate precursor," *J. Eur. Ceram. Soc.* **30**, pp. 485–488, Jan. 2010.

[5] M. Brinkmann, "Structure and morphology control in thin films of regioregular poly(3-hexylthiophene)," *J. Polym. Sci. Part B Polym. Phys.* **49**, pp. 1218–1233, Sept. 2011.

[6] D. H. Kim, Y. D. Park, Y. Jang, H. Yang, Y. H. Kim, J. I. Han, D. G. Moon, S. Park, T. Chang, C. Chang, M. Joo, C. Y. Ryu, and K. Cho, "Enhancement of field-effect mobility due to surface-mediated molecular ordering in regioregular polythiophene thin film transistors," *Adv. Funct. Mater.* **15**, pp. 77–82, Jan. 2005.

[7] M. T. Lloyd, Y.-J. Lee, R. J. Davis, E. Fang, R. M. Fleming, J. W. P. Hsu, R. J. Kline, and M. F. Toney, "Improved efficiency in poly(3-hexylthiophene)/zinc oxide solar cells via lithium incorporation," *J. Phys. Chem. C* **113**(41), pp. 17608–17612, 2009.

[8] P. Eaton and P. West, *Atomic Force Microscopy*, Oxford University Press, Oxford, 1st ed., 2010.

[9] M.-X. Zhou, Z.-W. Li, B. Chen, J.-G. Wan, and J.-M. Liu, "Tunable resistive switching behaviour in ferroelectric–ZnO bilayer films," *J. Phys. D. Appl. Phys.* **46**, p. 5304, Apr. 2013.

[10] R. Proksch and S. V. Kalinin, "Piezoresponse Force Microscopy with Asylum Research AFMs," tech. rep., Asylum Research.

[11] M. A. McLachlan, D. W. McComb, M. P. Ryan, A. N. Morozovska, E. A. Eliseev, E. A. Payzant, S. Jesse, K. Seal, A. P. Baddorf, and S. V. Kalinin, "Probing local and global ferroelectric phase stability and polarization switching in ordered macroporous PZT," *Adv. Funct. Mater.* **21**(5), pp. 941–947, 2011.

[12] S. Dunn, C. P. Shaw, Z. Huang, and R. W. Whatmore, "Ultrahigh resolution of lead zirconate titanate 30/70 domains as imaged by piezoforce microscopy," *Nanotechnology* **13**, pp. 456–459, Aug. 2002.

[13] C. P. Shaw, S. S. Roy, R. W. Whatmore, H. Gleeson, Z. Huang, Q. Zhang, and S. Dunn, "Growth and characterisation of lead zirconate titanate (30/70) thin films using TiO_2 seeding for oxide ferroelectric-liquid crystal display application," *Ferroelectrics* **256**, pp. 159–174, Jan. 2001.

[14] Y.-H. Liau, N. F. Scherer, and K. Rhodes, "Nanoscale electrical conductivity and surface spectroscopic studies of indium–tin oxide," *J. Phys. Chem. B* **105**(16), pp. 3282–3288, 2001.

[15] M. Guide, X.-D. Dang, and T.-Q. Nguyen, "Nanoscale characterization of tetrabenzoporphyrin and fullerene-based solar cells by photoconductive atomic force microscopy," *Adv. Mater.* **23**(20), p. 2313, 2011.

[16] J. M. Marshall, Q. Zhang, and R. W. Whatmore, "Corona poling of highly (*001*)/(*100*)-oriented lead zirconate titanate thin films," *Thin Solid Films* **516**(15), pp. 4679–4684, 2008.

[17] Y. Yuan, T. J. Reece, P. Sharma, S. Poddar, S. Ducharme, A. Gruverman, Y. Yang, and J. Huang, "Efficiency enhancement in organic solar cells with ferroelectric polymers," *Nat. Mater.* **10**(4), pp. 296–302, 2011.

[18] Y. Yuan, P. Sharma, Z. Xiao, S. Poddar, A. Gruverman, S. Ducharme, and J. Huang, "Understanding the effect of ferroelectric polarization on power conversion efficiency of organic photovoltaic devices," *Energy & Environ. Sci.* , 2012.

[19] K. Asadi, P. de Bruyn, P. W. M. Blom, and D. M. de Leeuw, "Origin of the efficiency enhancement in ferroelectric functionalized organic solar cells," *Appl. Phys. Lett.* **98**(18), pp. 3301–3303, 2011.

[20] Y. Vaynzof, D. Kabra, L. Zhao, P. K. H. Ho, A. T.-S. Wee, and R. H. Friend, "Improved photoinduced charge carriers separation in organic–inorganic hybrid photovoltaic devices," *Appl. Phys. Lett.* **97**(3), p. 3309, 2010.

[21] Y. Vaynzof, A. A. Bakulin, S. Gélinas, and R. H. Friend, "Direct observation of photoinduced bound charge-pair states at an organic–inorganic semiconductor interface," *Phys. Rev. Lett.* **108**, p. 6605, June 2012.

[22] B. Min, J. Lee, J. Hwang, K. Keem, M. Kang, K. Cho, M. Sung, S. Kim, M.-S. Lee, S. Park, and J. Moon, "Al_2O_3 coating of ZnO nanorods by atomic layer deposition," *J. Cryst. Growth* **252**, pp. 565–569, May 2003.

[23] T. Watanabe, S. Hoffmann-Eifert, R. Waser, and C. S. Hwang, "Atomic layer deposition of Pb(Zr,Ti)O_x, thin films by a combination of binary atomic layer deposition processes," in *2006 IEEE Int. Symp. Appl. Ferroelectr.*, pp. 89–92, IEEE, July 2006.

[24] S. Kawasaki, H. J. Fan, G. Catalan, F. D. Morrison, T. Tatsuta, O. Tsuji, and J. F. Scott, "Solution-process coating of vertical ZnO nanowires with ferroelectrics.," *Nanotechnology* **19**, p. 5302, Sept. 2008.

Appendices

Appendix A

Growth and Structure of Sol-Gel-Derived PZT Films on ZnO

A.1 ITO Diffraction Data

Peak	(h k l)	**JCPDS Ref.**		**PsiOTec ITO**	
		2θ Pos. (°)	d-spacing nm	2θ Pos. (°)	d-spacing nm
1	(*1 1 2*)	22.81	0.390	21.34	0.416
2	(*1 2* $\bar{1}$)	30.56	0.292	30.32	0.295
3	(*2 1* $\bar{2}$)	35.34	0.254	35.29	0.254
4	(*2 2 0*)	38.02	0.237	37.48	0.240
5	(*1 0 4*)	42.24	0.214	41.54	0.217
6	(*4 0 1*)	45.41	0.200	45.33	0.200
7	(*0 4 2*)	48.96	0.186	48.90	0.186
8	(*1 2* $\bar{4}$)	50.63	0.180	50.64	0.180
9	(*2 0 5*)	56.55	0.163	55.63	0.165
10	(*4 2* $\bar{1}$)	60.67	0.154	60.20	0.154

Table A.1 – ITO X-ray diffraction peak data from JCPDS reference 01-088-0773 (rhombohedral $In_4Sn_3O_{12}$) compared with XRD data obtained from an ITO thin-film substrate used in this work (from PsiOTec Ltd.).

A.2 ZnO Characterisation

Peak	(*h k l*)	**ZnO Reference**		**Spray ZnO**		**Sol-gel ZnO**		***d*-spacing**
		2θ Pos. (°)	RPI %	2θ Pos. (°)	RPI %	2θ Pos. (°)	RPI %	nm
1	(*1 0 0*)	31.82	50.0	–	0.0	31.86	30.2	0.281
2	(*0 0 2*)	34.33	30.0	34.47	100.0	34.52	100.0	0.260
3	(*1 0 1*)	36.50	100.0	36.26	27.3	36.40	36.1	0.247
4	(*1 0 2*)	47.57	16.0	47.58	22.4	–	0.0	0.191
5	(*1 1 0*)	57.17	30.0	–	0.0	56.80	8.0	0.162
6	(*1 0 3*)	63.20	30.0	62.89	30.3	62.99	7.8	0.148
7	(*2 0 0*)	66.76	2.0	–	0.0	–	0.0	0.140
8	(*1 1 2*)	67.86	20.0	–	0.0	–	0.0	0.138
9	(*2 0 1*)	69.00	8.0	–	0.0	–	0.0	0.136

Table A.2 – XRD peak data for spray-pyrolysed and sol-gel-derived ZnO thin-films on glass compared to a ZnO reference pattern (zincite, JCPDS 00-001-1136). RPI is the relative peak intensity, expressed as a percentage. The *d*-spacings were used in the analysis of high-resolution transmission micrographs.

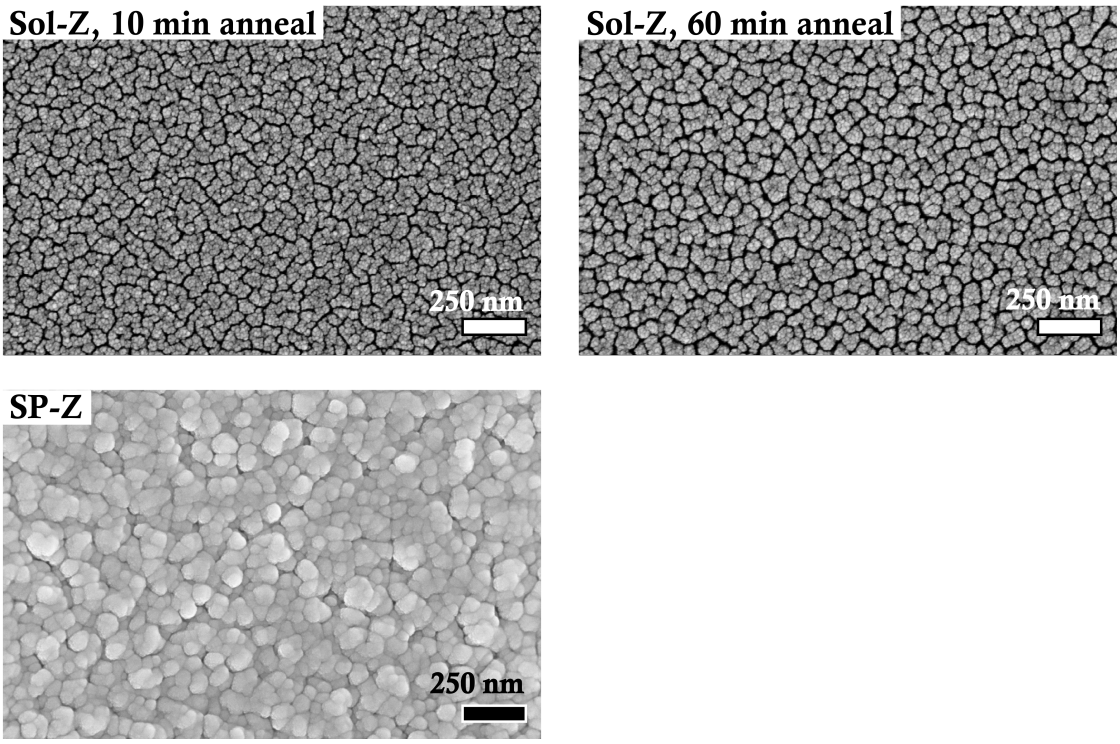

Figure A.1 – Scanning electron micrographs for ZnO thin-films acquired using a 5.0 kV electron beam at a magnification of 150,000 x. **Top**: sol-gel-derived ZnO thin-films annealed at 450 °C for 10 minutes (left) and 60 minutes (right) — the fine granular texture is due to a coating of a thin layer of Au to improve sample conductivity. **Bottom**: a spray-pyrolysed ZnO thin-film deposited using conditions outlined in Section 3.2.2.

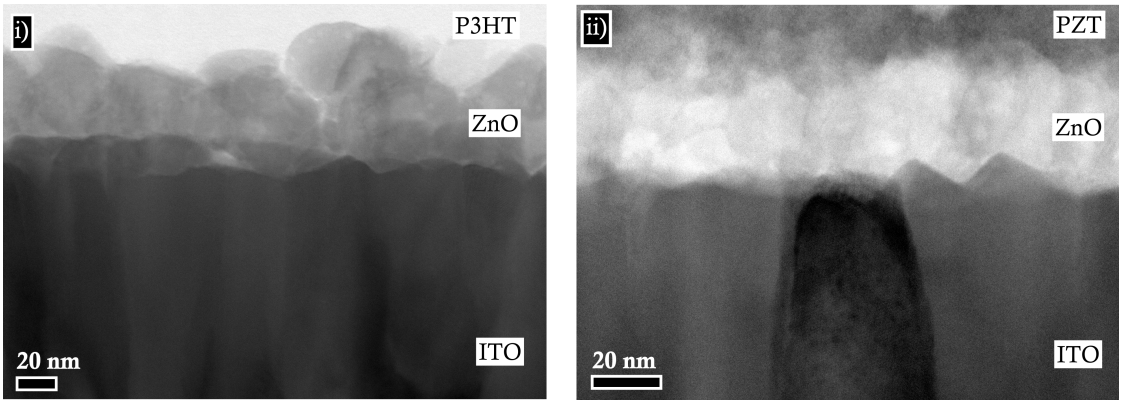

Figure A.2 – Bright field TEM micrographs of *i)* SP-Z–P3HT film and *ii)* SP-Z–PZT–P3HT film showing the microstructure of the ZnO layer before and after PZT modification. Note the different magnification of the two images. Sample preparation carried out by C. Burgess and Dr J. B. Gilchrist, images acquired by Dr C. McGilvery.

A.3 PZT Growth on ITO

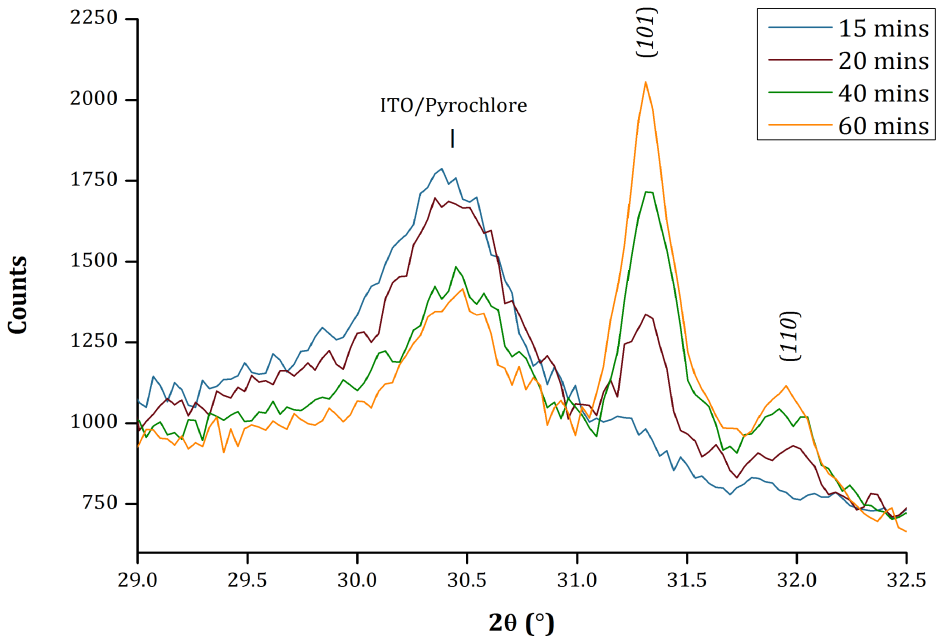

Figure A.3 – Small-angle region of XRD patterns acquired for ITO–PZT thin-films annealed at 500 °C in a preheated furnace (no temperature ramp) for different time periods. The region displays the PZT (*101*) and (*110*) peaks, as well as a peak at $\sim 30.5°$ containing a peak consisting of contributions from both the substrate and the intermediate pyrochlore phase.

A.4 PZT Growth on ZnO

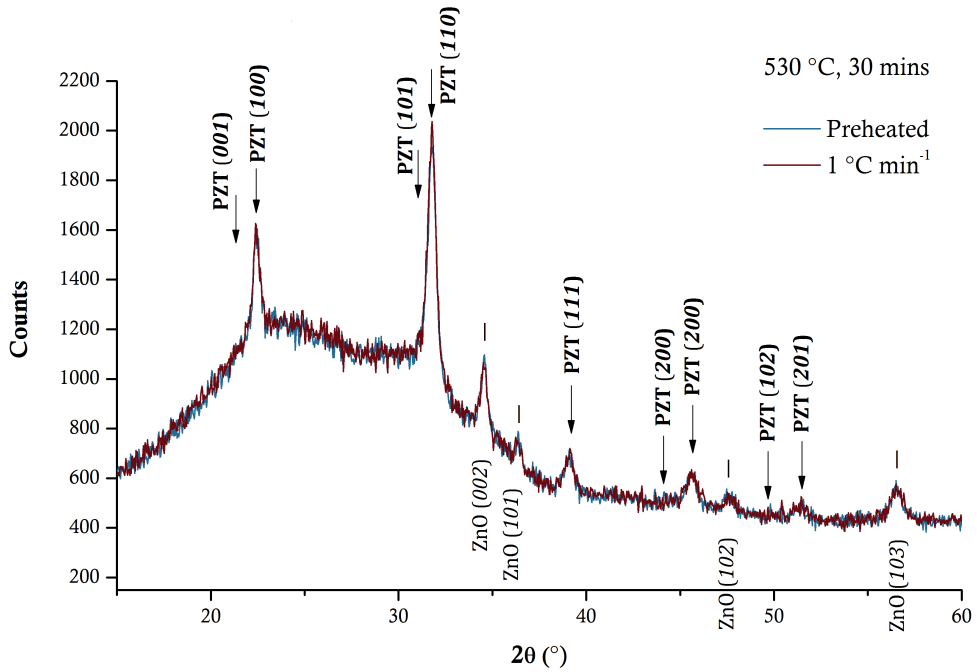

Figure A.4 – Overlayed XRD patterns for ZnO–PZT thin-films annealed at 530 °C for 30 minutes with different heating rates.

A.4.1 Topography

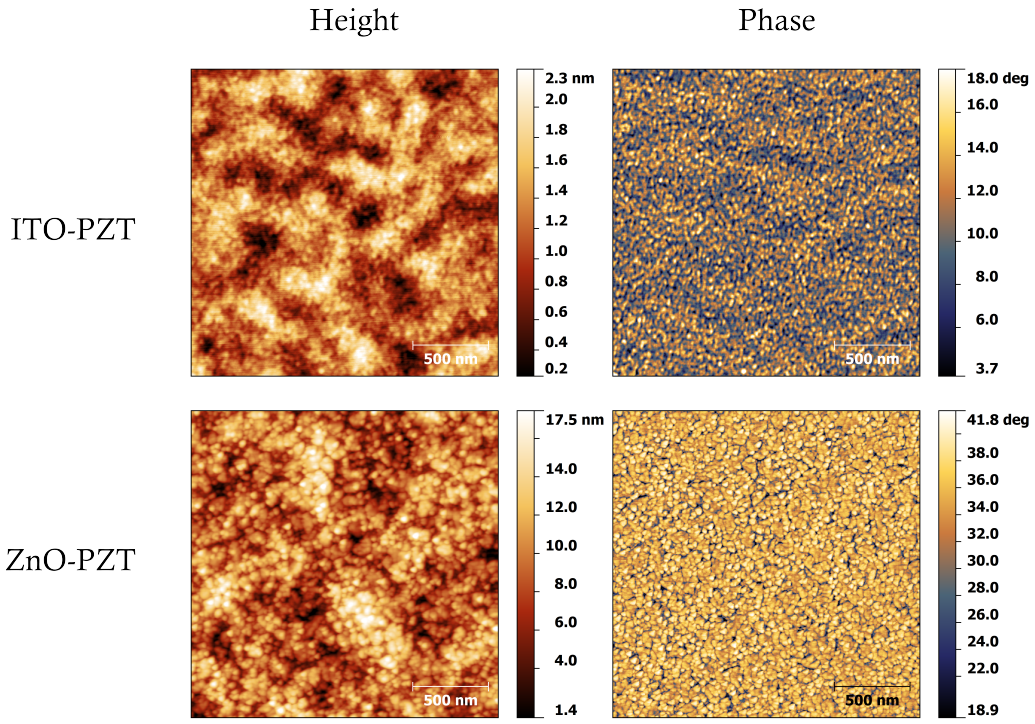

Figure A.5 – 2 x 2 μm tapping mode AFM topographical and phase scans for ITO–PZT and ZnO–PZT thin-films.

A.4.2 ZnO Acid Wash Tests

To evaluate the effect of the acidity of the PZT sol-gel on ZnO, a solution of acetic acid in methanol was made to the same pH (3.4) and deposited on spray-pyrolysed ZnO thin-films using the same conditions for PZT layer formation (annealing at 560 °C in a preheated furnace for 30 minutes). XRD and AFM scans of the films were acquired before and after the acid wash treatments: these are displayed in Figure A.6. Little change in the XRD patterns was observed, suggesting minimal changes in crystal structure of the films; the roughness parameters from the AFM data show a decrease in surface roughness on acid treatment, suggesting a degree of etching; however, there is little discernible change in the microstructure either by inspection or in the fractal dimension of the films.

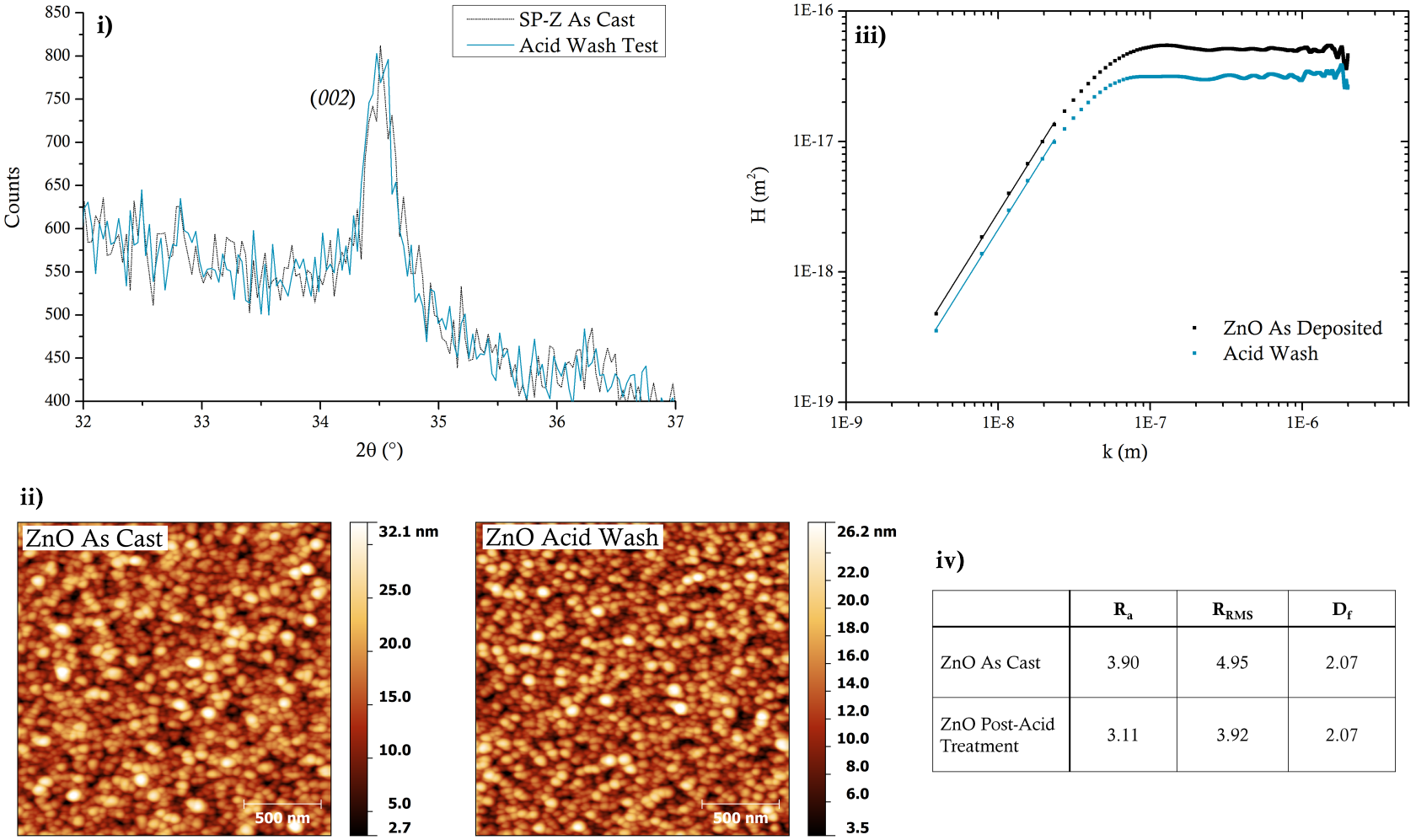

iv)

	R_a	R_{RMS}	D_f
ZnO As Cast	3.90	4.95	2.07
ZnO Post-Acid Treatment	3.11	3.92	2.07

Figure A.6 – XRD and AFM data acquired for ZnO thin-films before and after 'wash' treatment with a pH 3.4 solution of acetic acid in methanol. *i)* XRD data showing the effect of acid treatment on the dominant (*002*) ZnO peak. *ii)* 2 x 2 μm tapping mode AFM height scans before (left) and after (right) acid wash treatment. *iii)* height-height correlation curves acquired from *ii)* used to calculate the fractal dimension, D_f of the ZnO films before and after treatment (method described in Section 4.4.1.1. *iv)* roughness parameters and fractal dimensions derived from the AFM data of the films before and after treatment.

A.4.3 PZT XRD Data

Peak	$(h\ k\ l)$	**Powder Ref.**		**SPZ–PZT**	
		2θ Pos. (°)	d-spacing nm	2θ Pos. (°)	d-spacing nm
1	(*0 0 1*)	21.38	0.415	–	–
2	(*1 0 0*)	22.30	0.398	22.43	0.396
3	(*1 0 1*)	31.12	0.287	–	–
4	(*1 1 0*)	31.74	0.282	31.78	0.281
5	(*1 1 1*)	38.61	0.233	39.16	0.230
6	(*0 0 2*)	43.54	0.208	–	–
7	(*2 0 0*)	45.53	0.199	45.55	0.199
8	(*1 0 2*)	49.44	0.184	–	–
9	(*2 0 1*)	50.93	0.179	–	–
10	(*2 1 0*)	51.27	0.178	51.24	0.178
11	(*1 1 2*)	54.96	0.167	–	–
12	(*2 1 1*)	56.18	0.164	56.52	0.163

Table A.3 – PZT 30/70 XRD peak data obtained from a powder reference and an SPZ–PZT thin-film. The d-spacings obtained from these data were used in analysis of lattice fringes in high resolution transmission electron micrographs.

Appendix B

Towards PZT Interlayers

B.1 Sol-Z–PZT Transmission Electron Microscopy

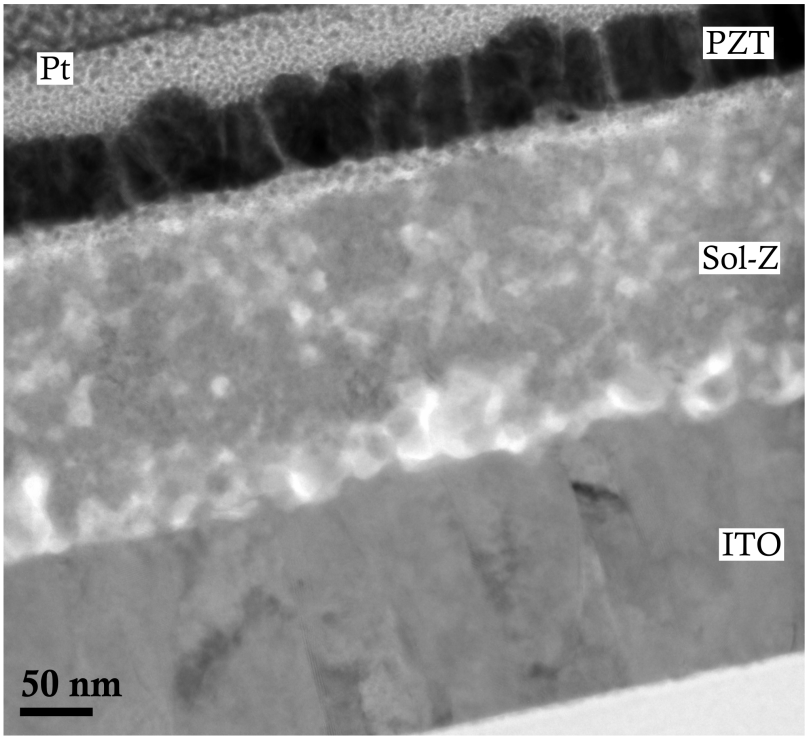

Figure B.1 – TEM micrograph of Sol-Z–PZT cross-section (PZT sol-gel with concentration 0.4 M in [Zr+Ti] used); films were annealed at 5 °C min^{-1} to 530 °C and heated for 30 minutes. The data show the formation of distinct columns of PZT on the ZnO. Micrograph was acquired at a magnification of 43,000 x and a beam energy of 300 kV. Sample preparation and imaging carried out by Dr F. Giuliani.

B.2 Atomic Force Microscopy Grain Analysis

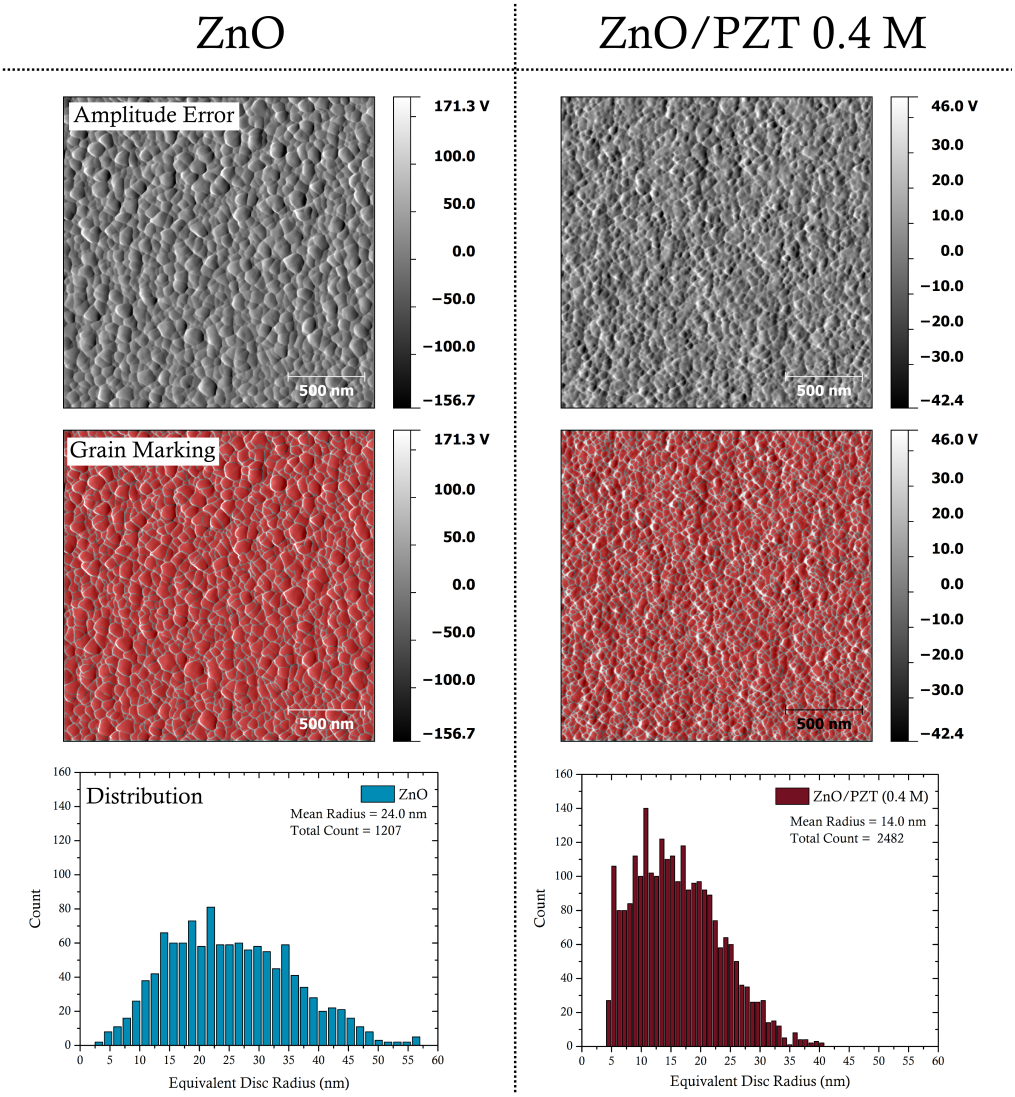

Figure B.2 – Grain radius distributions acquired from the tapping mode AFM amplitude error scans of ZnO and ZnO–PZT thin-films. Grains were marked using the watershed marking algorithm in Gwyddion, followed by minor manual correction. The grain radius distributions for the two films are given in the graphs at the bottom of the figure.

Appendix C

Incorporation of PZT into Hybrid Photovoltaic Devices

C.1 Spray-Pyrolysed ZnO–P3HT Devices

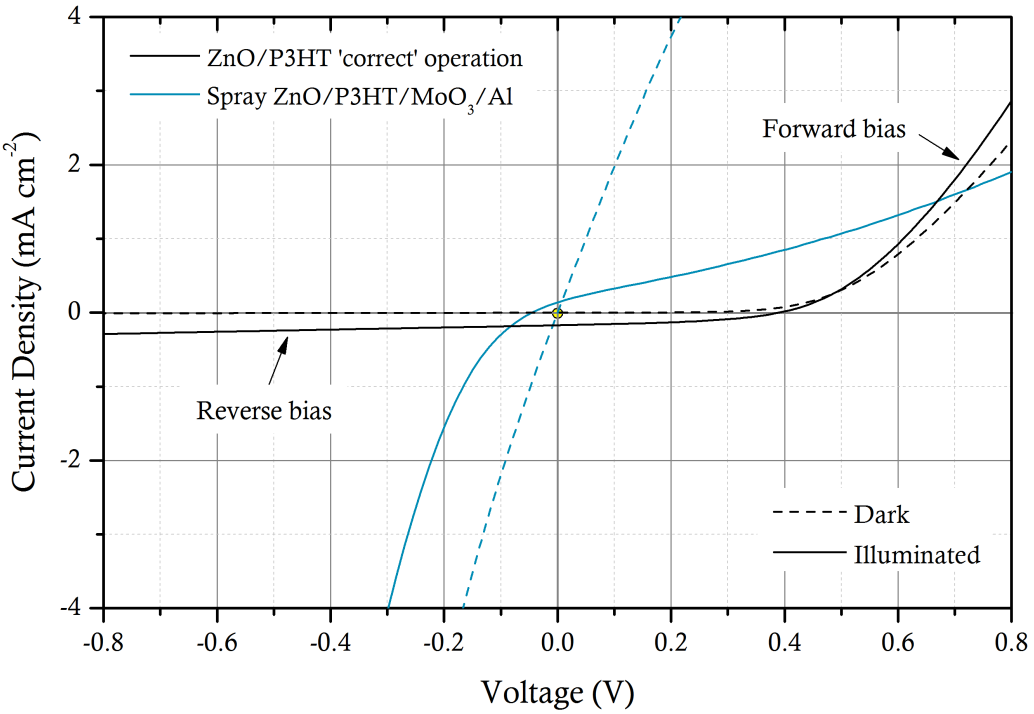

Figure C.1 – Dark and illuminated (100 mW cm^{-2}) current density–voltage curves for a normally functioning ZnO–P3HT inverted bilayer hPV device (*i.e.* reverse bias in the 3^{rd} quadrant), forward bias in the 1^{st} and for a device made using a spray-pyrolysed ZnO layer exhibiting anomalous rectification behaviour.

C.2 Optoelectronic Characterisation

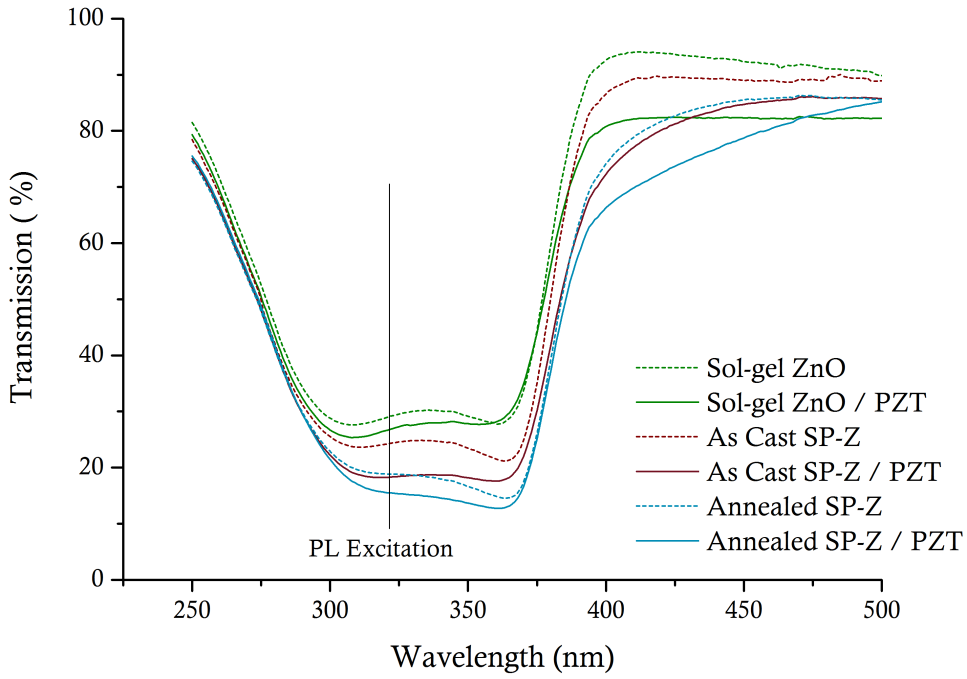

Figure C.2 – UV-vis transmission spectroscopy measurements for ZnO and ZnO–PZT thin-films (where the PZT sol-gel concentration was 0.05 M with respect to the Ti/Zr content) used to correct the PL data given in Figure 5.3. The absorption values used to correct these data were taken at 320 nm.

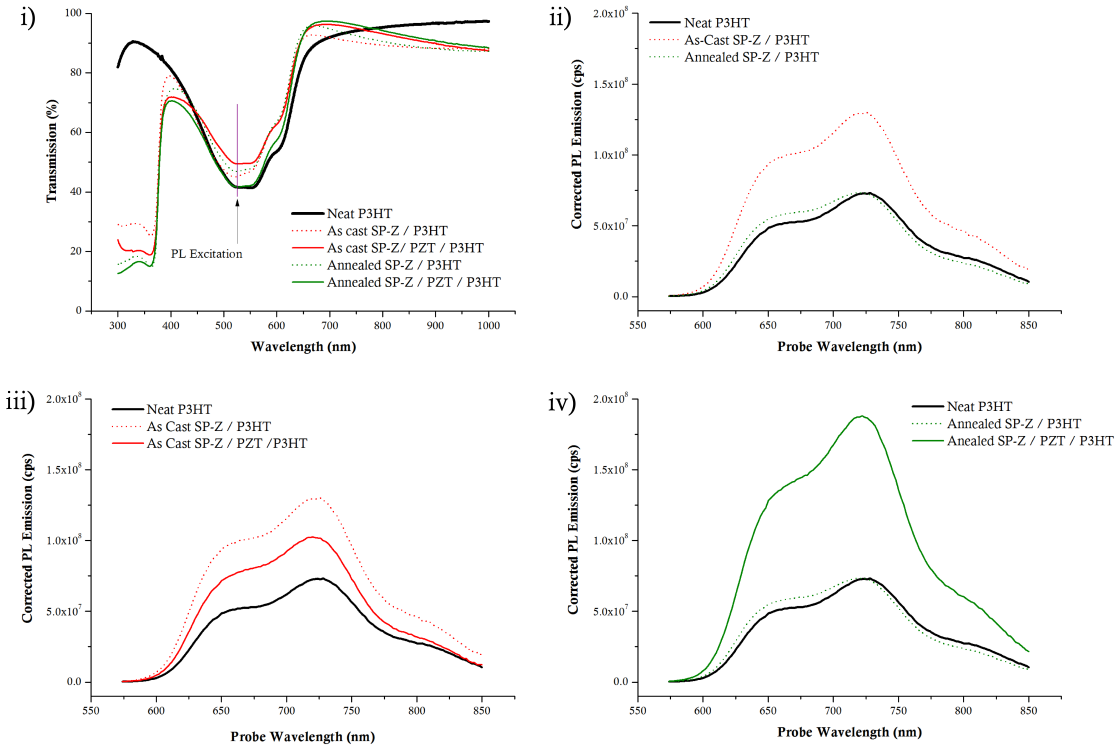

Figure C.3 – Optoelectronic characterisation of spray-pyrolysed ZnO thin-films capped with P3HT: this study compares ZnO films in an as-cast state and ones annealed at 450 °C for 1 hour. For PZT-modified ZnO films, the interlayer was processed from a 0.05 M sol-gel (with respect to Ti/Zr content). For PL measurements, the P3HT was probed by excitation at 520 nm whilst scanning for PL emission in the range 550 – 850 nm. *i)* UV-vis transmission spectroscopy for SP-ZnO–P3HT and SP-ZnO–PZT–P3HT thin-films used to correct the PL data shown in this figure. *ii)* PL emission spectra for SP-ZnO–P3HT films compared to a P3HT reference. *iii)* PL emission spectra showing effect of PZT modification on PL quenching in as-cast SP-ZnO–P3HT films; *iv)* PL emission spectra showing effect of PZT modification on PL quenching in annealed SP-ZnO–P3HT films.

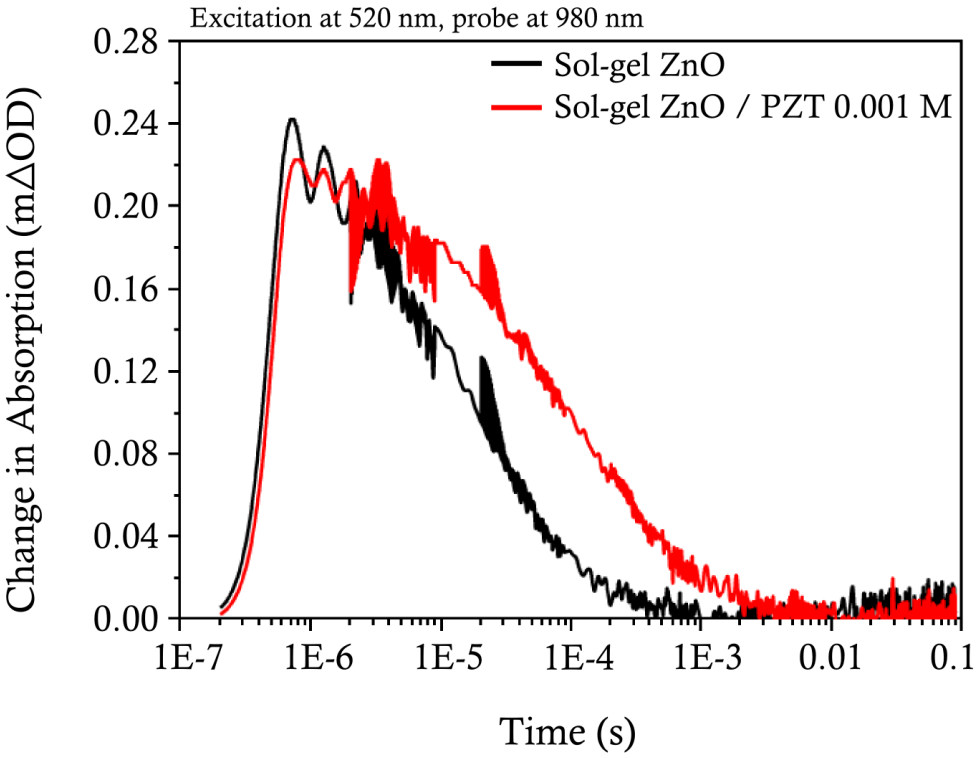

Figure C.4 – Absorption-corrected transient absorption spectroscopy comparing charge recombination in ZnO–P3HT and ZnO–PZT (0.001 M)–P3HT thin-films. The hole lifetimes in P3HT were probed by exciting the polymer at 510 nm and measuring the signal of hole polarons at 980 nm. Figure originally published in K. Prashanthan, *"Transient Absorption Studies on Hybrid Metal Oxide/Polymer Solar Cells"*, MRes Thesis, Imperial College London 2012 (data acquired by K. Prashanthan for samples made in this work); the figure is reproduced here with changes in presentation.

C.3 Devices

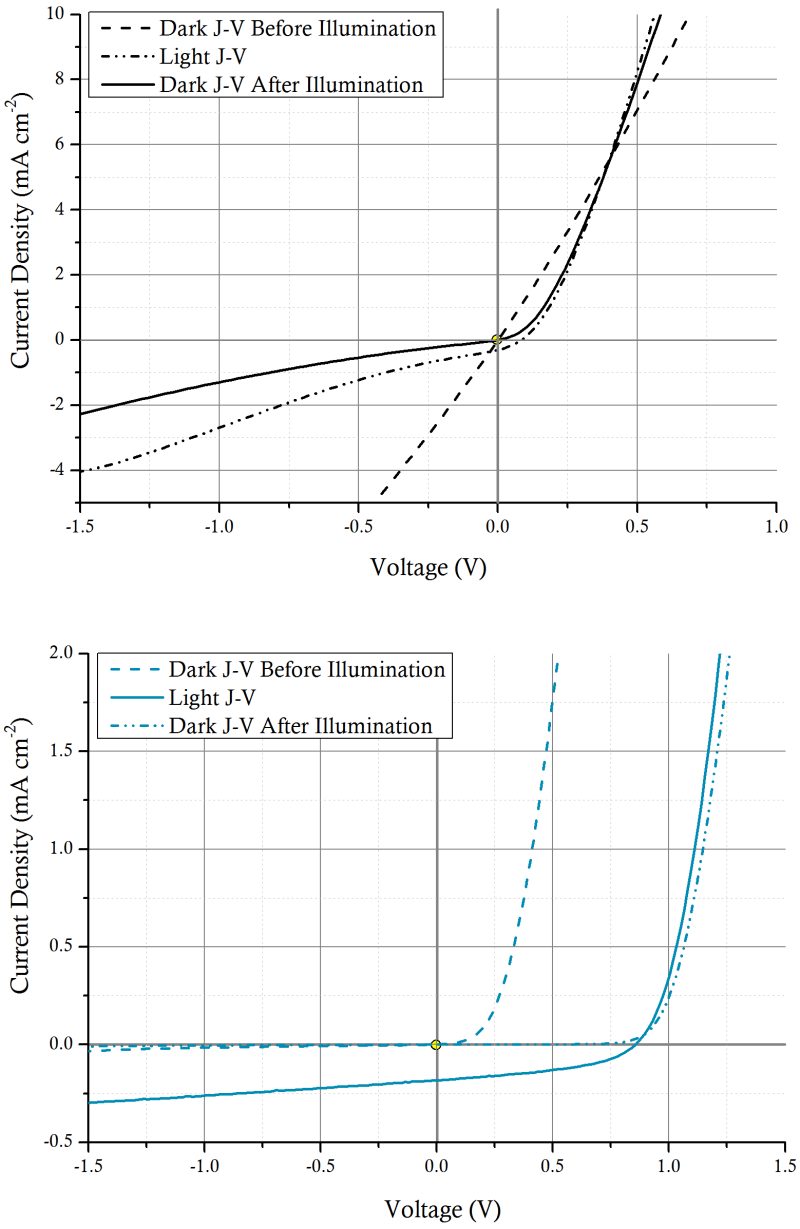

Figure C.5 – Current density–voltage curves for **Top**: Sol-gel ZnO–P3HT inverted bilayer hPV devices; **Bottom**: devices modified with 0.05 M PZT sol-gel (concentration with respect to Ti/Zr content). Figures show J–V characteristics under illumination (100 mW cm^{-2}) as well as curves acquired under dark conditions before and after illumination.